Université de Montréal

Analyse spectroscopique d'étoiles naines blanches riches en hydrogène (DA): vers des modèles d'atmosphère améliorés sans paramètres libres

par
Pier-Emmanuel Tremblay
Département de physique
Faculté des arts et des sciences

Thèse présentée à la Faculté des études supérieures
en vue de l'obtention du grade de
Philosophiæ Doctor (Ph.D.)
en physique

Mars, 2011

Université de Montréal
Faculté des études supérieures

Cette thèse intitulée:

Analyse spectroscopique d'étoiles naines blanches riches en hydrogène (DA): vers des modèles d'atmosphère améliorés sans paramètres libres

présentée par:

Pier-Emmanuel Tremblay

a été évaluée par un jury composé des personnes suivantes:

Paul Charbonneau,	Président-rapporteur
Pierre Bergeron,	Directeur de recherche
François Wesemael,	Membre du jury
Klaus Werner,	Examinateur externe
Jesús Vázquez-Abad,	Représentant du Doyen de la FES

Thèse acceptée le: ______________________

Sommaire

Le but de cette thèse est de raffiner et de mieux comprendre l'utilisation de la méthode spectroscopique, qui compare des spectres visibles de naines blanches à atmosphère riche en hydrogène (DA) à des spectres synthétiques pour en déterminer les paramètres atmosphériques (température effective et gravité de surface). Notre approche repose principalement sur le développement de modèles de spectres améliorés, qui proviennent eux-mêmes de modèles d'atmosphère de naines blanches de type DA.

Nous présentons une nouvelle grille de spectres synthétiques de DA avec la première implémentation cohérente de la théorie du gaz non-idéal de Hummer & Mihalas et de la théorie unifiée de l'élargissement Stark de Vidal, Cooper & Smith. Cela permet un traitement adéquat du chevauchement des raies de la série de Balmer, sans la nécessité d'un paramètre libre. Nous montrons que ces spectres améliorés prédisent des gravités de surface qui sont plus stables en fonction de la température effective.

Nous étudions ensuite le problème de longue date des gravités élevées pour les DA froides. L'hypothèse de Bergeron et al., selon laquelle les atmosphères sont contaminées par de l'hélium, est confrontée aux observations. À l'aide de spectres haute résolution récoltés au télescope Keck à Hawaii, nous trouvons des limites supérieures sur la quantité d'hélium dans les atmosphères de près de 10 fois moindres que celles requises par le scénario de Bergeron et al.

La grille de spectres conçue dans ces travaux est ensuite appliquée à une nouvelle analyse spectroscopique de l'échantillon de DA du SDSS. Notre approche minutieuse permet de définir un échantillon plus propre et d'identifier un nombre important de naines blanches binaires. Nous déterminons qu'une coupure à un rapport signal-sur-bruit $\gtrsim 15$ optimise la grandeur et la qualité de l'échantillon pour calculer la masse moyenne, pour laquelle nous trouvons une valeur de 0.613 $M_\odot$.

Finalement, huit nouveaux modèles 3D de naines blanches utilisant un traitement d'hydrodynamique radiative de la convection sont présentés. Nous avons également calculé des modèles avec la même physique, mais avec une traitement standard 1D de la convection avec la théorie de la longueur de mélange. Un analyse différentielle entre ces deux séries de modèles montre que les modèles 3D prédisent des gravités considérablement plus basses. Nous concluons que le problème des gravités élevées dans les naines blanches DA froides est fort probablement causé par une faiblesse dans la théorie de la longueur de mélange.

Mots clefs:

étoiles : atmosphères — étoiles : structure et évolution — naines blanches — élargissement spectral — convection

Abstract

The goal of this thesis is to refine and to understand better the spectroscopic method, which compares optical spectra of hydrogen-atmosphere white dwarfs (DA) with synthetic spectra to determine the atmospheric parameters (effective temperature and surface gravity). Our approach rests mainly on the development of improved model spectra, which come themselves from DA model atmospheres.

We present a new grid of DA synthetic spectra with the first consistent implementation of the non-ideal gas theory of Hummer & Mihalas and the unified theory of Stark broadening from Vidal, Cooper & Smith. This allows for an adequate treatment of the quenching effects in Balmer lines, without the need of a free parameter. We show that these improved spectra predict surface gravities that are much more stable as a function of the effective temperature.

We then study the long-standing problem that surface gravities in cool DA stars are significantly higher than those found in hotter DA white dwarfs. The hypothesis of Bergeron et al., according to which the atmospheres are contaminated by small amounts of helium, is constrained with observations. Using high-resolution spectra collected at the Keck in Hawaii, we find superior limits on the helium abundances in the atmospheres that are nearly 10 times lower than those required to sustain the Bergeron et al. scenario.

The grid of spectra calculated in this work is then applied to a new spectroscopic analysis of the DA in the SDSS. Our careful analysis allows us to define a cleaner sample and to identify a large number of double degenerates. We find that a cutoff at a signal-to-noise ratio $\gtrsim 15$ optimizes the size and quality of the sample for computing the average mass, for which we find a value of 0.613 $M_\odot$.

Finally, eight new 3D white dwarf models with a radiative-hydrodynamics treatment of the convection are presented. We also calculated models with the same physics, except for a treatment of the convection with the standard mixing-length theory. A differential analysis between these two sets of models shows that the 3D models predict considerably lower surface gravities. We conclude that the high-$\log g$ problem in cool DA white dwarfs is caused by a weakness in the mixing-length theory.

Subject headings:

stars: atmospheres — stars: structure and evolution — white dwarfs — line profiles — convection

Table des matières

Sommaire **i**

Abstract **iii**

Table des matières **v**

Liste des figures **ix**

Liste des tableaux **xiii**

Remerciements **xiv**

1 Introduction **1**

1.1 Les étoiles naines blanches 1

1.2 Approche théorique 5

1.3 Modèles d'atmosphère et spectres synthétiques 6

1.4 Le problème du paramètre libre pour décrire la dissolution des raies d'hydrogène 8

1.5 Le problème des gravités élevées pour les naines blanches froides 9

1.6 Format de cette thèse 10

2 Stark Broadening of Hydrogen Lines **12**

2.1 Abstract 13

2.2 Introduction 13

2.3 Line Broadening Theory 18

2.3.1 Stark Broadening 19

2.3.2 The Unified Theory of Stark Broadening 22

2.3.3 Non-Ideal Equation of State 23

2.4 Stark Broadening Profiles Including Non-Ideal Effects 28

2.4.1 Comparison with Laboratory Experiments 32

2.4.2 Further Theoretical Improvements 34

2.5 Application to White Dwarfs Atmospheres 37

2.5.1 Model Spectra 37

2.5.2 Analysis of the DA Stars in the PG Sample 39

2.5.3 A Reappraisal of Previous Studies of DA White Dwarfs 42

2.6 Conclusion 47

2.7 References 49

3 The High-log g Problem in Cool DAs 53

3.1 Abstract 54

3.2 Astrophysical Context 54

3.3 The Presence of Helium in Cool DA White Dwarfs 58

3.3.1 A Reassessment of the Convective Mixing Scenario 58

3.3.2 Direct Detection of Helium in Cool DA White Dwarfs 64

3.3.3 Helium Contamination in GD 362 67

3.4 Model Atmospheres with Improved Stark Profiles 70

3.5 Evidence from Trigonometric Parallax Measurements 76

3.6 Alternative Solutions to the High-log g Problem 80

3.6.1 Hummer & Mihalas equation-of-state: Neutral Interactions 82

3.6.2 Neutral Broadening 84

3.6.3 Hummer & Mihalas equation-of-state: Charged Particle Interactions . . . 85

3.6.4 H^- Continuum Opacities 86

3.6.5 Convective Energy Transport 86

3.7 Conclusion 89

3.8 References 91

4 Spectroscopic Analysis of DAs from the SDSS 94
4.1 Abstract 95
4.2 Introduction 95
4.3 Data Analysis 98
4.3.1 The SDSS Sample of DA White Dwarfs 98
4.3.2 Model Atmospheres 100
4.3.3 Fitting Procedure 101
4.3.4 *ugriz* Photometry 103
4.4 Results 105
4.4.1 Atmospheric Parameters 105
4.4.2 Mass distribution 110
4.4.3 Comparison of Spectroscopic and Photometric Temperatures 115
4.4.4 Double Degenerate Binaries 117
4.4.5 Helium-Rich DA White Dwarfs 130
4.5 Discussion 132
4.5.1 Reappraisal of Previous Analyses of the SDSS Data Release 4 132
4.5.2 Comparison with Bright DA White Dwarfs 135
4.5.3 Hot DA and DAO White Dwarfs 140
4.5.4 White Dwarf−M Dwarf Binaries 144
4.5.5 Outstanding Objects 145
4.6 Conclusion 148
4.7 References 150

5 Solution to the High-log g Problem 153
5.1 Abstract 154
5.2 Introduction 154
5.3 Improved 3D model atmospheres 157
5.4 Application to the high-$\log \mathbf{g}$ problem 160
5.5 Conclusion 163
5.6 References 164

6 Conclusion **166**

6.1 Profils Stark incluant des effets non-idéaux du gaz 166

6.2 Application de la technique spectroscopique 167

6.3 Le problème des gravités élevées 170

6.4 La prochaine génération de modèles 173

Bibliographie **177**

Annexes **181**

A Complément sur les modèles hydrodynamiques **181**

A.1 Structures 3D 181

A.2 Structures moyennes 182

A.3 Figures 184

Liste des figures

1.1 La séquence spectrale observée dans le visible d'étoiles naines blanches DA. . . 3

2.1 Theoretical line profiles of models at different $T_{\rm eff}$ and $\log g$. 15

2.2 Solutions in a $T_{\rm eff} - \log g$ diagram for a typical DA star using a different number of lines in the fitting procedure. 17

2.3 Total occupation probability for the bound states of hydrogen. 27

2.4 Atomic hydrogen opacity at the photosphere of a 20,000 K DA white dwarf. . . 29

2.5 Stark broadening profiles at $T = 10,000$ K and $\log N_e = 17$. 33

2.6 Emissivity of a hydrogen plasma for the low-density experiment of Wiese et al. (1972). 35

2.7 Same as previous but for the high-density experiment of Wiese et al. (1972). . . 36

2.8 Corrections that must be applied to transform the atmospheric parameters obtained from the VCS profiles to our improved models. 39

2.9 The average dispersion in $T_{\rm eff}$ and $\log g$ between solutions obtained from fits that include 2 to 5 lines. 41

2.10 Fit of WD 0205+250 with our improved line profiles and with the VCS profiles. 42

2.11 Mass versus $T_{\rm eff}$ distribution for the DA stars in the PG sample in the range 40,000 K $> T_{\rm eff} >$ 13,000 K. 43

2.12 Differences in $T_{\rm eff}$ and $\log g$ obtained with our improved models and with the previous grid. 45

2.13 Mass distributions for our subsample of PG stars. 46

2.14 Comparison of absolute visual magnitudes. 47

3.1 Distribution of $\log g$ as a function of $T_{\rm eff}$ for DA white dwarfs drawn from the sample of Gianninas et al. 57
3.2 Our best spectroscopic and photometric fits to the DA star LHS 3254. 60
3.3 Helium abundance determinations as a function of $T_{\rm eff}$ for cool DA white dwarfs. 61
3.4 Mass distribution as a function of $T_{\rm eff}$ with and without traces of helium in the atmospheres. 62
3.5 Location of the hydrogen convection zone as a function of effective temperature in the pure hydrogen envelope of a 0.6 $M_\odot$ DA white dwarf. 63
3.6 High-resolution spectra for the six white dwarfs observed with the HIRES spectrograph on the Keck I 10-m telescope. 66
3.7 The observed HIRES spectrum of GD 362 from the Keck Observatory Archive. 68
3.8 Effective temperatures of ZZ Ceti stars derived from UV spectra compared with the optical determinations. 72
3.9 Mass distribution as a function of $T_{\rm eff}$ for the DA white dwarfs in the sample of Gianninas et al. 74
3.10 Solutions in a $T_{\rm eff} - \log g$ diagram for a ZZ Ceti star using 2 to 5 lines in the fitting procedure. 75
3.11 Differences between white dwarf parameters determined from the spectroscopic and photometric methods. 78
3.12 Same as Figure 3.11 but with a photometric sample drawn from the survey of Subasavage et al. (2009). 80
3.13 Comparison of photometric and spectroscopic solutions to spectroscopic observations. 81
3.14 Experiments with the physiscs in the model atmospheres. 83

4.1 Distribution of S/N for all 8717 DA spectra in the SDSS-E06 sample. 98
4.2 Sample fits for 20 DA stars in the SDSS sample. 104
4.3 Mass distribution as a function of $T_{\rm eff}$ for DA stars in the SDSS. 109
4.4 Illustration of our visual inspection procedure. 111
4.5 Same as Figure 4.4. 112

4.6 Mean mass and mass dispersion of the DA stars in the SDSS as a function of the S/N of the observations. 113

4.7 Mass distribution for the DA stars in the SDSS with 40,000 K > $T_{\rm eff}$ > 13,000 K. 114

4.8 Comparison of spectroscopic and photometric temperatures. 116

4.9 Simulation of DA+DA and DA+DB/DC binaries with synthetic models. 118

4.10 Our best fits for 35 double degenerate candidates in the SDSS sample. 121

4.11 Same as Figure 4.10. 122

4.12 Superposition of the predicted and observed photometry for two objects taken from Figures 4.10 and 4.11. 123

4.13 The DA+DB and DAB solutions for J015221.12−003037.3. 127

4.14 Similar to Figure 4.10 but with an assumed hydrogen abundance of H/He = 10^{-3} for the helium-rich components. 128

4.15 Our best fits to two DA stars with mixed H/He model atmospheres. 132

4.16 Comparison of atmospheric parameters between our analysis and that of Eiseinstein et al. (2006). 134

4.17 $T_{\rm eff}$ and $\log g$ differences for the 89 DA stars in common between the SDSS and Gianninas et al. samples. 137

4.18 Mass distributions as a function of $T_{\rm eff}$ for the SDSS sample and the Gianninas et al. sample. 139

4.19 Mean mass of the SDSS sample for $T_{\rm eff} < 13,000$ K computed in 1000 K temperature bins. 140

4.20 Comparison of our $T_{\rm eff}$ and $\log g$ determinations with those of Silvestri et al. (2006) for the sample of DA−M dwarf binaries in the SDSS. 146

4.21 Mass distribution of our sample of DA−M dwarf binaries. 147

5.1 Surface gravity distribution as a function of $T_{\rm eff}$ for the SDSS sample; see Tremblay et al. (2011) for details on these determinations. An evolutionary model from Fontaine et al. (2001) at the median mass of the sample (0.59 $M_\odot$) is shown as a dashed line. 155

5.2 Temperature structure for the 3D white dwarf model at $T_{\rm eff} = 11,975$ K and $\log g = 8$, for a slice in the horizontal-vertical xz plane through a box with coordinates x, y, z (in km). The temperature is color coded from 60,000 K (yellow) to 8000 K (blue). The arrows represent relative convective velocities (integration time of 20 ms), while thick lines correspond to contours of constant Rosseland optical depth. 159

5.3 Temperatures versus Rosseland optical depth for $\langle 3{\rm D}\rangle$ (solid lines) and $1{\rm D}_{\rm MLT}$ (dashed lines) non-gray simulations at $T_{\rm eff}$ = 11,300, 11,975, 12,390 and 12,800 K (shifted on the vertical axis by 0, 2, 4 and 6 kK, respectively, for clarity). . 160

5.4 Comparison of Hβ line profiles calculated with Linfor3D for the 3D (solid lines, averaged over 12 selected snapshots) and $1{\rm D}_{\rm MLT}$ (dashed lines) models in the case of two non-gray simulations at $T_{\rm eff}$ of 11,300 K and 12,390 K (the latter shifted by 0.2 units of flux for clarity). The dotted lines (indistinguishable from the 3D spectra in the figure) also show the $\langle 3{\rm D}\rangle$ profiles resulting from spatial and temporal averages of the 3D structures. 161

5.5 Non-gray (filled circles) and gray (filled squares) 3D $\log g$ corrections. In comparison, we show the shifts in surface gravity required to obtain a stable $\log g$ distribution as a function of $T_{\rm eff}$ using the samples of the SDSS (open circles, also displayed in Fig. 5.1) and Gianninas et al. (2009; open squares). The points are connected for clarity. 162

6.1 Effet des profils Stark avec effets non-idéaux pour 140,000 K $> T_{\rm eff} >$ 6000 K. . 167

6.2 Changement prédit des paramètres atmosphériques pour les modèles calculés dans cette thèse par rapport à la génération précédente. 169

6.3 Profils Stark de raies de Lyman. 171

6.4 Ajustement du χ^2 pour des observations FUSE de DA. 172

A.1 Atmosphère trois dimensions à 12,800 K. 184

A.2 Atmosphère trois dimensions à 12,390 K. 185

A.3 Atmosphère trois dimensions à 11,300 K. 186

Liste des tableaux

2.1 Opacity Sources Included 37

3.1 Upper Limits on the Helium Abundance in Cool DA White Dwarfs 65

4.1 SDSS DR4 Sample of DA White Dwarfs with S/N > 12 107

4.2 DA White Dwarfs with Multiple Measurements 108

4.3 DA+DB/DC Binary Candidates 124

4.4 Mean Properties of DA White Dwarf Samples 136

4.5 SDSS DR4 Sample of DAO White Dwarfs with S/N > 12 143

5.1 Parameters of our 3D model atmospheres 158

Remerciements

Je tiens à remercier en premier lieu Pierre Bergeron, mon directeur de recherche, qui m'a permis de concevoir qu'il restait des problèmes à résoudre avec la méthode spectroscopique. Pierre doit être crédité pour avoir trouvé la démarche nécessaire et avoir obtenu les codes (par M. Lemke que nous remercions également) pour résoudre le problème des profils Stark. Je lui suis également reconnaissant pour m'avoir encouragé à chercher les pistes de solutions pour le problème des gravités élevées, même si nous étions loin d'être certain de trouver une solution. Les meilleurs projets de doctorat sont souvent ceux dont on commence juste à comprendre la solution, à l'étape de l'écriture de la thèse, et qui ouvrent la voie sur plusieurs applications.

Je remercie Hans Ludwig et Matthias Steffen pour l'utilisation de leurs codes et leur collaboration aux Chapitre 5. De plus, je tiens à remercier Dimitri Mihalas que j'ai rencontré à Denver en 2008. Pour résumer dans mes mots un de ses conseils: à la place de chercher à résoudre un problème avec des approximations ou des codes incomplets, autant mieux recommencer avec la meilleure approche physique possible, peu importe le temps et l'effort que cela prendra.

J'aimerais remercier en particulier mes parents, Michel et Guylaine, pour m'avoir donné l'occasion de partager les joies et les peines lors du travail menant à chacun des mes quatre articles, et d'avoir relu certains textes. Merci également à Gilles Fontaine, Detlev Koester, Alex Gianninas et Jason Kalirai pour leur apport scientifique. Je remercie finalement mais non les moindres, tous mes amis (incluant les collègues de bureau!) pour leur support moral!

À mon père

Chapitre 1

Introduction

1.1 Les étoiles naines blanches

Les naines blanches sont des astres évolués qui représentent l'état rémanent des étoiles de faible masse (environ de 0.07 à 8 $M_{\odot}$) de la séquence principale ayant terminé les phases de combustion nucléaire. C'est la phase ultime pour près de 97% des étoiles dans notre galaxie. Après avoir brûlé paisiblement de l'hydrogène sur la séquence principale pendant une large fraction de leur existence, ces étoiles de faible masse vont passer rapidement dans le haut du diagramme Hertzsprung-Russell (forte luminosité) en activant le brûlage de l'hélium, laissant au centre un coeur inerte de carbone et d'oxygène. Si la masse de l'étoile est plus faible que $\sim$8 $M_{\odot}$, la valeur centrale de la température ne sera pas assez élevée pour permettre la combustion d'éléments plus lourds que l'hélium. L'étoile entrera ultimement dans la branche des géantes asymptotiques où elle terminera la combustion nucléaire dans les couches externes et subira une forte perte de masse. Cette perte de masse vers le milieu interstellaire sera responsable de la création d'une nébuleuse planétaire. L'objet central aura entre-temps éliminé par combustion ou éjection l'essentiel de l'hélium et de l'hydrogène initialement présents dans l'astre, y laissant un coeur de carbone et d'oxygène, chaud et dénudé d'éléments plus légers. Sans l'énergie apportée par les réactions nucléaires, l'étoile sera forcée de se contracter jusqu'à ce que l'équilibre hydrostatique soit soutenu par la pression de dégénérescence électronique. C'est à ce moment que l'étoile devient une naine blanche.

L'évolution d'une naine blanche est largement déterminée par la dissipation de l'énergie interne par la voie de l'atmosphère, conduisant ainsi à la diminution de la température photosphérique. La température effective de l'atmosphère ($T_{\rm eff}$) est de l'ordre de la centaine de milliers de degrés pour les objets les plus jeunes. Une naine blanche de masse moyenne (0.6 $M_\odot$) évolue sur près de 9 milliards d'années pour se refroidir jusqu'à ∼4000 K. C'est donc, avec la séquence principale, l'une des deux phases longues et paisibles de l'existence d'un astre. Puisque l'opacité de l'atmosphère face au rayonnement sortant détermine le taux de perte d'énergie des naines blanches, notre compréhension de l'évolution des naines blanches commence ainsi par une compréhension des paramètres atmosphériques (température effective, composition et gravité de surface).

Les naines blanches ont une relation masse−rayon en raison de la pression de dégénérescence qui gouverne leur structure. Il est donc possible de convertir la gravité de surface ($\log g$) en masse stellaire avec l'aide d'un modèle de la structure interne. Puisque la pression de dégénérescence ne dépend pas de la température électronique, l'approximation d'une température nulle constitue généralement une bonne approximation (Hamada & Salpeter 1961). Cependant, pour atteindre une précision meilleure que ∼5% sur la détermination de la masse, on doit inclure l'effet de la température finie des couches stellaires, ces valeurs de températures étant calculées à partir d'un modèle évolutif (Wood 1995). C'est ensuite en comparant la distribution observée des gravités de surface et des températures effectives avec des modèles d'évolution qu'on pourra remonter dans le temps et retracer l'historique des naines blanches (âges, progéniteurs) et de notre galaxie (voir Fontaine et al. 2001, pour une introduction à la *cosmochronologie*). En principe, l'histoire complète de la formation stellaire dans notre galaxie peut être reconstruite, à condition qu'on ait une relation fiable entre la masse des naines blanches et celle de leur progéniteur de la séquence principale (Bergeron et al. 1992).

La composition chimique représente une caractéristique importante de l'atmosphère des naines blanches. On prédit, par le tri gravitationnel, que tous les éléments plus lourds que l'hydrogène vont rapidement chuter au bas de l'atmosphère lors de l'évolution de ces objets (Schatzman 1958; Paquette et al. 1986). En effet, une forte majorité (75%) des étoiles naines blanches possèdent une atmosphère dominée par l'hydrogène, dont la caractéristique principale

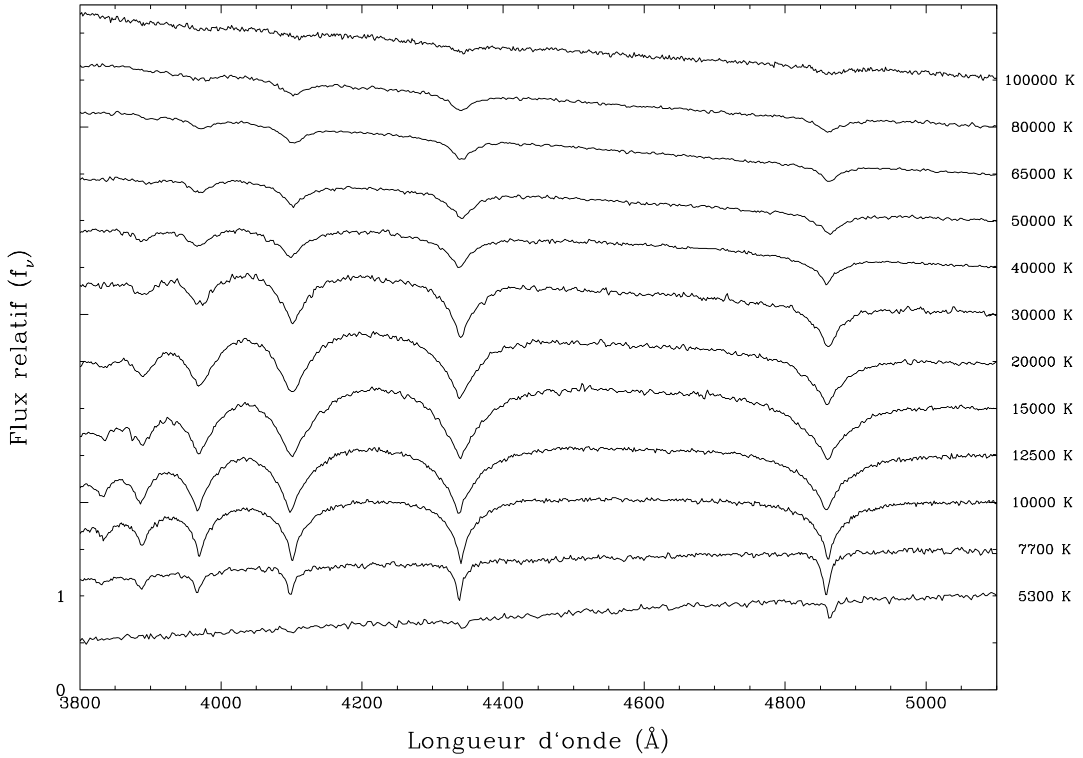

FIGURE 1.1 – La séquence spectrale observée dans le visible d'étoiles naines blanches DA. L'axe à la droite présente la température effective approximative de chaque étoile déterminée à l'aide de modèles d'atmosphère. Le flux maximum est normalisé à 5100 Å et les spectres sont déplacés d'une unité de flux pour plus de clarté.

est la présence de raies de la série Balmer dans le spectre visible (type spectral DA). La Figure 1.1 présente la séquence évolutive des étoiles DA avec des spectres observés à différentes températures effectives. L'opacité des raies de la série de Balmer possède un maximum autour de $T_{\rm eff} \sim 13,000$ K lorsque le niveau $n = 2$ de l'atome d'hydrogène devient le plus peuplé. En bas de $T_{\rm eff} \sim 5,000$ K, l'opacité des raies d'hydrogène est trop faible pour que ces dernières soient visibles dans le spectre. Le type spectral DC est utilisé pour désigner ces étoiles ne montrant aucune raie d'absorption[1]. Ce sont les naines blanches DA qui seront l'objet de cette thèse.

Même si la plupart des étoiles DA sont semblables du point de vue de leur spectre, ce

---

[1] Notons que les types spectraux DA et DC ne garantissent pas forcément que l'atmosphère soit composée majoritairement d'hydrogène; en bas de $T_{\rm eff} \sim 11,000$ K, l'hélium est invisible et peut être, en principe, en n'importe quelle proportion dans l'atmosphère.

n'est pas nécessairement le cas pour leur structure interne. On pense que les naines blanches naissent avec des fractions de masse d'éléments légers par rapport à la masse totale qui peuvent varier de façon significative. On obtient les fractions de masse canoniques d'éléments légers dans les naines blanches en considérant les masses supérieures permises sans qu'il y ait une destruction par combustion nucléaire ($M_{\rm He}/M_{\rm tot} \sim 10^{-2}$ et $M_{\rm H}/M_{\rm tot} \sim 10^{-4}$, voir Iben 1984). Ces éléments légers seraient superposés en couches distinctes apposées sur le coeur de carbone/oxygène. Il y aurait cependant une dichotomie dans la fraction de masse d'hydrogène, c'est-à-dire avec une classe d'étoiles ayant la fraction canonique de $M_{\rm H}/M_{\rm tot} \sim 10^{-4}$ et une classe d'étoiles dites "Born Again" ayant pratiquement épuisé leur hydrogène ($M_{\rm H}/M_{\rm tot} \sim 10^{-15}$) par le brûlage nucléaire lors de multiples excursions sur la branche des géantes asymptotiques (Werner & Herwig 2006). On pense que les objets avec une faible fraction totale d'hydrogène seraient la source des étoiles non-DA observées, la plupart ayant des atmosphères riches en hélium (type spectral DO, DB, DC, DQ ou DZ, voir Sion et al. 1983)[2].

L'inachèvement du tri gravitationnel ainsi que des processus physiques tels que la convection et l'accrétion seraient responsables de maintenir l'hélium en équilibre à la surface des naines blanches non-DA. Puisque ces processus varient en intensité lors de l'évolution de ces objets, ils pourraient causer une évolution spectrale où l'atmosphère change de composition (Strittmatter & Wickramasinghe 1971; Baglin & Vauclair 1973; Fontaine & Wesemael 1987, 1991). On observe empiriquement ce phénomène avec un changement du ratio de DA sur non-DA autour de $T_{\rm eff} \sim 30,000$ K (Liebert et al. 1986; Eisenstein et al. 2006b), puis à $T_{\rm eff} \sim 10,000$ K (Sion 1984; Tremblay & Bergeron 2008). Dans les deux cas, un processus de mélange convectif (ou de dilution convective) entre les couches d'hélium et d'hydrogène serait en cause. Cela démontre que l'étude de tous les types de naines blanches est nécessaire pour bien comprendre leur évolution. Néanmoins, l'analyse du comportement des étoiles DA, qui constituent de loin le plus grand échantillon homogène à toutes les phases de l'évolution, est certainement le point de départ de cette étude. De plus, en considérant que la microphysique

---

[2] Notons également une découverte récente de grande importance; dans de rares circonstances, des naines blanches auraient aussi éliminé la plupart de l'hélium, laissant une atmosphère majoritairement composée de carbone et d'oxygène (Dufour et al. 2007).

est mieux comprise pour l'hydrogène, l'étude des naines blanches DA constitue le moyen de déterminer les propriétés globales des naines blanches avec le plus de précision possible.

1.2 Approche théorique

La comparaison entre les profils observé et théorique des raies de la série de Balmer dans les étoiles naines blanches DA, aussi appelée la méthode spectroscopique, est historiquement la méthode qui a obtenu le plus de succès dans la détermination des paramètres atmosphériques (Weidemann & Koester 1980; Schulz & Wegner 1981; Holberg et al. 1985; Bergeron et al. 1992). Cela est dû au fait que le profil des raies est très sensible aux variations des valeurs de $T_{\rm eff}$ et $\log g$ (Wegner & Schulz 1981, voir aussi le Chapitre 2). Il est à noter que la technique spectroscopique peut également être étendue aux raies de la série de Lyman (Holberg et al. 1986; Barstow et al. 2003) afin de déterminer les paramètres atmosphériques de manière relativement indépendante à l'analyse du spectre visible. En comparaison avec les méthodes de minimisation photométrique utilisées auparavant (e.g., Shipman 1979; Koester et al. 1979; Fontaine et al. 1985), la méthode spectroscopique possède une erreur intrinsèque beaucoup plus faible, ce qui permet de comparer plus précisément les paramètres atmosphériques entre les différentes étoiles observées (paramètres *relatifs*). De plus, la photométrie est très peu sensible à la gravité, et on doit utiliser une autre mesure, en général la parallaxe trigonométrique, pour contraindre la gravité. Hormis pour les naines blanches les plus proches, de telles mesures sont généralement difficiles à prendre avec précision. L'objectif global de cette thèse est d'améliorer la précision ainsi que d'obtenir une meilleure compréhension de la technique spectroscopique.

Avec l'étude statistique de grands échantillons, c'est la méthode spectroscopique qui a permis de définir, entre autres, la forme de la distribution de masses des naines blanches (Bergeron et al. 1992; Eisenstein et al. 2006a; Koester et al. 2009b), l'efficacité convective et même la forme de la bande d'instabilité des naines blanches pulsantes ZZ Ceti (Koester et al. 1994; Bergeron et al. 1995). On connaît aujourd'hui plus de 10,000 étoiles naines blanches de type DA. La méthode la plus fiable pour analyser ces objets est d'utiliser des échantillons représentatifs (i.e. le plus complet en volume possible) et homogènes (i.e. avec des observations reproductibles). On retrouve aujourd'hui plusieurs échantillons qui possèdent ces propriétés, comme le relevé de Palomar-Green, le Sloan Digital Sky Survey, le White Dwarf Catalog et le SPY (dans l'ordre: Liebert et al. 2005; Eisenstein et al. 2006a; Gianninas et al. 2009; Koester et al. 2009b). L'analyse de ces banques de spectres et la détermination de leurs propriétés représentent le cadre astrophysique immédiat de notre développement théorique.

1.3 Modèles d'atmosphère et spectres synthétiques

Une composante importante du succès de la technique spectroscopique repose sur l'exactitude des modèles de spectres synthétiques. Ces spectres sont eux mêmes calculés à partir de modèles d'atmosphère. En particulier, la détermination des paramètres atmosphériques *absolus* dépend fortement du niveau de perfectionnement des modèles d'atmosphère. Ce sont ces paramètres qui peuvent ensuite décrire les propriétés moyennes des naines blanches. Les modèles d'atmosphère de naines blanches ont grandement évolué depuis qu'ils se sont formés à partir de la théorie de base des atmosphères 1D à plans parallèles (voir, e.g., Mihalas 1978). Depuis les premiers modèles de spectres de naines blanches (voir, e.g., Wickramasinghe 1972; Shipman 1977; Koester et al. 1979; Wesemael et al. 1980), des améliorations ont été proposées sur deux fronts, soit celui de la microphysique (un aspect local qui tient seulement compte de l'état du plasma), et celui de la physique des modèles (un aspect global qui est propre aux atmosphères stellaires).

La microphysique est la partie de base d'un modèle d'atmosphère et comprend le calcul de l'équation d'état et de l'opacité du gaz d'hydrogène. Ultimement, on cherche à déterminer, pour des valeurs de température et de pression données, quelles vont être les propriétés thermodynamiques et statistiques du gaz et quelle va être son opacité face au rayonnement incident. Au niveau de la détermination de l'équation d'état du gaz d'hydrogène, la plus grande révolution fut l'avènement de l'équation d'état non-idéale de Hummer & Mihalas (1988), propre aux atmosphères stellaires denses. Cette théorie, dite de probabilité d'occupation des états quantiques, fut intégrée dans les modèles de naines blanches par Bergeron et al. (1991), et ensuite par D. Koester de façon parallèle (Finley et al. 1997). Cette nouveauté a eu un impact immédiat et important sur la précision des modèles. Une fois qu'on a déterminé les populations des états possibles du gaz, on peut procéder au calcul de l'opacité.

Connaissant les propriétés du gaz, on commence par définir la structure en pression de l'atmosphère à l'aide de la contrainte de l'équilibre hydrostatique. Ensuite, l'équation de transfert radiatif est résolue de façon itérative sous la contrainte de l'équilibre radiatif (voir le Chapitre 2 de Mihalas 1978), pour finalement déterminer la structure thermodynamique (T, P) de l'atmosphère ainsi que le flux émergent. Une grande avancée dans cette partie du calcul de modèles est survenue avec la levée de l'approximation de l'équilibre thermodynamique local (Hubeny et al. 1994). Cette prise en compte des effets dits hors-ETL, où le rayonnement émergent influence les populations atomiques locales, devient importante pour les naines blanches chaudes ($T_{\rm eff} > 40,000$ K). Dans un autre ordre d'idée, des progrès ont été effectués au niveau de la modélisation du transfert d'énergie par convection, qui s'ajoute au transfert par radiation dans les DA plus froides que $T_{\rm eff} \sim 13,000$ K. Koester et al. (1994) et Bergeron et al. (1995) ont calibré la théorie de la longueur de mélange pour être en mesure de produire des spectres réalistes dans le cadre de ce formalisme.

L'analyse spectroscopique de Bergeron et al. (1992), la première à présenter une étude simultanée de plusieurs raies de la série de Balmer dans le cadre de l'analyse d'un grand échantillon de DA, présente des incertitudes *relatives* très faibles, de l'ordre de 1%, sur les paramètres atmosphériques. Ce résultat pourrait faire croire, à tort, que les modèles de naines blanches de DA sont essentiellement complets. Il est vrai que la simplicité apparente de l'atome d'hydrogène permet de croire que les modèles de naines blanches sont parmi les plus précis en comparaison, par exemple, avec des atmosphères où il y a plusieurs centaines, voire des milliers de raies provenant de divers éléments chimiques. Pourtant, des améliorations significatives ont été réalisées ces dernières années, même par rapport à la physique de l'hydrogène (e.g., Allard et al. 2004), et il reste certains problèmes importants à préciser et à résoudre. Nous aborderons deux grandes incertitudes sur la méthode spectroscopique au cours de cette thèse, les deux ayant comme source un paramètre libre qui remplace un aspect physique qui est mal compris.

1.4 Le problème du paramètre libre pour décrire la dissolution des raies d'hydrogène

La modélisation du profil des raies dépend fortement de notre compréhension de la structure quantique des niveaux atomiques. Dans les conditions atmosphériques des naines blanches, c'est l'effet des perturbations des particules chargées du plasma qui est la principale source d'élargissement spectral, qu'on appelle également l'élargissement par effet Stark[3]. À ce titre, la théorie unifiée de Vidal et al. (1970, aussi VCS) demeure celle qui a obtenu le plus de succès pour prédire les raies d'hydrogène. Cette théorie utilise l'approximation statique et un effet Stark linéaire pour la perturbation des protons, et la théorie d'impacts classique pour les collisions avec les électrons. La théorie unifiée de VCS est équivalente à considérer des transitions à deux niveaux quantiques principaux indépendants. Or, on s'aperçoit à la Figure 1.1 que les raies se chevauchent et donc, on ne peut pas considérer les transitions comme complètement indépendantes.

Dans les plasmas à haute densité, caractéristiques des atmosphères de naines blanches, les effets non-idéaux sur le gaz deviennent importants. Notamment, les forts microchamps électriques causés par les protons peuvent forcer la dissociation de niveaux atomiques excités. Les électrons peuvent aussi dissocier des niveaux, puisque pendant une collision rapide, l'énergie d'un état lié est incertaine (principe d'incertitude de Heisenberg). L'équation d'état de Hummer & Mihalas prend en considération ces interactions de façon probabiliste. Cependant, Seaton (1990) a été le premier à affirmer que le formalisme de Hummer & Mihalas doit également être inclus à l'intérieur même du calcul des profils d'élargissement spectral. En effet, lorsqu'un fort microchamp électrique est appliqué à un atome, il perd des états liés et donc, certaines transitions de type lié-lié ne sont plus possibles. La théorie unifiée de VCS, par exemple, ne tient pas compte de cet effet.

Sans ressource pour recalculer des nouveaux profils Stark, Bergeron (1993) proposa d'utiliser un paramètre libre pour imiter les effets non-idéaux dans le calcul des profils de raies. Le premier objectif de cette thèse est d'ajouter le formalisme du gaz non-idéal de Hummer &

---

[3] L'exception à cette règle est pour les naines blanches DA plus froides que $T_{\text{eff}} \sim 8000$ K, où l'élargissement par les neutres est le plus important.

Mihalas à l'intérieur même du cadre théorique de la théorie unifiée de VCS. Cela permettra finalement d'avoir une intégration cohérente des deux théories dans les modèles d'atmosphère et cela, sans la nécessité d'un paramètre libre. Une description réaliste du chevauchement entre les raies pourra ainsi être obtenue, à défaut d'avoir, pour notre plasma, une description quantique selon les principes premiers.

1.5 Le problème des gravités élevées pour les naines blanches froides

Un problème majeur qui est observé depuis les débuts de l'utilisation de la technique spectroscopique est que la valeur moyenne des gravités de surface des naines blanches froides en deçà de ∼13,000 K (Bergeron et al. 1990) est beaucoup plus élevée que celle des naines blanches plus chaudes (Bergeron et al. 1992). La différence observée correspond à un effet de ∼20% en terme de masse. On constate ce problème dans tous les grands échantillons de DA discutés à la Section 1.2. Il semble très peu probable que ce soit un effet réel puisqu'on prédit que les naines blanches se refroidissent à masse constante. On suspecte donc que le problème pourrait être relié à une mauvaise hypothèse de départ dans la technique spectroscopique (e.g., la supposition d'une composition pure en hydrogène) ou une modélisation inadéquate de la physique dans les modèles. Contrairement au problème de la section précédente, il n'y a pas de piste de solution unique. Jusqu'à maintenant, aucune explication robuste ne fut proposée.

On sait depuis longtemps que les effets d'une gravité élevée ou d'une atmosphère contaminée avec de l'hélium sont très similaires sur le spectre prédit d'une étoile DA froide (e.g., Liebert & Wehrse 1983). Bergeron et al. (1990) ont démontré quantitativement que l'on ne pouvait pas différencier les deux phénomènes. Bergeron et al. ont donc suggéré la première solution au problème des gravités élevées, soit que les naines blanches DA froides ont, en moyenne, des valeurs de $\log g$ normales, mais possèdent une contamination systématique de leur atmosphère par de l'hélium. Le mécanisme physique responsable de la composition mixte de l'atmosphère serait le mélange convectif entre les couches d'hélium et d'hydrogène (Strittmatter & Wickramasinghe 1971; Koester 1976; Vauclair & Reisse 1977; Dantona & Mazzitelli

1979). On a longtemps pensé qu'il était impossible de vérifier ce scénario directement parce que l'hélium est *invisible* dans ces conditions (i.e. il ne possèderait pas de raies observables aux abondances et températures prédites). Pourtant, dans les naines blanches les plus chaudes pour lesquelles on observe le problème des $\log g$ élevés, le scénario de mélange convectif prédit des raies d'hélium certes très faibles (d'une profondeur d'environ $\sim$1% par rapport au flux total), mais en principe observables à une résolution et un rapport signal sur bruit très élevés. En utilisant un télescope suffisamment gros ($>$ 8m), on a récemment pu observer des raies d'hélium dans des DA plus froides que $\sim$12,000 K (Koester et al. 2005; Zuckerman et al. 2007). Cela indique que le scénario de mélange convectif de Bergeron et al. (1990) pourrait être contraint de façon directe par les observations.

Bergeron et al. (2007) et Koester et al. (2009a) ont revu le problème des gravités élevées, en énumérant les pistes de solutions possibles. En particulier, Koester et al. (2009a) concluent que la théorie de la longueur de mélange (MLT), présentement utilisée dans les modèles pour traiter la convection (Bergeron et al. 1995), est la seule source d'incertitude assez grande pour expliquer le problème. Cette théorie est basée sur des paramètres libres, dont la longueur de mélange, qui décrit le trajet des bulles convectives jusqu'à leur dissolution dans le milieu ambiant (Böhm-Vitense 1958). Même sans avoir une preuve évidente que ce modèle est inadéquat, un traitement amélioré de la convection dans les modèles, sans l'usage de paramètres libres, serait souhaitable. Ludwig et al. (1994) et Steffen et al. (1995) ont, à ce titre, calculé des modèles de naines blanches avec un traitement d'hydrodynamique radiative de la convection, sans paramètre libre. Ils ont montré que les spectres résultants de leurs simulations 2D étaient similaires aux spectres standards. Néanmoins, une étude quantitative des différences entre ces deux théories convectives s'avère nécessaire pour mieux comprendre le problème des gravités élevées.

1.6 Format de cette thèse

Cette thèse comprend quatre articles publiés ou soumis dans le *Astrophysical Journal* ou le *Astronomy & Astrophysics*. L'ensemble de ces articles a comme point central la technique spectroscopique. Le Chapitre 2 y décrira, premièrement, l'état actuel des modèles d'atmosphère dont notre point de départ est la grille de modèles décrite dans Liebert et al. (2005). Nous aborderons ensuite le problème du paramètre libre pour imiter les effets non-idéaux dans les profils Stark. Nous présenterons des nouveaux profils avec une implémentation cohérente des théories de Hummer & Mihalas et Vidal, Cooper & Smith. Ces profils seront immédiatement utilisés dans le cadre de la technique spectroscopique, en s'intéressant d'abord aux naines blanches chaudes (40,000 K $> T_{\rm eff} >$ 13,000 K) observées dans l'échantillon Palomar-Green.

Dans le Chapitre 3, nous examinerons le problème des gravités élevées dans les naines blanches plus froides tout en tenant compte des nouveaux profils conçus dans le chapitre précédent. Le coeur de ce chapitre sera la vérification du scénario de la contamination des atmosphères par l'hélium en raison du mélange convectif. Nous présenterons les résultats d'une nuit d'observation au télescope Keck de 10 mètres sur le Mauna Kea à Hawaii (temps obtenu dans le cadre de cette thèse) pour tenter d'observer des raies d'hélium dans des DA froides.

Au Chapitre 4, un exemple de l'application à grande échelle de la technique spectroscopique sera présenté. Nous ferons une nouvelle analyse de l'échantillon de naines blanches DA du Sloan Digital Sky Survey, de loin le plus volumineux. En plus d'examiner l'impact de notre nouvelle grille de spectres, nous montrerons que notre application minutieuse de la technique spectroscopique fait ressortir des observations qui avaient été mal interprétées jusqu'à maintenant, notamment avec notre découverte de nombreuses naines blanches binaires. Notre méthode d'analyse précise nous amènera également à discuter de la qualité de la calibration des observations de cet échantillon.

Finalement, le Chapitre 5 constituera un retour au problème des gravités élevées avec la présentation du calcul des premiers modèles de naines blanches DA en trois dimensions, utilisant un traitement d'hydrodynamique radiative de la convection. Nous ferons une analyse différentielle entre ces modèles avec un traitement amélioré de la convection, et des modèles similaires traitant la convection avec la théorie MLT standard. En particulier, il sera question des corrections en $\log g$ que prédisent les modèles 3D par rapport aux modèles actuels et de l'impact que ces corrections auront sur le problème des gravités élevées. Nous terminerons cette thèse avec une conclusion au Chapitre 6.

Chapitre 2

SPECTROSCOPIC ANALYSIS OF DA WHITE DWARFS: STARK BROADENING OF HYDROGEN LINES INCLUDING NON-IDEAL EFFECTS

P.-E. Tremblay and P. Bergeron

Département de Physique, Université de Montréal, C.P. 6128, Succ. Centre-Ville, Montréal, Québec, H3C 3J7, Canada

Received 2009 January 5; accepted 2009 February 25

Published in *The Astrophysical Journal*,
May 2009, *Vol.* 696, *page* 1755

2.1 Abstract

We present improved calculations for the Stark broadening of hydrogen lines in dense plasmas typical of white dwarf atmospheres. Our new model is based on the unified theory of Stark broadening from Vidal, Cooper, & Smith. For the first time, we account for the non-ideal effects in a consistent way directly inside the line profile calculations. The Hummer & Mihalas theory is used to describe the non-ideal effects due to perturbations on the absorber from protons and electrons. We use a truncation of the electric microfield distribution in the quasi-static proton broadening to take into account the fact that high electric microfields dissociate the upper state of a transition. This approach represents a significant improvement over previous calculations that relied on the use of an ad hoc parameter to mimic these non-ideal effects. We obtain the first model spectra with line profiles that are consistent with the equation of state. We revisit the properties of DA stars in the range 40,000 K $> T_{\rm eff} >$ 13,000 K by analyzing the optical spectra with our improved models. The updated atmospheric parameters are shown to differ substantially from those published in previous studies, with a mean mass shifted by +0.034 $M_\odot$. We also show that these revised atmospheric parameters yield absolute visual magnitudes that remain in excellent agreement with trigonometric parallax measurements.

2.2 Introduction

The most successful technique used to determine the effective temperatures and surface gravities of hydrogen-line DA white dwarfs is to compare the observed and predicted hydrogen line profiles. This so-called spectroscopic technique was first applied to a large sample of DA stars by Bergeron et al. (1992, hereafter BSL92) in the case of the hydrogen Balmer lines. In recent years, the method has also been applied to the study of the Lyman line profiles in the ultraviolet (Barstow et al. 2003; Vennes et al. 2005). The success of this approach resides in the fact that the theoretical line profiles are very sensitive to variations of the atmospheric parameters (Wegner & Schulz 1981). This is illustrated in Figure 2.1 where the theoretical profiles of five Balmer lines are displayed for various values of $T_{\rm eff}$ and $\log g$. In comparison with the other fitting methods used before (see BSL92 for an extensive review), the spectroscopic method has the lowest intrinsic uncertainties, which allows for a more precise comparison, at least in a relative sense, of the atmospheric parameters between different DA stars. For instance, BSL92 used the spectroscopic method to determine the shape of the DA mass distribution (see also Liebert et al. 2005; Kepler et al. 2007), while Bergeron et al. (1995) applied the same method to define the location of the ZZ Ceti instability strip in a $\log g - T_{\rm eff}$ diagram (see also Gianninas et al. 2006). Since about 80% of the white dwarf population is of the DA type, the spectroscopic technique coupled with high signal-to-noise spectroscopic observations of the Balmer lines for large samples of DA stars (Gianninas et al. 2005; York et al. 2000) can reveal important details about the luminosity function and the evolution and the formation rate of DA white dwarfs (Liebert et al. 2005).

Even though the *relative* accuracy of the spectroscopic method is mostly limited by the quality of the observations (signal-to-noise ratio, flux calibration, etc.), the *absolute* values of the atmospheric parameters depend highly on the level of sophistication of the physics included in the calculations of model atmospheres with hydrogen-rich compositions. One starting point would be the efficient code of Wesemael et al. (1980) that allowed for the computation of radiative LTE atmospheres for hot DA white dwarfs. Similar codes have also been developed by D. Koester and described in Finley et al. (1997). Since then, the most important advance has certainly been the inclusion of NLTE effects — in the code of Hubeny & Lanz (1995) among others — which allowed the study of hot DA stars ($T_{\rm eff} > 40,000$ K). In terms of cooler white dwarfs, the code developed by Bergeron et al. (1991) made great advances and has been a reference ever since. It includes convective energy transport and the non-ideal equation of state of Hummer & Mihalas (1988, hereafter HM88) to describe the atomic populations. Otherwise, it is mostly in the atomic physics, with new or improved opacities and partition functions, that advances have been made.

The dominant features observed in DA spectra are the hydrogen lines. It is thus important to have a good understanding of the atomic transitions to exploit the power of the spectroscopic technique to its fullest. The main source of line broadening in most DA stars ($T_{\rm eff} >$ 10,000 K) is due to charged particle interactions, also called Stark broadening. The theory

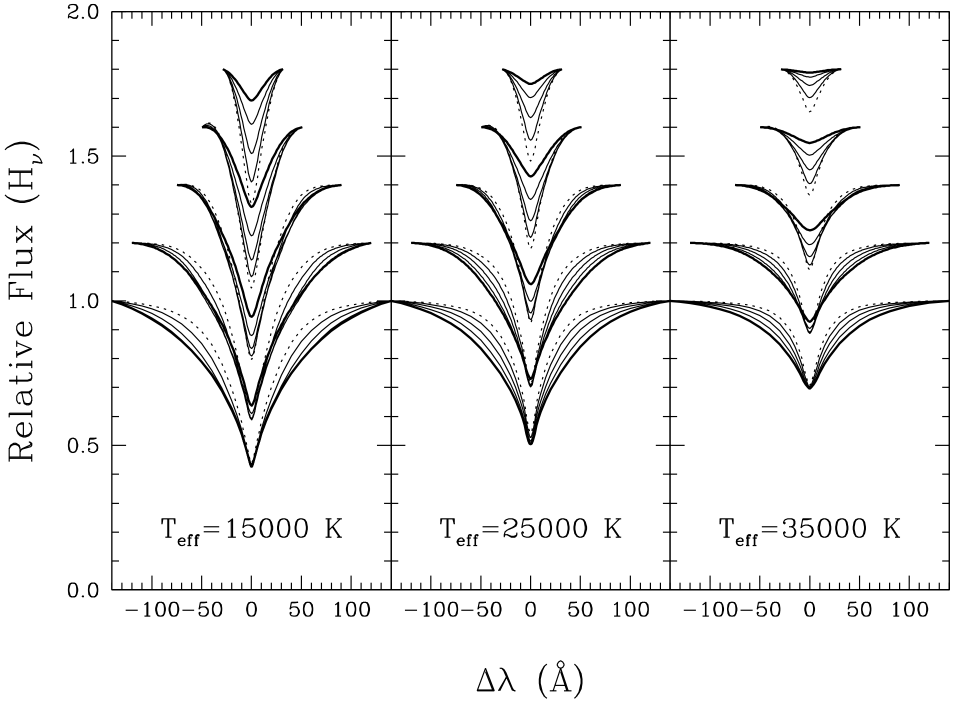

FIGURE 2.1 – Theoretical line profiles of models at different effective temperatures and surface gravities using our new line profiles discussed in Section 2.3. The lines correspond to Hβ to H8 (*bottom to top*) from the Balmer series of the hydrogen atom. In each panel, the line profiles range from $\log g = 7.0$ (*dashed line*) to 9.0 (*thick line*) by steps of 0.5 dex. The profiles have been convolved with a 6 Å FWHM Gaussian profile, normalized to a continuum set to unity, and offset vertically from each other for clarity.

that has been the most successful to describe these line profiles is the unified theory of Stark broadening from Vidal, Cooper, & Smith (1970, hereafter VCS; see also Smith et al. 1969; Vidal et al. 1971, 1973). This theory was used right from the beginning in the analysis of large samples of DA white dwarfs (BSL92) and it is the basis of most of the widely accepted results on the global properties of these stars. Even though the theoretical framework of the unified theory has been known since the original work of VCS, it is not until the calculations of Lemke (1997) that a complete grid of hydrogen line profiles from the unified theory became available, covering the full range of possible transitions, temperatures, and electronic densities encountered in DA white dwarf atmospheres. Before that, line profiles from the unified theory were either extrapolated to high densities (T. Schöning and K. Butler, private communication), or more drastically, less accurate broadening theories (Underhill & Waddell 1959; Edmonds et al. 1967) were used for the highest lines of the Balmer series (Hϵ and above). At $T_{\rm eff}$ below $\sim 10,000$ K for the Balmer lines and below 30,000 K for the Lyman lines, other types of line broadening, mostly due to neutral particles, must be included in the model atmospheres. The modeling of the quasi-molecular line opacity (Allard et al. 2004) has been one of the most significant advance in this domain.

Despite the development of these theoretical tools, the study of DA stars has suffered from several complications. For instance, in their preliminary analysis of 129 DA white dwarfs, BSL92 discovered a lack of internal consistency between the spectroscopic solutions obtained when an increasing number of Balmer lines were included in the fitting procedure. This is illustrated at the top of Figure 2.2 for a typical DA white dwarf where we can see that the solution drifts in the $T_{\rm eff}$ vs $\log g$ diagram as more lines are included in the fit. This correlation indicates that the physics included in the model calculations needed significant improvement. Bergeron (1993) traced back the problem to the neglect of non-ideal effects inside the Stark broadening calculations. Indeed, Seaton (1990) had argued that non-ideal effects, such as those taken into account in the HM88 equation of state, have also to be included directly in the line profile calculations to get a coherent physical framework. However, it was not possible at the time of the analysis of BSL92 to rework the line broadening calculations. Instead, the authors chose to include an ad hoc parameter inside the model atmosphere code to *mimic* the non-ideal effects in the line profiles (Bergeron 1993). By taking twice the value of the critical electric microfield ($\beta_{\rm crit}$, see Section 2.2.3) from the HM88 theory, it was found that the internal consistency improved substantially, as can be seen in the middle panel of Figure 2.2. *It should be stressed, however, that this does not imply that HM88 underestimated the value of the critical field.* This is just a quick and dirty way to simulate the non-ideal effects by reducing the line wing opacity, in particular where the line wings overlap (see Bergeron 1993 for further details). This ad hoc parameter has been used ever since in all model spectra of white dwarf stars (BSL92; Hubeny & Lanz 1995; Finley et al. 1997; Kawka & Vennes 2006).

In this paper, we solve the problem discussed above in a more elegant way, by computing improved Stark broadening profiles based of the unified theory of VCS, but by including

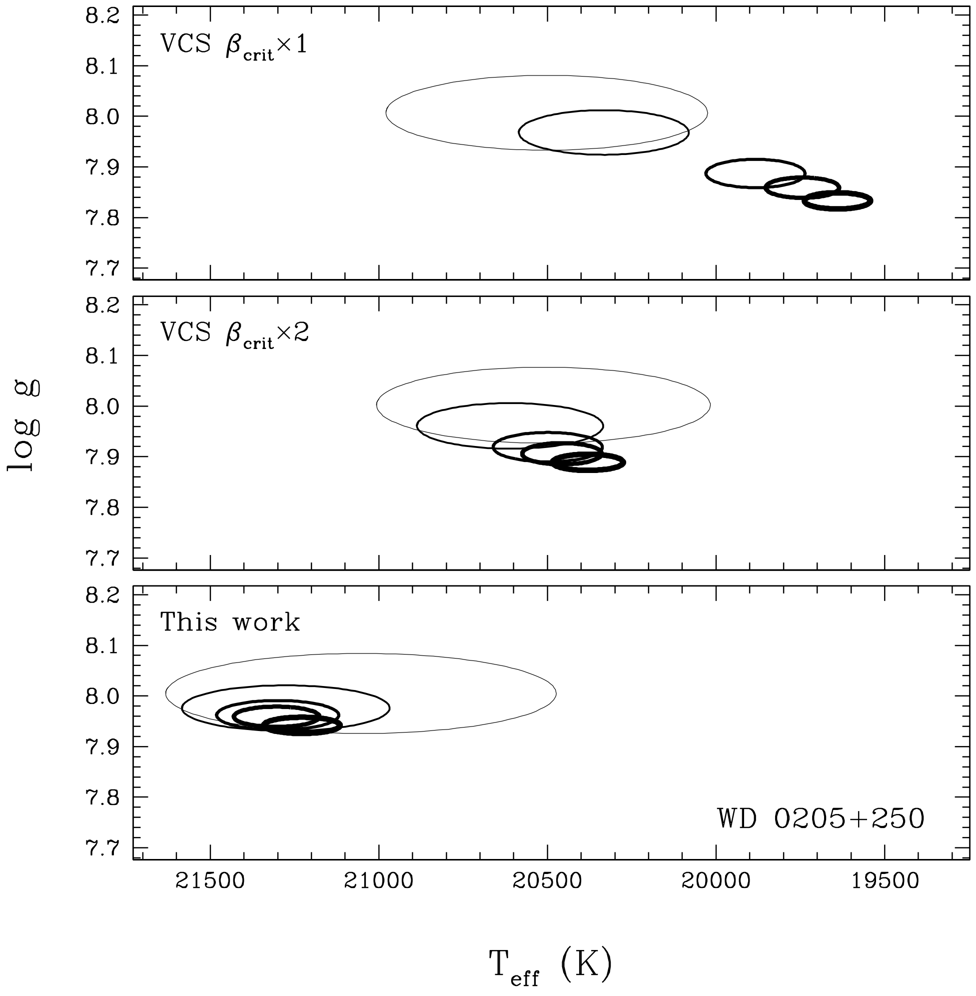

FIGURE 2.2 – Solutions in a $T_{\rm eff} - \log g$ diagram for a typical DA star using 1 line (Hβ), 2, 3, 4 and 5 lines (up to H8) in the fitting procedure (represented by thicker 1 σ uncertainty ellipses from our fitting procedure). The top panel shows the results with the VCS line profiles, while the middle panel also includes the ad hoc parameter proposed by Bergeron (1993). The bottom panel is with our new line profiles discussed in this work (Section 2.3).

non-ideal effects directly in the line profile calculations following an approach similar to that originally proposed by Seaton (1990). The non-ideal effects due to the proton and electron perturbations are taken into account using the HM88 theory. We begin in Section 2.2 by discussing the two successful theories at the heart of our calculations, namely the VCS unified theory of Stark broadening and the HM88 non-ideal equation of state. In Section 2.3, we describe how these two formalisms are combined for the first time to compute Stark broadening profiles that take into account non-ideal effects. We then evaluate in Section 2.4 the implications of our improved line profiles on the spectroscopic analysis of DA stars. Our conclusions follow in Section 2.5.

2.3 Line Broadening Theory

The basis of model atmospheres for DA white dwarfs resides in the equation of state and opacity calculations of the hydrogen gas. One of the most successful equations of state used to compute the populations of the different accessible states (bound states of hydrogen, H^-, molecular H_2, H_2^+ and H_3^+, as well as proton and electron populations) is the HM88 non-ideal equation of state described in more detail in Section 2.2.2. With these populations in hand for all states of the gas, we can proceed to calculate the gas opacity, which is generally split into true absorption and scattering processes. In particular, the bound-bound opacity (or line opacity) between one initial state i and one final state j is written as

$$\kappa_{ij}(\nu)\, d\nu = N_i \frac{\pi e^2}{m_e c} f_{ij} \phi(\nu)\, d\nu \ , \tag{2.1}$$

where N_i is the population of the initial state and f_{ij} is the oscillator strength of the transition. These two factors define the amplitude of the transition while $\phi(\nu)$ is the spectral broadening profile normalized to unity. In this paper, we are mostly interested in the broadening profile for the hydrogen lines. This opacity is the key ingredient of the spectroscopic method that relies on a detailed comparison of observed and predicted line profiles.

Generally speaking, the line profile is a convolution of different broadening mechanisms. The first source of broadening is due to the interaction between the absorber and the charged particles in the plasma. This process is referred to as Stark broadening and is discussed in more detail in Section 2.2.1. Stark broadening represents the dominant source of broadening for most transitions in DA white dwarfs. Accounting only for this source of broadening, the line profile can be expressed (Underhill & Waddell 1959; Edmonds et al. 1967) as

$$\phi(\nu)\, d\nu = \frac{\lambda^2}{cF_0} S^*(\alpha)\, d\nu \ , \tag{2.2}$$

where $\alpha = \Delta\lambda/F_0$ with $\Delta\lambda$ measured from the center of the line. F_0 is defined as the electric field at the mean distance between the plasma ions

$$F_0 = Z_p e(4\pi N_p/3)^{2/3} = 1.25 \times 10^{-9} Z_p N_e^{2/3} \ , \tag{2.3}$$

where Z_p and N_p are the charge and density of perturbers, respectively. The profile $S^*(\alpha)$ is a convolution of a pure Stark profile $S(\alpha)$ and a Voigt function $H(a, v)$ that takes into account thermal and natural broadening

$$S^*(\alpha) = \int_{-\infty}^{\infty} S\left(\alpha + \frac{\lambda_0 v}{F_0 c}\right) \frac{H(a, v)}{\sqrt{\pi}} dv \ , \tag{2.4}$$

where $a = \Gamma/4\pi\Delta\nu_D$, with Γ representing the natural broadening half-width and $\Delta\nu_D$ the Doppler width. The second type of broadening important in DA white dwarfs is the interaction of the absorber with neutral hydrogen. It is especially important at low effective temperatures for transitions involving an upper level with a low principal quantum number. In the case of Balmer lines, we must include resonance broadening (Ali & Griem 1965, 1966) and nonresonant broadening (Hammond et al. 1991) in cool white dwarfs with $T_{\rm eff} <$ 10,000 K. Since this source of broadening has a Lorentzian profile, the broadening parameter can be added directly to that of the natural broadening. For the lower Lyman lines (Lα, Lβ, and Lγ), close range collisions of the absorber with hydrogen atoms and protons cause the appearance of important satellites in the wings of the lines that are visible up to $T_{\rm eff} \sim 30,000$ K (Allard & Kielkopf 1982; Allard et al. 2004). This opacity also affects the thermodynamic structure of the atmosphere. Furthermore, at very low effective temperatures, H-H_2 collisions become the main source of broadening for Lα (Kowalski & Saumon 2006).

2.3.1 Stark Broadening

The Stark effect is defined as the shifting — or splitting — of spectral lines under the action of an electric field. In the following section, we assume that we have in the atmospheric plasma a local electric microfield due to protons that is constant with time. This static approximation is well justified since the characteristic time for the fluctuation of the local microfield due to a change in the proton distribution is much larger than the characteristic time of absorption and emission processes that we are studying (Stehlé & Jacquemot 1993). We also assume that the microfield is constant in space, a good approximation if the perturbers are far from the area occupied by the bound electron orbits. The regime where this approximation fails is discussed further in Section 2.2.3. The electric microfield, assumed to be along the z-axis, interacts with the dipolar moment of the atom and leads to a perturbation in the Hamiltonian of the form

$$H_s = e\vec{R} \cdot \vec{F} = eFz \ . \tag{2.5}$$

It is common to write the amplitude of the microfield in terms of the unitless parameter β such that

$$\beta = \frac{F}{F_0} \ , \tag{2.6}$$

where F_0 is the characteristic field defined by equation 2.3. The amplitude of the microfield can be expressed using a probability distribution $P(\beta)$. One such distribution that can be computed analytically is the Holtsmark distribution, which takes into account the interactions (vectorial sum) between the different perturbers. We use here the more physical distribution of Hooper (1968) that takes into account the Debye screening effect, and which corresponds also to the formulation included in the work of VCS. HM88 originally used the Holtsmark distribution, but for consistency we use the approach of Nayfonov et al. (1999) for the HM88 equation of state by replacing the Holtsmark distribution with the Hooper distribution. We note that this improved version of the HM88 equation of state is already included in our model atmosphere code, although it has never been properly documented.

We note that the perturbation H_s does not commute with the angular momentum $\vec{L}^2$ since it has a privileged direction in space. The effect of breaking this symmetry is to lift the degeneracy in energy of the hydrogen atomic levels. There are no exact solutions to this problem and we generally use quantum mechanical perturbation theory to determine corrections to the energy and wave functions. The first order corrections to the energy are linear in relation to the electric microfield that is applied, and represent the basis of the linear Stark effect. The linear corrections are found by diagonalizing the perturbation operator in the degenerate subspaces. For a hydrogen atom, we can write this expression analytically. First of all, knowing that the operator z conserves the azimuthal quantum number m, we can diagonalize the matrix $\langle\Psi_k|\, H_s\, |\Psi_l\rangle$ (Condon & Shortley 1935) by making use of the quantum numbers (n, m, q), where $q = q_1 - q_2$ with $q_1 + q_2 = n - |m| - 1$, and n is the principal quantum number. The shifts in energy are then given by

$$\Delta E^1_{n,m,q} = \frac{3ea_0F}{2} nq \ . \tag{2.7}$$

When the electric microfield becomes very high, or equivalently, when the Stark splitting is important enough that the Stark components of two levels with a different principal quantum number are crossing, the linear approximation is no longer valid. The second order corrections to the energy become quadratic in relation to the microfield, and we find

$$\Delta E^2_{n,m,q} = e^2F^2 \sum_{n' \neq n} \frac{|\left\langle\Psi_{n',m',q'}\right|\, z\, |\Psi_{n,m,q}\rangle|^2}{E^0_{n,m,q} - E^0_{n',m',q'}} \ . \tag{2.8}$$

The problem with this perturbation approach to the Stark effect is that the wave functions, using any order of the perturbation theory, are not necessarily normalizable (Friedrich 2006). This is because the perturbing potential goes to $-\infty$ when z goes to $-\infty$. In other words, states that were bound without a microfield are now only metastable states, and there is a finite probability that the atom will be ionized when the microfield has a sufficiently high amplitude. Classically, the sum of the electric potentials of the absorber and the nearby protons only allows bound states in the local potential minima up to a certain energy, called the saddle point. Part of this problem is because we have used a spatially uniform microfield (eq. 2.5). In reality, the microfield cannot be uniform beyond a distance of about the interparticle separation, and thus under normal conditions, most of the states will be bound. However, for sufficiently high microfields, some excited states will become unbound and this is where resides the problem discussed further in the next sections.

2.3.2 The Unified Theory of Stark Broadening

In addition to static protons, the absorber also interacts with free electrons. These particles being much faster than the protons, a collisional approach is generally used to describe this interaction. Since the collisions are rapid, the interaction is non-adiabatic and a proper quantum mechanical treatment of the collisions accounting for the internal structure of the hydrogen atom is required. Various theories of Stark broadening for hydrogen lines take into account both the electron and proton interactions (Vidal et al. 1971; Seaton 1990; Stehlé & Jacquemot 1993). Here we summarize the principal aspects of the unified theory of VCS, which even today stands as the most accurate theory for the conditions encountered in white dwarf atmospheres.

The unified theory of VCS uses the quasi-static proton broadening approximation with the distribution of electric microfields described in Section 2.2.1, assumed to be constant in space and time. The complete Stark profile is then defined as

$$S(\alpha) = \int_0^\infty P(\beta) I(\alpha, \beta) d\beta \ , \tag{2.9}$$

where $I(\alpha, \beta)$ is the electronic broadening profile. Therefore, the problem is reduced to the calculation of electronic broadening profiles for a fixed microfield of amplitude β. The full broadening profile is then the average of the electronic profiles over all possible microfields weighted by the probability distribution $P(\beta)$. The unified theory is a non-adiabatic quantum mechanical theory that uses the classical path approximation for the electron-absorber interactions, implying that the wave functions are well separable. The interaction potential considers only the first dipole term. The name of the unified theory comes from the fact that the electronic profile is valid at all detunings from the line center. In the asymptotic limit of the line core, the impact approximation is recovered. Furthermore, in the far wings of the lines, the one-electron theory is recovered and the electrons and protons have similar contributions to the broadening.

Now we want to compute the electronic profile for an initial Stark state n_a to a final state n'_a, where this abbreviated notation is used to designate any of the (n, m, q) states. Mostly to reduce the computing time and to simplify the inversion of the matrix involved (see below), the unified theory uses the no-quenching approximation, which means that there are only collision-induced transitions within the same principal level. The states after the collisions will be denoted by n_b and n'_b for the initial and final state, respectively. The calculations can then be performed by considering only two-level transitions. This last approximation is valid only if the difference in energy between the highest Stark state from level n' and the lowest state of level $n'+1$ is large, or in other words, when the different lines are well separated (i.e., when the line wings do not overlap). Only then is the regime of the linear Stark effect consistent with the basic assumptions of the unified theory.

The electronic broadening profile $I(\alpha,\beta)$ is given by the sum over all states

$$I(\alpha,\beta) = \frac{1}{\pi} \sum_{n_a,n'_a,n_b,n'_b} \rho(n_a)\,\mathrm{Im}\left[\langle n_a|\,\vec{d}\,|n'_a\rangle \langle n'_b|\,\vec{d}\,|n_b\rangle \langle n_b|\,\langle n'_b|\,\mathcal{K}^{-1}(\alpha,\beta)\,|n'_a\rangle\,|n_a\rangle\right] \ , \quad (2.10)$$

where $\vec{d}$ is the dipole operator, and ρ is the probability that the atom is in the initial state (Boltzmann factor). The operator $\mathcal{K}$ takes into account the linear Stark effect as well as the free electron-atom interactions (see Vidal et al. 1970, eq. XII.2 for more details). Since the operator $\mathcal{K}$ is generally not diagonal in the basis of the (n, m, q) states, it induces a coupling between the various Stark components.

2.3.3 Non-Ideal Equation of State

One important advance that has provided a better interpretation of the hydrogen lines in DA white dwarfs is a realistic modeling of non-ideal effects at high densities. Bergeron et al. (1991) were the first to include the occupation probability formalism of HM88 to determine the populations of the bound states of hydrogen in white dwarf atmospheres. This probabilistic approach considers the perturbations on each atom by charged and neutral particles. One advantage of this statistical interpretation is that there are no discontinuities in the populations and the opacities when the temperature and the pressure vary, in contrast with other formalisms that simply predict the last bound atomic level under given physical conditions.

Briefly, each atomic level n has a probability w_n of being bound and a probability $1 - w_n$ of being dissociated due to perturbations from other particles in the plasma. The partition function of a given species is then written as

$$Z = \sum_n w_n g_n \exp\left(-\frac{\chi_n}{kT}\right) \ , \tag{2.11}$$

where χ_n and g_n are respectively the excitation energy and multiplicity of the level. The occupation probability w_n is defined as

$$w_n = \exp\left(-\frac{\partial f/\partial N_n}{kT}\right) \ , \tag{2.12}$$

where f is the free energy of the non-ideal interaction. The different interactions being statistically independent, the total occupation probability can then be calculated simply as the product of the contributions from neutral and charged particles.

The interaction with neutral particles is treated within a hard sphere model. The configurational free energy is derived from the second virial coefficient in the van de Waals equation of state (excluded volume correction). The exact origin of this excluded volume term is the hard sphere equation of state of Carnahan & Starling (1969). The interaction with charged particles is the one closely related to the Stark effect. This interaction suggests that the electric microfields, fluctuating on long time scales due to changes in the spatial distribution of protons, can destabilize a bound state and cause its dissolution into the continuum. Indeed, we already discussed in Section 2.2.1 that the application of an intense electric field on a bound atom allow for the ionization of the atom. HM88 therefore suggest an occupation probability for proton perturbations of the form

$$w_n(\text{charged}) = \int_0^{\beta_{\text{crit}}} P(\beta)\, d\beta \ , \tag{2.13}$$

where $P(\beta)$ is the probability distribution of the electric microfields introduced in Section 2.2.1. This occupation probability implies that all microfields larger than the critical field β_{crit} will ionize the electrons in level n (it is implicit here that the critical field depends on the atomic level considered). The difficulty with this formulation is to find the value of the critical microfield, for which slightly different expressions can be found in the literature (HM88; Seaton 1990; Stehlé & Jacquemot 1993). The simplest formulation is that of Seaton (1990) which consists in taking the critical microfield as the point where the energy of the highest Stark state for a given level n crosses the energy of the lowest Stark state of the next level $n+1$. For hydrogen, and using the linear Stark effect, we find

$$\beta_{\mathrm{crit}} = \frac{2n+1}{6n^4(n+1)^2} \frac{e}{a_0^2 F_0} \ . \tag{2.14}$$

The assumption that the crossing of two atomic levels with different principal quantum numbers leads to the dissolution of the lower level is difficult to prove and it is based in part on laboratory experiments and theoretical considerations (see HM88 for a more detailed discussion). Let us consider one bound electron in one of its many Stark states of the n-th level. When the electric microfield, which fluctuates in time, gets to a value such that there is a *crossing*[1] between this level and the lowest Stark state of the $n+1$ level, there is a significant probability that when the microfield goes down, there will be a transition $n \rightarrow n+1$. The incessant fluctuations of the microfield imply that these transitions will continue until the electron becomes unbound. However, the bound electron will in fact be in a rather homogeneous superposition of all its accessible Stark states due to electronic collisions[2] on time scales much shorter than the fluctuation time for the microfields, and also due to fluctuations in the direction of the microfield. That is, as soon as the first Stark state from a level n crosses another one from the level $n+1$, the electron is allowed to cascade to the continuum.

The reader might have noticed that equation 2.14 is based on the linear Stark effect although this is not necessarily a good approximation when levels are crossing. This is why HM88 considered a formulation of the critical field that takes into account corrections of higher order from the perturbation theory as well as results from experiments[3]. They find that for levels with $n > 3$, the linear theory remains valid. For lower levels, however, the critical field

---

[1] Strictly speaking, direct degenerate crossings are avoided due to fine structures and non-uniformity in the microfields.

[2] See equation 2.10; the non-diagonal operator $\mathcal{K}$ introduces this coupling.

[3] Remember that even if we have the *exact* critical field, ionization does not necessarily occur exactly at that point and this is why experimental data are also required.

is large enough that it must have been created by a single proton very close to the absorber. In this case, the approximation of a uniform electric field in space fails and we must consider the full potential curve of the H_2^+ system to find the critical field (Stehlé & Jacquemot 1993), and also to compute the broadening profiles of the far line wings (Allard & Kielkopf 1982). Exact calculations show that no crossing is possible between levels $n = 1$, 2, and 3, which implies that Lα is not affected by non-ideal effects due to proton perturbations. Also, the crossing between $n = 3$ and 4 is close to the classical saddle point value, which means that the linear Stark theory is in error by $\sim 14\%$. Therefore, HM88 added a smoothing factor to equation 2.14 so that the exact result is recovered for $n = 3$. For levels with a high value of n, HM88 obtain the same results as Seaton (1990). For the Balmer lines, these different values of $\beta_{\rm crit}$ are not an issue since the non-ideal effects discussed above are never important for Hα in DA white dwarfs. This is not the case for Lα and Lβ, however, for which non-ideal effects should be treated with caution, or simply neglected (for instance in TLUSTY and in our code discussed in Section 2.4).

We have seen in Section 2.2.2 that the interaction of hydrogen atoms with rapid electrons was better described with a collisional approach since the quasi-static theory is generally not valid in this case. These perturbations are also considered in the HM88 model. We must keep in mind that because the plasma is in thermal equilibrium, the equation of state already accounts for the inelastic electronic collisions that cause transitions and ionization. However, we expect that if the time between collisions is small, the energy of a bound level will be left undefined by a certain amount given by the uncertainty principle. If this energy uncertainty is of the order of the ionization potential, we expect the state to become unbound after the collision. As stated in HM88, this contribution to the occupation probability is always much lower than the proton contributions and can be neglected in DA atmospheres. However, the electronic perturbations should not be neglected when calculating the line profiles, as discussed in Section 2.3. We must also remember that the electrons contribute indirectly to the occupation probability due to proton perturbations by mixing the Stark states. The occupation probability for the bound states of hydrogen are displayed in Figure 2.3 for typical conditions encountered at the photosphere of white dwarf stars. Non-ideal effects are shown to be extremely important except for the very lowest transitions. The solution of the HM88 equation of state yields the populations for all states.

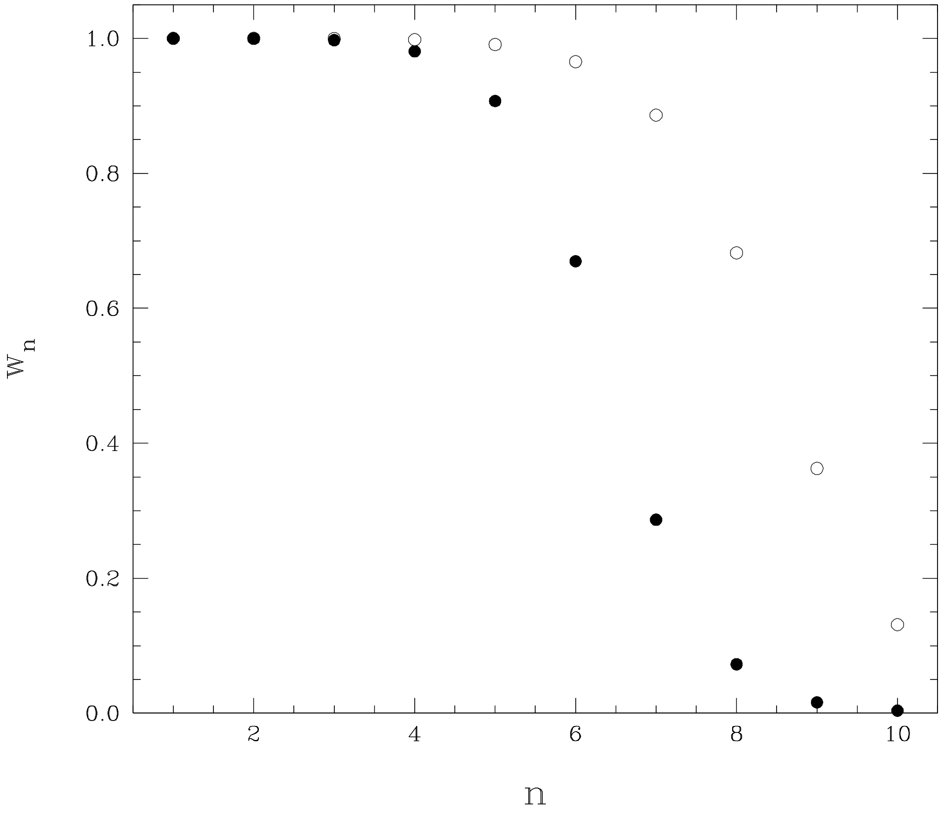

FIGURE 2.3 – Total occupation probability w_n for the bound states of hydrogen with principal quantum number n for $T = 10,000$ K, $\log N_e = 17$ (*filled circles*) and $T = 20,000$ K, $\log N_e = 16$ (*open circles*).

Finally, the opacity calculation must also be modified to take into account the occupation probability formalism, as described by Däppen et al. (1987). The bound-bound (line) opacity for a transition between levels i and j (equation 2.1) is multiplied by w_j/w_i to take into account the fact that these levels can be dissolved when a photon is absorbed. We thus obtain

$$\kappa_{ij}(\nu)\,d\nu = N_i \frac{\pi e^2}{m_e} \frac{w_j}{w_i} f_{ij} \phi(\nu)\,d\nu \ . \tag{2.15}$$

When the absorption is from a bound state to a final state that has been dissolved by non-ideal interactions (with a probability $1 - w_j/w_i$), we obtain instead a bound-free opacity since this process is equivalent to the ionization of the atom. We can directly extrapolate, in this case, the bound-free cross section at frequencies below the usual cutoff frequency ν_c. Däppen et al. (1987) have treated this opacity by considering the absorption from a level i of a photon of energy $h\nu$ that yields a transition to a fictitious upper level n^* given by

$$n^* = \left(\frac{1}{n_i^2} - \frac{h\nu}{\chi^I}\right)^{-1/2} \quad . \tag{2.16}$$

The hydrogen bound-free opacity for $\nu < \nu_c$ — also called the pseudo-continuum opacity — can then be written as

$$\kappa_i(\nu)d\nu = N_i \left(1 - \frac{w_{n^*}}{w_i}\right) \frac{64\pi^4 m_e e^{10}}{3\sqrt{3}ch^6} \frac{g_{bf,i}(\nu)}{n_i^5 \nu^3}\, d\nu \ . \tag{2.17}$$

In Figure 2.4, we show the individual contributions of the line and pseudo-continuum opacities at the photosphere of a 20,000 K DA white dwarf in the spectral region of the Balmer lines. We can see how the pseudo-continuum opacity extends to wavelengths longward of the Balmer jump, potentially affecting the opacity between the lines, and in particular the high Balmer lines.

2.4 Stark Broadening Profiles Including Non-Ideal Effects

The VCS line profiles (Section 2.2.2) and the HM88 equation of state (Section 2.2.3) have long been included in modern white dwarf model atmospheres (BSL92; Hubeny & Lanz 1995; Finley et al. 1997; Kawka & Vennes 2006). The HM88 theory has been used, in particular, to calculate populations as well as line and pseudo-continuum opacities. However, all model spectra currently available and calculated within the HM88 framework suffer from a major inconsistency. Seaton (1990) was the first to point out that not only the line strengths will be affected by non-ideal effects, but the *shape* of the line profiles as well. The Stark broadening profiles $S(\alpha)$ from VCS, for instance, do not take into account such non-ideal effects. It is possible to describe qualitatively the behavior of non-ideal line profiles. The high electric microfields, normally responsible for the absorption in the far wings of the line profiles, will not contribute as much to the line opacity in the non-ideal case since these fields are mostly

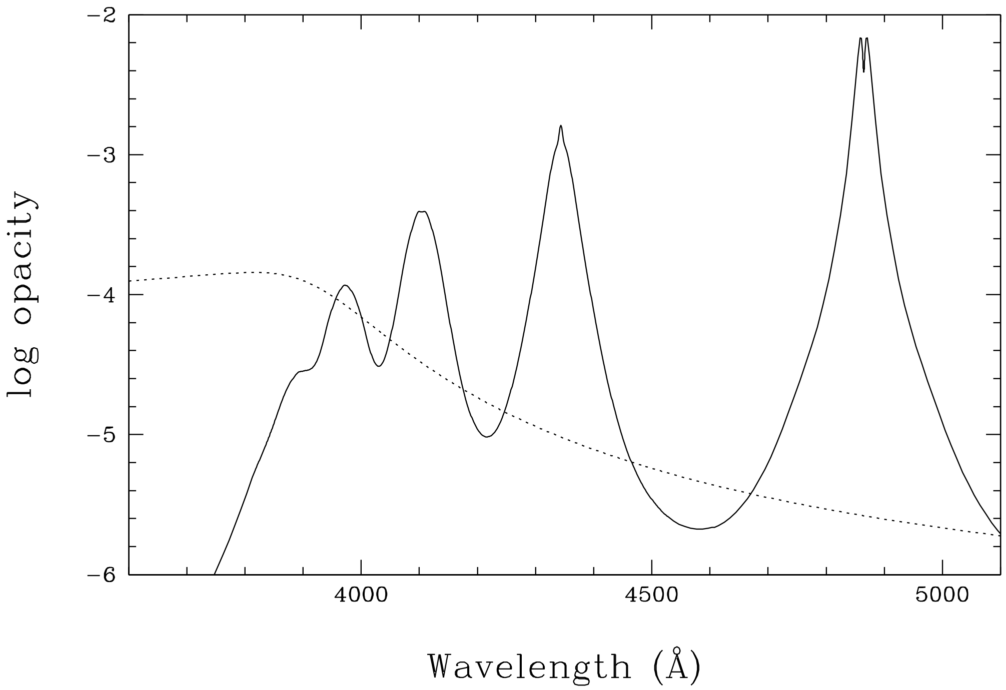

Figure 2.4 – Atomic hydrogen opacity at the photosphere of a 20,000 K DA white dwarf. The contributions of line and pseudo-continuum opacities are shown as solid and dotted lines, respectively.

responsible for dissolving the atomic levels. Consequently, the opacity in the line wings will be significantly reduced with respect to the ideal case. But since by definition the profiles are normalized to unity, the non-ideal line profiles will have deeper cores and appear narrower in comparison with the ideal case.

Instead of including the non-ideal effects discussed above, Bergeron (1993) proposed a solution that could be easily implemented in model atmosphere calculations. As mentioned in the Introduction, this is the solution adopted by BSL92 in their analysis of a large spectroscopic sample of DA stars. The authors found in their preliminary analysis that the atmospheric parameters varied significantly when an increasing number of Balmer lines was included in the fitting procedure. Furthermore, the mean mass of their sample was uncomfortably low ($\langle M \rangle \sim 0.53\ M_\odot$; Bergeron et al. 1990a). The solution proposed by Bergeron (1993) was to parameterize the value of the critical field in equation 2.14. The effect of varying the value of $\beta_{\rm crit}$ is, among other things, to change the relative importance of the line wing and pseudo-continuum opacities. By increasing *arbitrarily* the value of the critical field, one mimics the non-ideal effects by reducing the line wing opacity. One problem with this approach, of course, is that the determination of the multiplicative factor in the expression for $\beta_{\rm crit}$ has absolutely no physical basis. This factor can only be determined from an empirical analysis of the internal consistency of the fitting procedure, similar to that shown in Figure 2.2 (see also Bergeron 1993). Furthermore, there is no reason to expect this ad hoc parameter to be the same for all hydrogen levels (i.e., Balmer or Lyman series) or for different atmospheric parameters. Another side effect of this approach is to artificially change the atomic populations in the HM88 equation of state, which in turn could have an unexpected impact on other parts of the model calculations. It should be clear by now that a more physical approach is seriously required, especially given the high quality spectra that have become available in recent years, either in the visible or the ultraviolet. This ad hoc parameter represents an important hurdle towards our understanding of the global properties of white dwarfs.

A coherent way to combine the Stark broadening profiles and the HM88 equation of state is described at length in Seaton (1990). Seaton proposed to replace equation 2.9 by

$$S(\alpha) = \frac{\displaystyle\int_0^{\beta_{\rm crit}} P(\beta) I(\alpha,\beta) d\beta}{\displaystyle\int_0^{\beta_{\rm crit}} P(\beta) d\beta} \ , \tag{2.18}$$

where only electric microfields β with an amplitude inferior to the critical field $\beta_{\rm crit}$ for the upper level of the transition now contribute to the broadening of the lines by the protons. The higher fields contribute instead to the pseudo-continuum opacity. The denominator, which turns out to be the occupation probability due to proton perturbations, allows for the renormalization of the line profiles[4].

Seaton (1990) was the first to calculate Stark broadening profiles taking into account non-ideal effects. However, his calculations made for the Opacity Project rely on an approximate electron broadening theory that is inappropriate in the context of white dwarf atmospheres. Stehlé & Jacquemot (1993) also discuss the implementation of non-ideal effects inside the line

---

[4] In the definition of Seaton (1990), the line profiles are not renormalized but instead the factor w_j is omitted in equation 2.15.

profile calculations using an alternative electron broadening theory. This theory also lifts in part the static approximation for the protons and therefore gives better results in the center of the profiles, but this has no effect on the spectrum at the high densities found in white dwarf atmospheres. In the line wings, the results are equivalent to the VCS formulation. We must mention, however, that all published tables and subsequent papers for this theory (Stehlé 1994; Stehlé & Hutcheon 1999) do not include non-ideal effects.

In this work, we use the Seaton approach (equation 2.18) to include non-ideal effects due to proton perturbations inside the unified theory of Stark broadening from VCS. We also include non-ideal corrections due to electronic perturbations according to the HM88 theory. This was neglected by Seaton (1990), likely because it was estimated that the effects would be negligible in the context studied. As discussed in Section 2.2.3, the collisions between free electrons and the absorber leave a bound level in a state of indefinite energy. Therefore, the HM88 model states that if the uncertainty on the energy becomes equal to the ionization energy of the level, the electron has a good probability of becoming unbound. Here we have at hand the electronic broadening profiles given by equation 2.10, and their wings generally extend to infinity in terms of the detuning $\Delta\nu$ (measured from the line center). However, according to the HM88 theory, it is obvious that the detuning induced by the electronic collisions cannot extend much beyond ν_c (i.e. the ionization threshold frequency for this level) or there would be line opacity shortward of the Balmer or Lyman jumps. An abrupt cutoff is not desirable since this could cause discontinuities in the spectra. We adopt here an exponential cutoff so that the electronic broadening profiles are reduced by a factor of e^{-1} at $\Delta\nu = \nu_c - \nu_0$, where ν_0 is the central frequency of the transition, and then we renormalize the total broadening profiles. Since the exponential factor is independent of β, we can easily represent this correction in the form

$$\phi'(\nu) = \frac{\phi(\nu)e^{-|\nu-\nu_0|/(\nu_c-\nu_0)}}{\displaystyle\int_0^\infty \phi(\nu)e^{-|\nu-\nu_0|/(\nu_c-\nu_0)}\,d\nu} \ . \tag{2.19}$$

This has a small but non-negligible effect on the line wings, especially for the higher members of the series. Both $T_{\rm eff}$ and $\log g$ are increased by ~ 0.5 % when this correction is introduced in our calculations. Using alternative types of cutoff, we estimate that the uncertainties on this part of the theory can be as high as half of the shifts found here. As mentioned in HM88, a more physical approach is certainly much needed but such a theory still does not exist.

Figure 2.5 presents the Stark broadening profiles $S(\alpha)$ for the Balmer lines Hγ and H8 at typical photospheric conditions of DA stars. Along with the results from this work, we show the original calculations of VCS (Lemke 1997) and the approximate profiles from Seaton (1990). We note that our profiles including non-ideal effects due to proton and electron perturbations are very different from the original ideal gas calculations of VCS, even though we are using the same broadening theory. Our profiles have significantly less opacity in the line wings, and higher lines of the series have much sharper profiles, as anticipated. To have a better idea of the relative importance of the two improvements discussed above, we have estimated that the electronic corrections account for 12% and 16% of the reduction of the opacity at 100 Å from the line center of Hγ and H8, respectively. Finally, we show that our profiles are not in agreement with the calculations of Seaton (1990), which include non-ideal effects due to proton perturbations but use only an approximate treatment for the electronic broadening. These results confirm that this last approximation is not suitable for typical conditions encountered in DA white dwarf atmospheres. The comparison of our Lyman line profiles with the calculations of VCS or Seaton is similar to those displayed in Figure 2.5.

We have demonstrated in the previous sections that our approach to Stark broadening provides significant physical improvements over previously available calculations. When included in a model atmosphere, the equation of state and the opacity calculations become entirely consistent without the need of the ad hoc parameter introduced by Bergeron (1993). By including non-ideal effects, we have shown that the line profiles from the unified theory are dramatically modified in typical white dwarf atmospheres. These improved profiles now need to be validated using spectroscopic data.

2.4.1 Comparison with Laboratory Experiments

The preferred way to validate Stark broadening theories for hydrogen has been the comparison with laboratory plasma emissivity measurements from Wiese et al. (1972). These

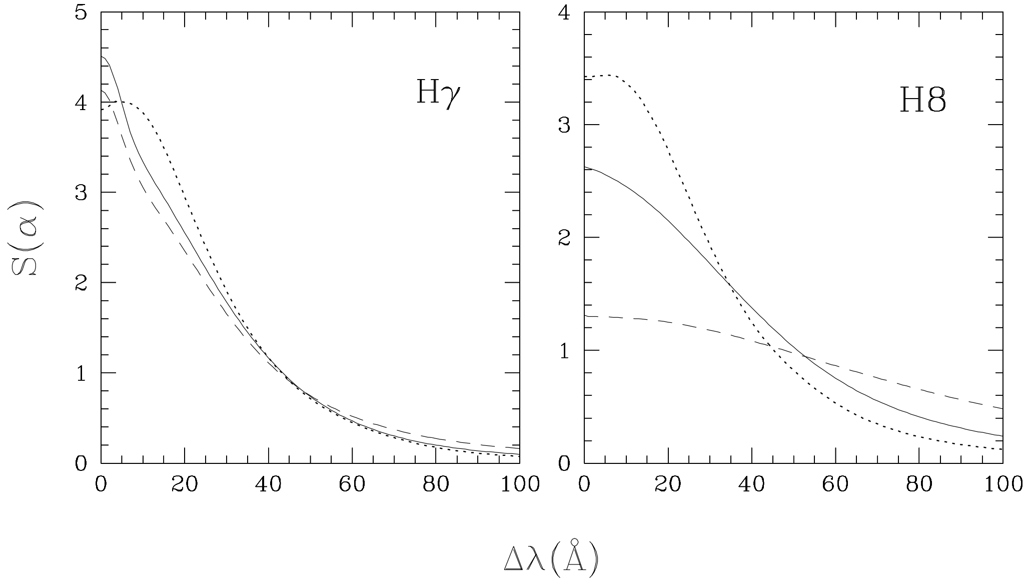

FIGURE 2.5 – Stark broadening profiles as a function of wavelength measured from the line center at $T = 10,000$ K and $\log N_e = 17$. Results are shown for Hγ (*left*) and H8 (*right*). In each panel, we compare the results from this work (based on the VCS theory coupled with non-ideal effects from HM88; *solid lines*) with the original VCS calculations (*dashed lines*). Also shown are the approximate calculations of Seaton (1990, *dotted lines)*, which also include non-ideal effects.

pure hydrogen plasma arc experiments were performed at high densities and temperatures, comparable to the photospheric conditions of cool white dwarfs. The main advantage of this experiment is that it is not under the constraint of radiative equilibrium, unlike a stellar atmosphere. In other words, the emergent flux at one wavelength is not affected by what occurs at other wavelengths. The emissivity can then be simply written as

$$j_\lambda(\lambda) = \frac{2c}{\lambda^4}\kappa(\lambda)e^{-hc/\lambda kT} \ , \tag{2.20}$$

where $\kappa(\lambda)$ represents the total monochromatic opacity. Another advantage, at least from a theoretical point of view, is that it is easier to control the experiments and the results are independent of various sources of uncertainty intrinsic to DA model atmospheres (i.e., convection, contamination from heavy elements, etc.). We use the data for the lowest and highest density experiments (the most extreme positions on the plasma arc) from Wiese et al., which were compared to broadening theories in various studies (Däppen et al. 1987; Seaton 1990; Bergeron 1993; Stehlé & Jacquemot 1993). Wiese et al. estimate the LTE plasma parameters for these two experiments at $\log T = 4.00$, $\log N_e = 16.26$ and $\log T = 4.12$, $\log N_e = 16.97$, respectively. However, there is no simple way to measure the plasma state parameters and it is not clear whether LTE is reached or not. The authors used the total intensity from two lines, together with the intensity at two continuum points, and fitted the data with an approximate plasma model. Since then, slightly different parameters have been used to compare with broadening theories. Instead of choosing approximate values for the parameters like in previous analyses, we performed a χ^2 fit to the full data sets, using the same input physics as for our white dwarf models. The results with the original VCS calculations and our improved line profiles are displayed in Figures 2.6 and 2.7 in terms of absolute predicted fluxes (i.e., without any renormalization).

For the lower density experiment of Figure 2.6, our improved profiles provide a much better fit to the laboratory data, in particular in the regions of the high Balmer lines where the wings overlap. The higher density experiment of Figure 2.7 is more problematic. We find that there is a partial $T - N_e$ degeneracy in the χ^2 diagram; it is indeed possible to find many acceptable solutions from visual inspection by increasing both T and N_e. However, to provide the best overall fit with our new profiles, we have to increase the plasma state parameters significantly compared to the Wiese et al. values. We see that our profiles provide the best fit for the higher lines, although the red wings of Hβ and Hγ are predicted a bit too weak. All in all, we conclude that the experiments of Wiese et al. do not provide such a stringent constraint on the broadening theories because of the large range of acceptable plasma state parameters, and also because of potential departures from LTE.

2.4.2 Further Theoretical Improvements

While our work represents a significant advance over previous calculations, second order effects in the theory of Stark broadening could still come into play. Such second order effects have been studied extensively in the literature in the case of high density hydrogen plasma experiments (Lee & Oks 1998; Stehlé et al. 2000; Demura et al. 2008). The sources of these

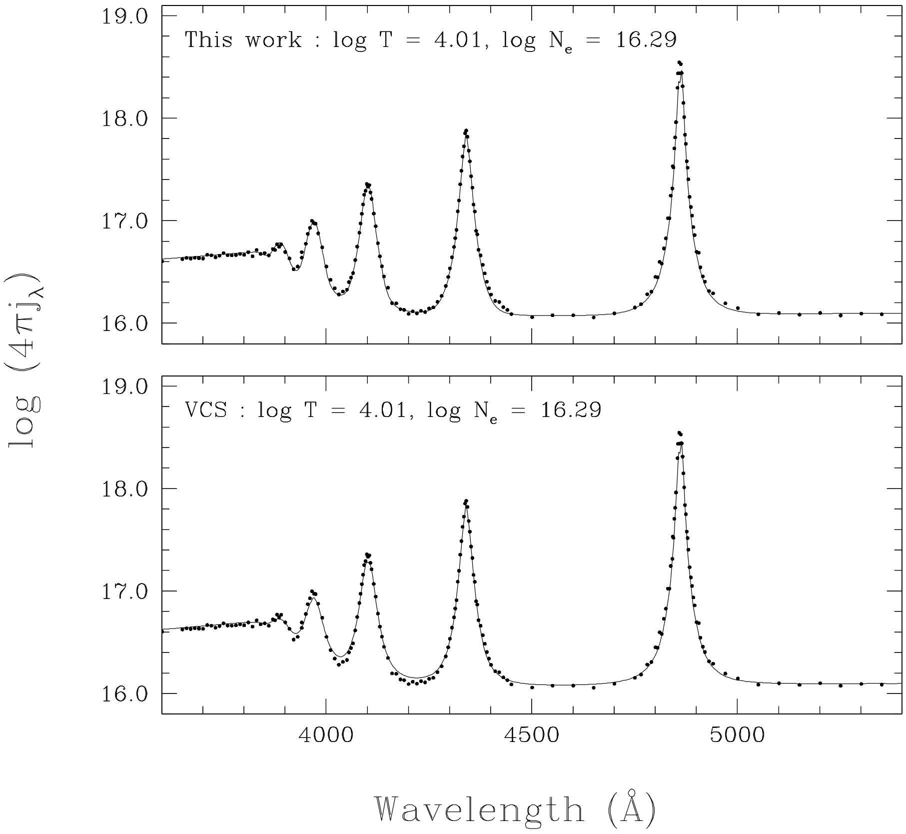

FIGURE 2.6 – Emissivity of a hydrogen plasma (*filled dots*) for the low-density experiment of Wiese et al. (1972). Our best fits (*solid line*) to the data are shown for different line broadening theories identified at the top of each panel along with the plasma state parameters obtained from the minimization procedure.

second order effects are plentiful but they all have the same impact on the line profiles: they produce asymmetries and they shift the central wavelengths, the latter being unimportant for the spectroscopic technique used to measure the atmospheric parameters of white dwarfs. The recent study of Demura et al. (2008) reveals that the various second order effects compete and interact together in a complex way and that they should all be included in the models simultaneously. The most important effects are due to quadrupole proton-absorber interactions and to the quadratic Stark effect, but second order effects due to quadrupole electron-absorber interactions are noticeable as well. The lifting of the no-quenching approximation could also be considered a second order effect, although it was shown by Lee & Oks (1998) to have an impact mostly on the line cores. Furthermore, some of these quenching effects have already

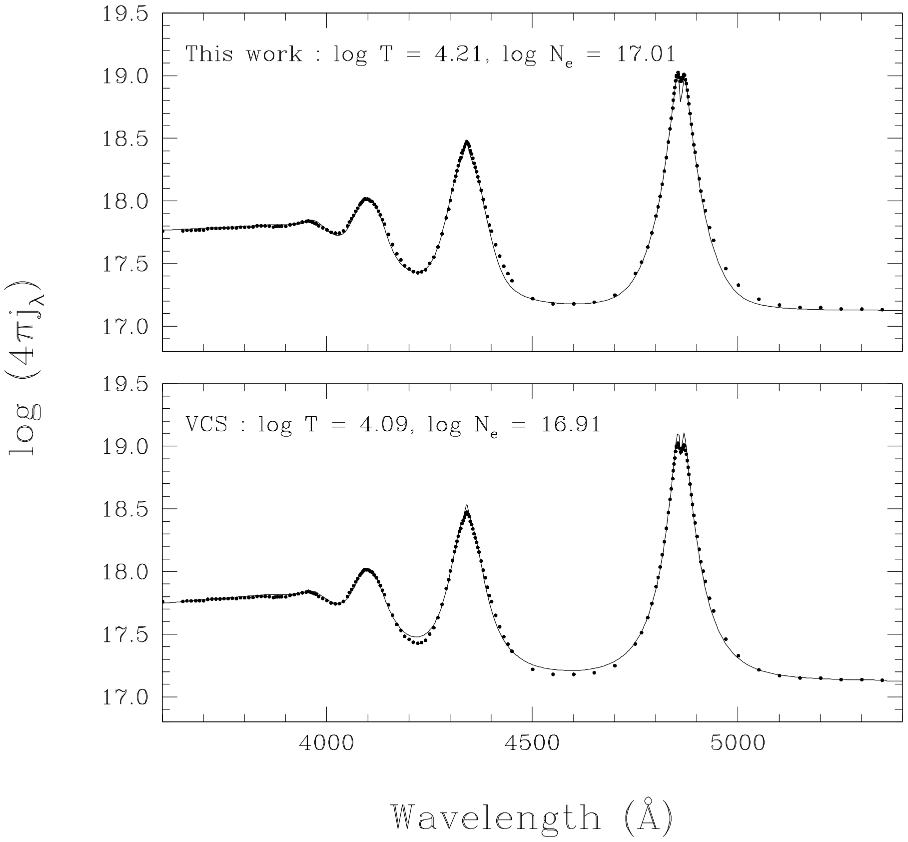

FIGURE 2.7 – Same as Figure 6 but with the data set for the high-density experiment of Wiese et al. (1972).

been accounted for implicitly by including here the HM88 non-ideal effects directly inside the line profile calculations. Finally, even if we include better physics for the atomic transitions, we still have to rely on the HM88 equation of state, which is, or may become, the main source of uncertainty.

Our analysis above of the Wiese et al. experiments, with our improved profiles has already revealed the existence of line profile asymmetries. For the lower density experiment (see Fig. 2.6), it is only a mild effect in the far wings, however. It is not clear if such second order effects would be significant in a typical DA white dwarf at $\log g \sim 8$, for which the electronic density at the photosphere is roughly halfway between the two Wiese et al. experiments. Therefore, it is probably premature at this stage to include second order effects in our calculations, and it is not clear whether such changes would affect our line profiles significantly. We come back to this point in the analysis of the PG spectroscopic sample discussed below.

2.5 Application to White Dwarfs Atmospheres

2.5.1 Model Spectra

We now discuss the astrophysical implications of our improved line profiles described in Section 2.3 on the modeling of DA white dwarfs. Our model atmosphere code is based on the program originally developed by Bergeron et al. (1991); Bergeron et al. (1995a) and references therein. The main difference is that we have updated several sources of opacity and partition functions (all within the occupation probability formalism). For completeness, we provide in Table 2.1 the complete list of opacity sources included in our code. We have not included the Lα line broadening due to H_2 collisions (Kowalski & Saumon 2006) since these calculations are still not available, although this has no impact over the range of effective temperature considered here.

TABLE 2.1 – Opacity Sources Included

Opacity	Populations	Cross Section
H bound-bound, Stark broadening (H–H^+, $H-e^-$)	$N_i(H)$	This work
H bound-bound, quasi-molecular (H–H, H–H^+)	$N(H)$	Allard et al. (2004)
H bound-bound, neutral broadening (H–H)	$N_i(H)$	Ali & Griem (1965, 1966)
H bound-free	$N_i(H)$	Mihalas (1978)
H free-free	$N_eN(H^+)$	Mihalas (1978)
H_2 free-free	$N_eN(H_2^+)$	we assume that of H I
H_3 free-free	$N_eN(H_3^+)$	we assume that of H I
H^- bound-free	$N(H^-)$	John (1988)
H^- free-free	$N_eN(H)$	John (1988)
H_2^+ bound-free	$N(H_2^+)$	Kurucz (1970)
H_2^+ free-free	$N(H)N(H^+)$	Kurucz (1970)
H_2^- free-free	$N_eN(H_2)$	Bell (1980)
CIA H-H_2	$N(H)N(H_2)$	Gustafsson & Frommhold (2003)
CIA H_2-H_2	$N(H_2)N(H_2)$	Borysow et al. (2001)
Rayleigh H	$N(H)$	Kissel (2000)
Rayleigh H_2	$N(H_2)$	Dalgarno & Williams (1962)
Thompson e scattering	N_e	Mihalas (1978)

The bound-bound H_2 and H_3^+ opacities are always negligible in DA white dwarfs.

We restrain our analysis to effective temperatures above $\sim 13,000$ K to avoid additional uncertainties related to convective energy transport. Indeed, the atmospheric structure of DA white dwarfs below this temperature depends sensitively on the assumed convective efficiency. The most commonly used approach to include convection in model atmosphere calculations, the mixing-length theory, is at best a very crude approximation, and the convective efficiency must be parameterized by carefully adjusting the value of the mixing length (Bergeron et al. 1995). It is also believed that large amounts of helium can be brought to the surface by convection while remaining spectroscopically invisible (Bergeron et al. 1990b; Tremblay & Bergeron 2008). Hence, it is not even clear whether cool DA stars have hydrogen-rich atmospheres. Another reason for restricting our analysis to hotter stars is that neutral line broadening becomes important for the Balmer lines below $T_{\rm eff} \sim 10,000$ K, preventing us from performing a direct comparison of the observed and predicted Stark broadened absorption lines. We also set an upper limit of $T_{\rm eff} = 40,000$ K because NLTE effects become important above this temperature. Also, absorption from heavier elements, particularly in the UV, is likely to affect the atmospheric structure of hot white dwarfs.

We thus computed two grids of model atmospheres, one with the VCS profiles and the other with our improved profiles (both calculated with $\beta_{\rm crit} \times 1$), covering the range of $T_{\rm eff} = 12,000$ K to 45,000 K (with steps of 500 K up to 15,000 K, 1000 K up to 18,000 K, 2000 K up to 30,000 K, and 5000 K above) and of $\log g = 6.5$ to 9.5 (by steps of 0.5 dex with additional models at 7.75 and 8.25). To compare the model spectra calculated from both sets of line profiles, we simply fit the VCS spectra with our improved spectra. The results of this exercise are illustrated in Figure 2.8. In general, our new models yield systematically higher effective temperatures (by $1000 - 2000$ K) and surface gravities (by ~ 0.1 dex) over the entire range of atmospheric parameters considered here. One exception is a region at low temperatures and high surface gravities where the trend in temperature is reversed. The strip, inclined in the diagram near $T_{\rm eff} \sim 15,000$ K, where this separation occurs corresponds to the region where the strength of the Balmer lines reaches its maximum (Bergeron et al. 1995). Our new models predict Balmer lines that are stronger, hence the temperatures in this region are pushed towards lower values.

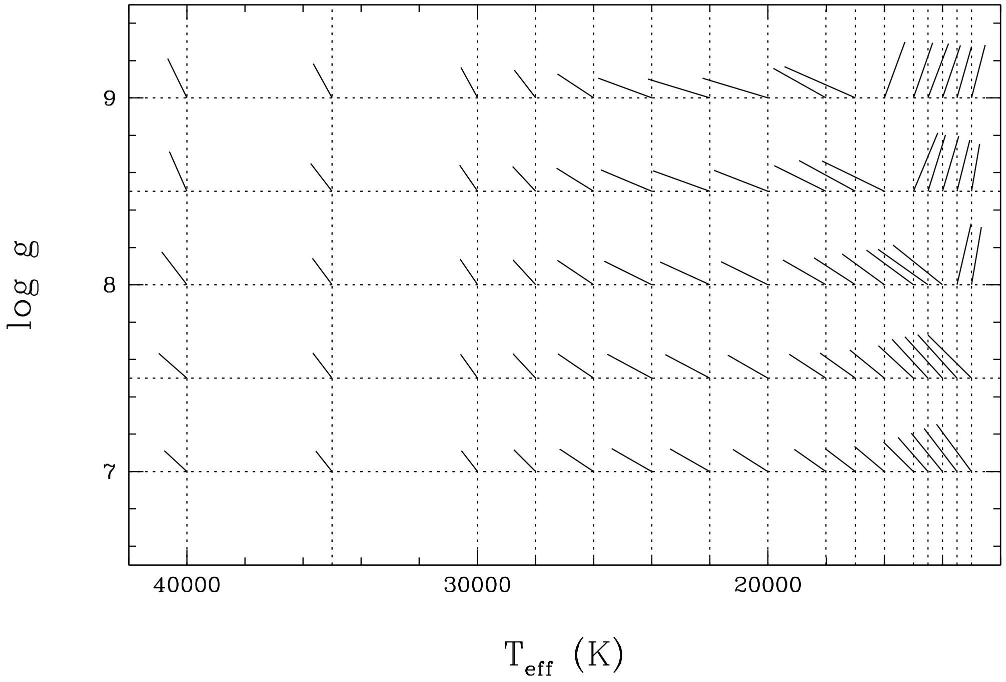

FIGURE 2.8 – Corrections that must be applied to transform the atmospheric parameters obtained from the VCS profiles to our improved models. These have been obtained by simply fitting the Balmer line profiles of the VCS model grid with our new spectra. For clarity, we have omitted the grid points at $\log g = 7.75$ and 8.25.

2.5.2 Analysis of the DA Stars in the PG Sample

In this section, we measure the implications of our improved Stark profiles on the analysis of Balmer line observations of DA stars by considering the Palomar-Green sample of Liebert et al. (2005). This sample of 348 DA stars has been studied in great detail, and the range of effective temperatures for these objects corresponds very well to that considered in our analysis. About 250 white dwarfs fall in the appropriate range of $T_{\rm eff}$, depending on which model grid is used. The data set and the fitting procedure of the optical spectra are identical to those described at length in Liebert et al. (2005, and references therein). Briefly, we first normalize the observed and model flux from each line to a continuum set to unity at a fixed distance from the line center. The observed profiles are then compared with the predicted profiles, convolved with a Gaussian instrumental profile. The atmospheric parameters are then obtained using the non-linear least-squared method of Levenberg-Marquardt, fitting simultaneously five lines (Hβ to H8). In some cases where the spectrum is contaminated by a M dwarf companion, one or two lines are excluded from the fit.

As discussed in the Introduction, model spectra calculated with standard Stark broadening profiles yield inconsistent atmospheric parameters when different lines are included in the fitting procedure. As shown in the bottom panel of Figure 2.2, our improved Stark profiles provide an even better internal consistency than the previous calculations displayed in the two upper panels. To better quantify this internal consistency, we perform for each star in the PG sample the same exercise as that shown in Figure 2.2 using the VCS profiles and our improved profiles. We then compute for the 250 stars in our sample the average absolute deviations in $T_{\rm eff}$ and $\log g$ between the solutions obtained with a different number of lines included in the fit. The results of this exercise are presented as filled circles in Figure 2.9 together with the mean uncertainties from the fitting procedure as a reference point (the open circles will be discussed in Section 2.4.3). We can see that the deviations with our improved profiles have been significantly reduced by a factor of ~ 1.6 in $T_{\rm eff}$ and ~ 1.8 in $\log g$. Furthermore, these deviations now both lie within the mean uncertainties of the fitting procedure, a result which is extremely reassuring.

The quality of the fits is also an important aspect of the comparison between model grids. We compare in Figure 2.10 our best fit to WD 0205+250 (same star as in Fig. 2.2) using the VCS profiles and our improved Stark profiles. This comparison reveals that while the atmospheric parameters are significantly different, the quality of the fits is similar. We thus conclude that the quality of the fits cannot help to discriminate between both sets of Stark profiles.

We can also explore the global properties of the PG sample with our two model grids. We first convert the $\log g$ values into mass using evolutionary models appropriate for white dwarfs with thick hydrogen layers (see Liebert et al. 2005 for details). Our results are presented in Figure 2.11 in a mass versus effective temperature diagram. As expected from the previous comparison displayed in Figure 2.10, our improved line profiles yield significantly larger masses and higher effective temperatures. We note that the results displayed in the bottom panel are

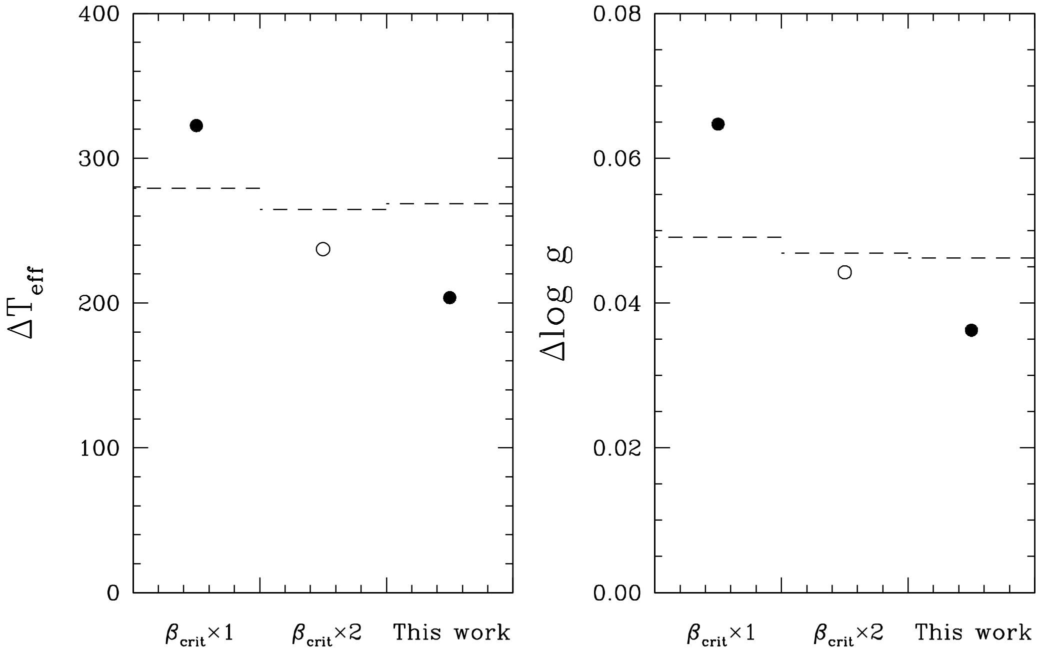

FIGURE 2.9 – *Left:* For each star in the PG sample with 40,000 K > $T_{\rm eff}$ > $13,000$ K, we computed the average absolute deviation in $T_{\rm eff}$ between solutions obtained from fits that include 2 to 5 lines (similar to Fig. 2.2). These deviations were then averaged for all DA stars in our sample (*filled dots*). The results are shown for the three grids discussed in the text and identified on the $x-$axis. For comparison, the mean uncertainty of the fitting procedure is shown as dotted lines. *Right:* Same as left panel but for the dispersion in log g.

qualitatively similar to the early spectroscopic determination of the mass distribution of DA stars by Bergeron et al. (1990a), which was based on the VCS profiles without any modification of the critical field. In this case, the mass distribution has a mean value near 0.53 $M_{\odot}$, which is uncomfortably low compared to what is expected from earlier phases of stellar evolution (see the discussion in Bergeron et al. 1990a).

Finally, we have also investigated whether second order effects in the Stark broadening theory, such as those discussed in Section 2.3.2, could be detected in our analysis. In particular, if such effects are present, we would expect to observe differences in the fits of the blue and red wings of the Balmer lines. We have thus reanalyzed the PG sample by including in the fit (1) only the red wing of the Balmer lines and (2) only the lines cores (this is accomplished by fitting only half of the wavelength range we normally use for each line). We find that the

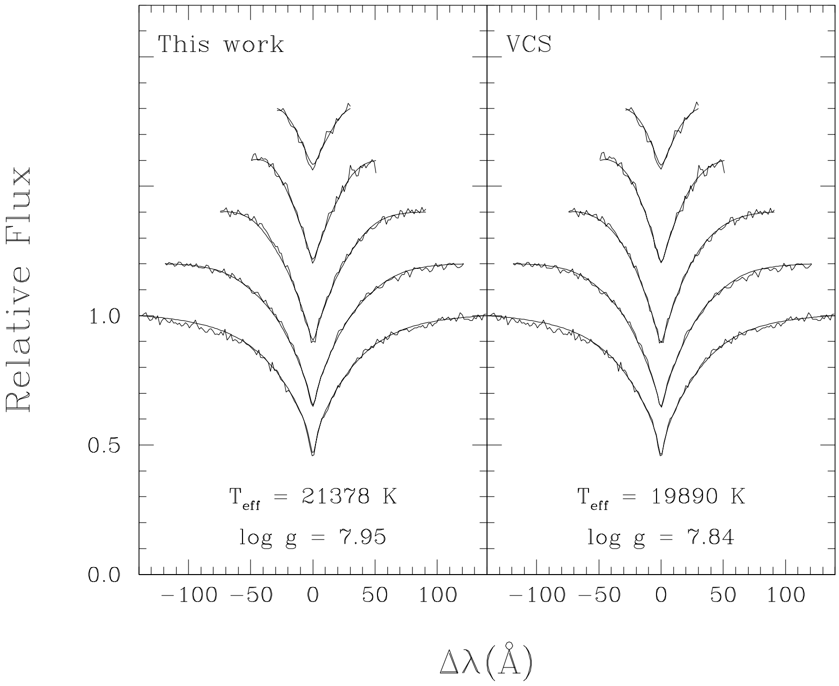

FIGURE 2.10 – Our best fit to the Balmer lines of WD 0205+250 with our improved line profiles (*left panel*) and with the VCS profiles (*right panel*). The atmospheric parameters are given in each panel.

atmospheric parameters obtained in this manner are entirely consistent, and we thus conclude that second order effects can be safely neglected in DA white dwarfs.

2.5.3 A Reappraisal of Previous Studies of DA White Dwarfs

The spectroscopic determination of the mass distribution by BSL92 was based on model spectra that include the solution proposed by Bergeron (1993) to mimic the non-ideal effects, namely by taking twice the value of the critical field ($\beta_{\rm crit} \times 2$) in the HM88 formalism. This ad hoc procedure had the effect of artificially reducing the pseudo-continuum opacity, and thus the opacity in the wings of the high Balmer lines. The internal consistency of the solutions obtained from different lines was consequently improved, as can be judged from the results displayed in Figures 2.2 and 2.9 (open circles). Since this ad hoc solution has been adopted by BSL92 and in all white dwarf models used in the literature, it is important to evaluate the

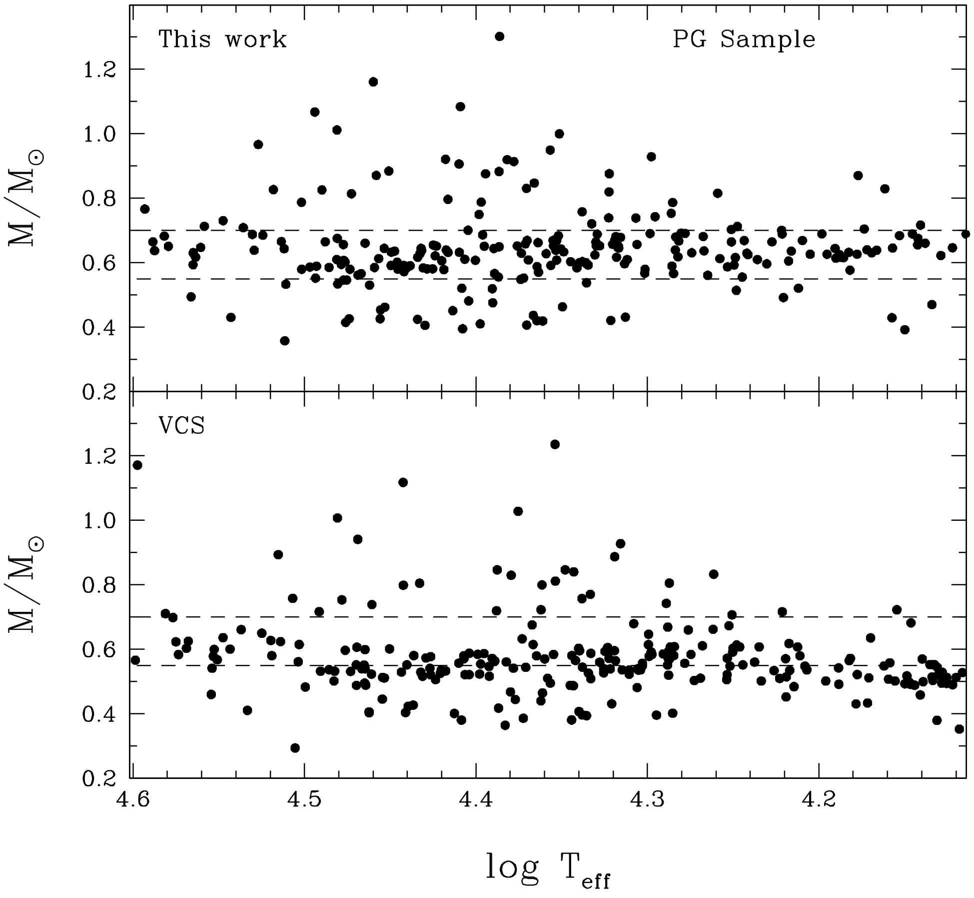

FIGURE 2.11 – Mass versus $T_{\rm eff}$ distribution for the DA stars in the PG sample in the range 40,000 K > $T_{\rm eff}$ > 13,000 K. Results are shown for both our improved lines profiles (*top panel*) and the VCS profiles (*bottom panel*). Lines of constant mass at 0.55 and 0.70 $M_\odot$ are shown as a reference.

differences between our revised atmospheric parameters and those published in the literature based on these approximate model spectra. For this purpose, we have also calculated another model atmosphere grid using the original VCS profiles from Lemke (1997) but with twice the value of the critical field. This grid is similar to that used by the Montreal group in the past ten years or so, and which has been applied to several studies of DA white dwarfs using the spectroscopic technique.

Once again, we rely on the PG sample of DA stars analyzed above. A comparison similar to that shown in Figure 2.11 is not very instructive here since the differences in $T_{\rm eff}$ and $\log g$

are considerably smaller. Instead, we use the representation displayed in Figure 2.12 where the differences $\Delta T_{\rm eff}$ and $\Delta \log g$ are shown as a function of effective temperature. This comparison reveals that our improved line profiles yield higher effective temperatures and surface gravities, with an important correlation with $T_{\rm eff}$. In particular, the $\log g$ values are about 0.05 dex larger above 20,000 K but can be as much as 0.1 dex larger near 15,000 K. Similarly, the differences in temperatures reach a maximum near 25,000 K but decrease at both lower and higher effective temperatures. The corresponding mass distributions, displayed in Figure 2.13, indicate that the mean mass is shifted by $+0.034$ $M_\odot$ when our new models are used. The shape of the mass distributions is statistically equivalent, however, and the dispersion remains the same. We must also point out that according to the results of Tremblay & Bergeron (2008), 15% of the DA white dwarfs in the temperature range considered here probably have thin hydrogen layers ($M_{\rm H}/M_{\rm tot} < 10^{-8}$). Consequently, the typical values for the mean mass are probably ~ 0.005 to 0.01 $M_\odot$ lower than the values reported in Figure 2.13.

As discussed in the Introduction, the spectroscopic technique provides very accurate measurements of the atmospheric parameters, allowing for a relative comparison of these parameters among individual stars. However, the *absolute* values of the atmospheric parameters may suffer from an offset due to uncertainties in the physics included in the model calculations. Hence it is very important to compare the results with independent methods. The most reliable independent observational constraint for DA white dwarfs comes from trigonometric parallax measurements. Holberg et al. (2008a) have shown using the recent photometric calibrations of Holberg & Bergeron (2006) that there exists a very good correlation between spectroscopically based photometric distance estimates and those derived from trigonometric parallaxes. Here we compare absolute visual magnitudes instead of distances. We first combine trigonometric parallax measurements with V magnitudes to derive $M_V(\pi)$ values. We then use the calibration of Holberg & Bergeron (2006) to obtain $M_V(\rm spec)$ from spectroscopic measurements of $T_{\rm eff}$ and $\log g$. We selected 92 DA stars with known parallaxes from the sample of Bergeron et al. (2007) (the uncertainties on the parallaxes must be less than 30%). The M_V values obtained from both model grids described in this section are compared in Figure 2.14. The agreement is very good within the parallax uncertainties for both model grids. Hence, despite

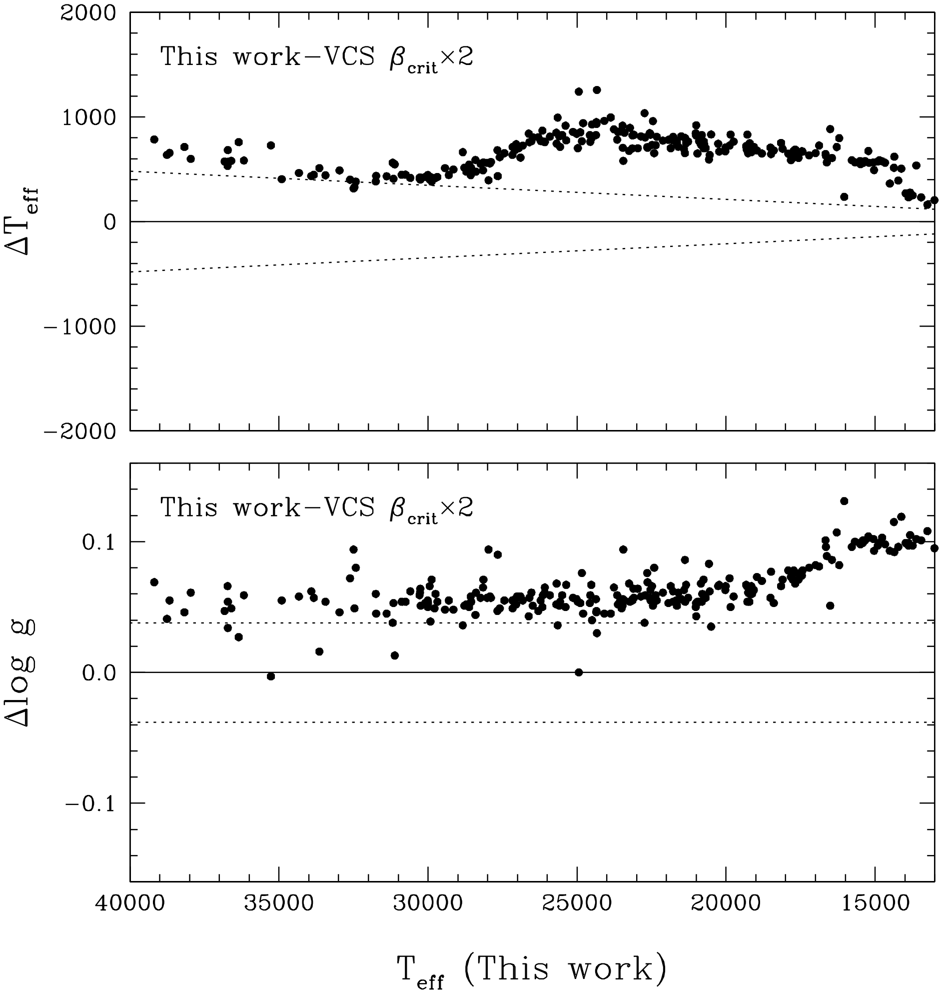

FIGURE 2.12 – Differences in $T_{\rm eff}$ and $\log g$ obtained with our improved models and with the VCS profiles ($\beta_{\rm crit} \times 2$) as a function of effective temperature for the DA stars in the PG sample in the range 40,000 K > $T_{\rm eff}$ > 13,000 K. The solid lines represent the 1:1 correlation while the dotted lines correspond to the uncertainties of the spectroscopic method as determined by Liebert et al. (2005).

the fact that our new models yield higher values of $T_{\rm eff}$ and $\log g$ (i.e., smaller radii), these two effects almost cancel each other and the predicted luminosities (or M_V) remain unchanged, and so are the conclusions of Holberg et al. (2008a). Another important constraint is provided by the bright white dwarf 40 Eri B for which a very precise trigonometric parallax and visual magnitude have been measured by Hipparcos. These measurements yield $M_V = 11.01 \pm 0.01$, while we predict $M_V = 11.02 \pm 0.07$ and 10.97 ± 0.07 based on our new and VCS models,

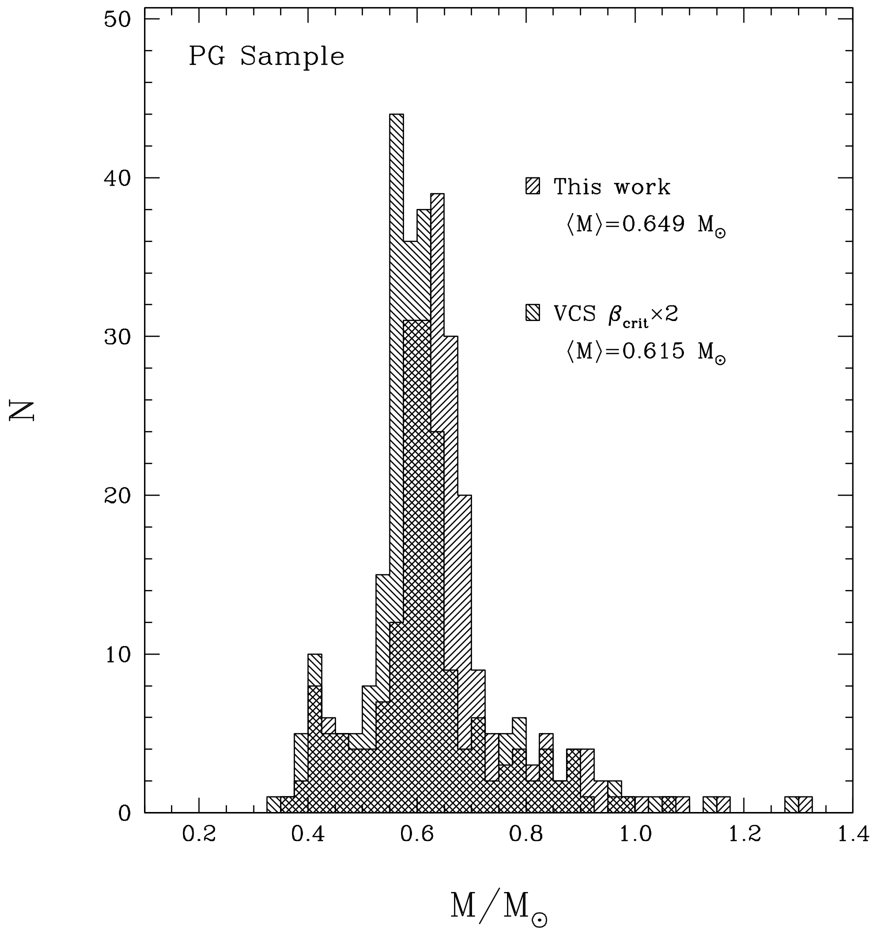

FIGURE 2.13 – Mass distributions for the subsample of PG stars studied in Figure 2.12. The mean masses are reported in the figure.

respectively. Although both determinations agree within the uncertainties with the observed value, our new grid provides an exact match to the measured M_V value.

We also point out that trigonometric parallax measurements are available mostly for cool white dwarfs (Bergeron et al. 1997) and nearby white dwarfs (Holberg et al. 2008b), which are excluded from our analysis. In contrast with our approach here, Bergeron et al. (1997) and Holberg et al. (2008b) make use of photometric measurements that cover the full spectral energy distributions, and both studies find mean masses near 0.65-0.66 $M_\odot$, consistent with our spectroscopic determinations for the PG sample.

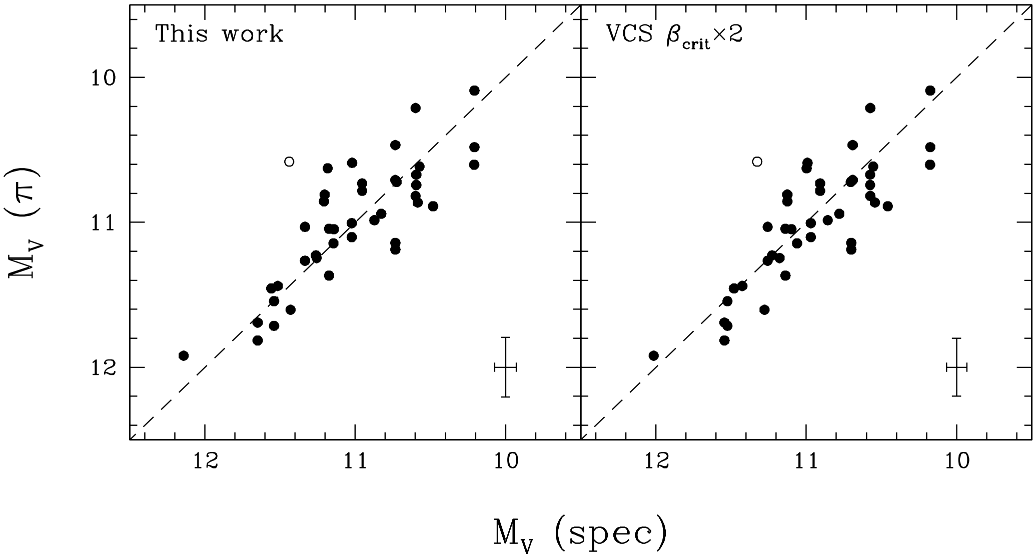

FIGURE 2.14 – Comparison of the absolute visual magnitudes obtained from trigonometric parallax measurements and from the spectroscopic technique using both model grids. The analysis is restricted to 40,000 K > $T_{\rm eff}$ > 13,000 K. The error bars represent the average uncertainties. WD 1606+422 (*open circle*) is a suspected double degenerate binary (Bergeron et al. 2001).

2.6 Conclusion

We have combined for the first time in a consistent physical framework the unified theory of Stark broadening from Vidal, Cooper, & Smith and the HM88 non-ideal equation of state. Both of these well known theories represent the basis of our current knowledge of DA white dwarfs. Following the suggestion of the late Mike Seaton, we have taken into account the non-ideal effects due to proton and electron perturbations directly into the line profile calculations. We have shown that our improved line profiles are significantly different from other Stark profiles that have been used in previous studies. We have computed the first grid of model spectra without the need of the parameterization of the critical field introduced by Bergeron (1993) and used in *all* previous models to mimic these non-ideal effects. We have demonstrated that our new profiles have important astrophysical implications. In particular, the mean mass of DA white dwarfs is $\sim 0.03\ M_\odot$ higher than previously measured. Yet, our updated atmospheric parameters determined from the spectroscopic technique remain in excellent agreement with the constraints imposed by trigonometric parallax measurements.

Future work will confront our improved models with observations in the more complex regime of higher and lower effective temperatures. An exhaustive look at the Lyman line analysis of UV observations from FUSE is also much needed since the model spectra are highly sensitive to the non-ideal effects in that particular spectral region. For cooler white dwarfs, we must also investigate the abrupt cut-off that has been introduced to limit the effects of the Lyman pseudo-continuum opacity.

We thank A. Gianninas for a careful reading of our manuscript, and M. Lemke for providing us with his computer version of the VCS code. We also thank the two referees for their constructive comments, which have greatly helped improving the presentation of our results. This work was supported in part by the NSERC Canada and by the Fund FQRNT (Québec). P. Bergeron is a Cottrell Scholar of Research Corporation for Science Advancement.

2.7 References

Ali, A. W., & Griem, H. R. 1965, Physical Review, 140, 1044

Ali, A. W., & Griem, H. R. 1966, Physical Review, 144, 366

Allard, N., & Kielkopf, J. 1982, Reviews of Modern Physics, 54, 1103

Allard, N. F., Kielkopf, J. F., & Loeillet, B. 2004, A&A, 424, 347

Barstow, M. A., Good, S. A., Burleigh, M. R., Hubeny, I., Holberg, J. B., & Levan, A. J. 2003, MNRAS, 344, 562

Bell, K. L. 1980, Journal of Physics B Atomic Molecular Physics, 13, 1859

Bergeron, P. 1993, NATO ASIC Proc. 403: White Dwarfs: Advances in Observation and Theory, 267

Bergeron, P., Gianninas, A., & Boudreault, S. 2007, in Proc. 15th European Workshop on White Dwarfs, ed. R. Napiwotzki & M. Burleigh (San Francisco: ASP), 372, 29

Bergeron, P., Leggett, S. K., & Ruiz, M. T. 2001, ApJS, 133, 413

Bergeron, P., Ruiz, M. T., & Leggett, S. K. 1997, ApJS, 108, 339

Bergeron, P., Saffer, R. A., & Liebert, J. 1990a, in Confrontation between Stellar Pulsation and Evolution, ed. C. Cacciari, A. S. P. Conference Series (Astronomical Society of the Pacific : Provo, Utah), 513

Bergeron, P., Saffer, R. A., & Liebert, J. 1992, ApJ, 394, 228 (BSL92)

Bergeron, P., Saumon, D., & Wesemael, F. 1995a, ApJ, 443, 764

Bergeron, P., Wesemael, F., & Fontaine, G. 1991, ApJ, 367, 253

Bergeron, P., Wesemael, F., Fontaine, G., & Liebert, J. 1990b, ApJ, 351, L21

Bergeron, P., Wesemael, F., Lamontagne, R., Fontaine, G., Saffer, R. A., & Allard, N. F. 1995b, ApJ, 449, 258

Borysow, U. G., Jorgensen, A. & Fu, Y. 1991, J. Quant. Spec. Radiat. Transf., 68, 235

Carnahan, N. F., & Starling, K. E. 1969, J. Chem. Phys., 51, 635

Condon, E. U., & Shortley, G. H. 1935, The Theory of Atomic Spectra (Cambridge: University Press)

Dalgarno, A., & Williams, D. A. 1962, ApJ, 136, 690

Däppen, W., Anderson, L., & Mihalas, D. 1987, ApJ, 319, 195

Demura, A. V., Demchenko, G. V., & Nikolić, D. 2008, European Physical Journal D, 46, 203

Edmonds, F. N., Jr., Schluter, H., & Wells, D. C. 1967, MmRAS, 71, 271

Eisenstein, D. J., et al. 2006, ApJS, 167, 40

Finley, D. S., Koester, D., & Basri, G. 1997, ApJ, 488, 375

Friedrich, H. 2006, Theoretical Atomic Physics (3d ed., Berlin: Springer)

Gianninas, A., Bergeron, P., & Dufour, P. 2005, in ASP Conf. Ser. 334, 14th European Workshop on White Dwarfs, ed. D. Koester & S. Moehler (San Francisco: ASP), 139

Gianninas, A., Bergeron, P., & Fontaine, G. 2006, AJ, 132, 831

Gustafsson, M., & Frommhold, L. 2003, A&A, 400, 1161

Hammond, G. L., Sion, E. M., Kenyon, S. J., & Aannestad, P. A. 1991, in 7th European Workshop on White Dwarfs, NATO ASI Series, ed. G. Vauclair & E. M. Sion (Dordrecht: Kluwer Academic Publishers), 317

Holberg, J. B., & Bergeron, P. 2006, ApJ, 132, 1221

Holberg, J. B., Bergeron, P., & Gianninas, A. 2008a, AJ, 135, 1239

Holberg, J. B., Sion, E. M., Oswalt, T., McCook, G. P., Foran, S., & Subasavage, J. P. 2008b, AJ, 135, 1225

Hooper, C. F. 1968, Physical Review, 169, 193

Hubeny, I., & Lanz, T. 1995, ApJ, 439, 875

Hummer, D. G., & Mihalas, D. 1988, ApJ, 331, 794 (HM88)

John, T. L. 1988, A&A, 193, 189

Kawka, A., & Vennes, S. 2006, ApJ, 643, 402

Kepler, S. O., Kleinman, S. J., Nitta, A., Koester, D., Castanheira, B. G., Giovannini, O., Costa, A. F. M., & Althaus, L. 2007, MNRAS, 375, 1315

Kissel, L. 2000, Radiation Physics and Chemistry, 59, 185

Koester, D. 1976, A&A, 52, 415

Kowalski, P. M., & Saumon, D. 2006, ApJ, 651, L137

Kurucz, R. L. 1970, SAO Special Report, 309,

Lee, R. W., & Oks, E. 1998, Phys. Rev. E, 58, 2441

Lemke, M. 1997, A&AS, 122, 285

Liebert, J., Bergeron, P., & Holberg, J. B. 2005, ApJS, 156, 47

Mihalas, D. 1978, Stellar Atmospheres (2nd ed., San Francisco: Freeman)

Nayfonov, A., Däppen, W., Hummer, D. G., & Mihalas, D. 1999, ApJ, 526, 451

Seaton, M. J. 1990, Journal of Physics B Atomic Molecular Physics, 23, 3255

Smith, E. W., Cooper, J., & Vidal, C. R. 1969, Physical Review, 185, 140

Stehlé, C. 1994, A&AS, 104, 509

Stehlé, C., Gilles, D., & Demura, A. V. 2000, European Physical Journal D, 12, 355

Stehlé, C., & Hutcheon, R. 1999, A&AS, 140, 93

Stehlé, C., & Jacquemot, S. 1993, A&A, 271, 348

Tremblay, P.-E., & Bergeron, P. 2008, ApJ, 672, 1144

Underhill, A. & Waddell, J. 1959, Stark Broadening Functions for the Hydrogen Lines (Washington, D.C.: U.S. Dept. of Commerce)

Vennes, S., Chayer, P., Dupuis, J., & Lanz, T. 2005, in ASP Conf. Ser. 334, 14th European Workshop on White Dwarfs, ed. D. Koester & S. Moehler (San Francisco: ASP), 185

Vidal, C. R., Cooper, J., & Smith, E. W. 1970, Journal of Quantitative Spectroscopy and Radiative Transfer, 10, 1011 (VCS)

Vidal, C. R., Cooper, J., & Smith, E. W. 1971, Journal of Quantitative Spectroscopy and Radiative Transfer, 11, 263

Vidal, C. R., Cooper, J., & Smith, E. W. 1973, ApJS, 25, 37

Wegner, G., & Schulz, H. 1981, A&AS, 43, 473

Wesemael, F., van Horn, H. M., Savedoff, M. P., & Auer, L. H. 1980, ApJS, 43, 159

Wiese, W. L., Kelleher, D. E., & Paquette, D. R. 1972, Phys. Rev. A, 6, 1132

Chapitre 3

NEW INSIGHTS INTO THE PROBLEM OF THE SURFACE GRAVITY DISTRIBUTION OF COOL DA WHITE DWARFS

P.-E. Tremblay[1], P. Bergeron[1], J. S. Kalirai[2], and A. Gianninas[1]

[1]*Département de Physique, Université de Montréal, C.P. 6128, Succ. Centre-Ville,*
Montréal, Québec, H3C 3J7, Canada

[2]*Space Telescope Science Institute, 3700 San Martin Drive, Baltimore, MD 21218, USA*

Received 2010 January 2; accepted 2010 February 18

Published in *The Astrophysical Journal*,
April 2010, *Vol.* 712, *page* 1345

3.1 Abstract

We review at length the longstanding problem in the spectroscopic analysis of cool hydrogen-line (DA) white dwarfs ($T_{\rm eff} < 13,000$ K) where gravities are significantly higher than those found in hotter DA stars. The first solution that has been proposed for this problem is a mild and systematic helium contamination from convective mixing that would mimic the high gravities. We constrain this scenario by determining the helium abundances in six cool DA white dwarfs using high-resolution spectra from the Keck I 10-m telescope. We obtain no detections, with upper limits as low as He/H = 0.04 in some cases. This allows us to put this scenario to rest for good. We also extend our model grid to lower temperatures using improved Stark profiles with non-ideal gas effects from Tremblay & Bergeron and find that the gravity distribution of cool objects remains suspiciously high. Finally, we find that photometric masses are, on average, in agreement with expected values, and that the high-$\log g$ problem is so far unique to the spectroscopic approach.

3.2 Astrophysical Context

The most accurate method for determining the atmospheric parameters of hydrogen-line (DA) white dwarfs — $T_{\rm eff}$ and $\log g$ — is through a detailed comparison of the observed Balmer line profiles with the predictions of model atmospheres. This so-called spectroscopic technique was applied to a sample of 37 cool ($T_{\rm eff} \lesssim 12,000$ K) DA stars by Bergeron et al. (1990) who showed that the surface gravities inferred from spectroscopic measurements were significantly larger than the canonical value of $\log g \sim 8$ expected for these stars. This result was readily interpreted as evidence for convective mixing between the thin superficial hydrogen layer with the more massive underlying helium envelope, a process originally, and independently, proposed by Koester (1976), Vauclair & Reisse (1977), and Dantona & Mazzitelli (1979). In this mixing process, helium brought to the surface would remain spectroscopically invisible because of the low photospheric temperatures. However, the helium abundance can still be determined from a detailed examination of the high Balmer lines, since the presence of helium increases the photospheric pressure, and thus produces a quenching of the upper levels of the hydrogen atom which, in turn, affects the line profiles (Liebert & Wehrse 1983). Bergeron et al. (1991) showed on a more quantitative basis that the effects produced on the hydrogen lines at high $\log g$ — or high masses — could not be distinguished from those produced by the presence of large amounts of helium in the atmospheres of cool DA stars. Such helium-enriched DA white dwarfs would simply *appear* to have high surface gravities when analyzed under the assumption of pure hydrogen atmospheres. By assuming instead a canonical value of $\log g = 8$ for all stars in their sample, Bergeron et al. (1990) were able to demonstrate that the surface compositions of most cool DA white dwarfs are contaminated by large amounts of helium, sometimes as high as He/H ~ 20.

This astrophysical interpretation, however, rests heavily on the theoretical framework, based on the occupation probability formalism of Hummer & Mihalas (1988), which was implemented by Bergeron et al. (1991) to properly model the hydrogen line profiles. It is thus entirely plausible that these improved model spectra yield large spectroscopic $\log g$ values simply because of inaccuracies in the input physics. With this idea in mind, Bergeron et al. (1992, hereafter BSL92) applied the spectroscopic technique to a large sample of DA white dwarfs that are sufficiently hot ($T_{\rm eff} \gtrsim 13,000$ K) to avoid any theoretical uncertainties related to the onset of convective energy transport at low effective temperatures, and to the possible presence of spectroscopically invisible traces of helium. The assumptions of radiative atmospheres with pure hydrogen compositions were then perfectly justified. The spectroscopic analysis of BSL92 allowed the first measurement of the $\log g$ and mass distributions of DA stars with an unprecedented accuracy. In particular, the spectroscopic $\log g$ distribution showed a sharp peak with a mean value of 7.909 with a dispersion of only 0.257, in agreement with the expected mean value for DA stars. Hence the spectroscopic technique and model spectra seemed to produce reasonably sound results, at least in this temperature range.

Around the same time, Bergeron et al. (1992) showed that the assumed parametrization of the convective efficiency, treated within the mixing-length theory in white dwarf models, could affect the emergent fluxes, and in particular the predicted line profiles of DA stars in the range $T_{\rm eff} \sim 8000 - 14,000$ K. This sensitivity suggests that perhaps the earlier interpretation of the presence of invisible traces of helium in cool DA stars could be caused by an inadequate parametrization of the mixing-length theory. In an attempt to properly calibrate the convective efficiency in the atmospheres of DA stars, Bergeron et al. (1995, hereafter B95) studied a sample of 22 ZZ Ceti stars and showed that the so-called ML2/$\alpha = 0.6$ version of the mixing-length theory (where α is the mixing-length to pressure scale height ratio) yielded the best internal consistency between optical and UV effective temperatures, trigonometric parallaxes, V magnitudes, and gravitational redshift measurements[1]. Yet, despite this adopted calibration, the large $\log g$ values observed in cool DA stars remained.

Our current view of what we will now refer to as the "high-$\log g$ problem" is best summarized in Figure 3.1, where we show the distribution of surface gravity as a function of effective temperature for the sample of over 1200 relatively bright DA white dwarfs of Gianninas et al. (2009), drawn from the online version of the Villanova White Dwarf Catalog[2] (see also similar results in Liebert et al. 2005; Bergeron et al. 2007; Kepler et al. 2007; Koester et al. 2009a; Gianninas et al. 2009). The model spectra used to determine our atmospheric parameters rely on the improved Stark broadening profiles of Tremblay & Bergeron (2009, hereafter TB09); these models are discussed further in Section 3.3. While the hotter DA stars in Figure 3.1 follow a distribution close to the canonical mean of $\log g = 8$, the surface gravities are shown to increase suddenly below $T_{\rm eff} \sim 12,500$ K to a constant average value of $\log g \sim 8.2$. Such high $\log g$ values cannot be real, of course, since white dwarf stars are expected to cool at constant radii. Furthermore, DA white dwarfs at $T_{\rm eff} \sim 12,500$ K have cooling ages of the order of 1 Gyr or so, and they can hardly represent a distinct galactic population (see additional discussions in Kepler et al. 2007 and Koester et al. 2009a). Consequently, inaccuracies in the model atmosphere calculations or inadequate assumptions about the composition of these stars need to be called upon to account for the observed trend. This longstanding problem represents a serious hurdle to obtaining reliable atmospheric parameters at the cool end of the white dwarf evolutionary sequence. This, in turn, may affect our determination of the white dwarf luminosity function (e.g., Harris et al. 2006) and our ability to use white dwarfs as reliable cosmochronometers and distance indicators (Fontaine et al. 2001; Hansen et al.

---

[1] Koester et al. (1994) arrived at a similar conclusion with a somewhat equivalent version of the mixing-length theory, ML1/$\alpha = 2.0$, although their analysis was based on a single object.

[2] http://www.astronomy.villanova.edu/WDCatalog/index.html

2007).

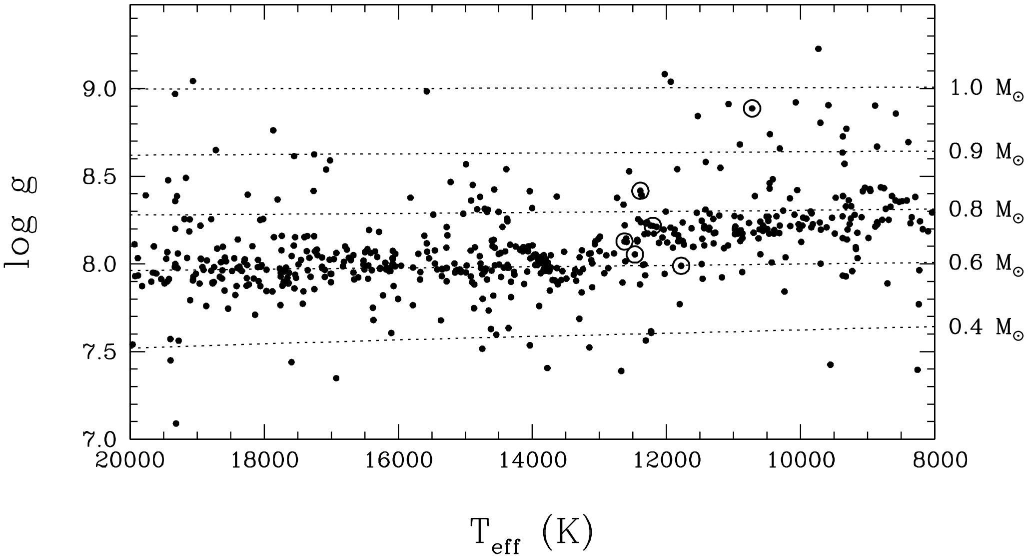

FIGURE 3.1 – Distribution of $\log g$ as a function of effective temperature for DA white dwarfs drawn from the sample of Gianninas et al. (2009). The atmospheric parameters are determined using the reference model grid described in this work (see Section 3.3), which is based on the improved Stark broadening profiles of TB09. Evolutionary models at constant mass from Fontaine et al. (2001) are shown with dashed lines and identified on the righthand side. The circles indicate the location of the six white dwarfs observed with HIRES on the Keck I 10-m telescope, and identified in Table 3.1.

Bergeron et al. (2007) and Koester et al. (2009a) have produced the most recent and extensive reviews of the high-$\log g$ problem and the possible solutions, but none appear very satisfactory to date. In particular, Koester concludes that inaccuracies in the treatment of convection in model atmospheres is responsible for the problem, for the lack of a better alternative. The mixing-length theory currently used in the models is indeed a crude approximation that makes use of a free parameter, but model spectra properly calibrated yield atmospheric parameters that are quite reasonable, in particular for stars near the ZZ Ceti instability strip (see, e.g., Gianninas et al. 2006). Furthermore, Ludwig et al. (1994) showed with more sophisticated 2D hydrodynamic models that the mixing-length theory was roughly correct to predict the temperature structure of the photospheric regions of DA white dwarfs. More detailed comparisons may prove otherwise, however. Their results do suggest that deeper layers have a significantly higher convective efficiency than predicted from the mixing-length theory, but this has little effect on the predicted spectra.

The solution originally proposed by Bergeron et al. (1990) that the presence of helium in the atmospheres of cool DA stars is responsible for the high-$\log g$ problem cannot be tested directly since helium becomes spectroscopically invisible at the effective temperatures and expected helium-to-hydrogen abundance ratios where the problem manifests itself. Or at least, this used to be our common understanding. This view has recently been challenged by two important discoveries. Koester et al. (2005) were the first to report the detection of weak helium lines in a DA star (HS 0146+1847) with a temperature slightly below $T_{\rm eff} \sim 13,000$ K; this white dwarf turns out to be a peculiar helium-dominated and metal-rich DAZB star. More importantly, HIRES spectroscopic observations with Keck of the metal-rich DAZ star GD 362 revealed the presence of a very weak He I λ5877 absorption feature (Zuckerman et al. 2007), in a white dwarf with an estimated temperature of only $T_{\rm eff} \sim 10,000$ K. The detailed model atmosphere analysis by Zuckerman et al. also revealed that GD 362 has in fact a helium-dominated atmosphere. Interestingly enough, GD 362 and HS 0146+1847 are also surrounded by a circumstellar disk (Becklin et al. 2005; Farihi et al. 2009). These findings clearly demonstrate that helium can indeed be detected *directly* in this temperature range when observed at sufficiently high signal-to-noise ratio and high dispersion. The weak helium lines detected in both white dwarfs could even be reproduced with model spectra.

In this paper, we provide new insights into the problem of the surface gravity distribution of cool DA white dwarfs by presenting observations of six objects with the High Resolution Echelle Spectrometer (HIRES, Vogt et al. 1994) on the Keck I 10-m telescope and attempt to measure, or constrain, *directly* the helium abundance in the atmosphere of DA white dwarfs.

3.3 The Presence of Helium in Cool DA White Dwarfs

3.3.1 A Reassessment of the Convective Mixing Scenario

As discussed above, the contamination of DA white dwarf atmospheres by trace amounts of helium has been the first and longest running solution to the high-$\log g$ problem. In particular, Bergeron et al. (1991) showed that at low effective temperatures ($T_{\rm eff} \lesssim 12,000$ K), a high surface gravity DA white dwarf with a pure hydrogen atmosphere would appear identical to a helium-enriched DA star with a normal mass. On the right panels of Figure 3.2, we illustrate a typical example of this degeneracy for the cool DA star LHS 3254, where the spectroscopic fit with pure hydrogen models ($T_{\rm eff} = 9370$ K, $\log g = 8.27$) is qualitatively equivalent to the fit with a mixed helium/hydrogen composition of He/H = 1.0 at a comparable temperature ($T_{\rm eff} = 9300$ K), but with a much lower $\log g$ value of 7.81. On the left panels are shown the corresponding fits to the optical $BVRI$ and infrared JHK photometry. Here, only the effective temperature and the solid angle $\pi(R/D)^2$ are considered free parameters (R is the radius of the star and D its distance from Earth), while the distance is obtained from the trigonometric parallax measurement. It can be seen that the $T_{\rm eff}$ and $\log g$ values obtained from the photometric solutions are not as sensitive to the assumed helium abundance as the spectroscopic solutions. In the example shown here, the helium abundance has in fact been *adjusted* to ensure that the photometric and spectroscopic $\log g$ values agree. We also note that the photometric and spectroscopic temperatures agree even better when helium is included. Hence, photometric and spectroscopic measurements combined with trigonometric parallaxes can effectively provide, in principle, a unique and self-consistent solution for the atmospheric parameters of cool DA stars, assuming of course that the presence of helium is responsible for the high-$\log g$ problem. Unfortunately, parallax measurements are generally not accurate enough, or even unavailable, and there are many instances where photometric $\log g$ values are already larger than spectroscopic values, even with pure hydrogen models (see Boudreault & Bergeron 2005 and the paragraph below).

With this in mind, it is generally preferable to use a statistical approach to quantify the He/H ratio in cool DA stars. If we assume for instance that the masses of cool DA stars are normal — i.e. the same as for hot DA stars — we can fix the mass and consider the effective temperature and the He/H ratio as free parameters in the spectroscopic fitting technique. The results of this experiment are presented in Figure 3.3, where we show the helium abundance as a function of $T_{\rm eff}$ for the same sample of cool DA stars used in Figure 3.1, but with the mass of each star set to 0.649 $M_\odot$, which corresponds to the mean mass derived by TB09

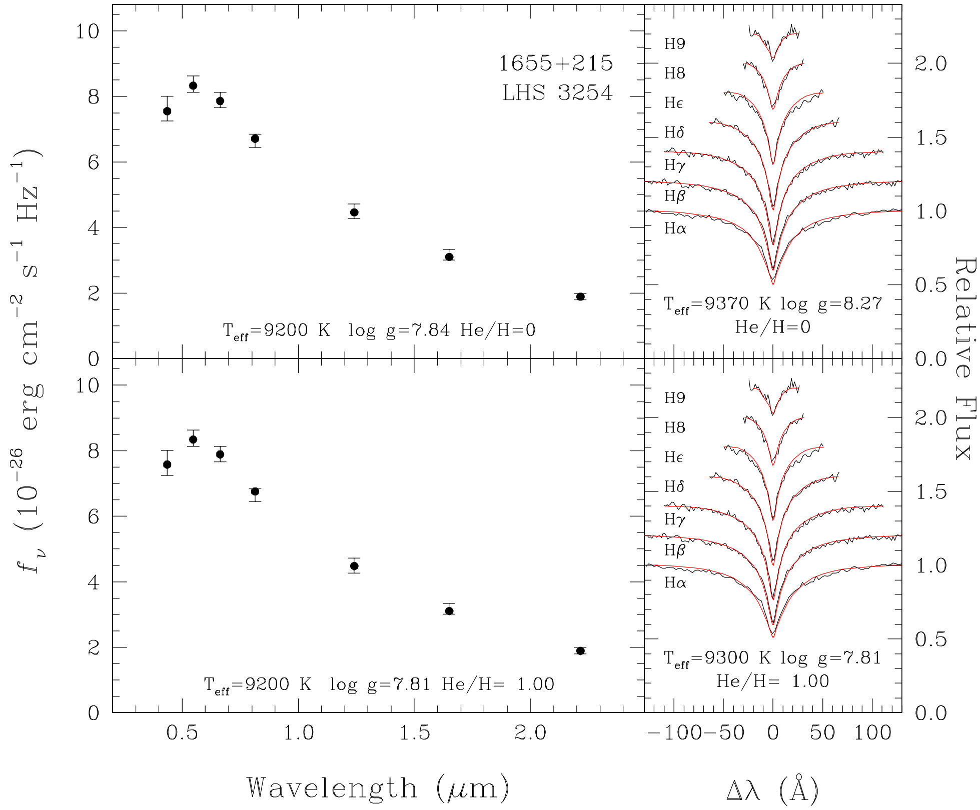

FIGURE 3.2 – Our best spectroscopic and photometric fits to the DA star LHS 3254 (1655+215) using pure hydrogen models (*top panels*). In the left panel, the error bars represent the observed fluxes derived from optical $BVRI$ and infrared JHK magnitudes, while the corresponding model fluxes are shown as filled circles. The 0.43 dex discrepancy in $\log g$ between both fitting techniques can be resolved if helium is allowed in the atmosphere (*bottom panels*). From a qualitative point of view, both the pure hydrogen and mixed He/H solutions are indistinguishable. This is an updated version of Figure 20 from Bergeron et al. (2001).

for the DA stars above $T_{\rm eff} = 13,000$ K in the Palomar-Green sample. The upper limits at the bottom of the figure correspond to objects for which the spectroscopic masses are already below the mean value adopted here. We can clearly see that there is a concentration of stars with helium abundances in the range He/H $\sim 0.1 - 0.3$. These results suggest that a mild but *systematic* helium contamination could shift the mass distribution to the expected lower value. For a better illustration, we refitted the same sample of cool DA stars with a constant value of He/H = 0.25 — the average helium abundance in this sample — and plotted the results in Figure 3.4 together with the pure hydrogen solutions. Hence, with a sudden onset of helium contamination near $T_{\rm eff} \sim 12,500$ K, we can obtain a stable mass distribution throughout the entire white dwarf temperature regime. It must be stressed that this systematic contamination does not prevent *individual* objects like GD 362 from having much larger helium abundances, or even some stars from having pure hydrogen atmospheres. These objects must be rare, however, since the constant mass distribution achieved in Figure 3.4 can only be recovered if the vast majority of cool DA stars have a mild helium contamination.

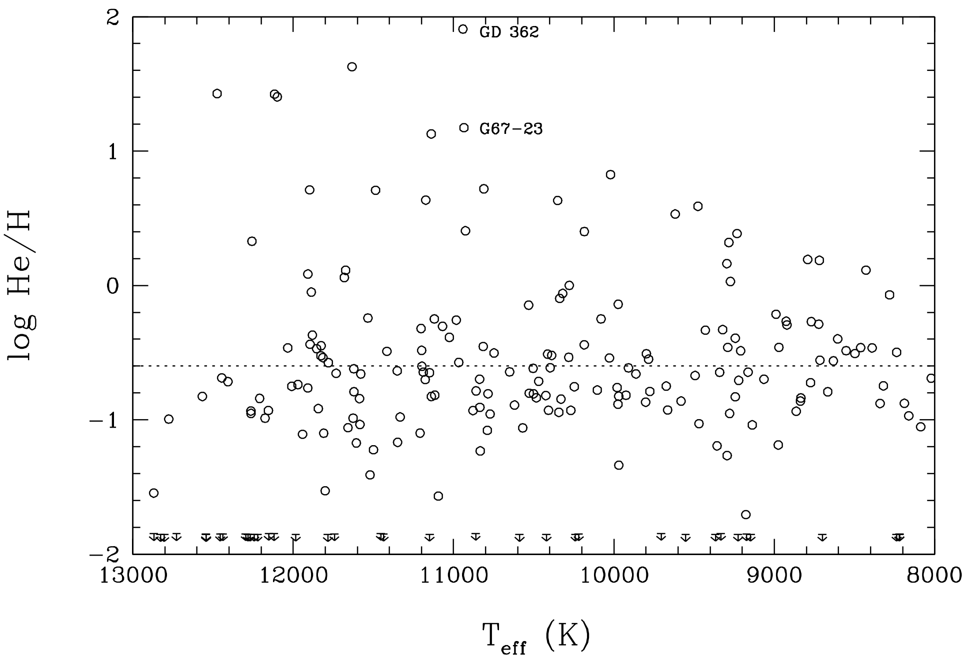

FIGURE 3.3 – Helium abundance determinations as a function of $T_{\rm eff}$ for the cool DA white dwarfs in the sample of Gianninas et al. (2009, same as Fig. 3.1), assuming a mass of 0.649 $M_{\odot}$ for all stars. The two objects labeled in the figure are discussed in the text. The downward arrows at the bottom of the figure represent the objects for which the spectroscopic mass is already smaller than 0.649 $M_{\odot}$. The dashed line indicates a systematic contamination of He/H = 0.25 used in our discussion.

As discussed above, the source of this helium contamination could be most easily explained by convective mixing between the thin hydrogen layer and the deeper and more massive helium envelope. The extent of the hydrogen convection zone is displayed in Figure 3.5 as a function of effective temperature for a 0.6 $M_{\odot}$ DA white dwarf, based on evolutionary models with thick hydrogen layers similar to those described by Fontaine et al. (2001). These

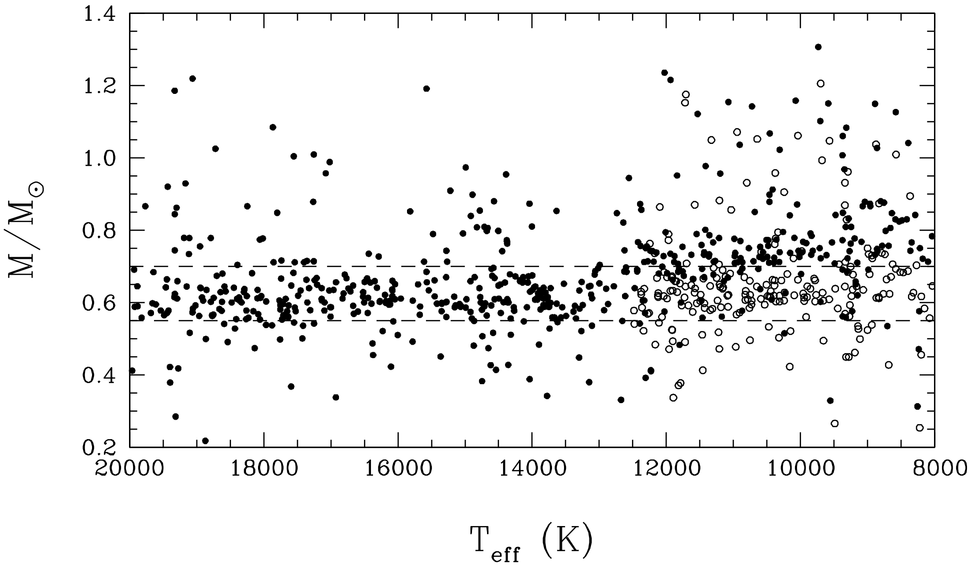

FIGURE 3.4 – Filled circles: same as Figure 3.1 but with the $\log g$ values converted into mass using the evolutionary models of Fontaine et al. (2001) with thick hydrogen layers; lines of constant mass at 0.55 and 0.70 $M_\odot$ are shown as a reference. Open circles: mass distribution of white dwarfs below $T_{\rm eff} = 12,500$ K obtained from model spectra that contain small traces of helium with He/H = 0.25. Such a mild but systematic helium contamination produces a consistent mass distribution throughout the entire temperature range displayed here.

calculations show that if the hydrogen envelope is thin enough, the bottom of the hydrogen convection zone may eventually reach the underlying and more massive convective helium layer, resulting in a mixing of the hydrogen and helium layers. This figure also indicates that the effective temperature at which mixing occurs will depend on the thickness of the hydrogen envelope. The thicker the envelope, the lower the mixing temperature; if the hydrogen layer is more massive than $M_{\rm H}/M_{\rm tot} \sim 10^{-6}$, mixing will never occur. The simplest physical model that can be used to describe this convective mixing process is to assume that hydrogen and helium are homogeneously mixed. Since the helium convection zone is much more massive ($M_{\rm He-conv}/M_{\rm tot} \sim 10^{-6}$) than the hydrogen layer when mixing occurs, it is generally assumed that a DA star would be transformed into a helium-atmosphere non-DA white dwarf with only a trace abundance of hydrogen. By performing a statistical analysis of the ratio of hydrogen- versus helium-rich white dwarfs as a function of $T_{\rm eff}$, Tremblay & Bergeron (2008) demonstrated that such mixing does indeed occur, but not until white dwarfs reach temperatures below ~ 9000 K. Even then, mixing seems to occur for only 15% of all DA stars. This view is consistent with our current understanding that most DA stars probably have thick hydrogen layers with $M_{\rm H}/M_{\rm tot} \gtrsim 10^{-6}$ (see Table 7 of Fontaine & Brassard 2008).

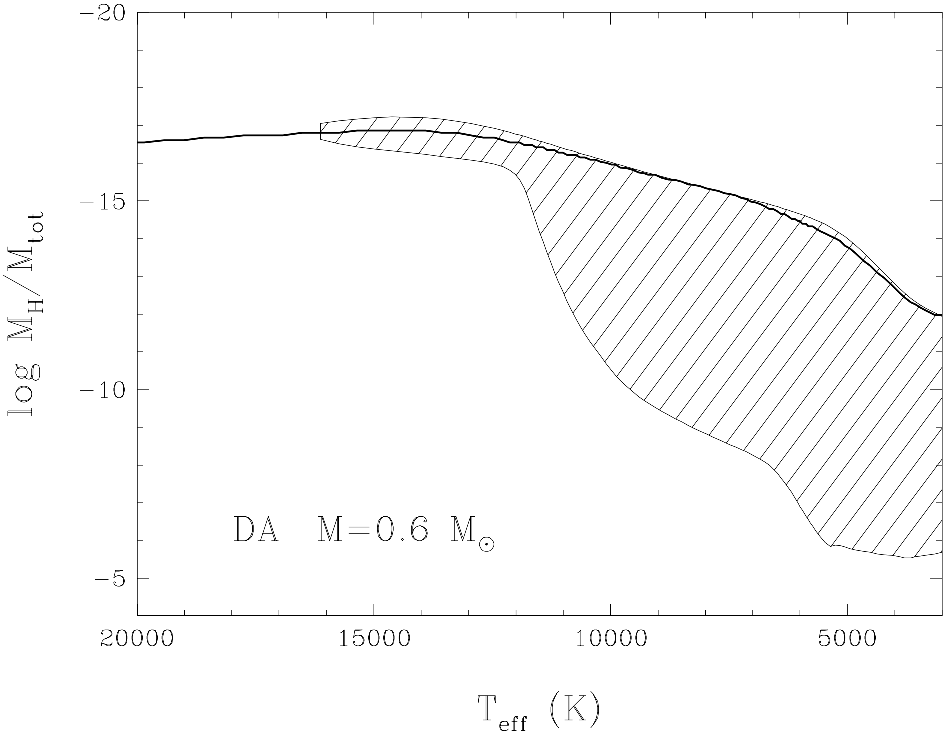

FIGURE 3.5 – Location of the hydrogen convection zone (*hatched region*) as a function of effective temperature in the pure hydrogen envelope of a 0.6 $M_{\odot}$ DA white dwarf calculated with the ML2/$\alpha = 0.6$ version of the mixing-length theory (from G. Fontaine & P. Brassard 2006, private communication). The depth is expressed as the fractional mass above the point of interest with respect to the total mass of the star. The thick solid line corresponds to the photosphere ($\tau_R \sim 1$).

Since the helium abundances inferred from Figure 3.3 are significantly lower than those expected from this standard convective mixing scenario, it is necessary to invoke an alternative and incomplete mixing process that would systematically contaminate the atmospheres of DA stars with only small amounts of helium, perhaps through overshooting. However, the hydrogen convection zone in a 12,000 K DA white dwarf is very thin according to Figure 3.5, much smaller than the ~ 10^{-6} $M_{\odot}$ or so expected for the total hydrogen layer mass of most

DA stars, and any type of convective overshooting thus appears improbable. If we were to confirm such an incomplete mixing scenario, we would have to review our assumption that hydrogen and helium are homogeneously mixed when convection zones connect, as well as our estimates of the thickness of the hydrogen layers in DA stars.

3.3.2 Direct Detection of Helium in Cool DA White Dwarfs

According to the incomplete convective mixing scenario, a systematic helium contamination estimated at He/H = 0.25 (see Fig. 3.3) would be able to explain the high-$\log g$ problem. Obviously, the actual ratio may vary from star to star, but on average, the helium abundance of individual DA stars must be close to this value if this interpretation is correct. In this section, we attempt to test this scenario through direct observations of helium in the photospheres of cool DA stars. For this purpose, we used our model atmospheres to predict the strength of the He I $\lambda5877$ line for a wide range of atmospheric parameters. These are similar to those described in TB09, with the exception that we now include the detailed helium line opacity calculations of Beauchamp et al. (1996, and references therein) and Beauchamp et al. (1997), which also take into account the Hummer-Mihalas occupation probability formalism (more details are provided in Section 3.3). In line with the results for GD 362 and HS 0146+1847, we find that helium can indeed be detected spectroscopically in the range of temperatures where the incomplete mixing scenario is believed to occur, but the detection of this helium line requires high-resolution ($R \sim 20,000$) and high signal-to-noise (S/N $\gtrsim$ 100) spectroscopic observations. Since the brightest white dwarfs in this temperature range have $V \sim 12.5 - 15.0$, an echelle spectrograph on an 8-meter class telescope is absolutely necessary to detect this weak absorption feature.

With these predictions in hand, we requested one night of observing time on the Keck I 10-m telescope on Mauna Kea with HIRES. Our objective was to observe the spectral region around the He I $\lambda5877$ line for at least five DA stars with $T_{\rm eff} < 12,500$ K to investigate whether the helium contamination is indeed systematic. We first computed the S/N and integration time required to achieve a 3σ detection for DA stars selected from the sample of Gianninas et al. (2009). We found that stars below $T_{\rm eff} \sim 10,500$ K would require more than five hours of observation time to achieve our detection threshold, even for the brightest stars, compromising our original strategy. We thus reduced our target list to a representative sample of six bright DA stars in the range $12,500 \gtrsim T_{\rm eff} \gtrsim 10,500$ K. The atmospheric parameters for all six white dwarfs are given in Table 3.1; these are obtained by fitting lower resolution spectra taken from the spectroscopic survey of Gianninas et al. (2009) with pure hydrogen model atmospheres. The location of these objects in Figure 3.1 (circles) indicates that they occupy a region in $T_{\rm eff}$ and $\log g$ where the spectroscopic $\log g$ values rise significantly. We note that four DA stars in our sample have surface gravities significantly in excess of the canonical value of $\log g = 8$. Our coolest target, G67-23 (labeled in Fig. 3.3), is predicted to be a very massive ($M \sim 1.14\ M_\odot$) white dwarf under the assumption of a pure hydrogen composition. Not surprisingly, five out of six objects also turn out to be ZZ Ceti pulsators.

TABLE 3.1 – Upper Limits on the Helium Abundance in Cool DA White Dwarfs

WD	Name	$T_{\rm eff}$ (K)$^{\rm a}$	$\log g^{\rm a}$	He/H (3σ)	Note
0133−116	Ross 548	12470	8.05	<0.04	1
0415+271	HL Tau 76	11780	7.99	<0.11	1
1855+338	G207-9	12390	8.42	<0.09	1
1935+276	G185-32	12630	8.13	<0.04	1
2246+223	G67-23	10720	8.89	<1.42	
2326+049	G29-38	12200	8.22	<0.04	1,2

$^{\rm a}$ $T_{\rm eff}$ and $\log g$ assume pure hydrogen models. Notes: (1) ZZ Ceti stars; (2) DAZ star with a circumstellar disk.

High S/N spectroscopic observations for all stars in Table 3.1 were secured on 2009, August 26 using the HIRES instrument with the red collimator and the 0.”86 slit ($R \sim 50,000$). The spectroscopic data were reduced using the MAKEE reduction software (version 5.2.4) and carefully calibrated to vacuum wavelengths. We show in Figure 3.6 the high-resolution spectra for the six stars in the region of the He I λ5877 line, along with the predicted helium line profiles. The thick solid lines correspond to the predictions with a systematic helium contamination of He/H = 0.25, while the dotted lines assume a 0.649 $M_\odot$ stellar mass. This last assumption implies that any surface gravity measurement above $\log g \sim 8.08$ is attributed to the presence of helium; this applies to only four stars in Table 3.1 and in Figure 3.6. *Our results clearly indicate a non-detection of helium for all objects in our sample.*

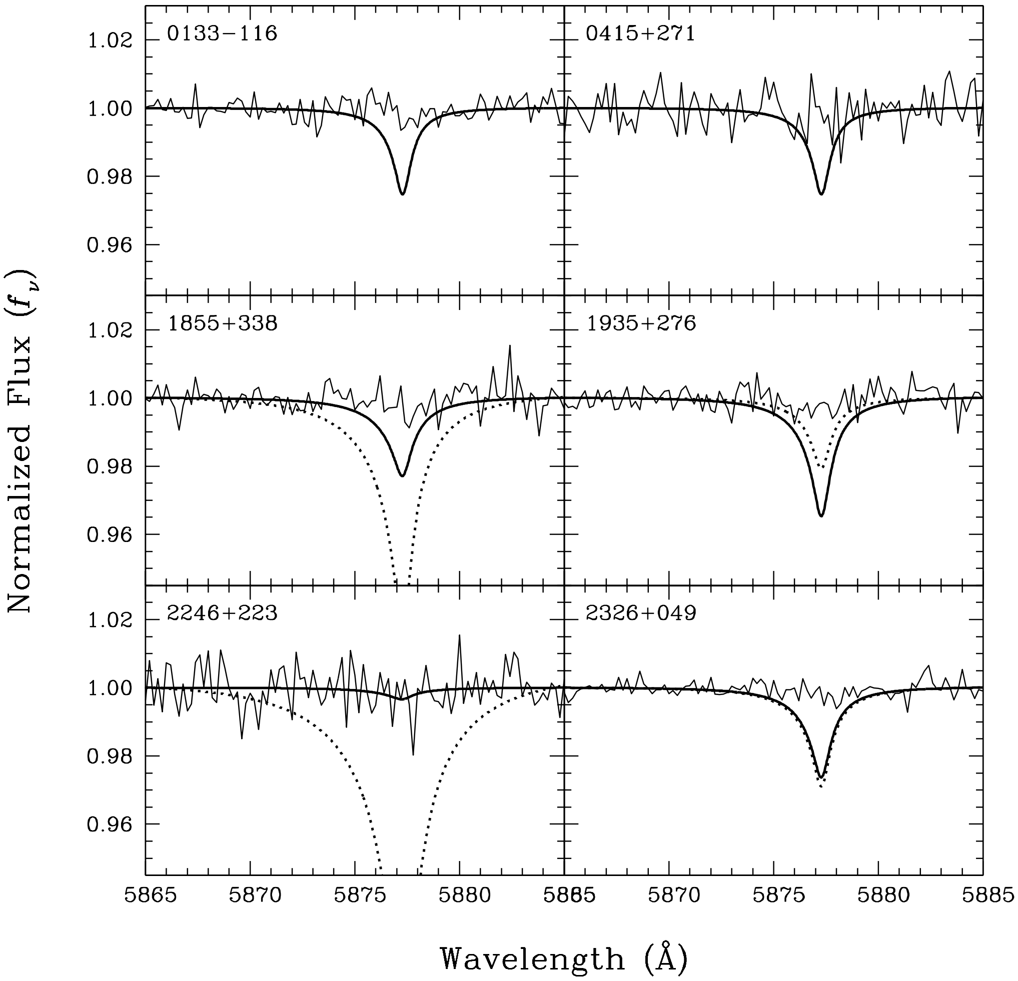

FIGURE 3.6 – High-resolution spectra for the six white dwarfs observed with the HIRES spectrograph on the Keck I 10-m telescope. Predictions from model atmospheres with a systematic helium contamination of He/H = 0.25 are shown as thick solid lines. For four objects (1855+338, 1935+276, 2246+223, and 2326+049), we also show as dotted lines the predicted spectra for an assumed mass of 0.649 $M_\odot$ and helium abundances determined from our spectroscopic fits to low-resolution spectra (the two other objects have spectroscopic masses already lower than 0.649 $M_\odot$). Both the observed and model spectra are shown with a 0.2 Å resolution for clarity.

Our spectroscopic data can provide upper limits on the helium abundance in the photosphere of these stars. We first obtain from our low-resolution spectra the best fitted parameters $T_{\rm eff}$ and $\log g$ for a given helium abundance. We then increase the helium abundance until the depth of the predicted He I $\lambda5877$ line profile is 3σ above the noise level of our HIRES data[3]. These upper limits on the helium abundance are reported in Table 3.1 for each star. For five objects, we find very low upper limits for the He/H abundance ratio (less than one tenth). We must therefore conclude that a mild and systematic helium contamination in the atmospheres of cool DA white dwarfs cannot be the origin of the high-$\log g$ problem.

The case of G67-23 (2246+223) is particularly of interest since our low-resolution optical spectrum exhibits high Balmer lines characteristics of a massive DA star (see Fig. 1b of Lajoie & Bergeron 2007), or alternatively, of a normal mass white dwarf with a helium-dominated atmosphere, such as GD 362. According to Figure 3.6, however, our observations can rule out this last possibility, although our limit on the helium abundance in this star is not as stringent as for the other five objects in our sample. Finally, we note that another target, G29-38, is a peculiar DAZ star with a circumstellar disk. The detection of helium in this star would have been problematic since the source of the contamination could have been non-stellar. However, our non-detection implies that this object can effectively be used to constrain the incomplete mixing scenario.

We thus demonstrated for the first time that there is probably little to no helium in the photospheres of most cool DA white dwarfs. We believe our results put to rest the scenario invoking an incomplete convective mixing between the hydrogen atmosphere and the underlying helium envelope, and alternative explanations must be sought to solve the high-$\log g$ problem in cool DA stars.

3.3.3 Helium Contamination in GD 362

For completeness and internal consistency, we reanalyze in this section the available data for GD 362. This object represents the coolest DA star with a direct detection of the He I λ5877 line. We reproduce in Figure 3.7 the observations of GD 362 from Zuckerman et al. (2007) taken from the Keck Observatory Archive (KOA)[4]. We combine in our analysis this HIRES spectrum with the lower resolution optical spectrum of Gianninas et al. (2004) to determine the atmospheric parameters ($T_{\rm eff}$, $\log g$, and He/H). The general fitting procedure

---

[3] Since we oversample the predicted line profiles with the 0.1 Å resolution, we binned by a factor of 4 to provide better, but still conservative upper limits.

[4] www2.keck.hawaii.edu/inst/hires/

is described in Liebert et al. (2005), although here we only use the lines from Hβ to Hδ in the fit because the higher Balmer lines are heavily contaminated by metallic lines.

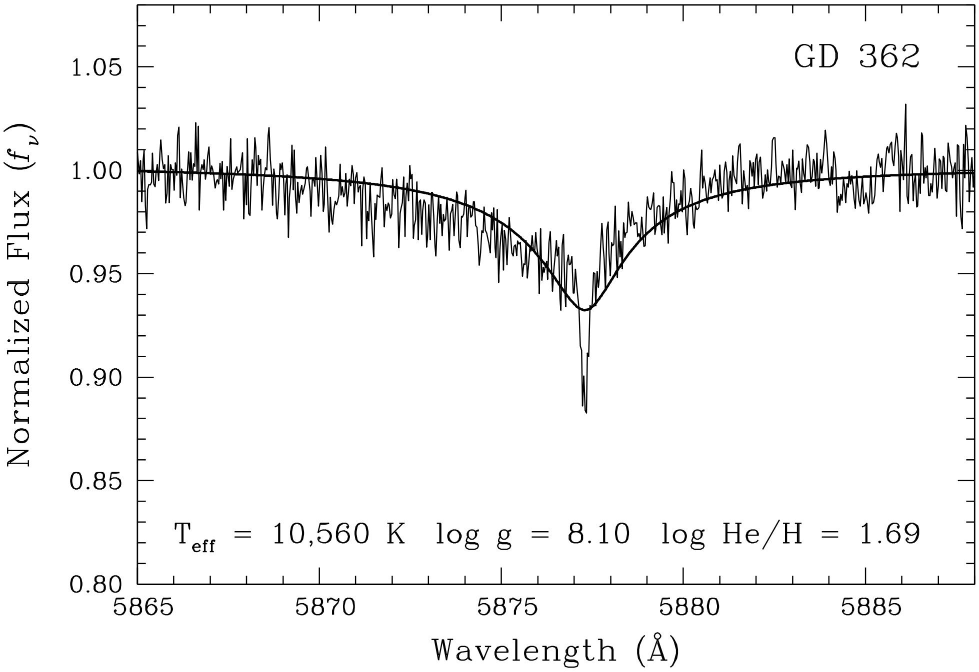

FIGURE 3.7 – The observed HIRES spectrum of GD 362 (Zuckerman et al. 2007) from the Keck Observatory Archive. The raw data were reduced using MAKEE and calibrated to vacuum wavelength. We added the six similar exposures obtained over three different nights. The spectrum is used to constrain the He/H ratio using the best fit to the equivalent width of the line. The $T_{\rm eff}$ and $\log g$ values are determined from a fit to our low-resolution Balmer spectrum with mixed He/H models. The resulting atmospheric parameters are given in the figure.

Our determination of the helium abundance in GD 362 proceeds in the same way as in Zuckerman et al. (2007). The degeneracy between the He/H abundance ratio and $\log g$ allows us to compute a sequence of best fitting models from the Balmer line analysis, with a set of parameters ($T_{\rm eff}$ and $\log g$) assigned to each helium abundance. The optimal He/H abundance ratio, and the corresponding $T_{\rm eff}$ and $\log g$ values, are then found by fitting the equivalent width of the He I λ5877 line profile. Our best fitted parameters for GD 362 are given in Figure 3.7 together with our prediction of the helium line profile. While the overall strength of the absorption feature is well reproduced, the line core is not predicted as sharp and deep, a discrepancy similar to that reported by Zuckerman et al. (2007, see their Fig. 1). Our value for the effective temperature, $T_{\rm eff} = 10,560$ K is in excellent agreement with that of Zuckerman et al. (2007, $T_{\rm eff} = 10,540\pm200$ K), although both our $\log g$ and helium abundance determinations differ, within the uncertainties, from the values obtained by Zuckerman et al. (2007), $\log g = 8.24 \pm 0.04$ and $\log {\rm He/H} = 1.14 \pm 0.1$ (our internal errors are comparable to those of Zuckerman et al.). The solution obtained by Zuckerman et al. is actually a poor match to our low-resolution spectrum, although the predicted helium line strength agrees with the HIRES observations. Hence the mass we derive for GD 362, $M = 0.64\ M_\odot$ (using evolutionary models with thin hydrogen layers), is actually quite average (Zuckerman et al. obtained 0.73 $M_\odot$). The independent mass determination reported by Kilic et al. (2008), $M = 0.74\ M_\odot$, which is based on a measurement of the trigonometric parallax of GD 362, actually favors the solution of Zuckerman et al., but see our discussion below.

Since the overall procedures are similar, some of the differences between our results and those of Zuckerman et al. might be attributed to our particular analysis of the higher Balmer lines, or to the treatment of the non-ideal effects in the Hummer-Mihalas occupation probability formalism. In any case, these atmospheric parameter determinations must be taken with caution. First of all, the strength of the hydrogen lines at such high helium abundances is particularly sensitive to the Hummer-Mihalas occupation probability for neutral particles (Koester et al. 2005), and a slight change in the hard sphere radius used in the description of the neutral particle interaction may result in significantly different atmospheric parameters. The current parameterization (see Section 3.5.1) is uncertain in this high-density regime and one could adjust the theory until there is match between our spectroscopic solution and the constraints obtained from the trigonometric parallax measurement of Kilic et al. (2008). Gianninas et al. (2004) also showed that the presence of metals does not affect significantly the atmospheric structure of GD 362 for pure-hydrogen atmospheres, but this assumption has not been fully tested for helium-rich compositions. And finally, as mentioned above, the sharp core of the helium line is not well reproduced by the models, a feature that is not observed in the slightly hotter white dwarf HS 0146+1847. Perhaps hydrogen is not homogeneously distributed in the atmosphere of GD 362, especially if hydrogen is being accreted (Jura et al.

2009).

Despite the preceding discussion, it is clear that GD 362, which was interpreted by Gianninas et al. (2004) as a massive ($M \sim 1.24\ M_\odot$) white dwarf with a hydrogen-dominated and metal-rich atmospheric composition, is in fact a more average mass white dwarf with a helium-dominated atmosphere. According to the helium abundances inferred in cool DA stars and displayed in Figure 3.3, such objects must be rare since there are very few stars in the upper part of this diagram. GD 362 (labeled in Fig. 3.3) is actually the object with the largest helium abundance according to our statistical analysis. Also labeled in this figure is one of our targets, G67-23 (2246+223), which does not show any trace of helium (see Fig. 3.6). The peculiar helium-dominated star HS 0146+1847, the hotter counterpart of GD 362, was discovered in the SPY sample containing more than ~ 1800 high-resolution spectra; Koester et al. (2009a) searched this sample for DA stars with traces of helium, including a fairly large number with temperatures below 13,000 K. The search was also negative, but with a much larger detection limit than provided here with our Keck I observations. Nevertheless, it is an additional argument that such objects must be very rare.

The existence of the peculiar atmospheric composition of GD 362 and HS 0146+1847 may be explained by two different scenarios. We may be witnessing white dwarfs in the process of being convectively mixed, a process believed to occur in cooler white dwarfs (Tremblay & Bergeron 2008). This would imply, however, unusually thin hydrogen layers according to the results shown in Figure 3.5. Alternatively, the mixed H/He composition could have a non-stellar origin, perhaps related to the collision with a water-rich asteroid in the case of GD 362 (Jura et al. 2009), resulting in the accretion of hydrogen onto a helium-rich atmosphere. The fact that these two objects are metal-rich with circumstellar disks suggests that the latter is the most likely explanation until we discover more similar objects.

3.4 Model Atmospheres with Improved Stark Profiles

As discussed in the introduction, our approach with respect to the spectroscopic technique has always been to start with the simplest white dwarf atmospheres to validate the method. For instance, BSL92 demonstrated that the spectroscopic technique is the most accurate method for determining the atmospheric parameters of DA stars using a sample of pure hydrogen atmosphere white dwarfs where convective energy transport can be neglected ($T_{\rm eff} > 13,000$ K). B95 later extended this spectroscopic analysis to ZZ Ceti stars, which are located in the temperature range where the atmospheric structures are the most sensitive to the assumed convective efficiency. They found in particular that the ML2/$\alpha = 0.6$ parameterization of the mixing length theory (MLT) provided the best internal consistency between optical and UV temperatures. However, this calibration of the convective efficiency in DA stars did not change the persisting problem that higher than average masses were found at low effective temperatures. More recently, TB09 published Stark broadening profiles with the first consistent implementation of the Hummer-Mihalas equation of state. They included non-ideal perturbations from protons and electrons directly inside the Vidal et al. (1970) unified theory of Stark broadening. As a first step, they revisited the BSL92 temperature regime with improved model atmospheres of hot DA stars. They showed convincingly that these models were adequate to describe the observations, resulting also in $T_{\rm eff}$ and $\log g$ measurements significantly larger than those obtained from previous models. In this section, we explore the implications of these improved models on the sepctroscopic analysis of cooler DA white dwarfs, including the ZZ Ceti stars.

Following our approach with the spectroscopic technique, we must first recalibrate the convective efficiency using the same approach as B95. The tightest constraint comes from the comparison of effective temperatures measured independently from optical and UV spectra (see B95 for details). Other constraints, such as trigonometric parallaxes and gravitational redshifts, are not used for this calibration; they will be compared to our models in Section 3.4. We use an improved set of *HST* and *IUE* near-UV observations (Holberg et al. 2003), some of which were not available at the time of the B95 study. We first fit the optical spectra to find $T_{\rm eff}$ and $\log g$ values. In the case of the near-UV spectra, solutions are degenerate in $T_{\rm eff}$ and $\log g$ and both atmospheric parameters cannot be fitted simultaneously. Therefore, we fit the UV spectra by forcing the spectroscopic value of $\log g$, and the parameter α is then varied until an internal consistency is achieved between UV and optical temperatures. Figure 3.8 (which is an updated version of Figure 11 of B95) indicates that the ML2/$\alpha = 0.8$ version of the MLT provides the best overall internal consistency. This is a significantly more efficient version of the MLT than estimated by B95 ($\alpha = 0.6$), in closer agreement with that required by nonadiabatic models ($\alpha = 1.0$) to match the empirical blue edge of the ZZ ceti instability strip (see Fig. 9 of Fontaine & Brassard 2008).

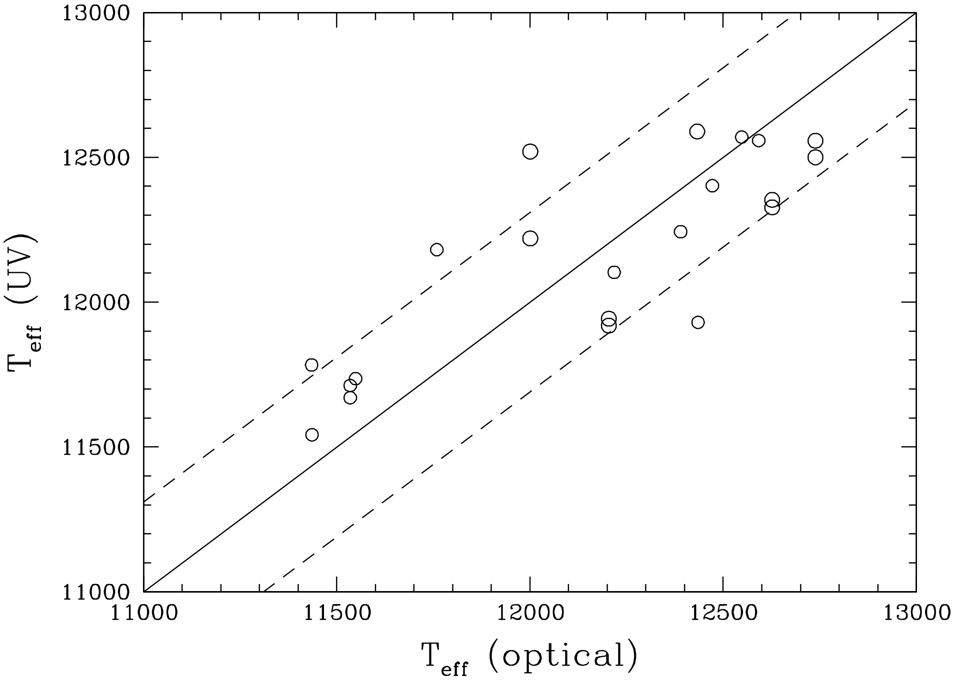

FIGURE 3.8 – Effective temperatures of ZZ Ceti stars derived from UV spectra compared with the optical determinations. Optical $\log g$ values are assumed in the determination of the UV temperatures. The size of the symbols reflects the different weights assigned to the UV spectra, as discussed in B95. The solid line indicates the locus where $T_{\rm eff}$(optical) = $T_{\rm eff}$(UV), while the dashed lines represent the ±350 K uncertainty allowed by the optical analysis. The results indicate that model atmospheres calculated with the ML2/$\alpha = 0.8$ parameterization of the mixing-length theory provide the best internal consistency between optical and UV temperatures.

We have then computed extensive grids of models down to $T_{\rm eff} = 1500$ K that connect with the grids used in TB09 at $T_{\rm eff} = 12,000$ K. Our model grid is calculated with temperature steps of 500 K, and $\log g$ values from 6.5 to 9.5 with steps of 0.5 dex (with two additional grid points at 7.75 and 8.25). We use the improved Stark profiles of TB09 and the updated mixing-length parameter, as discussed above. Since we are mostly interested here in investigating the influence of our improved profiles on the high-log g problem, we also computed a second grid similar to that used by the Montreal group for the past ten years. These models rely on the Stark profiles of Lemke (1997) with the value of the critical field $\beta_{\rm crit}$ in the Hummer-Mihalas formalism multiplied by a factor of 2; a more detailed discussion of this ad hoc parameter is provided in TB09. The mass distributions for the cool DA white dwarfs in the sample of Gianninas et al. (2009) are displayed in Figure 3.9 for both sets of model spectra. These results clearly indicate that our improved line profiles do not help in any way to solve the long lasting problem that the mean spectroscopic mass increases significantly below $T_{\rm eff} \sim 12,500$ K. However, there is a significant improvement in the range $30,000 > T_{\rm eff} > 12,500$ K, where the mass distribution appears more constant, in contrast with our previous results where the mean mass slightly decreases at lower temperatures, leading to an unexpected dip in the distribution near $T_{\rm eff} \sim 13,000$ K (see also Fig. 3 of Gianninas et al. 2009, for a more obvious illustration of this problem). With our improved models, we can now observe a more stable mass distribution down to $T_{\rm eff} \sim 12,500$ K, followed by a sudden increase in the mean mass below this temperature.

It has been previously suggested that uncertainties in the treatment of the Stark profiles combined with that of the pseudocontinuum opacity originating from the dissolved atomic levels within the occupation probability formalism of Hummer-Mihalas, and in particular the ad hoc parameterization of $\beta_{\rm crit}$, could be responsible for the high-log g problem (Koester et al. 2009a). Our results presented in Figure 3.9 show that this is likely not the case. The unified theory of Stark broadening from Vidal et al. (1970) still suffers from some approximations, but it would be surprising that additional corrections, such as second order effects, would change the masses by more than 1%. Moreover, the sudden increase in the average mass of DA stars below $\sim 12,500$ K can hardly be explained by a change in Stark profiles since these have a fairly smooth temperature-dependence in this regime.

We finish this section by presenting additional evidence that inaccuracies in the physics included in the model atmospheres are at the heart of the high-log g problem. We first refer the reader to Figure 2 of TB09, which depicts the effect of including additional lines in the fitting procedure on the measurement of the atmospheric parameters. The top panel shows

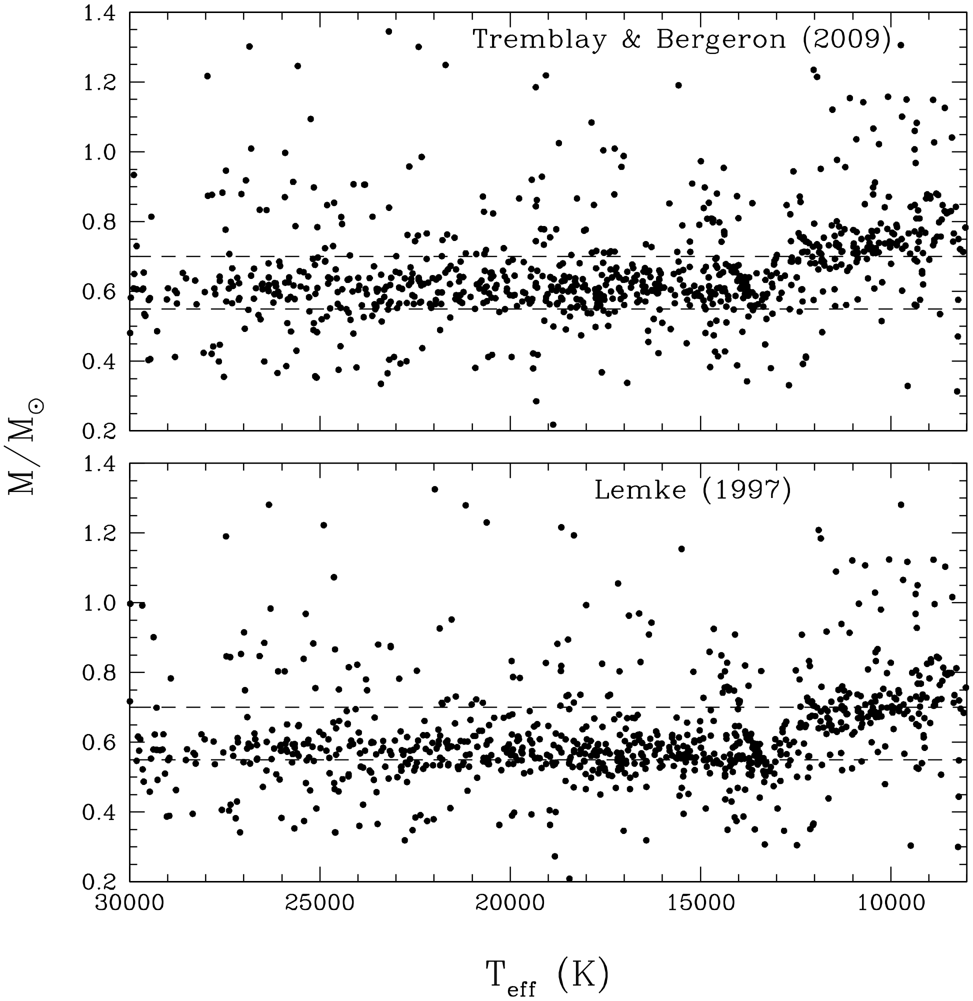

FIGURE 3.9 – Mass distribution as a function of $T_{\rm eff}$ for the DA white dwarfs in the sample of Gianninas et al. (2009). The atmospheric parameters are derived from spectroscopic fits using model spectra calculated with the Stark broadening profiles of TB09 (*top panel*) and with the Stark profiles from Lemke (1997) and the value of the critical field ($\beta_{\rm crit}$) multiplied by factor of 2 (*bottom panel*). Lines of constant mass at 0.55 and 0.70 $M_\odot$ are shown as a reference.

how both $T_{\rm eff}$ and $\log g$ *decrease* as more lines are considered in the fit. This problem has been discussed at length by Bergeron (1993) who proposed to multiply by a factor of 2 the value of the critical field, $\beta_{\rm crit}$, to partially overcome this discrepancy (see middle panel of Fig. 2 of TB09). By including the Hummer-Mihalas formalism directly into the line profile calculations, TB09 managed not only to get rid of this ad hoc factor, but achieved an even better internal consistency between the various Balmer lines (bottom panel of Fig. 2 of TB09).

We show in Figure 3.10 a similar exercise for a typical cool DA star in our sample. The results indicate that the $\log g$ solution shifts towards lower values, by roughly ~ 0.5 dex, as more lines are included in the fitting procedure. This trend occurs for all cool DA stars in our sample, and it is observed with all the model grids we have computed, no matter what atmospheric composition (i.e. mixed H/He models) or line profile theory we assumed. We believe that the results shown here represent the ultimate proof that best fitted models fail to properly match the spectroscopic data.

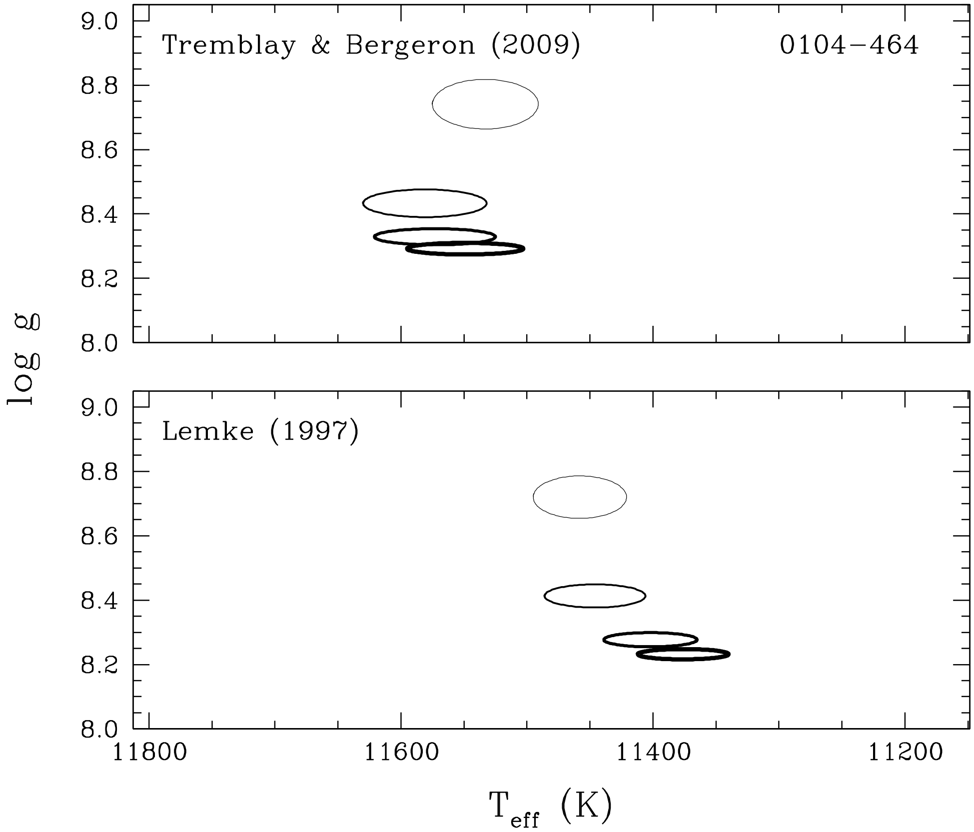

FIGURE 3.10 – Solutions in a $T_{\rm eff} - \log g$ diagram for a ZZ Ceti star using 2, 3, 4 and 5 lines (Hβ up to H8) in the fitting procedure (represented by progressively thicker 1 σ uncertainty ellipses from our fitting procedure). The different panels show the results for the two grids discussed in the text.

3.5 Evidence from Trigonometric Parallax Measurements

In this section, we look at alternative methods, independent of spectroscopy, to measure the surface gravity — or equivalently the radius or the mass — of cool DA stars. The best independent method for measuring the atmospheric parameters of cool white dwarfs is the photometric technique, illustrated in the left panels of Figure 3.2, where optical and near-infrared photometric data are compared with the predictions of model atmospheres (see, e.g., Bergeron et al. 2001, for details). With this method, only the effective temperature and the solid angle $\pi(R/D)^2$ are considered free parameters. When the distance D is known from trigonometric parallax measurements, one directly obtains the radius R of the star, which can then be converted into mass or $\log g$ using evolutionary models. This method works best for cool white dwarfs since the spectral energy distributions of hotter stars become less sensitive to temperature. Also, since they are generally more distant, accurate trigonometric parallaxes are more difficult to obtain.

Boudreault & Bergeron (2005) used trigonometric parallax measurements for 52 DA stars to compare the photometric masses with those obtained from the spectroscopic technique. The results (see their Fig. 1) reveal that the spectroscopic masses are in many cases larger than the photometric masses. Bergeron et al. (2007) extended this analysis by comparing photometric and spectroscopic masses for 92 DA stars. While the mean photometric mass of the sample appears slightly larger than the spectroscopic mean for hot DA stars ($M \sim 0.6\ M_\odot$; see their Fig. 4), the dispersion of the photometric masses is significantly larger than that obtained from spectroscopy, a result that suggests a variable level of accuracy in the trigonometric parallax measurements. Bergeron et al. (2007) also compared their spectroscopic masses with those inferred from gravitational redshift measurements, although the comparison remained inconclusive because of the large uncertainties associated with the redshift velocities, which are intrinsically more difficult to obtain than any other measurement made with other techniques.

We conduct here a new comparison of photometric and spectroscopic masses, but in light view of the previous studies discussed above, we restrict our analysis to a well defined sample of homogeneous parallax measurements for which we can better account for the uncertainties. For instance, Bergeron et al. (2001, and later studies) relied on trigonometric parallaxes taken from the Yale parallax catalog (van Altena et al. 1994). However, since this catalog represents a compilation of different sources of parallax measurements, properly averaged with various weights, the adopted values may exhibit a larger dispersion than the original sources. Because it is also not clear what other corrections are used in the Yale Catalog, we decided to go back to the original measurements in order to build a more homogeneous sample. The first sample discussed here is drawn from the original USNO parallax measurements obtained from photographic plates (Harrington & Dahn 1980, and follow-up papers). This sample includes 26 DA white dwarfs with parallax uncertainties less than 12%, and for which we also have high signal-to-noise spectroscopy (from Gianninas et al. 2009) as well as optical $BVRI$ and infrared JHK photometry (from Bergeron et al. 2001). We then compute the atmospheric parameters by using both photometric and spectroscopic techniques. For the former method, we rely on the prescription of Holberg & Bergeron (2006) to convert the magnitudes into average fluxes. The differences between spectroscopic and photometric masses (and temperatures) are displayed in Figure 3.11 as a function of $T_{\rm eff}$ (photometric); known or suspected double degenerate binaries are shown as open circles (see Table 2 of Bergeron et al. 2001). The temperatures obtained from both methods are generally in agreement, within the uncertainties, with the exception of some doubles degenerates and the two hottest stars in our sample. For the mass comparison, no clear conclusion can be drawn for individual objects since the observed dispersion is rather large. However, if we exclude the double degenerates, the spectroscopic masses are larger than the photometric masses by $\sim 0.08\ M_\odot$, on average, although the differences appear larger for stars above 8000 K; in fact, if we consider only stars with $T_{\rm eff} > 8000$ K, the difference in mean mass increases to a value of 0.11 $M_\odot$. This result can be compared to the estimated increase in mass below $T_{\rm eff} = 12,500$ K observed in the top panel of Figure 3.9, which is of the order of 0.13 $M_\odot$, a value entirely compatible with the mass difference observed in Figure 3.11. We must therefore conclude that the photometric masses are reasonably sound, and that the high-$\log g$ problem rests with the spectroscopic approach.

Next, we use a more recent sample drawn from the CCD parallax survey of nearby white dwarfs of Subasavage et al. (2009). This sample contains 8 DA stars for which we perform the same analysis as above, with $VRIJHK$ photometry (with CTIO passbands for the R and

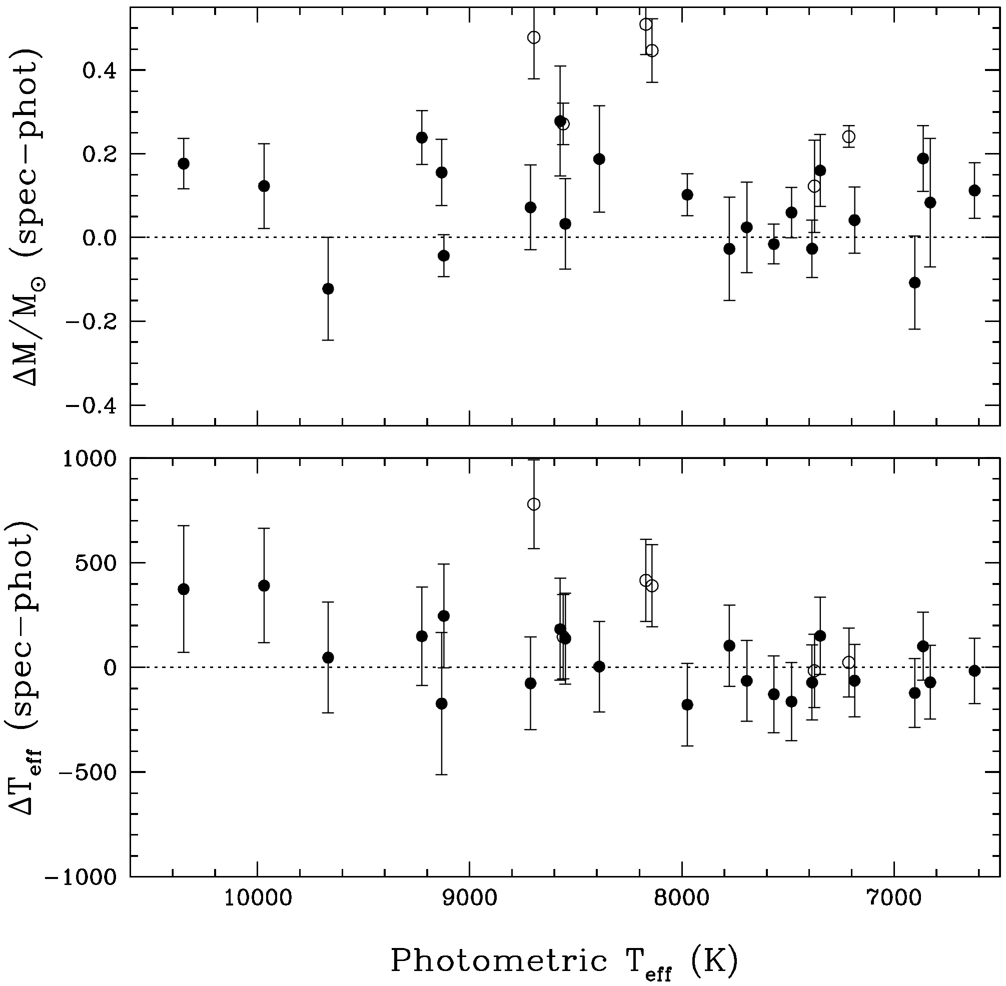

FIGURE 3.11 – Differences between white dwarf parameters (effective temperature and mass) determined from the spectroscopic and photometric methods as a function of photometric temperatures. The *BVRIJHK* photometric data used in these determinations are taken from Bergeron et al. (2001) with trigonometric parallaxes from the USNO catalogs, while the optical spectra are from our own archive. The open circles represent suspected or known double degenerates. The horizontal dotted lines correspond to a perfect match between spectroscopic and photometric parameters.

I filters) and trigonometric parallaxes taken from Subasavage et al. The comparison of the photometric and spectroscopic parameters is displayed in Figure 3.12. First of all, we can see that the high accuracy of the parallax data significantly reduces the error bars. The object shown by the open circle is LHS 4040 (2351−335), for which the *JHK* photometry has the largest uncertainties in Table 3 of Subasavage et al. (2009) because of some contamination from a nearby M dwarf (LHS 4039). If we exclude this star, the mean mass difference is about 0.12 $M_\odot$, a value comparable to that obtained from the USNO sample. We cannot help noticing, once again, that the largest temperature differences occur for the hottest stars in the sample. If we assume that the atmospheric parameters obtained from the photometric technique are reliable, it is possible to compute model spectra with these parameters and compare them with the observed optical spectra. This exercise is illustrated in the right panels of Figure 3.13 for the three hottest stars in the Subasavage et al. sample, while the left panels show the best fits obtained from the spectroscopic technique. This comparison allows us to evaluate how the model spectra need to be corrected to yield lower spectroscopic masses. The results suggest that the higher Balmer lines are predicted to be too sharp by the models and the lower series are predicted to be somewhat too narrow. Nevertheless, the differences in the model spectra are obviously a lot more subtle than the high-mass problem they give rise to (see Fig. 3.9).

There are unfortunately very few other independent verifications of $\log g$ or mass measurements that can be used below $T_{\rm eff} = 13,000$ K. More recent USNO parallaxes with CCD observations have not been published yet, except for a very small sample (Monet et al. 1992). One very interesting result with this ongoing survey is the very massive DA star LHS 4033, for which the high mass near the Chandrasekhar limit is predicted both from the spectroscopic and the photometric methods (Dahn et al. 2004). There are also a few more recent parallax samples, such as that of Ducourant et al. (2007), but these are mostly oriented towards very cool and faint halo white dwarfs, with very few DA stars above 7000 K. Another way to estimate masses near the ZZ Ceti instability strip is based on color indices that measure the strength of the Balmer jump, which becomes sensitive to $\log g$ in this temperature range (see, e.g., Weidemann & Koester 1984). Even then, very high precision photometry is required to measure individual masses. Koester et al. (2009a) applied this technique to the large SDSS sample to compute the average photometric $\log g$ value as a function of temperature (see their Fig. 2). On average, the photometric $\log g$ values are not shown to rise significantly in the range of 16,000 K $< T_{\rm eff} <$ 9000 K, pointing again to a problem with the spectroscopic approach.

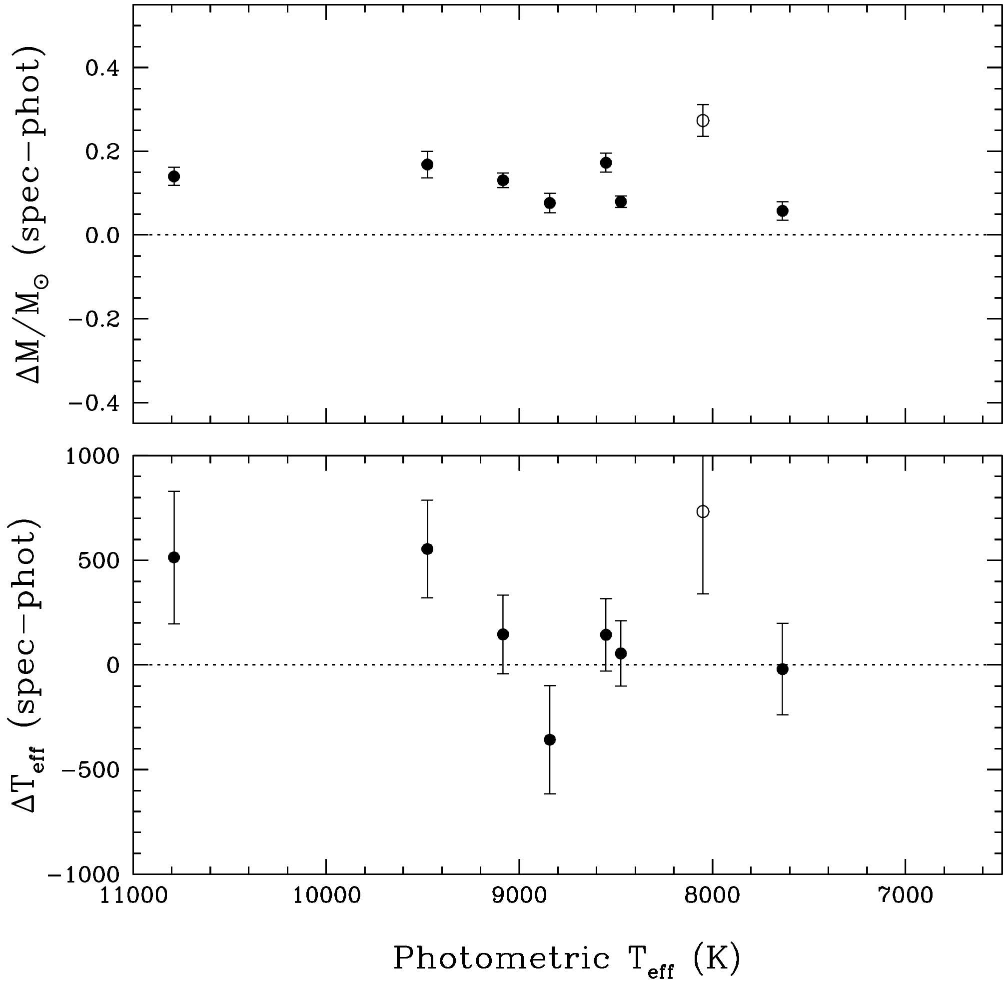

FIGURE 3.12 – Same as Figure 3.11 but with a photometric sample drawn from the survey of Subasavage et al. (2009) with *VRIJHK* photometry and accurate CCD trigonometric parallax measurements. The object represented by a circle (LHS 4040) is discussed in the text.

3.6 Alternative Solutions to the High-log g Problem

In the remainder of this paper, we explore alternative solutions to the high-log g problem in cool DA stars. Some of these solutions have already been discussed by Koester et al. (2009a), but we present here some additional arguments. The first thing to realize is that with the exception of the sudden increase in $\log g$ below $T_{\rm eff} \sim 12,500$ K, the *dispersion* of $\log g$ values in a given range of temperatures remains nearly identical down to $T_{\rm eff} = 8000$ K (see Fig. 3.1).

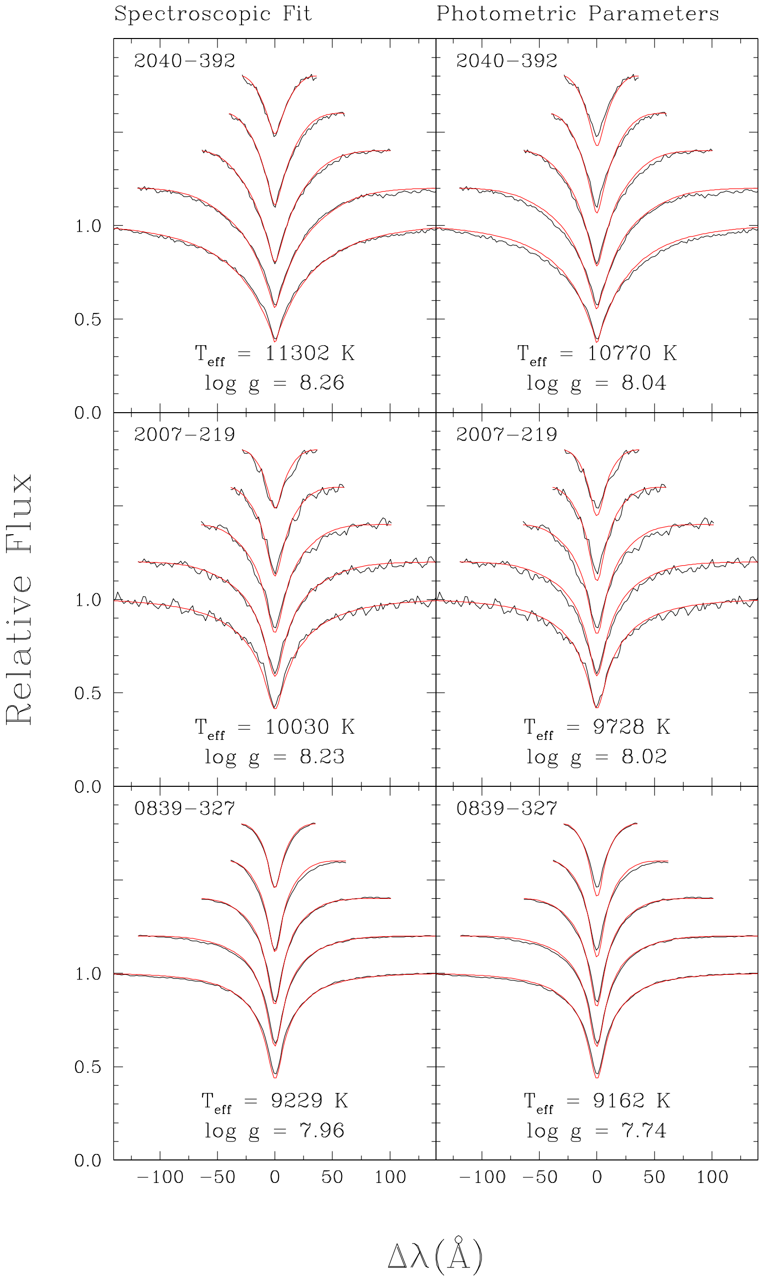

FIGURE 3.13 – Left panels: Best spectroscopic fits for three DA stars from the sample of Subasavage et al. (2009); the atmospheric parameters are given in each panel. Right panels: Spectroscopic data for the same stars compared with model spectra *interpolated* at the $T_{\rm eff}$ and $\log g$ values obtained from the photometric method.

Therefore, the solution we are looking for is expected to impact *all* cool DA white dwarfs in a systematic fashion. We begin by showing in panel (a) of Figure 3.14 the shifts in $\log g$ as a function of effective temperature required to obtain a mean mass comparable to that of hotter DA stars. These shifts have been estimated by computing, in 1000 K temperature bins, the mean $\log g$ value for the sample displayed in Figure 3.1. Then, to estimate the effects of each experiment (described below) on the spectroscopic determinations of $T_{\rm eff}$ and $\log g$, we simply fit our reference grid of model spectra with our test grid, and report the results in the various panels of Figure 3.14.

3.6.1 Hummer & Mihalas equation-of-state: Neutral Interactions

The modeling of cool and dense plasma for a non-ideal gas — mostly volume effects accounting for the finite size of the neutral particles that can lead to pressure ionization at higher densities — has always remained one of the most difficult areas in physics. Fortunately, non-ideal effects due to neutral particles are fairly unimportant for the thermodynamical structure of hydrogen-rich white dwarf atmospheres, and they only have an impact on the excited states of hydrogen. For these applications, the simple Hummer-Mihalas occupation probability model, in which the atoms are considered as hard spheres with a constant radius, has been used in most white dwarf atmosphere codes. In this theory, the atomic states are effectively destroyed when the distance between two particles is smaller than the corresponding atomic radii. The radius of the hydrogen hard sphere is usually taken as n^2a_0 where n is the principal quantum number and a_0 is the Bohr radius. This is obviously a crude approximation that does not take into account interaction potentials. Bergeron et al. (1991) found that a direct implementation of the occupation probability formalism yields $\log g$ values that are too low in the regime where non-ideal effects become dominated by neutral interactions ($T_{\rm eff} \lesssim$ 8000 K). The problem is that the higher Balmer lines are predicted too weak at normal surface gravities. Therefore, Bergeron et al. divided the hydrogen radius by a factor of two to reduce the non-ideal effects for the higher lines of the series. In view of the preceding discussion of

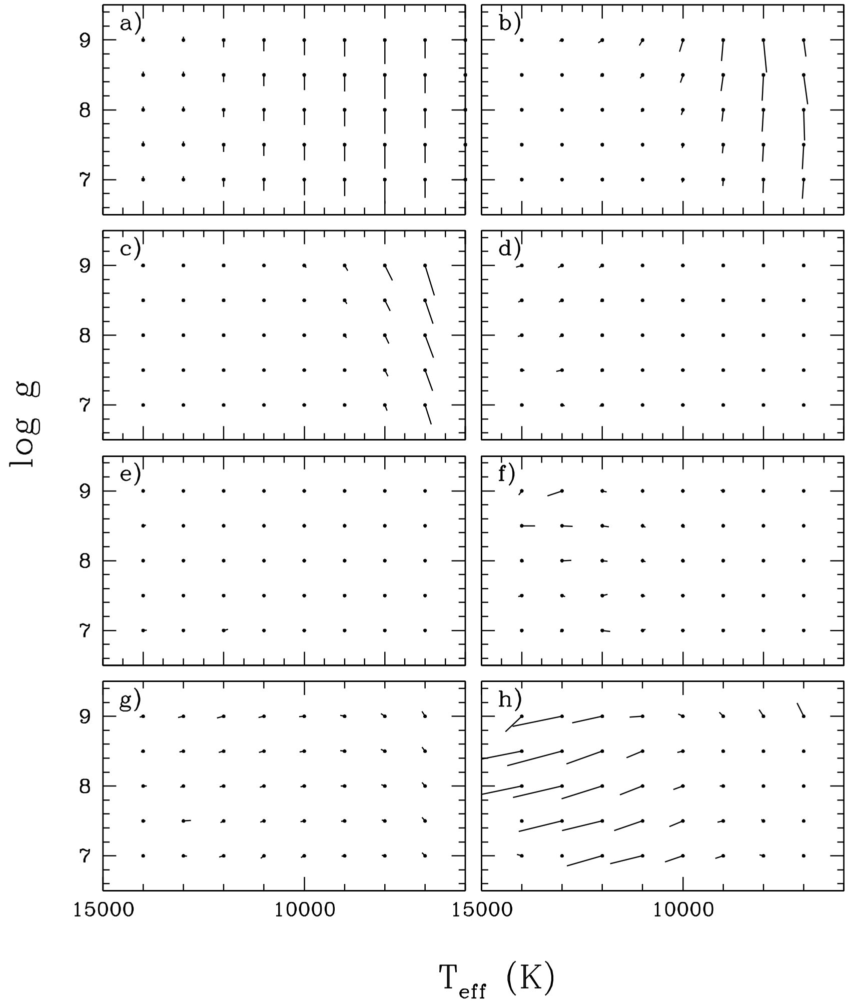

FIGURE 3.14 – Panel (a) illustrates the shift in spectroscopic $\log g$ values as a function of $T_{\rm eff}$ required to have at each temperature a mean mass comparable to that of hotter DA stars. We assume for simplicity that the shift is the same for all values of $\log g$ at a given temperature. This panel serves as reference for the various experiments described at length in the text, and whose results are presented in the other panels. In each case, our reference model grid is fitted with a test grid, and the differences in the atmospheric parameters are reported in the figure. The changes in the models are: (b) the hydrogen radius taken as the Bohr radius in the HM88 theory, (c) the neutral broadening enhanced by a factor of two, (d) the Potekhin et al. (2002) proton microfield distribution instead of the Hooper (1968) distribution, (e) an alternative cut-off for the non-ideal gas effects in the UV at 1215 Å instead of 972 Å, (f) the neglect of non-ideal effects due to electronic collisions in the Hummer-Mihalas formalism, (g) the H^- opacity enhanced by 15%, and (h) the ML2/$\alpha = 1.5$ parameterization of the MLT.

the simple model used to describe neutral interactions, a 50% change of the effective atomic radius is not physically unrealistic.

One problem with the parameterization of the hard sphere model used by Bergeron et al. (1991) is that, since $\log g$ values are already too high for all DA stars below $T_{\rm eff} \sim 12,500$ K, is not clear what value of the mean surface gravity should be used to "calibrate" the hard sphere radius. In view of these uncertainties, we simply show in panel (b) of Figure 3.14 how the atmospheric parameters are changed if we use the original parameterization of Hummer & Mihalas (1988) where the hydrogen radius is set to its standard value (n^2a_0). The effects are small at temperatures higher than $T_{\rm eff} \sim 10,000$ K. However, if we increase the hydrogen radius even more, the atmospheric parameters become totally unrealistic at low temperatures. The conclusion, which was understood early-on (see Section 2.6 of B95), is that an inaccurate treatment of the hard sphere model in the occupation probability formalism cannot be the source of the high-$\log g$ problem.

We finally note that there is another discrepancy in the Hummer-Mihalas formalism for neutral interactions, which predicts — in cool hydrogen-atmosphere white dwarfs — a largely overestimated contribution of the bound-free opacity from the Lyman edge associated with the so-called dissolved atomic levels of the hydrogen atom, or pseudocontinuum opacity (Kowalski 2006). This is partially because the theory fails to take into account the interaction potentials for the H-H and H-H_2 collisions. More realistic calculations (Kowalski & Saumon 2006) actually show that this opacity source is completely negligible in cool DA stars and should have no effect on the spectroscopic results discussed here.

3.6.2 Neutral Broadening

The broadening profiles of hydrogen lines in cool DA stars become increasingly dominated by neutral broadening, for which resonance broadening is the dominant source. It has traditionally been taken into account by using broadening parameters from Ali & Griem (1965), but new theories (Barklem et al. 2000) claim that these parameters could be in error by a factor of two, although the exact numbers are still being disputed (Allard et al. 2008). In panel (c) of Figure 3.14, we show how the atmospheric parameters are affected when we multiply arbitrarily the resonant broadening parameter by a factor of two. Not surprisingly, the temperature range where the effect is observed is similar to that of the non-ideal gas effects due to neutral particles, shown in panel (b). Therefore, even if neutral broadening was much in error, any improvement could not account for a shift in the mean $\log g$ values at higher temperatures.

3.6.3 Hummer & Mihalas equation-of-state: Charged Particle Interactions

TB09 presented the first model spectra for DA stars that took into account in a consistent way the non-ideal effects described in the Hummer-Mihalas theory both in the occupation probability and line profiles calculations. The non-ideal effects due to protons are fairly well understood and we can safely say that, with the help of plasma experiments, these effects are well described to within a few percent, especially for the hydrogen Balmer lines. One matter discussed in TB09 is that the Hummer-Mihalas formalism originally used the Holtsmark distribution to describe the proton microfields. It was later upgraded with the Hooper (1968) distribution (Nayfonov et al. 1999), including the Debye shielding effect. In panel (d) of Figure 3.14, we show that even by using the more general and precise microfield distribution of Potekhin et al. (2002), differences in the models remain extremely small.

It must be understood, however, that the Hummer-Mihalas occupation probability formalism is based on a dipole interaction between the absorber and the protons, an approach that fails for very close collisions. Such collisions are better described with a proper account of the colliding particle potential (see TB09 for details). Proper calculations show that the non-ideal effects described in Hummer & Mihalas (1988) cannot lower the ionization potential to energies that correspond usually to transitions between the first two levels. Therefore, the bound-free pseudocontinuum opacity from the Lyman edge can be considered negligible near the Lα region. The transition to the Hummer-Mihalas theory at lower wavelengths is still not well understood, and a sharp cutoff of the Lyman pseudocontinuum opacity longward of Lγ ($\lambda > 972.5$ Å) is currently used in our models. However, as seen in panel (e) of Figure 3.14, even if we extend our arbitrary cutoff to Lα ($\lambda > 1216$ Å), the impact on the Balmer line analysis remains completely negligible.

Finally, the Hummer-Mihalas theory also takes into account non-ideal effects due to electronic collisions. These have never been included in white dwarf model atmospheres until the work of TB09. In panel (f) of Figure 3.14, we show how the atmospheric parameters are changed if this additional contribution to the occupation probability is removed from *both* the line profile and equation-of-state calculations. While these non-ideal effects cannot be neglected altogether, they have little influence on the atmospheric parameters determined from spectroscopy. Our conclusion for this section is that the high-$\log g$ problem cannot be easily explained by some inaccurate treatment of non-ideal effects due to charged particles.

3.6.4 H^- Continuum Opacities

The dominant source of opacity in cool DA atmospheres is the bound-free and free-free H^- opacity. The main uncertainty in the calculation of the H^- opacity is the approximation used in the wave function expansions, although the current accuracy is believed to be better than 1% (John 1988). In panel (g) of Figure 3.14, we artificially increased the contribution of the H^- opacity in our models by 15%. The results indicate that such uncertainties would have absolutely no effect on the spectroscopic determination of the atmospheric parameters of cool DA stars.

3.6.5 Convective Energy Transport

We discussed in our introduction that the use of the mixing-length theory to treat the convective energy transport in white dwarf atmospheres may represent a significant source of physical uncertainty in the calculations of the atmospheric structures. It has even been considered the only viable solution to the high-$\log g$ problem by Koester et al. (2009a). Using our improved model atmospheres, we proceeded in Section 3.3 to a recalibration of the MLT free-parameter α that describes the convective efficiency. None of the discrepancies presented in this work provide any *direct* evidence that something is wrong with the MLT framework. The only circumstantial evidence is that the sudden increase in $\log g$ values below $T_{\rm eff} \sim 12,500$ K coincide precisely with the temperature where the extent of the hydrogen convection zone becomes significant (see Fig. 3.5). It is also the temperature range where our models predict that a majority of the energy flux is transported by convection in the photosphere ($\tau_R = 1$). Since convective energy transport may change dramatically the temperature and pressure structures of the atmosphere, the predicted line profiles can be affected significantly since different parts of the line profiles are formed at different optical depths.

Our first objective is to evaluate the sensitivity of the high-$\log g$ problem to the current MLT models, and investigate whether there is any way to solve the problem within the theory. We previously discussed in Section 3.3 that the spectroscopic technique yields different solutions for $T_{\rm eff}$ and $\log g$ depending on the particular choice of the free parameter α. This is why we constrained the convective efficiency by relying on independent near-UV observations. If we ignore this constraint, it is possible to achieve reasonable fits in the optical using any value of α. However, B95 showed (see their Fig. 3) that the distribution of DA stars as a function of effective temperature shows unexpected gaps or clumps both in the limit of low and high convective efficiencies. This is because the hydrogen Balmer lines, which reach their maximum strength near $\sim 13,000$ K, are predicted too strong or too weak, respectively. In panel (h) of Figure 3.14, we show the effect of adopting a value of ML2/$\alpha = 1.5$ (instead of 0.8) in our model calculations. The surface gravities are indeed lowered in the range $13,000 > T_{\rm eff} > 10,000$ K, but as discussed above, the distribution of DA stars now shows an important clump in temperature since the Balmer lines are predicted too weak near $T_{\rm eff} \sim 13,000$ K (see Fig. 4 of B95), and DA stars with the strongest lines accumulate in this region.

Even with a significantly increased convective efficiency, the $\log g$ values below 10,000 K remain too high. A variation of the convective efficiency in this particular range of temperature has little effect on the predicted line profiles, and the spectroscopic determinations of $\log g$ become somewhat independent of the particular choice of the parameter α. Indeed, convection becomes increasingly adiabatic in this range of effective temperature, and thus the convective flux becomes independent of the MLT. The temperature gradient at $\tau_R = 1$, however, is still significantly different from the adiabatic gradient ($> 5\%$) in models with $T_{\rm eff} \sim 8000$ K. Therefore, there is still room for another convection theory that could yield different temperature profiles in the range $10,000 > T_{\rm eff} > 8000$ K. In other words, the fact that the

$\log g$ values become independent of the particular choice of α does not guarantee that we converged to the correct solution. The only conclusion we can reach so far is that *within* the MLT framework, we are unable to solve the high-$\log g$ problem.

As reviewed by Fontaine & Brassard (2008, see their Section 4.1), nonadiabatic calculations require a higher convective efficiency ($\alpha = 1.0$) to account for the empirical blue edge of the ZZ Ceti instability strip. Taken at face value, this conclusion implies that convection in the atmospheric layers is less efficient than in the deeper layers. From 2D hydrodynamic simulations, Ludwig et al. (1994) also concluded that the convective efficiency must increase with depth, with a value of α at $\tau_R \sim 10$ in the range of 4 to 5. In light of these findings, we performed a final test by using a variable mixing-length as a function of depth, keeping the current value at $\tau_R = 1$.[5] The results, not shown here, reveal that the effects produced on the temperature structure deep in the atmosphere have absolutely no impact on the predicted spectra. Therefore, while an increase in convective efficiency with depth may affect the predictions from pulsational models, it has little effect on model spectra of cool DA stars.

It seems we may now have reached the limit of the 1D mixing-length theory, and one is naturally looking at solutions from more realistic radiation hydrodynamic calculations, such as the 2D simulations of Ludwig et al. (1994). These calculations have not been followed up, unfortunately, since 3D stellar atmospheres with radiation hydrodynamics have become more stable and accurate (Nordlund & Stein 2009). From a limited set of models representing a typical ZZ Ceti star, Ludwig et al. (1994) concluded that the mixing-length theory is roughly correct. However, since the differences between the current model spectra and the expected spectra are rather small (see the right panels of Fig. 3.13), this conclusion about the validity of the MLT framework should be taken with caution since the calculations of Ludwig et al. have not been confronted to real stellar spectra. A complete grid of 2D, or even 3D models should be compared with observations before reaching this conclusion. This represents the obvious next step in attempting to solve the high-$\log g$ problem.

---

[5] More specifically, we used a linear variation with depth from $\alpha = 0.8$ at $\tau_R = 1$ to $\alpha = 3.2$ at $\tau_R = 100$.

3.7 Conclusion

The starting point of our study was the longstanding problem that spectroscopic values of $\log g$ — or masses — of DA white dwarfs cooler than $T_{\rm eff} \lesssim 12,500$ K are significantly higher than those of hotter DA stars, a feature observed in *all spectroscopic analyses* published to date. This discrepancy limits our ability to accurately measure the atmospheric parameters of the vast majority of DA white dwarfs older than ~ 1 Gyr, and may affect the results of ZZ Ceti pulsation analyses, as well as our ability to use white dwarf stars as precise cosmochronometers or distance indicators. The first solution proposed to explain the high-$\log g$ problem has been to recognize that a mild and systematic helium contamination from convective mixing could mimic the effects of high surface gravities. In this paper, we presented high signal-to-noise, high-resolution spectroscopic observations obtained with the Keck I telescope of the region near the He I $\lambda5877$ line for six cool DA white dwarfs. *We did not detect helium in any of our target stars.* Upper limits on the helium abundance in five of our targets allowed us to rule out the incomplete convective mixing scenario as the source of the high-$\log g$ problem. This result is in line with the conclusions of Tremblay & Bergeron (2008) that most DA white dwarfs (∼85%) have thick hydrogen layers ($M_{\rm H}/M_{\rm tot} > 10^{-6}$). In view of our results, we revisited the nature of the high-$\log g$ problem and presented evidence based on photometric masses that the conundrum lies with the spectroscopic technique itself. We showed in this context that the improved Stark profiles of Tremblay & Bergeron (2009) for the modeling of cool DA spectra did not help to solve the problem.

In our review of alternative solutions, we concluded — as Koester et al. (2009a) did — that a problem with the treatment of convective energy transport, currently the mixing-length theory, is the most plausible explanation for the high-$\log g$ problem. While nothing points to a specific discrepancy with the MLT framework, the next obvious step is to compare our current atmospheric parameters for DA stars with those eventually obtained from more detailed hydrodynamic models. Only then will we be able to confirm this hypothesis.

This work was supported in part by the NSERC Canada and by the Fund FQRNT (Québec). P.B. is a Cottrell Scholar of Research Corporation for Science Advancement. Some of the data presented here were obtained at the W. M. Keck Observatory, which is operated as a scientific partnership among the California Institute of Technology, the University of California and the National Aeronautics and Space Administration. The Observatory was made possible by the generous financial support of the W. M. Keck Foundation. This research has made use of the Keck Observatory Archive (KOA), which is operated by the W. M. Keck Observatory and the NASA Exoplanet Science Institute (NExScI), under contract with the National Aeronautics and Space Administration.

3.8 References

Ali, A. W., & Griem, H. R. 1965, Physical Review, 140, 1044

Allard, N. F., Kielkopf, J. F., Cayrel, R., & van't Veer-Menneret, C. 2008, A&A, 480, 581

Barklem, P. S., Piskunov, N., & O'Mara, B. J. 2000, A&A, 363, 1091

Beauchamp, A., Wesemael, F., & Bergeron, P. 1997, ApJS, 108, 559

Beauchamp, A., Wesemael, F., Bergeron, P., Liebert, J., & Saffer, R. A. 1996, in ASP Conf. Ser. Vol. 96, Hydrogen-Deficient Stars, ed. S. Jeffery & U. Heber (San Francisco: ASP), 295

Becklin, E. E., Farihi, J., Jura, M., Song, I., Weinberger, A. J., & Zuckerman, B. 2005, ApJ, 632, L119

Bergeron, P. 1993, in White Dwarfs: Advances in Observation and Theory, NATO ASI Series, ed. M. A. Barstow (Dordrecht: Kluwer Academic Publishers), 267

Bergeron, P., Gianninas, A., & Boudreault, S. 2007, in Proc. 15th European Workshop on White Dwarfs, eds. R. Napiwotzki & M. Burleigh (San Francisco: ASP), 372, 29

Bergeron, P., Leggett, S. K., & Ruiz, M. T. 2001, ApJS, 133, 413

Bergeron, P., Saffer, R. A., & Liebert, J. 1992, ApJ, 394, 228 (BSL92)

Bergeron, P., Wesemael, F., & Fontaine, G. 1991, ApJ, 367, 253

Bergeron, P., Wesemael, F., & Fontaine, G. 1992, ApJ, 387, 288

Bergeron, P., Wesemael, F., Fontaine, G., & Liebert, J. 1990, ApJ, 351, L21

Bergeron, P., Wesemael, F., Lamontagne, R., Fontaine, G., Saffer, R. A., & Allard, N. F. 1995, ApJ, 449, 258 (B95)

Boudreault, S., & Bergeron, P. 2005, in Proc. 14th European Workshop on White Dwarfs, eds. D. Koester & S. Moehler (San Francisco: ASP), 334, 249

Dahn, C. C., Bergeron, P., Liebert, J., Harris, H. C., Canzian, B., Leggett, S. K., & Boudreault, S. 2004, ApJ, 605, 400

D'Antona, F., & Mazzitelli, I. 1979, A&A, 74, 161

Ducourant, C., Teixeira, R., Hambly, N. C., Oppenheimer, B. R., Hawkins, M. R. S., Rapaport, M., Modolo, J., & Lecampion, J. F. 2007, A&A, 470, 387

Farihi, J., Jura, M., & Zuckerman, B. 2009, ApJ, 694, 805

Fontaine, G., & Brassard, P. 2008, PASP, 120, 1043

Fontaine, G., Brassard, P., & Bergeron, P. 2001, PASP, 113, 409

Gianninas, A., Bergeron, P., & Fontaine, G. 2006, AJ, 132, 831

Gianninas, A., Bergeron, P., & Ruiz, M. T. 2009, Journal of Physics Conference Series, 172, 012021

Gianninas, A., Dufour, P., & Bergeron, P. 2004, ApJ, 617, L57

Hansen, B. M. S., et al. 2007, ApJ, 671, 380

Harrington, R. S., & Dahn, C. C. 1980, AJ, 85, 454

Harris, H. C., et al. 2006, AJ, 131, 571

Holberg, J. B., Barstow, M. A., & Burleigh, M.R. 2003, ApJS, 147, 145

Holberg, J. B., & Bergeron, P. 2006, ApJ, 132, 1221

Hooper, C. F. 1968, Physical Review, 169, 193

Hummer, D. G., & Mihalas, D. 1988, ApJ, 331, 794

John, T. L. 1988, A&A, 193, 189

Jura, M., Muno, M. P., Farihi, J., & Zuckerman, B. 2009, ApJ, 699, 1473

Kepler, S.O., Kleinman, S.J., Nitta, A., Koester, D., Castanheira, B.G., Giovannini, O., Costa, A.F.M., & Althaus, L. 2007, MNRAS, 375, 1315

Kilic, M., Thorstensen, J. R., & Koester, D. 2008, ApJ, 689, L45

Koester, D. 1976, A&A, 52, 415

Koester, D., Allard, N. F., & Vauclair, G. 1994, A&A, 291, L9

Koester, D., Kepler, S. O., Kleinman, S. J., & Nitta, A. 2009, Journal of Physics Conference Series, 172, 012006

Koester, D., Napiwotzki, R., Voss, B., Homeier, D., & Reimers, D. 2005, A&A, 439, 317

Kowalski, P. M. 2006, ApJ, 651, 1120

Kowalski, P. M., & Saumon, D. 2006, ApJ, 651, L137

Lajoie, C.-P., & Bergeron, P. 2007, ApJ, 667, 1126

Lemke, M. 1997, A&AS, 122, 285

Liebert, J., Bergeron, P., & Holberg, J. B. 2005, ApJS, 156, 47

Liebert, J., & Wehrse R. 1983, A&A, 122, 297

Ludwig, H.-G., Jordan, S., & Steffen, M. 1994, A&A, 284, 105

Monet, D. G., Dahn, C. C., Vrba, F. J., Harris, H. C., Pier, J. R., Luginbuhl, C. B., & Ables, H. D. 1992, AJ, 103, 638

Nayfonov, A., Däppen, W., Hummer, D. G., & Mihalas, D. 1999, ApJ, 526, 451

Nordlund, Å., & Stein, R. F. 2009, American Institute of Physics Conference Series, 1171, 242

Potekhin, A. Y., Chabrier, G., & Gilles, D. 2002, Phys. Rev. E, 65, 036412

Subasavage, J. P., Jao, W.-C., Henry, T. J., Bergeron, P., Dufour, P., Ianna, P. A., Costa, E., & Méndez, R. A. 2009, AJ, 137, 4547

Tremblay, P.-E., & Bergeron, P. 2008, ApJ, 672, 1144

Tremblay, P.-E., & Bergeron, P. 2009, ApJ, 696, 1755 (TB09)

van Altena, W. F., Lee, J. T., & Hoffleit, E. D. 1994, The General Catalogue of Trigonometric Parallaxes (New Haven: Yale University Observatory)

Vauclair, G., & Reisse, C. 1977, A&A, 61, 415

Vidal, C. R., Cooper, J., & Smith, E. W. 1970, Journal of Quantitative Spectroscopy and Radiative Transfer, 10, 1011

Vogt, S. S., et al. 1994, Proc. SPIE, 2198, 362

Weidemann, V., & Koester, D. 1984, A&A, 132, 195

Zuckerman, B., Koester, D., Melis, C., Hansen, B. M., & Jura, M. 2007, ApJ, 671, 872

Chapitre 4

AN IMPROVED SPECTROSCOPIC ANALYSIS OF DA WHITE DWARFS FROM THE SLOAN DIGITAL SKY SURVEY DATA RELEASE 4

P.-E. Tremblay, P. Bergeron and A. Gianninas

Département de Physique, Université de Montréal, C.P. 6128, Succ. Centre-Ville, Montréal, Québec, H3C 3J7, Canada

Received 2010 December 30; accepted 2011 January 31

Accepted for publication in *The Astrophysical Journal*

4.1 Abstract

We present an improved spectroscopic and photometric analysis of hydrogen-line DA white dwarfs from the Sloan Digital Sky Survey Data Release 4 based on model atmospheres that include improved Stark broadening profiles with non-ideal gas effects. We also perform a careful visual inspection of all spectroscopic fits with high signal-to-noise ratios (S/N > 12) and present improved atmospheric parameters ($T_{\rm eff}$ and $\log g$) for each white dwarf. Through a comparison of spectroscopic and photometric temperatures, we report the discovery of 35 DA+DB/DC double degenerate candidates and 2 helium-rich DA stars. We also determine that a cutoff at S/N $= 15$ optimizes the size and quality of the sample for computing the mean mass of DA white dwarfs, for which we report a value of 0.613 $M_\odot$. In the following step, we compare our results to previous analyses of the SDSS DR4 and find a good agreement if we account for the shift produced by the improved Stark profiles. Finally, the properties of DA white dwarfs in the SDSS are weighed against those of the Villanova White Dwarf Catalog sample of Gianninas et al. We find systematically lower masses (by about 3% on average), a difference that we trace back to the data reduction procedure of the SDSS. We conclude that a better understanding of these differences will be important to determine the absolute temperature scale and mean mass of DA white dwarfs.

4.2 Introduction

The now completed Sloan Digital Sky Survey (SDSS; York et al. 2000) has rapidly grown to be, by far, the largest source of newly discovered white dwarfs in our galaxy. This project started as a survey of faint blue point sources and finally covered 9380 square degrees of the sky in the latest data release (Abazajian et al. 2009, Data Release 7). They mostly surveyed the North Galactic Cap region, with a completeness of about 95% for the point-source *ugriz* photometry. They performed a spectroscopic follow-up of nearly 1.6 million objects, mainly selected for their blue colors. White dwarfs from the different data releases have been identified in a series of papers (Harris et al. 2003; Kleinman et al. 2004; Harris et al. 2006), with the latest catalog published by Eisenstein et al. (2006a) containing 9316 white dwarfs drawn from the Data Release 4 (the SDSS-E06 catalog hereafter), covering 4783 square degrees of the sky. The final catalog from the DR7 is currently in preparation (Kleinman et al. 2009) and will increase the total number of white dwarfs discovered in the SDSS by nearly a factor of two. While the SDSS survey has been the source of numerous discoveries of peculiar objects (this subject is too wide to review here), and even a new class of white dwarfs — the so called hot-DQ stars (Dufour et al. 2007), the most common class of objects – the hydrogen-line (DA) white dwarfs – has been at the center of only a few studies (Eisenstein et al. 2006a; Kepler et al. 2007).

The largest published sample of spectroscopically identified DA white dwarfs can be found in the SDSS-E06 catalog. Considering the large number of SDSS spectra of all types, only the *most obvious* white dwarfs were recovered in this catalog. The main problem in the identification of white dwarfs in the SDSS is that at cool temperatures ($T_{\rm eff} \lesssim 8000$ K), they overlap in a color-color diagram with A and F main-sequence stars. However, for hotter objects, they claim their catalog should recover most of the single DA stars observed spectroscopically by the SDSS. We will review their selection procedure in more detail in Section 4.2. The catalog provided individual atmospheric parameters — $T_{\rm eff}$ and $\log g$ — for each DA white dwarf, but this was not meant to be a careful analysis of these stars, especially given that many objects have been catalogued without a visual inspection. The only thorough follow-up analysis, so far, of the bulk of these white dwarfs has been reported by Kepler et al. (2007), who refitted more carefully all objects with $g < 19$, and concentrated in particular on the mass distribution, including a comparison with previous determinations from independent surveys, and a comparison of the mass distribution of DA stars with that obtained for the helium-line (DB) white dwarfs identified in the SDSS-E06. However, Kepler et al. did not provide any update of the atmospheric parameters (which differed from those published by Eisenstein et al.). DeGennaro et al. (2008) reviewed the luminosity function and completeness of the SDSS-E06 sample, but used the atmospheric parameters previously published by Eisenstein et al. In parallel, subclasses of the DA spectral type — e.g. magnetic white dwarfs, DAO stars with detectable He II λ4686, and the DA$-$M dwarf binaries — have been analyzed in various independent studies, covering partially, or in full, the SDSS-E06 catalog.

We have recently computed a new set of model atmospheres for DA white dwarfs, described in Section 4.2.2, which rely on the improved Stark broadening profiles developed by Tremblay & Bergeron (2009). These model spectra have already been applied to the hot white dwarfs in the Palomar-Green (PG) sample (Tremblay & Bergeron 2009), and they are also currently being applied to the large scale analysis of the DA stars in the Villanova White Dwarf Catalog[1] (Gianninas et al. 2009; Gianninas et al. 2011). In this paper, the same models are used in an independent analysis of the hydrogen-line (DA) stars identified in the SDSS-E06 catalog. In particular, we will obtain improved stellar parameters, which can be readily compared to those found in the PG sample and the Gianninas et al. sample based on the same model spectra and fitting technique. This will allow for a more robust test of the quality of the SDSS data reduction and sample selection.

The SDSS sample is unique in the sense that it includes many more objects than any other sample of white dwarfs previously compiled. This is certainly an advantage since it provides better statistics on rare peculiar objects. However, for the bulk of the regular DA stars, we can see in Figure 4.1 that the average signal-to-noise ratio (S/N) of the observed spectra is low, much lower than any other sample previously analyzed (see, e.g., Fig. 1 of Liebert et al. 2005). Therefore, we think it is essential to better quantify the reliability of lower S/N data, a point also raised by Koester et al. (2009a). Kepler et al. (2007) used a simple magnitude cutoff, but here we propose a more detailed study of how the size of the sample can be optimized to yield average properties of the sample that have the most statistical significance. Finally, we have carried out a careful visual inspection of all the fits for objects with S/N > 12, a task that has not been accomplished until now, to our knowledge. In the course of this inspection, we have identified many new peculiar objects, misclassified in previous analyses, including a large number of degenerate binaries.

The goals outlined in the previous paragraphs led us to perform a complete and detailed follow-up of the studies of Eisenstein et al. and Kepler et al. by re-analyzing all DA white dwarfs in the SDSS-E06 sample. In Section 4.2, we summarize the set of SDSS observations and also describe our model atmospheres and fitting technique. We then present the results of

---

[1] http://www.astronomy.villanova.edu/WDCatalog/index.html

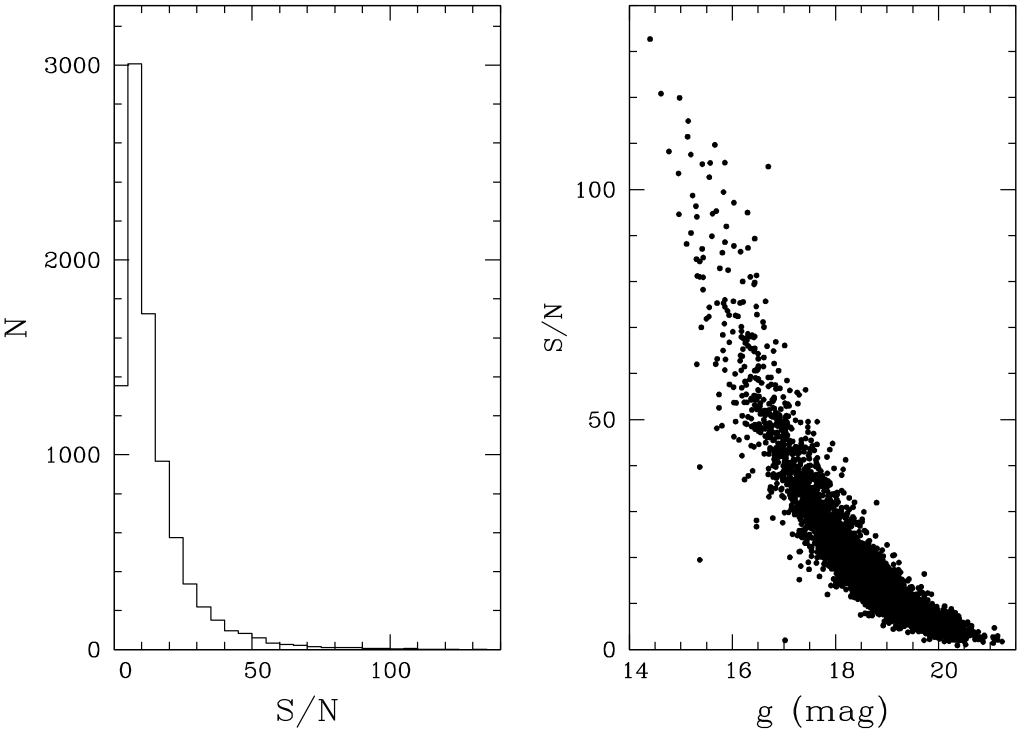

FIGURE 4.1 – Left panel: distribution of S/N for all 8717 DA spectra in the SDSS-E06 sample. Right panel: S/N as a function of the observed g magnitude.

our updated analysis in Section 4.3, where we define our optimal sample and also report the discovery of new degenerate binaries. Our results are compared in Section 4.4 with those of previous analyses of the SDSS-E06 sample as well as other samples of DA stars. Concluding remarks follow in Section 4.5.

4.3 Data Analysis

4.3.1 The SDSS Sample of DA White Dwarfs

The SDSS-E06 catalog relies on an automatic procedure to recover the white dwarf spectra in the survey. We briefly summarize this procedure in three main steps. A blue portion of the $g-r$ vs. $u-g$ diagram (see Fig. 1 of Eisenstein et al. 2006a) is first defined to identify white dwarf candidates. As mentioned in the Introduction, white dwarfs cooler than ∼8000 K occupy the same region as main-sequence stars in this two-color diagram, and most of them are therefore excluded by this first color cutoff. A second step is to eliminate candidates with a galaxy classification and a redshift larger than 0.003, although a few of them remain when a proper motion measurement is available with a value consistent with a nearby galactic source. Finally, the resulting photometric and spectroscopic observations for ∼13,000 white dwarf candidates are compared to white dwarf models with a χ^2 minimization fitting technique. The outliers and objects with a poor fit are reclassified manually and in some cases rejected from the final catalog altogether. These steps seem quite robust in recovering all typical, hot, single DA white dwarfs. The authors of the catalog claim that it should be fairly complete for DA white dwarfs with $T_{\rm eff} \gtrsim 8000$ K. However, they also remind us that the completeness of the SDSS spectroscopic survey itself can be anywhere between 15% and 50%, in part due to the neglect of blended point sources, as well as an incomplete spectroscopic follow-up of the point sources identified in the SDSS fields (Eisenstein et al. 2006a; DeGennaro et al. 2008). For all other DA subtypes (e.g, magnetics, DA$-$M dwarf binaries, etc.), the picture is less clear. The most common subtype are the DA $-$ M dwarf binaries where the presence of a cool main-sequence companion often changes the observed colors and contaminates the line profiles. The SDSS-E06 catalog is not tuned to identify systematically these objects. Other subtypes with spectra significantly different from that of a normal DA white dwarf, such as magnetics or DA stars diluted by a featureless DC companion, are also more likely to be rejected.

The basis of our analysis are the 8717 spectroscopic observations from the SDSS-E06 catalog with spectral type DA as the main classification, including some multiple spectra of the same objects. We obtained the spectroscopic and photometric observations from the SDSS Data Archive and Sky Server[2]. The spectra, which cover a wavelength range of 3800 to ∼10,000 Å with a resolution of $R \sim 1800$, rely on the improved data reduction from the Data Release 7, where some data reduction problems observed in previous data releases have been corrected (Kleinman et al. 2009). We next computed the S/N for each object in the range from 4450 to 4750 Å, a featureless spectral region between Hβ and Hγ, which provides a representative average for our spectroscopic technique. As expected, we can see in Figure

---

[2] das.sdss.org, cas.sdss.org

4.1 that the S/N of the spectra is closely correlated with the observed g magnitudes. We prefer to constrain the size of our sample based on S/N rather than magnitude because the former value is more directly related to the uncertainties in our fitting procedure described below. It is immediately clear that the faintest objects in the SDSS will not be included in the mean properties computation, because their atmospheric parameters carry large individual uncertainties. It also becomes increasingly difficult to identify DA subtypes (e.g. magnetics, DAB) when the noise level is high. For these reasons, we break the complete sample of DA spectra into two categories. The higher quality data (S/N $>$ 12), for a total of 3249 stars (3550 different observations), are carefully analyzed through a visual inspection of each fit. The remaining lower quality data of the sample are fitted with automatic programs and used for reference only. Unless it is noted explicitly, all the numbers and figures in our analysis are based on the higher quality data only. The reason for the S/N $=$ 12 cutoff is simply that a visual inspection of the lower quality spectra would not yield a significant number of interesting detections, and the publication of updated atmospheric parameters was deemed of low importance.

4.3.2 Model Atmospheres

For this work, we use the improved DA white dwarf model spectra that have been developed by our group in recent years. First of all, we rely on the Stark broadening tables of Tremblay & Bergeron (2009) with the non-ideal gas effects from Hummer & Mihalas (1988) included directly in the line profile calculations. Our models are similar to those used in their analysis in the range 40,000 K $> T_{\rm eff} >$ 12,000 K, with the exception that we now add the non-ideal effects due to the electronic collisions in the equation of state as well (i.e., in addition to the line profiles). Tremblay & Bergeron (2009, see Sec. 2.3) argued that these effects could be neglected compared to proton perturbations, but we actually find that this physical ingredient still changes the mean properties by $\sim$1%. For cooler temperatures, we employ the same model grid as that described in Tremblay et al. (2010). In particular, we make use of the ML2/$\alpha = 0.8$ version of the mixing-length theory, which provides, within the context of our improved broadening profiles, the best overall internal consistency between optical and

UV temperatures.

For the purpose of analyzing the hottest DA stars in the SDSS sample, we also computed new non-LTE model spectra with $T_{\rm eff} > 40,000$ K using the publically available TLUSTY model atmosphere code and the accompanying spectral synthesis extension SYNSPEC (Hubeny & Lanz 1995). The only difference between this grid and that previously described in Liebert et al. (2005) is that we are now using our improved Stark broadening profiles, and the $\beta_{\rm crit}$ parameter was also set back to its original value (see Tremblay & Bergeron 2009 for details). It is worth mentioning that we include these new Stark profiles in both the atmospheric structure (TLUSTY) and model spectrum (SYNSPEC) calculations, while previous non-LTE grids calculated with TLUSTY relied on approximate analytical Stark profiles, based on the two-level approximation (similar to the assumptions of Lemke 1997), to compute the atmospheric structures. Because such analytical profiles could not be easily modified to take into account non-ideal effects, it was deemed necessary to replace these approximate profiles with our more detailed calculations. This improvement ensures that our Stark profiles are now included in a self-consistent way throughout all our calculations. Our complete grid of model atmospheres and spectra covers a range of $T_{\rm eff}$ = 1500 K to 140,000 K (by steps of 250 K for $T_{\rm eff} <$ 5500 K, 500 K for 6000 K $< T_{\rm eff} <$ 17,000 K, 5000 K for 20,000 K $< T_{\rm eff} <$ 90,000 K, and 10,000 K for $T_{\rm eff} >$ 90,000 K), with log g values from 6.0 to 10.0 (by steps of 0.5 dex with additional points at 7.75 and 8.25 dex).

4.3.3 Fitting Procedure

Our fitting procedure is similar to that outlined in detail in Liebert et al. (2005). Briefly, we first normalize the flux from the individual Balmer lines, in both the observed and predicted spectra, to a continuum set to unity. This continuum is defined by fitting the observed line profiles with a theoretical spectrum including a polynomial with several free parameters to account for residual errors in the flux calibration. We have slightly improved the method by using a larger wavelength range compared to previous analyses. In this first step, the models are not used in any way to infer the atmospheric parameters. This approach for normalizing the observed spectra is used for $T_{\rm eff} > 16,000$ K and for $T_{\rm eff} <$ 9000 K, while at intermediate temperatures — where the Balmer lines reach their maximum strengths — we use several pseudo-Gaussians profiles, which constitute a more robust approach (Bergeron et al. 1995). Finally, the Hα line is normalized independently from all other lines, using theoretical line profiles in all cases. We then proceed to a χ^2 minimization between the observed and predicted line profiles, convolved with a Gaussian instrumental profile with a resolution of 3 Å (FWHM) appropriate for the SDSS spectra.

Our atmospheric parameters determinations for the DA stars in the SDSS is meant to be completely independent of previous analyses, other than the use of the DA designation from Eisenstein et al. (2006a) for the main spectral type in the definition of our sample. It is well known that there is generally a cool and a hot solution for the fit to normalized Balmer lines, centered on the maximum strength of the hydrogen lines near $T_{\rm eff} \sim 13,500$ K. In a first iteration, we determine the atmospheric parameters for each star assuming both a cool and a hot solution, and adopting as a preliminary solution that which provides the best agreement between the spectroscopic temperature ($T_{\rm spec}$) and the photometric temperature ($T_{\rm phot}$; the photometric fits are described in Section 4.2.4).

The major improvement of our analysis is that we go through a second iteration for all stars with S/N > 12 and perform a careful visual inspection of each individual fit. While we only consider normalized Balmer line profiles to determine the atmospheric parameters, we also rely on two additional diagnostics to reclassify and to flag interesting objects. The first diagnostic is the dereddened *ugriz* photometry, which we fit with the same model fluxes. The second diagnostic is the direct comparison of the synthetic and observed absolute fluxes, assuming that the SDSS spectra are properly flux calibrated. Note that in the SDSS, the spectroscopic and photometric observations are independent. These two additional diagnostics are usually lacking in other large DA surveys, and this certainly represents a significant advantage of the SDSS sample. Our visual inspection revealed 52 confirmed magnetic white dwarfs, or magnetic candidates, and we remove these objects from our sample because these cannot be fitted, even approximately, with our non-magnetic models. We refer to the studies of Schmidt et al. (2003), Vanlandingham et al. (2005), and Külebi et al. (2009) for a more detailed analysis of these stars. We also remove 3 objects that are most likely not white dwarfs (J090917.09+002514.0, J204949.78+000547.3, and J205455.83+005129.7). The second object has actually been reobserved by Kilic et al. (2007) and confirmed as a non-degenerate. Finally we remove two DA stars for which the SDSS observations cannot be fit with our spectroscopic technique because more than two lines were unavailable or unusable.

The most common flag in our analysis is the presence of a red flux excess in 345 objects, generally with non-degenerate absorption lines, which in almost all cases reveals the presence of an M dwarf companion[3]. For 65 of these systems, there is an obvious contamination blueward of Hβ, and these are simply too difficult to analyze with our spectroscopic approach. For the remaining systems with a smaller contamination, we use a simple technique that has proven to be sufficient in the present context. We exclude one or two lines (Hα, Hβ) from the χ^2 fit, and in some cases the line cores when emission is present. We also carefully inspected each fit, and were conservative in excluding all possibly contaminated lines. We find out that in most cases, the direct comparison of the synthetic and observed absolute fluxes is good in the region where the lines are fitted. We also use the $u - g$ color index to help in discriminating between the cool or hot solutions since the quality of the fit is generally a poor indicator due to possible contamination.

Even if the SDSS contains mostly faint white dwarfs (see, e.g., Fig. 4.1), there is still a large sample of high quality data — i.e. 665 spectra with S/N > 30, which is comparable in quality and quantity to other large surveys of DA stars (the PG survey for instance; Liebert et al. 2005). In Figure 4.2, we show sample fits from these high S/N observations. It is clear that by taking only the best spectroscopic data in the SDSS sample, one can still construct one of the best available sample of DA stars.

4.3.4 *ugriz* Photometry

In our overall fitting procedure, we also make use of *ugriz* photometric observations, which are available for most DA stars in the SDSS-E06 catalog. We fit the observed photometry of each object by using the grid of model atmospheres discussed in Section 4.2.2. We removed

---

[3] We use the terminology of DA$-$M dwarf binaries throughout this work but it must be understood that some of them are merely candidates because the red excess is weak, and some companions are actually L dwarfs.

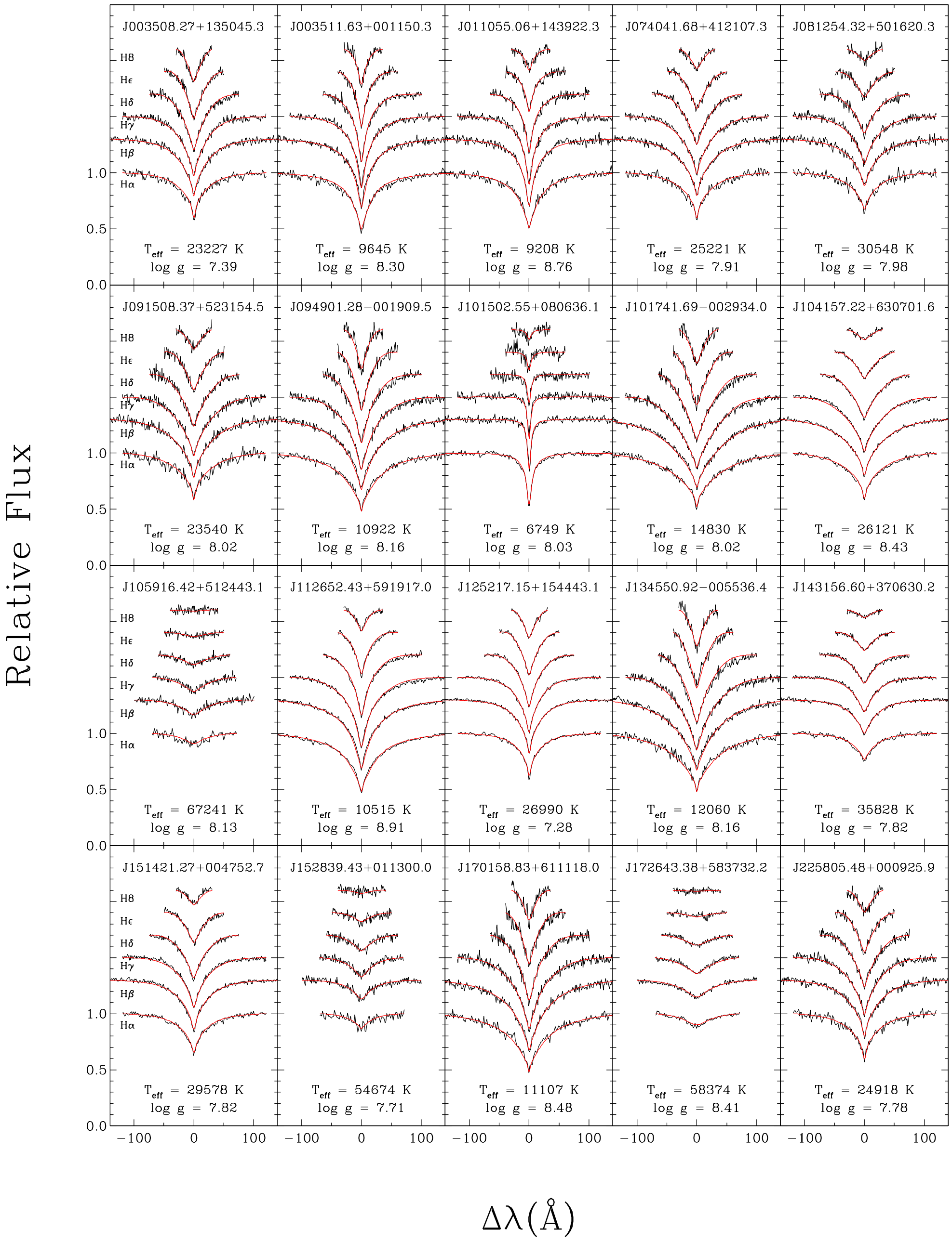

FIGURE 4.2 – Sample fits for 20 DA stars in the SDSS sample with high signal-to-noise spectroscopic data (S/N > 30). The atmospheric parameters are given in each panel.

all individual magnitudes with a flag indicating that there might be a problem. Since the photometry is not sensitive to surface gravity, we simply assume the spectroscopic $\log g$ value and fit only the effective temperature $T_{\rm phot}$ and the solid angle $\pi(R/D)^2$, where R is the stellar radius and D is the distance from Earth. We apply a correction to the u, i, and z bands of -0.040, $+0.015$ and $+0.030$, respectively, to account for the transformation from the SDSS to the AB magnitude system, as explained in Eisenstein et al. (2006a). Finally, we deredden the photometry, in an iterative fashion, using the distance of the star found from the previous iteration, and the parameterization of Harris et al. (2006) for the amount of reddening as a function of distance[4].

In the course of our inspection of the photometric and spectroscopic fits, we identified 37 double degenerates or helium-rich DA candidates that will be discussed in Section 4.3.4 and 4.3.5[5] together with a more general comparison of spectroscopic and photometric temperatures. Note that we do not make any direct use of the photometric temperatures since these are intrinsically less accurate, with larger internal uncertainties from the fitting procedure, and additional external uncertainties from interstellar reddening and photometric calibration.

4.4 Results

4.4.1 Atmospheric Parameters

We present in Table 4.1 the atmospheric parameters for our final sample of 3072 DA stars with S/N > 12 whose fits were visually inspected. We exclude 161 objects, as discussed in the previous section, and we postpone the analysis of 16 DAO stars to Section 4.4.3. When multiple spectra of the same star are available in the DR4, we simply adopt the solution obtained with the highest signal-to-noise spectrum. We convert $\log g$ values into stellar masses using the evolutionary models with thick hydrogen layers of Fontaine et al. (2001) below $T_{\rm eff} < 30,000$ K and of Wood (1995) above this temperature; we also provide in Table 4.1 the corresponding

---

[4] We would like to point out here that interstellar absorption is assumed to be negligible for stars with distances < 100 pc, and that the absorption is maximum for stars with distances from the Galactic plane $|z| > 250$ pc. The absorption varies linearly along the line of sight between these distances.

[5] We also remove the double lined binary J125733.63+542850.5 identified by Badenes et al. (2009), and the magnetic DAH+DB system J084716.21+484220.3 first identified by Schmidt et al. (2003)

white dwarf cooling time ($\log \tau$). Low-mass white dwarfs, below 0.46 $M_{\odot}$ and $T_{\rm eff} < 50,000$ K, are likely helium core white dwarfs, and we rely instead on evolutionary models from Althaus et al. (2001). For masses higher than 1.3 $M_{\odot}$, we use the zero temperature calculations of Hamada & Salpeter (1961). The absolute visual magnitude M_V obtained from spectroscopic measurements of $T_{\rm eff}$ and $\log g$ is also given for each object following the calibration of Holberg & Bergeron (2006).

The errors of the atmospheric parameters given in Table 4.1 are the *internal* uncertainties of our fitting procedure, which are correlated to the S/N (see, e.g., Bergeron et al. 1992). The true error budget also needs to take into account the *external* uncertainties from the data calibration. There are 301 repeated observations for stars in Table 4.1 that can be used to quantify the external errors. These alternative observations, in general with S/N only slightly lower than the primary observation, were fitted and visually inspected with our standard procedure. In Table 4.2, we compare the internal and external errors for these multiple observations. A similar procedure has been used by Eisenstein et al. (2006a), but since uncertainties are expected to be a function of both $T_{\rm eff}$ and S/N, here we break the sample into various bins for each quantity. We find that external uncertainties are always very similar to the internal uncertainties. This confirms the consistency of the data acquisition and pipeline reduction procedure of the SDSS spectra. We note that our comparison cannot reveal systematic reduction problems, however, and such effects will be discussed in Section 4.4.2 from a comparison with independent observations.

In Figure 4.3, we present the mass distribution as a function of effective temperature for our sample of DA stars. As we want to illustrate the effect of the quality of the observations on this distribution, we show in the upper panel the results with the higher quality spectra (S/N $>$ 20) and in the bottom panel with the lower quality spectra (20 $>$ S/N $>$ 12); each subsample has a roughly equal number of stars. For clarity, we postpone the discussion of the hottest stars ($T_{\rm eff} > 40,000$ K) to Section 4.4.3. Below $T_{\rm eff} \sim 13,000$ K, we observe the well-known increase in the mean mass, the so-called high-$\log g$ problem discussed at length in Tremblay et al. (2010) and references therein. The bottom panel indicates that the mass distribution obtained with lower S/N data is similar to that with higher quality spectra in the

TABLE 4.1 – SDSS DR4 Sample of DA White Dwarfs with S/N > 12

SDSS name	Plate−MJD−Fiber	$T_{\rm eff}$ (K)	$\log g$	$M/M_\odot$	M_V	$\log \tau$	Notes
J000006.75−004653.8	0685-52203-225	10850 (160)	8.39 (0.10)	0.85 (0.07)	12.52	8.95	
J000022.53−105142.1	0650-52143-217	8620 (110)	8.31 (0.15)	0.79 (0.10)	13.24	9.18	1
J000022.87−000635.7	0387-51791-166	23010 (470)	7.44 (0.06)	0.42 (0.01)	9.57	7.59	
J000034.07−010819.9	0685-52203-187	13090 (220)	8.01 (0.05)	0.61 (0.03)	11.52	8.50	
J000104.05+000355.8	0685-52203-490	13710 (600)	8.06 (0.08)	0.64 (0.05)	11.51	8.50	
J000127.48+003759.1	0685-52203-491	18560 (490)	7.84 (0.09)	0.53 (0.04)	10.66	7.88	
J000308.32−094147.0	0650-52143-550	8690 (90)	8.50 (0.12)	0.92 (0.08)	13.53	9.36	
J000357.63−004939.1	0387-51791-005	9740 (100)	8.95 (0.10)	1.18 (0.04)	13.98	9.41	
J000428.98+005801.9	0685-52203-621	16410 (500)	7.85 (0.10)	0.54 (0.05)	10.90	8.10	
J000441.75+152841.1	0751-52251-393	8710 (60)	8.20 (0.09)	0.72 (0.06)	13.02	9.07	
J000622.61+010958.7	0388-51793-448	39040 (1930)	7.73 (0.23)	0.54 (0.09)	9.03	6.69	
J000630.56+002323.9	0388-51793-424	23590 (770)	7.89 (0.11)	0.58 (0.06)	10.30	7.45	
J000636.61+160237.7	0751-52251-528	9620 (100)	8.30 (0.12)	0.79 (0.08)	12.80	9.03	
J000716.84−101908.4	0651-52141-230	20150 (740)	7.87 (0.11)	0.55 (0.06)	10.56	7.75	
J000737.18−090629.3	0651-52141-416	20240 (410)	7.88 (0.06)	0.56 (0.03)	10.56	7.71	
J000738.03+004003.3	1490-52994-507	10460 (70)	8.32 (0.06)	0.81 (0.04)	12.53	8.95	
J000946.45+144310.6	0751-52251-101	24570 (240)	7.89 (0.03)	0.57 (0.02)	10.22	7.31	
J001038.78−003241.5	0388-51793-074	10240 (120)	8.47 (0.11)	0.90 (0.07)	12.86	9.10	
J001148.19−092110.2	0652-52138-348	12680 (180)	7.84 (0.06)	0.52 (0.03)	11.34	8.43	
J001245.60+143956.4	0752-52251-221	11270 (120)	7.89 (0.07)	0.54 (0.04)	11.65	8.60	
J001339.19+001924.3	0389-51795-431	9600 (10)	8.32 (0.02)	0.80 (0.01)	12.84	9.04	2
J001415.59−103505.8	0651-52141-023	9920 (90)	8.42 (0.09)	0.86 (0.06)	12.87	9.09	
J001427.04+135058.4	0752-52251-135	8870 (60)	8.32 (0.08)	0.80 (0.05)	13.15	9.14	
J001448.82+002027.3	0687-52518-468	8960 (90)	8.08 (0.13)	0.64 (0.08)	12.72	8.97	2

Table 1 is available in its entirety in the electronic edition of the *Astrophysical Journal*. A portion is shown here for guidance regarding its form and content.

For one object where the fitted $T_{\rm eff}$ exceeds our models grid limit, we fix the parameters at $T_{\rm eff} = 140,000$ K and $\log g = 8$. Notes: (1) Incomplete wavelength coverage or glitches in the Balmer lines; (2) poor match between the slope of the observed spectra and the *ugriz* photometry; (3) main-sequence companion, one or two lines removed from the fit, and the line cores also removed due to emission; (4) same as previous but with no emission; (5) flagged in our visual inspection with a poor fit but no clear explanation was found; the atmospheric parameters under the assumption of a normal single DA should be regarded with caution; (6) DA with the Balmer-line problem and models with CNO were used; (7) emission in the line cores but no red excess; (8) DAZ; (9) DAO+dM.

TABLE 4.2 – DA White Dwarfs with Multiple Measurements

S/N range	N[a]	$\langle\sigma_{\mathrm{Teff}}\rangle^b$ (%)	$\langle\sigma_{\mathrm{Teff-multiple}}\rangle^c$ (%)	$\langle\sigma_{\log\mathrm{g}}\rangle^b$	$\langle\sigma_{\log\mathrm{g-multiple}}\rangle^c$
$T_{\mathrm{eff}} < 13,000$ K					
$12 < \langle$S/N$\rangle < 15$	18	1.3	1.0	0.12	0.14
$15 < \langle$S/N$\rangle < 20$	31	1.2	1.0	0.10	0.14
$\langle$S/N$\rangle > 20$	57	0.7	0.7	0.05	0.07
$T_{\mathrm{eff}} > 13,000$ K					
$12 < \langle$S/N$\rangle < 15$	10	3.2	1.3	0.11	0.06
$15 < \langle$S/N$\rangle < 20$	24	2.7	2.6	0.08	0.07
$\langle$S/N$\rangle > 20$	54	1.8	1.8	0.05	0.05

[a] Number of stars with multiple measurements. Subtypes (DAO, DAZ, DA+dM and DA+DB) are not considered.
[b] Mean internal uncertainty from the fitting procedure.
[c] Average of the standard deviation between multiple observations.

intermediate range of effective temperature where the hydrogen lines are particularly strong (30,000 K > $T_{\mathrm{eff}} > 10,000$ K). However, larger spreads in the mass distribution can been seen at the high and low temperature limits of our sample, in a region where hydrogen lines become weaker and more sensitive to the quality of the observations. Furthermore, since the flux in the blue portion of the spectrum is intrinsically less important in cooler stars, the S/N also becomes much smaller below 4000 Å — a region sensitive to $\log g$ — than at longer wavelengths, and the atmospheric parameters of cooler stars are thus expected to become less accurate. An examination of our error budget in Table 4.2 indeed confirms that at cool temperatures and low S/N, the external error of $\log g$ is indeed roughly twice that of the average of the sample.

As already mentioned, one of the most important aspects of our analysis is the careful visual inspection of each individual fit. In Figures 4.4 and 4.5 we show illustrative examples for three objects. We specifically look at the following diagnostics: (1) the quality of the spectroscopic fit (left panels), (2) the quality of the photometric fit (right panels), (3) the comparison of the spectroscopic and photometric temperatures, (4) the superposition of the observed photometry and fluxed spectra, and finally (5) the superposition of the model fluxes normalized at r and calculated at the spectroscopic values of T_{eff} and $\log g$. On the top panels of Figure 4.4 is an example of a case with an excellent internal consistency between model and spectroscopic/photometric observations, a situation we observe for about 95% of single

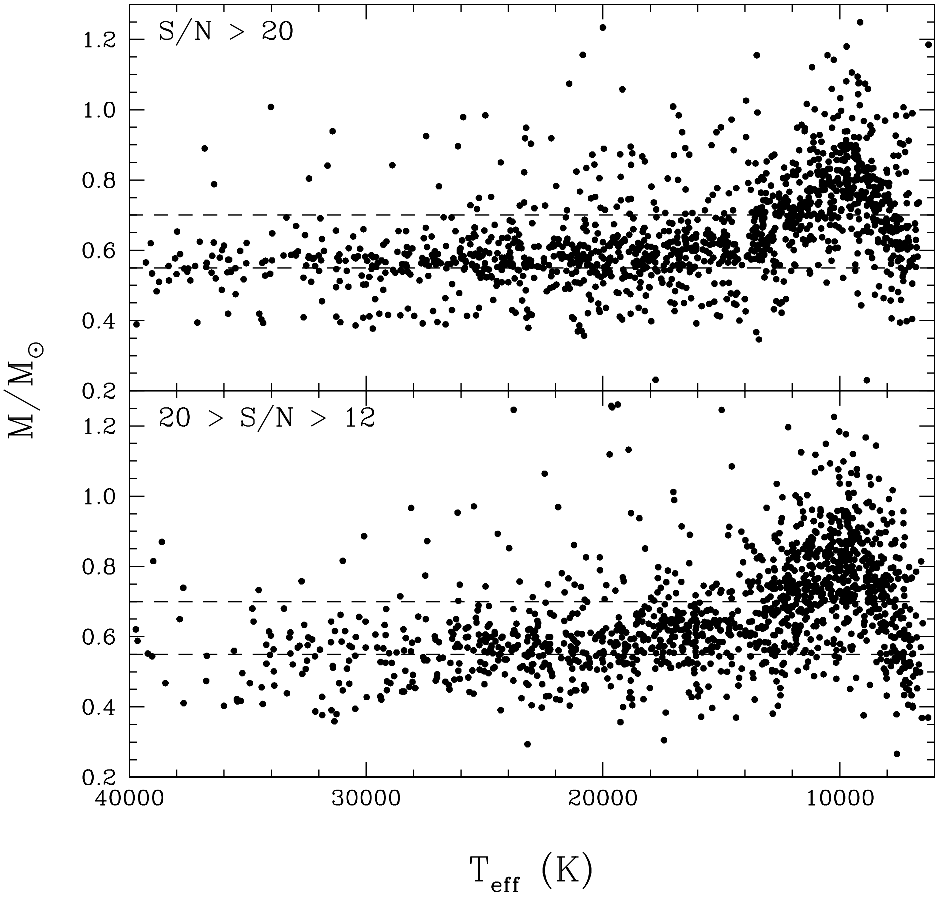

FIGURE 4.3 – Mass distribution as a function of effective temperature for DA stars in the SDSS with $T_{\rm eff} < 40,000$ K, for two separate ranges of S/N. Lines of constant mass at 0.55 $M_\odot$ and 0.70 $M_\odot$ are shown as a reference.

DA stars. On the bottom panels of Figure 4.4 is an example of a problem we encounter in about 5% of the stars in our sample (although, generally, to a lesser extent than what is shown here). In these situations, the slope of the observed spectrum disagrees with that inferred from photometric colors. This occurs more often for the reddest and coolest white dwarfs in the sample. In most cases, all other aspects of the visual inspection are as expected (i.e., a good spectroscopic fit, and a good agreement between spectroscopic and photometric temperatures). This clearly suggests that errors in the flux calibration are the most likely explanation for this discrepancy. The observed spectrum of J003511.63+001150.3 shown in Figure 4.4 is actually a repeated observation; a primary spectrum with a slightly higher S/N was used to determine the atmospheric parameters given in Table 4.1. The primary spectrum is actually in agreement with the photometric colors, confirming the hypothesis that a fraction of SDSS spectra may have an erroneous flux calibration. Kleinman et al. (2004) claim that the SDSS spectra are spectrophotometrically calibrated to within about 10%, on average, so some discrepancy, such as that shown in Figure 4.4, should not be totally unexpected. The trend we observe, however, is that the flux calibration is good to within a few percent for most objects, but is significantly worse for a minority (∼5%) of cases. We added a note in Table 4.1 (see Note 2) to flag these particular observations, but these objects should not be considered as peculiar white dwarfs. On the other hand, there are a few cases (about 1%) where the predicted energy distribution inferred from the spectroscopic solution disagrees with both the slope of the observed spectrum *and* the photometric colors, as illustrated on the top panel of Figure 4.5. In other words, there is a poor match between $T_{\rm spec}$ and $T_{\rm phot}$, even though the spectroscopic fit appears normal. We note that one could also select the cool spectroscopic solution for this object, to obtain a better match with the photometric temperature. This case is displayed on the bottom panel of Figure 4.5, and while the agreement between $T_{\rm spec}$ and $T_{\rm phot}$ is better, the Balmer line profiles are clearly at odds with the model predictions. Objects similar to those shown here are believed to be genuine peculiar stars and these are further discussed in Sections 4.3.3 and 4.3.4.

4.4.2 Mass distribution

In this section, we attempt to best characterize the mass distribution of DA stars using the SDSS-E06 sample. We restrict our analysis to stars cooler than $T_{\rm eff} = 40,000$ K due to possible systematic effects from metal contaminations (see Section 4.4.3), and to stars hotter than 13,000 K because of the high-$\log g$ problem discussed above. We also eliminate, for the time being, all DA$-$M dwarf binaries; these will be discussed further in Section 4.4.4. As a first step, we look for a compromise between the quality of the spectra and the size of the sample, as discussed in the Introduction. We saw in the preceding section that we could obtain sound results using all stars with S/N > 12, but we should be cautious at the hot and cool ends of the distribution.

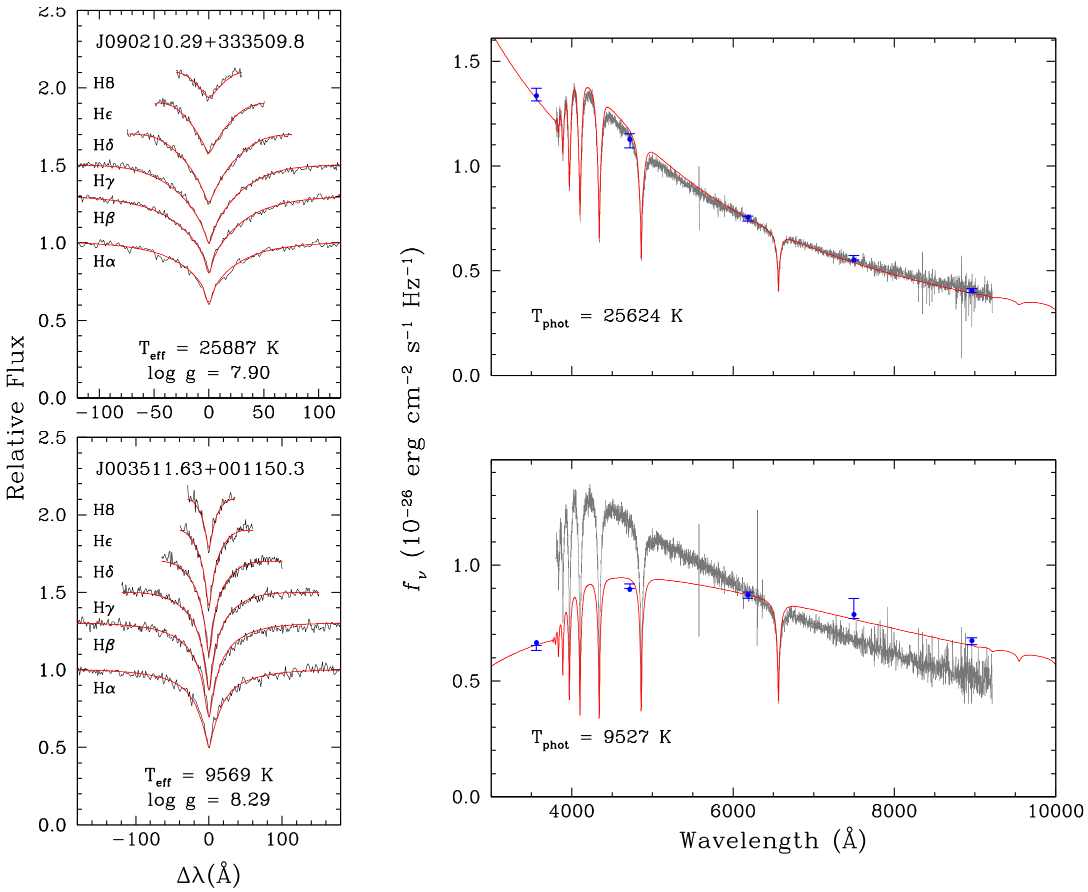

FIGURE 4.4 – Sample fits of DA stars in the SDSS sample with the atmospheric parameters given in each panel (left panels). In the right panels, we show complementary data used in our visual inspection. The y-axis scale is fixed by the observed photometric fluxes (blue error bars) that are fitted with average model fluxes (blue filled dots). The photometric temperature is given in each panel. Both the fluxed spectra (in gray) and synthetic model fluxes (in red), calculated at the spectroscopic parameters given in the left panel, are then scaled to the r photometric band. The objects are discussed in the text.

To make a more quantitative assessment of the optimal sample for computing the mass distribution, we break our sample into S/N bins containing a nearly equal number of stars. In Figure 4.6, we present the mean mass and standard deviation as a function of S/N[6]. In the ideal case of a homogeneous spectroscopic data reduction as a function of S/N, the mean mass should be constant over the whole sample. The standard deviation, however, should be close

---

[6] For S/N $<$ 12, we used an automatic fitting procedure similar to that employed for the higher quality spectra. In order to get a relatively clean sample, we removed DA$-$M dwarf composite systems using color criteria and all other outliers that did not fall within the range of $6.5 < \log g < 9.5$

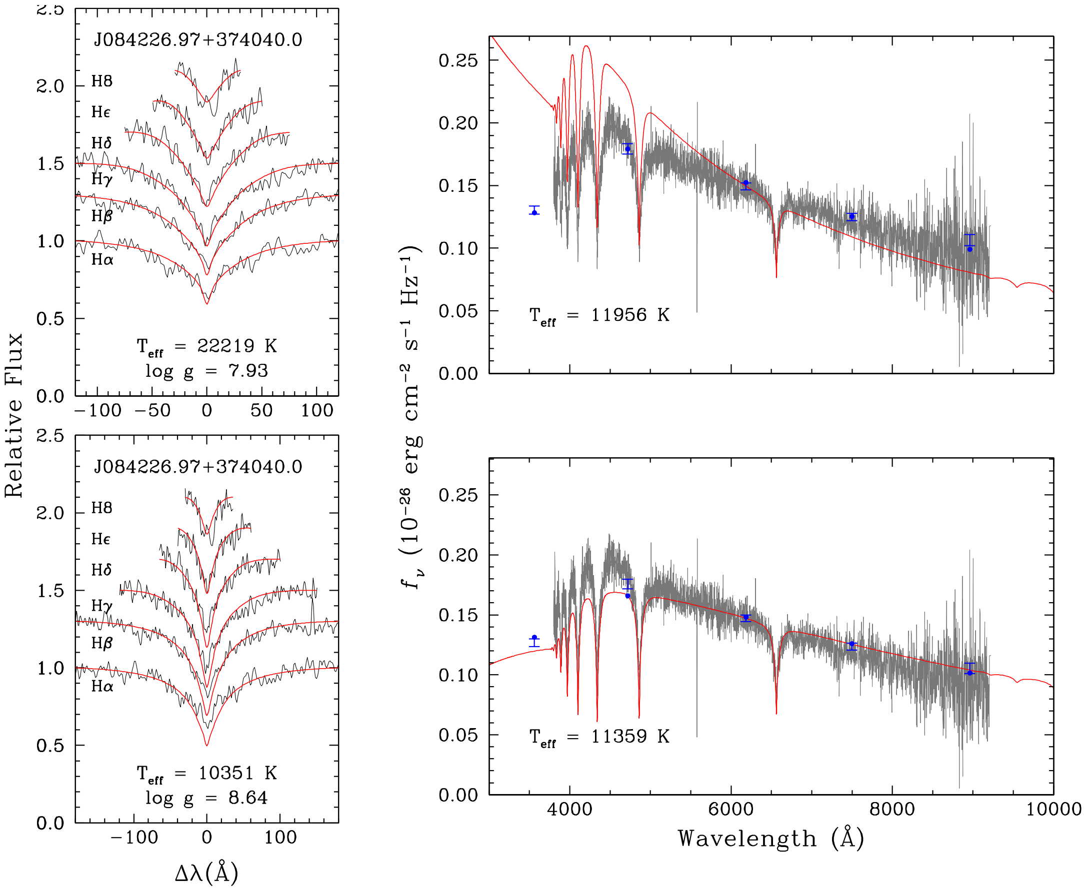

FIGURE 4.5 – Similar to Figure 4.4 for both the hot and cool spectroscopic solutions of J084226.97+374040.0 (top and bottom panels, respectively). The observed and model spectra on the left panels are binned by a factor of two for clarity. This object is actually a DA+DC binary candidate.

to the intrinsic value of the underlying mass distribution at high S/N, but should increase when the errors of the individual mass measurements become significant compared to the true dispersion of the sample. We can see in the upper panel of Figure 4.6 that the mean mass remains fairly constant, even down to very low S/N values (S/N $\sim$ 8), which implies that as a whole, we can trust the SDSS spectroscopic data in this range of S/N. The standard deviation, displayed in the bottom panel of Figure 4.6, appears as a more efficient means of selecting an appropriate S/N cutoff. It shows clearly that for low S/N, the large individual uncertainties in the mass measurements alter significantly the mass dispersion. We conclude that a cutoff at S/N = 15 is a good compromise to obtain the best statistical significance, that is, a large sample with sufficiently accurate spectroscopic measurements. As can be seen from Figure 4.1, this cutoff corresponds to a $g \sim 19$ cutoff, similar to the value used by Kepler et al. (2007) and DeGennaro et al. (2008) based on analogous arguments.

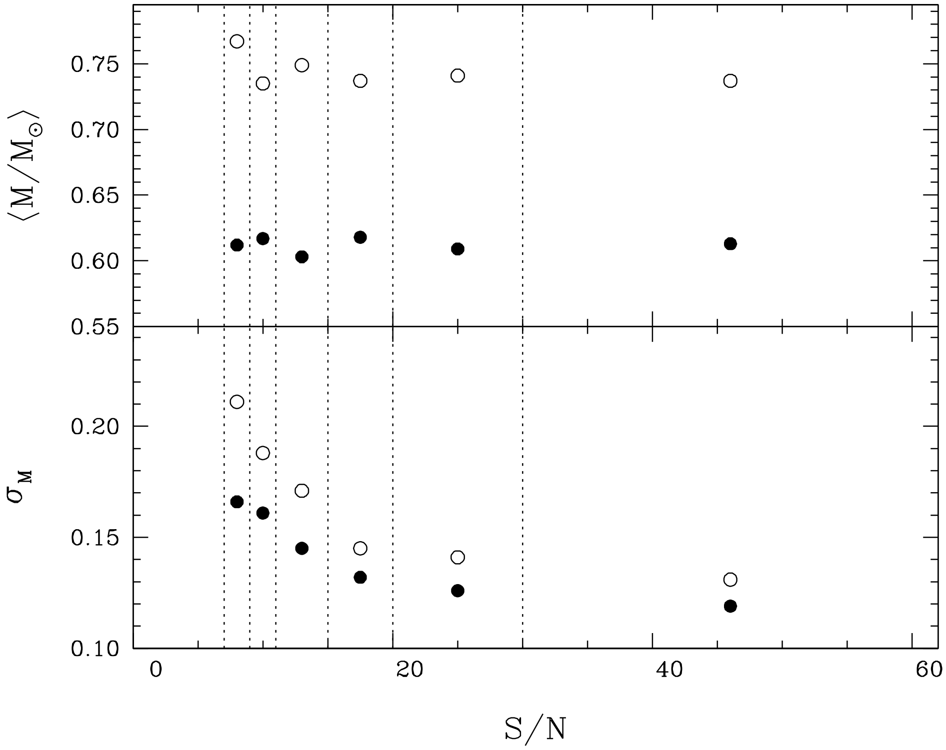

FIGURE 4.6 – Top panel: mean mass of the DA stars in the SDSS as a function of the S/N of the observations. The objects have been separated in bins of nearly equal number of stars, identified by dotted vertical lines. Filled circles correspond to DA stars with 40,000 K > $T_{\rm eff}$ > 13,000 K, while open circles represent cooler objects. Bottom panel: similar to the top panel but for the mass standard deviation as a function S/N.

In Figure 4.7, we show our final mass distribution for the DR4 sample (40,000 K > $T_{\rm eff}$ > $13,000$ K), which yields a mean mass of $\langle M \rangle = 0.613\ M_\odot$. We note the presence of an excess of low-mass objects and a high-mass tail, which are qualitatively similar to those reported by Kepler et al. (2007) in their analysis of the same sample. We also demonstrate in this plot that the adoption of a slightly larger S/N cutoff of 20, rather than 15, does not change significantly the mean properties, or even the shape, of the mass distribution. While it is obviously much more difficult to identify subtypes (i.e., magnetics, DAZ, DAO, etc.) or to pinpoint the exact boundaries of the ZZ Ceti instability strip (Gianninas et al. 2005), the atmospheric parameters of normal DA white dwarfs appear reasonable down to low S/N, with admittedly increasing uncertainties.

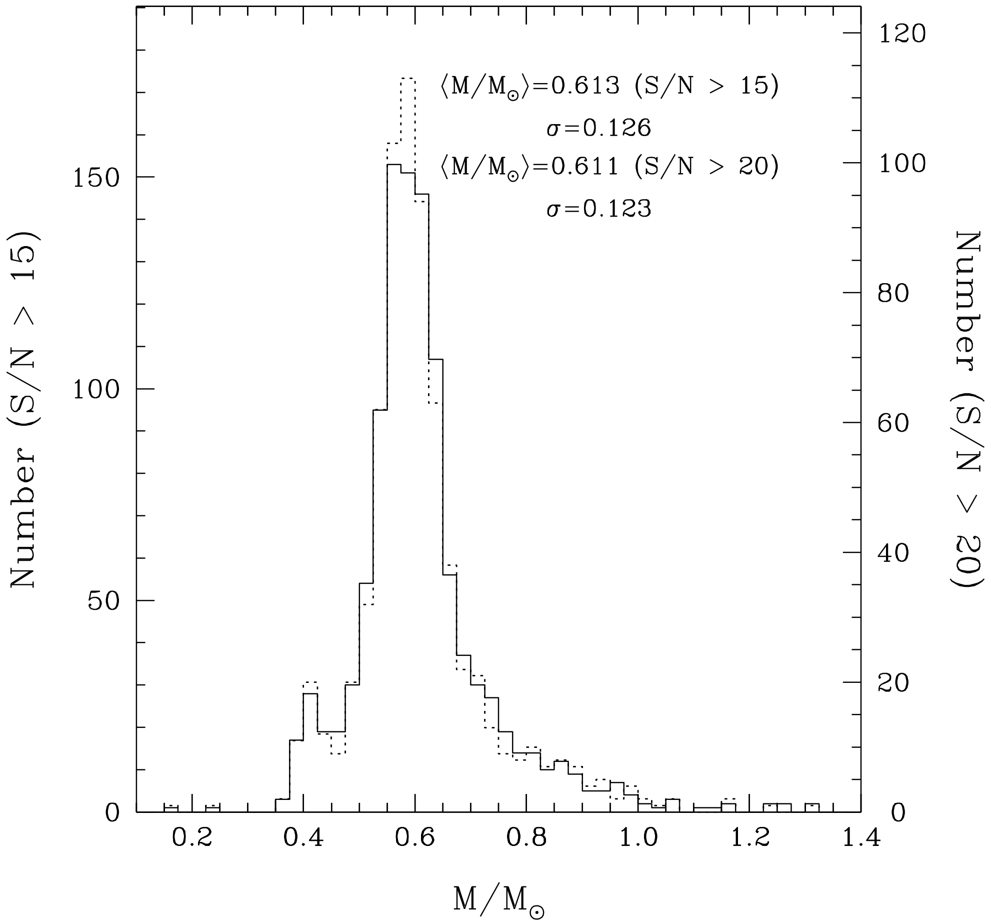

FIGURE 4.7 – Mass distribution for the DA stars in the SDSS with 40,000 K > $T_{\rm eff}$ > 13,000 K. The distribution shown with a solid line corresponds to our optimal sample of 1089 DA stars with S/N > 15. In comparison, we show as a dashed line the distribution with an alternate cutoff of S/N > 20, scaled to match the former (the number of stars is given on the right-hand scale). The mean mass and standard deviation are given in the figure.

4.4.3 Comparison of Spectroscopic and Photometric Temperatures

The comparison of our spectroscopic and photometric effective temperatures is displayed in Figure 4.8. For clarity, we only show the results for DA spectra with S/N > 20; the comparison with lower S/N data is similar, with a slightly higher dispersion. Since the photometry becomes increasingly insensitive to effective temperature at the hot end of the sample, we do not consider objects with both $T_{\rm spec}$ and $T_{\rm phot}$ over 40,000 K. We find that the agreement is generally good, with a small standard deviation of ∼8%, although some outliers are also clearly present. More importantly, there is a significant offset, with the spectroscopic temperatures being higher than the photometric temperatures by ∼4%, on average. There could be different explanations for this discrepancy, which we discuss in turn.

One important uncertainty is the dereddening procedure, which has an effect even for the brightest stars in the sample. The procedure used here, taken from Harris et al. (2006), seems realistic in terms of the galactic structure, but the ratio of the actual to the full galactic reddening along the line of sight is uncertain by at least a few percent, due to the simplicity of the parameterization. The offset in Figure 4.8 increases to ∼6% if we do not apply any reddening correction to the photometry; conversely, a large and unrealistic extinction, close to the maximum value, is necessary to remove the offset at $T_{\rm eff} \sim 20,000$ K. The reddening uncertainty is therefore not large enough to be the main source of the observed offset. The second possible explanation for the offset is related to the photometric system transformations discussed in Section 4.2.4. Since these corrections are based on older models and data reductions (from Data Release 4), they might have to be revisited, although Eisenstein et al. (2006a) quote uncertainties of the order of 1%, smaller than the discrepancy observed here. Furthermore, we verified that, on average, the observed and predicted photometry are in agreement within less than 0.01 magnitudes for all filters.

A third source of error might be related to a problem with the spectroscopic temperatures. It is shown later in this work (Section 4.4.2) that the spectroscopic temperatures obtained using SDSS spectra are on average 2% higher (for $T_{\rm eff} > 13,000$ K) than those obtained using data from Gianninas et al. (2011) for objects in common. This discrepancy, likely due to systematic data reduction problems, could easily explain half of the offset observed in Figure

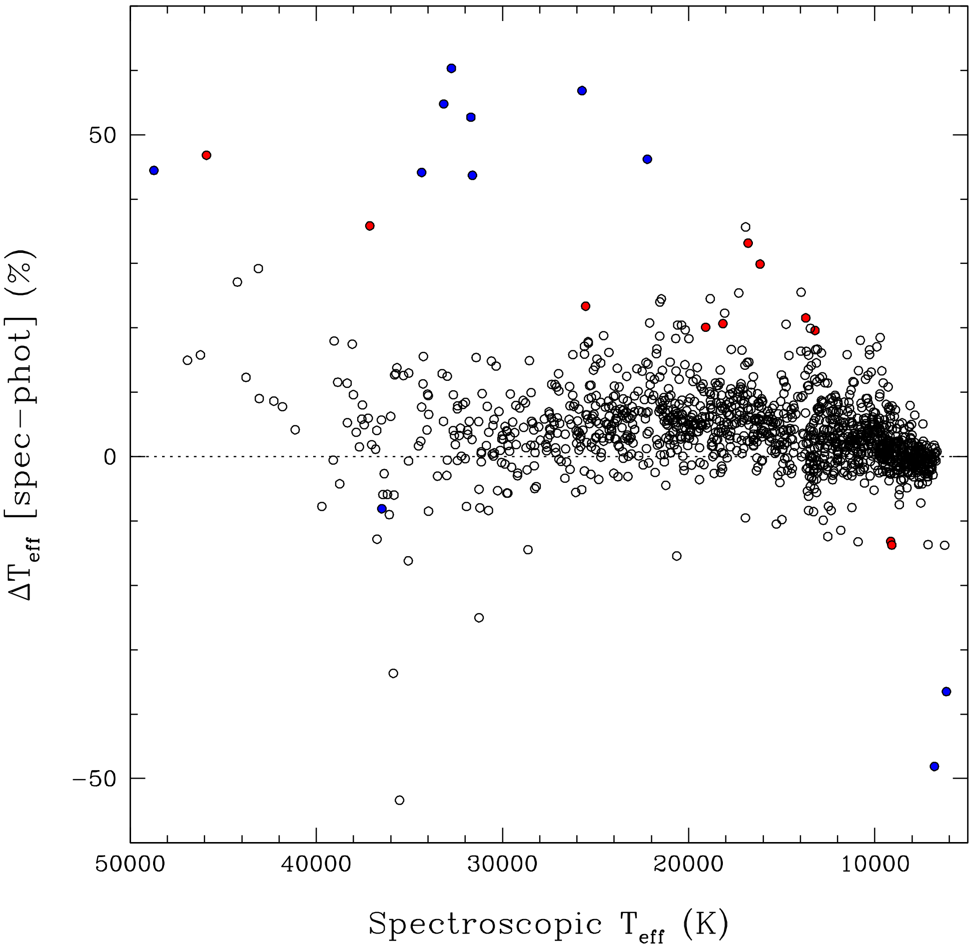

FIGURE 4.8 – Comparison of spectroscopic and photometric temperatures (in % with respect to spectroscopic temperatures) as a function of spectroscopic temperature for all DA stars with S/N > 20 (open circles), excluding DA−M dwarf binaries. Blue filled circles correspond to double degenerate candidates discussed in the text, while red symbols represent outliers (2σ discrepancy) that have been flagged in Table 4.1 as problematic observations — see Notes (1) or (2) in Table 4.1. The horizontal dotted line represents a perfect match between both temperature estimates.

4.8. A fourth possible source of uncertainty is that we cannot claim to be more accurate than 1% in terms of the physics of the models, and therefore on the absolute scale of the spectroscopic temperatures. However, we can at least claim that our improved models yield absolute visual magnitude measurements, derived from spectroscopic values of $T_{\rm eff}$ and $\log g$, that are consistent with those derived from trigonometric parallax measurements (see Fig. 14

of Tremblay & Bergeron 2009). Finally, another option would be that the offset is real, at least for some objects. In the next section, we demonstrate that unresolved DA+DA binaries may indeed cause a systematic positive offset between spectroscopic and photometric temperatures.

We conclude that each of the uncertainties discussed above are able to explain about half of the observed offset, and there is thus no easy way to interpret the absolute spectroscopic and photometric temperature scales of white dwarfs at this point. Until these issues are resolved, the photometric temperature scale should not be discarded too easily, even if the internal uncertainties are larger.

Finally, we find in the comparison of spectroscopic and photometric temperatures displayed in Figure 4.8 a small number of outliers. A closer inspection of all objects with a 2σ discrepancy reveals that some of these outliers (red circles in Fig. 4.8) have already been flagged in Table 4.1 as being problematic due to poor spectrophotometry or glitches in the observed spectra. These objects are thus unlikely to be real peculiar white dwarfs. However, many other outliers exhibit He I lines in their spectra and/or have poor fits. This suggests that these objects most likely represent DA+DB or DA+DC unresolved degenerate binaries. We analyze these systems further in the following section.

4.4.4 Double Degenerate Binaries

To better understand, from an observational point of view, how double degenerate binaries can be detected in the SDSS, we first present a simulation performed using a set of synthetic models. Since we are mostly interested here in the DA stars found in the SDSS, we simulate double degenerate systems containing at least a DA star together with another white dwarf of the DA, DB, or helium-rich DC spectral type. Individual model fluxes are thus combined for each assumed component of the system, properly averaged by their respective radius, to which we add a Gaussian noise of S/N = 30; synthetic *ugriz* photometry is also extracted from the resulting spectrum. The simulated data are then analyzed with our standard fitting procedure under the assumption of single DA star models. For the sake of simplicity, all calculations are made for a sequence of $T_{\rm eff}$ from 6000 to 40,000 K with steps of 2000 K for both components of the system. We computed all possible combinations in this range of temperatures with equal values of $\log g = 8$ for both components, as well as with a $\log g$ difference of 0.5 dex ($\log g = 7.75$ and 8.25 to be explicit). The results of this experiment are presented in Figure 4.9 where we compare spectroscopic and photometric effective temperatures; open circles represent DA+DA binaries, while filled circles correspond to DA+DB/DC binaries.

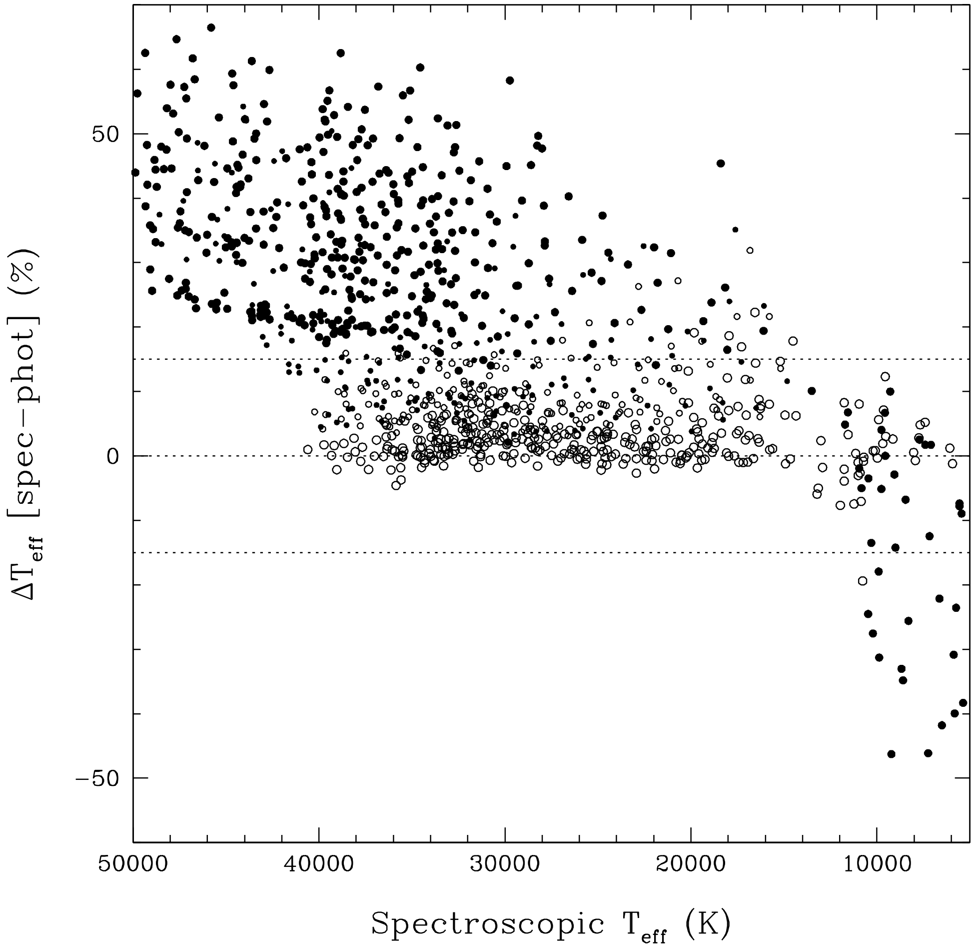

FIGURE 4.9 – Simulation of DA+DA (open circles) and DA+DB/DC (filled circles) binaries with synthetic models computed for every component combination in the range of 40,000 K $> T_{\rm eff} >$ 6000 K with steps of 2000 K. We studied the cases of two equal surface gravities ($\log g = 8$), and a difference of 0.5 dex ($\log g = 7.75, 8.25$). The resulting model spectra, with noise added, are fitted using the same procedure as that used to analyze the SDSS stars in Figure 4.8 (see text for more details). The smaller points correspond to simulations where the ratio in temperature between the hotter and cooler components is larger than a factor of two. The middle horizontal line represents the 1:1 relation, while the two other horizontal lines correspond to the 2σ region obtained from the SDSS distribution displayed in Figure 4.8.

An examination of our results first reveals that all DA+DA binaries are indistinguishable from single DA stars in this diagram. Therefore, one absolutely needs additional constraints, such as trigonometric parallax or radial velocity measurements, to identify DA+DA binaries in the SDSS. Liebert et al. (1991) have already shown that combining the model spectra of two DA white dwarfs results, in general, in an apparently normal object that can be fitted successfully with single star models. What we find here is that the combined $ugriz$ photometry can also be fitted with single star models, and that the photometric temperature happens to be within ∼10% of the spectroscopic solution, even if the two DA components of the system have large temperature differences. Figure 4.9 also reveals that the spectroscopic temperatures are systematically larger than the photometric temperatures for DA+DA composites. A careful examination of this puzzling result reveals that the offset is due to the fact that the average spectroscopic temperatures just happen to be systematically larger than the average photometric temperatures. Since the observed offset in Figure 4.8 is of exactly the same order as that simulated in Figure 4.9, it is of course tantalizing to suggest that most DA stars might actually be DA+DA composite systems! But we will refrain from doing so since, coincidentally, various systematic uncertainties in the spectroscopic and photometric temperature determinations are expected to produce similar offsets, as discussed in the previous section.

The situation is very different for the DA+DB/DC binary simulations shown in Figure 4.9, for which a large number of outliers can be easily identified. The spectroscopic fit of these objects would also often be flagged due to the presence of He I lines and a poor fit of the lower Balmer lines (typically the depth of Hα is too shallow compared to a single star model). Even when the temperature of the DB/DC component is only half that of the DA component ($T_{\rm eff-DB/DC}/T_{\rm eff-DA} = 0.5$), these objects still appear as outliers in Figure 4.9 since the ∼5% additional continuum flux is still important in the core of the deep Balmer lines. For lower values of $T_{\rm eff-DB/DC}/T_{\rm eff-DA}$, it becomes almost impossible to confirm the presence of a companion, unless the He-rich component shows strong He I lines and the S/N is particularly high.

In light of these results, we refined our criteria to find all DA+DB/DC in our sample by specifically searching for He I lines, but found only one additional star[7] that was not in the $> 2\sigma$ outlier region in Figure 4.8. In our simulation of double degenerates, we also find a temperature regime ($T_{\rm spec} \sim 10,000$ K in Fig. 4.9) where we obtain a good match between photometric and spectroscopic temperatures, yet the spectroscopic fit is poor at Hα (and possibly additional low Balmer lines). One example of such a system is shown at the bottom of Figure 4.5, where Hα (and to a lesser extent Hβ and Hγ) is clearly at odds with the model predictions, and appears *diluted* by a companion. Six double degenerate candidates were identified in this manner from our DA sample.

We now proceed to fit all our double degenerate candidates with appropriate model spectra; our grid of DB models is described, for instance, in Limoges & Bergeron (2010) and references therein. We use an alternative version of our fitting program described above to extract the normalized hydrogen and helium (if present) line profiles of all candidates. Then a χ^2 minimization is performed between the observations and our set of DA and DB/DC models, with the $T_{\rm eff}$ and $\log g$ of each component of the system considered a free parameter. We assume that all objects are physical binaries, i.e. at the same distance, and therefore the flux ratio between the components is fixed by the set of atmospheric parameters.

We find in our sample a total of 35 binary candidates, including 10 DA+DB and 25 DA+DC systems. The fits are displayed in Figures 4.10 and 4.11, and the corresponding atmospheric parameters are reported in Table 4.3 along with additional comments for each system. For all DA+DC candidates, it is not possible to fit all four parameters since the dilution effects produced by a more massive (smaller radius) DC component are qualitatively comparable to those of a cooler object. Therefore, we simply assume a value of $\log g = 8$ for all DC stars. Furthermore, we observe that when the S/N is low, or when the hottest object is a DB/DC star, it is difficult to constrain the $\log g$ value of any component; in these cases a value of $\log g = 8$ is assumed for both stars. We find that, in general, the errors of the atmospheric parameters are significantly larger than those obtained for single stars. This is a direct consequence of considering two additional free parameters in our fitting procedure, and also results from the weakness of some of the observed spectral features.

---

[7] We exclude here hot DAO stars with $T_{\rm eff} > 40,000$ K.

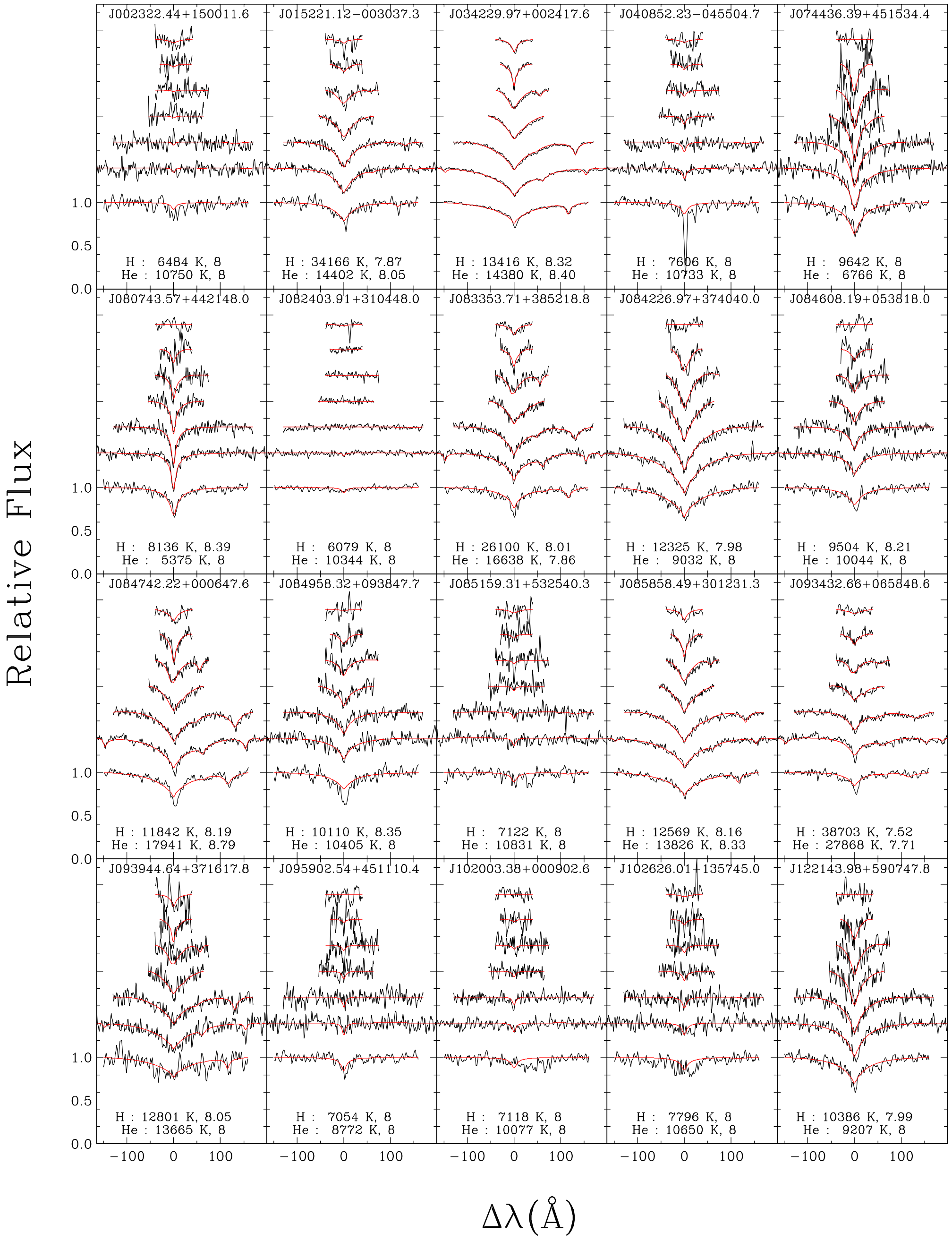

FIGURE 4.10 – Our best fits to the Balmer lines and He I lines, if present, for 35 double degenerate candidates in the SDSS sample. The lines are, from bottom to top, Hα to H8, and He I λ5877. Both the predicted and observed spectra have been binned by a factor of two for clarity. The atmospheric parameters, $T_{\rm eff}$ and $\log g$, of both H-rich and He-rich components are given in each panel; a value of $\log g = 8$ without decimals indicates that the value is assumed. The unexpected features in the core of Hα for some objects (i.e., J040852.23−045504.7) are a common occurrence in the SDSS spectra, and the origin of these features is unknown to us.

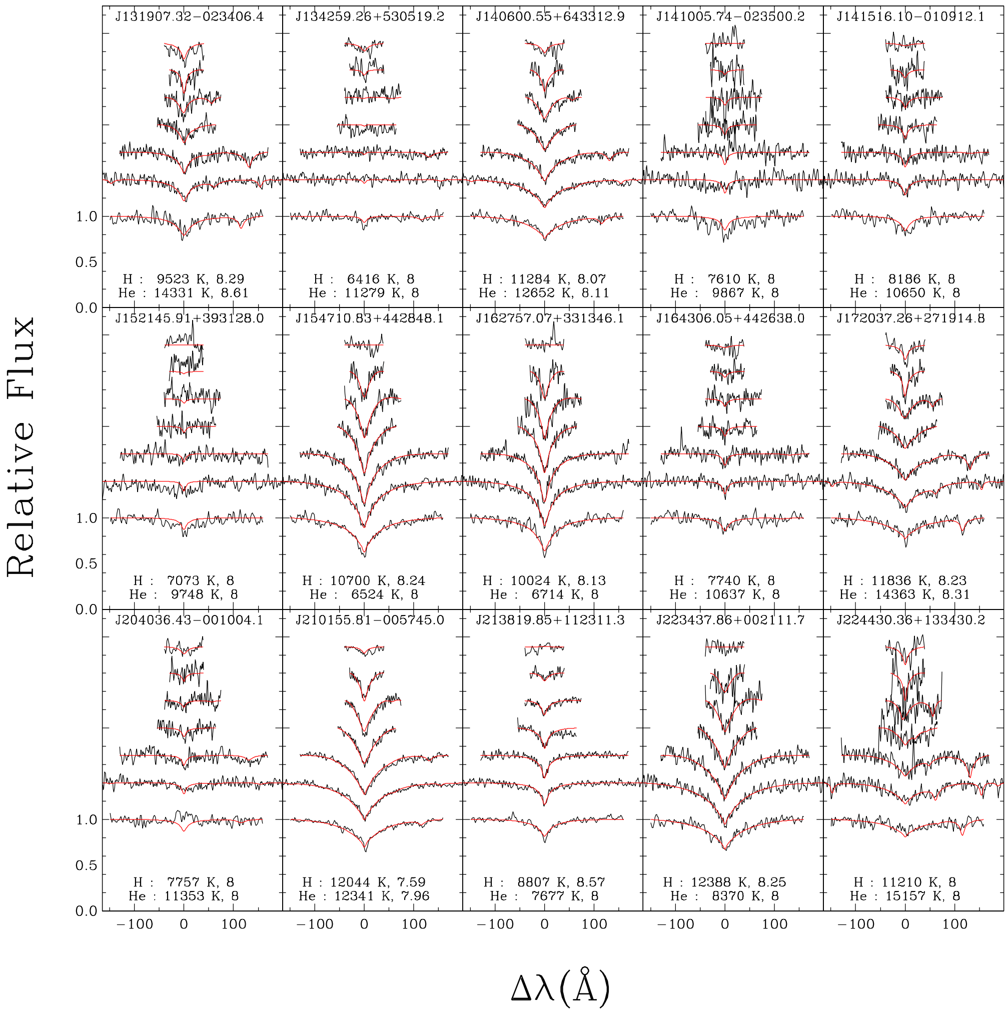

FIGURE 4.11 – Same as Figure 4.10.

We also compared for all binary candidates the predicted and observed *ugriz* photometry. We show an example for DA+DB and DA+DC systems in Figure 4.12. Here we calculate the predicted *ugriz* photometry with the atmospheric parameters given in Table 4.3, and simply match it to the observed photometry using a single scaling factor. We thus make no attempt to actually fit the observed photometry since there would be too many free parameters in our fitting procedure. In general, we find that this straightforward comparison between predicted and observed photometry yields an acceptable match, which is better or similar to that obtained under the assumption of a single star model, with the exception of a few objects identified in Table 4.3. We note that, unlike single stars, the predicted photometry is sensitive to the surface gravity of both stars since the relative contribution of each component of the system to the total flux — and thus the shape of the energy distribution — depends on their respective stellar radius. Therefore we do not put too much emphasis on small discrepancies, especially when the $\log g$ values are assumed in the spectroscopic fits.

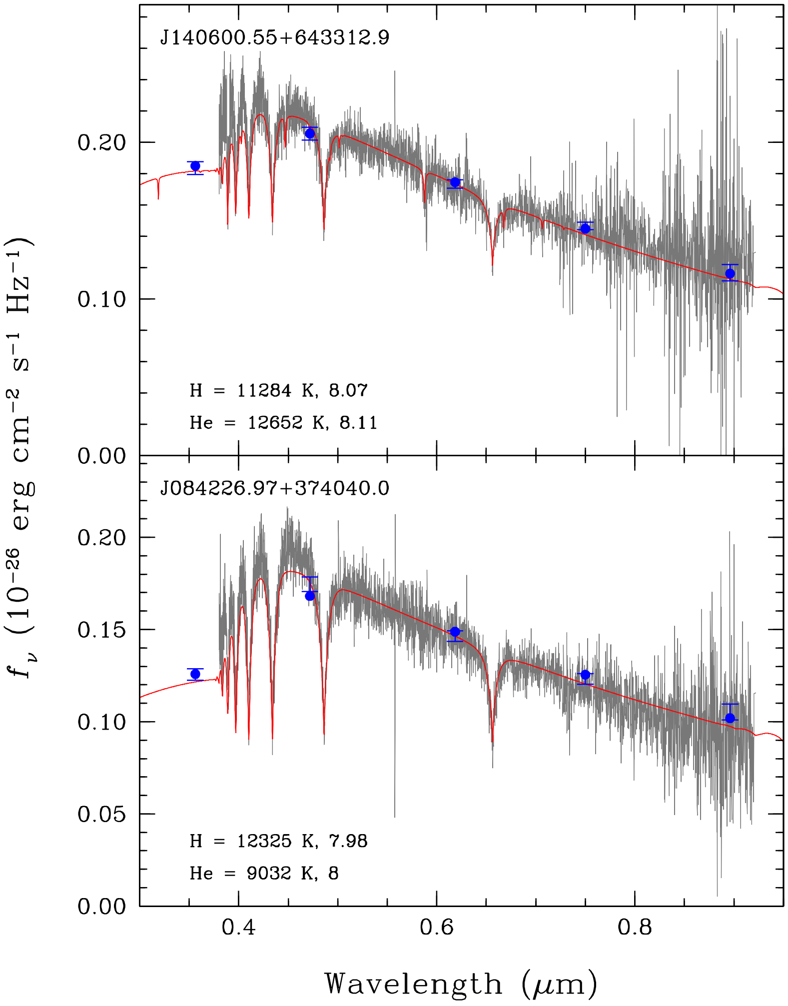

FIGURE 4.12 – Superposition of the predicted (blue dots) and observed (blue error bars) photometry for two objects taken from Figures 4.10 and 4.11 (and in Table 4.3). The atmospheric parameters obtained from our spectroscopic fits are used here to compute the predicted photometry; only the solid angle is adjusted. Both the observed (gray) and synthetic (red) absolute fluxes are then scaled to the r photometric band.

TABLE 4.3 – DA+DB/DC Binary Candidates

SDSS name	Plate-MJD-Fiber	$T_{\rm eff}$ (K) H-comp	$\log g$ H-comp	$T_{\rm eff}$ (K) He-comp	$\log g$ He-comp	Notes
J002322.44+150011.6	0753-52233-177	6490 (420)	8	10750 (390)	8	1,2
J015221.12−003037.3	0402-51793-114	34170 (1640)	7.87 (0.14)	14400 (3580)	8.05 (0.95)	3
J034229.97+002417.6	0714-52201-551	13420 (170)	8.32 (0.04)	14380 (160)	8.40 (0.06)	4
J040852.23−045504.7	0465-51910-482	7610 (200)	8	10730 (380)	8	2,5
J074436.39+451534.4	1737-53055-281	9640 (230)	8	6770 (580)	8	6
J080743.57+442148.0	0439-51877-188	8140 (170)	8.39 (0.14)	5380 (420)	8	5,6
J082403.91+310448.0	0931-52619-558	6080 (220)	8	10340 (210)	8	1,2
J083353.71+385218.8	0828-52317-277	26100 (1250)	8.01 (0.10)	16640 (910)	7.86 (0.17)	5
J084226.97+374040.0	0864-52320-524	12330 (300)	7.98 (0.20)	9030 (900)	8	
J084608.19+053818.0	1187-52708-630	9500 (260)	8.21 (0.16)	10040 (820)	8	6
J084742.22+000647.6	0467-51901-052	11840 (320)	8.19 (0.11)	17940 (790)	8.79 (0.15)	7
J084958.32+093847.7	1760-53086-411	10110 (320)	8.35 (0.13)	10410 (570)	8	5,6,7
J085159.31+532540.3	0449-51900-311	7120 (270)	8	10830 (370)	8	1,2
J085858.49+301231.3	1590-52974-148	12570 (290)	8.16 (0.09)	13830 (320)	8.33 (0.13)	
J093432.66+065848.6	1196-52733-093	38700 (1620)	7.52 (0.08)	27870 (9140)	7.71 (0.28)	5,7
J093944.64+371617.8	1275-52996-630	12800 (890)	8.05 (0.13)	13670 (530)	8	
J095902.54+451110.4	0942-52703-455	7060 (730)	8	8770 (2730)	8	2
J102003.38+000902.6	0271-51883-557	7120 (240)	8	10080 (710)	8	1,2
J102626.01+135745.0	1747-53075-430	7800 (230)	8	10650 (510)	8	1,2
J122143.98+590747.8	0955-52409-041	10390 (260)	7.99 (0.36)	9210 (1730)	8	6
J131907.32−023406.4	0341-51690-266	9520 (300)	8.29 (0.23)	14330 (630)	8.61 (0.30)	
J134259.26+530519.2	1042-52725-076	6420 (340)	8	11280 (220)	8	1,2
J140600.55+643312.9	0498-51984-163	11280 (310)	8.07 (0.17)	12650 (470)	8.11 (0.28)	
J141005.74−023500.2	0916-52378-266	7610 (470)	8	9870 (1760)	8	1,2
J141516.10−010912.1	0303-51615-057	8190 (170)	8	10650 (440)	8	6
J152145.91+393128.0	1293-52765-385	7070 (560)	8	9750 (2380)	8	1,2
J154710.83+442848.1	1333-52782-119	10700 (160)	8.24 (0.12)	6520 (510)	8	6
J162757.07+331346.1	1058-52520-221	10020 (150)	8.13 (0.16)	6710 (650)	8	6
J164306.05+442638.0	0629-52051-493	7740 (180)	8	10640 (390)	8	
J172037.26+271914.8	0979-52427-501	11840 (500)	8.23 (0.17)	14360 (530)	8.31 (0.25)	

Table 4.3 – Suite

SDSS name	Plate-MJD-Fiber	$T_{\rm eff}$ (K) H-comp	$\log g$ H-comp	$T_{\rm eff}$ (K) He-comp	$\log g$ He-comp	Notes
J204036.43−001004.1	0981-52435-139	7760 (180)	8	11350 (280)	8	2
J210155.81−005745.0	0984-52442-049	12040 (180)	7.59 (0.07)	12340 (360)	7.96 (0.15)	5
J213819.85+112311.3	0731-52460-632	8810 (190)	8.57 (0.17)	7680 (770)	8	5
J223437.86+002111.7	0673-52162-630	12390 (560)	8.25 (0.19)	8370 (1000)	8	5,6
J224430.36+133430.2	0740-52263-264	11210 (300)	8	15160 (400)	8	

(1) Helium-rich DA an equally valid possibility; (2) very faint H lines, difficult to fit in any cases; (3) could also be a DAB; (4) also in Limoges & Bergeron (2010); (5) average photometric match; (6) weakly magnetic also a possibility, good photometric fit to a single star; (7) cores of the Hα and Hβ lines poorly fitted.

All 35 binary systems listed in Table 4.3 represent new discoveries, with the exception of J034229.97+002417.6 (also known as KUV 03399+0015) first identified as a DA+DB system by Limoges & Bergeron (2010) as part of their spectroscopic analysis of the white dwarfs found in the Kiso survey. Our findings suggest that $\sim$1% of all white dwarfs are in compact DA+DB/DC double degenerate systems. We note, however, that a binary system containing a fairly hot DB component is likely to be classified as a DBA star in the DR4, and not be included in our analysis. The mean $\log g$ value for the 20 DA components for which the surface gravity could be constrained is $\langle \log g \rangle = 8.12$. Since most of these DA stars are in the range of effective temperature where the high-$\log g$ problem is observed ($T_{\rm eff} \lesssim 13,000$ K), this average value thus appears entirely consistent with that of single DA stars. The mean surface gravity for the 10 DB components is $\langle \log g \rangle = 8.21$, a value significantly larger than that of DA stars. This is perhaps not surprising since DB stars with $T_{\rm eff} \lesssim 15,000$ K (7 out of 10 DB components in Table 4.3) have a tendency to have spectroscopic $\log g$ values larger than average (see, e.g., Beauchamp et al. 1996; Kepler et al. 2007).

We have also considered the alternative possibility that our composite systems are single DAB stars. By computing a grid of DAB model spectra with a homogeneous composition, and using the same physics as that discussed above for the DA and DB models, we find that in all but one case, the spectroscopic and photometric fits are less satisfactory than for the DA+DB composite fits. This is not surprising since for a DAB star, we expect a good match between $T_{\rm phot}$ and $T_{\rm spec}$, similar to a single DA star, but most of our DA+DB binary candidates appear as outliers in Figure 4.8. The only object for which we could not clearly distinguish between a DA+DB and a DAB solution is J015221.12−003037.3, displayed in Figure 4.13.

For a few additional objects (see, e.g., J084742.22+000647.6, J084958.32+093847.7 and J093432.66+065848.6), the core of the lower Balmer lines (especially Hα and Hβ) is poorly reproduced by the models, despite a good overall spectroscopic fit and a decent match to the observed photometry. One possible solution to this problem is that the DB component might actually be a DBA star. The DBA subtype is common enough to suggest that a few of them should be hiding in our sample, and at least one DA+DBA composite system has previously been identified in the MCT survey (Wesemael et al. 1994). Due to higher atmospheric pressures

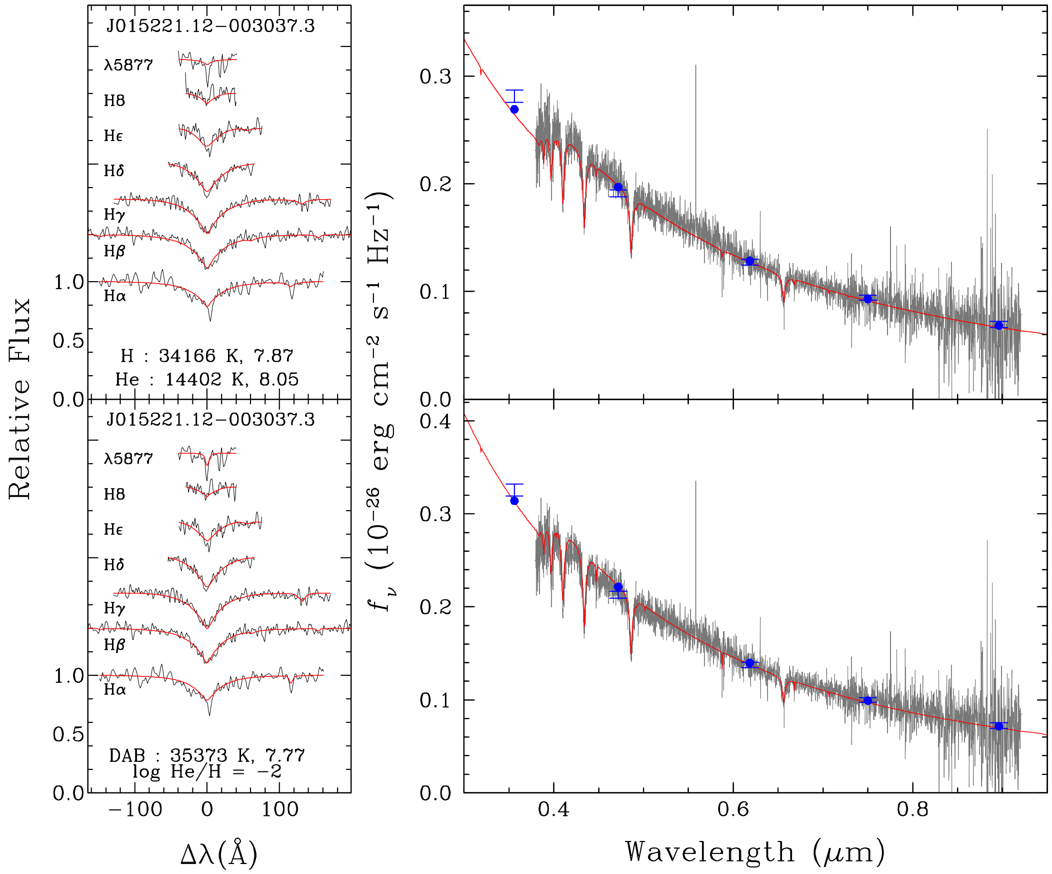

FIGURE 4.13 – Top: our DA+DB solution for J015221.12−003037.3. The left panel shows our best spectroscopic fit reproduced from Figure 4.10, while the right panel shows the superposition of the observed and predicted photometry (only the scaling factor is adjusted here) using the same presentation format as previous figures. Bottom: our DAB homogeneous solution for the same object. The left panel shows our spectroscopic fit with an *assumed* helium abundance of He/H $= 10^{-2}$. Again, the right side represents a superposition of the observed and predicted photometry using the spectroscopic atmospheric parameters.

in DBA stars compared to DA stars, the hydrogen lines will be more quenched, or in other words, Hα and Hβ are expected to be much stronger than the higher Balmer lines. Hence, a DA+DBA composite system will first be identified from unusually large equivalent widths of the lower Balmer lines. We confirm, in Figure 4.14, that the use of a grid of DBA models (with fixed H/He $= 10^{-3}$ abundances) can slightly improve the quality of the spectroscopic fits for the three objects mentioned above. The addition of a free parameter — the hydrogen abundance in the DBA star — could be used to improve the fits. However, it is not easy to constrain, and we postpone any determination of this parameter until independent, higher S/N observations are secured.

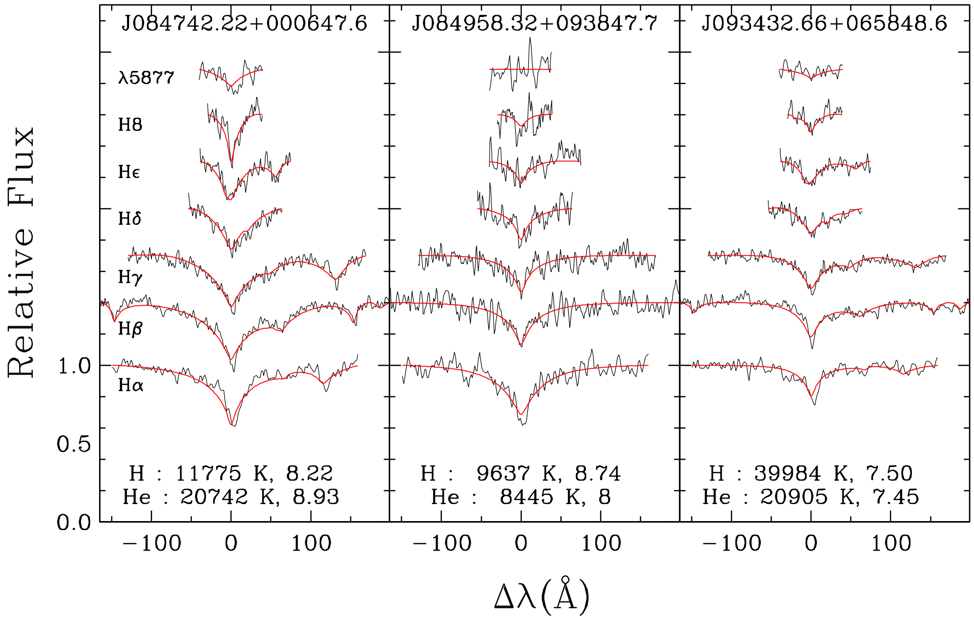

FIGURE 4.14 – Same as Figure 4.10 for three objects but with an *assumed* hydrogen abundance of H/He $= 10^{-3}$ for the helium-rich components.

We find that cool, weakly magnetic white dwarfs, especially at low S/N, often resemble DA+DC degenerate binaries since their lines appear broader and weaker compared to non-magnetic DA stars. The photometric fits of these magnetic stars are generally good, but a discrepancy between the photometric and spectroscopic temperatures is also present, obviously due to the fact that our non-magnetic models fail to reproduce the observed spectrum. The presence of Zeeman-split line cores can, in such cases, confirm the magnetic interpretation. However, there is one published magnetic star candidate (J231951.72+010909.0; Vanlandingham et al. 2005) which could easily fool our fitting procedure, since the Zeeman splitting is not apparent, and the *diluted* Balmer lines can be fitted almost perfectly with a DA+DC composite, although with a poor photometric match. We have thus been cautious to inspect every object that was initially flagged as a possible DA+DC composite, and were able to eliminate six DA stars that are more likely to be weakly magnetic stars rather than binaries

(J075842.68+365731.6, J132340.34+003338.7, J133007.57+104830.5, J144244.18+002714.8, J150856.93+013557.0 and J224444.62+130521.5). All these objects indeed show hints of triple or enlarged cores, and good photometric fits can be achieved with single star models. We also identify nine DA+DC candidates in Table 4.3, where the presence of a weak magnetic field remains a valid option. In conclusion, it is now clear that better S/N observations are needed to properly identify DA+DC candidates.

Many binary candidates in our sample show very weak hydrogen lines superposed on an otherwise flat spectrum, where the DC star is obviously the hotter and more luminous component of the system. These objects could alternatively be interpreted as single helium-rich DA stars with only small traces of hydrogen in their atmospheres. In principle, however, such stars could be differentiated from degenerate binaries since the hydrogen lines in a helium-dominated atmosphere would be heavily quenched by the high photospheric pressure, with only Hα and Hβ visible in their spectrum. In contrast, most hydrogen lines in the Balmer series will be detectable in the spectrum of a lower pressure $T_{\rm eff} \sim 7000$ K DA atmosphere, diluted by a $T_{\rm eff} \sim 10,000$ K DC[8]. Unfortunately, both scenarios predict hydrogen lines that are extremely weak and difficult to detect unambiguously at low S/N. We attempted to fit all our binary candidates with a grid of mixed hydrogen and helium models and we find that in eight cases, the fits are equally as good as the binary fits. The reason is that the S/N is too low to detect the higher Balmer lines even if they were present.

To conclude this section, we are fairly confident that we have correctly identified nine DA+DB degenerate binaries in the SDSS-E06 sample, since the quality of the fits as well as the comparison between the observed and predicted photometry clearly rules out the possibility of a single DAB star. The picture is less obvious for our DA+DC binary candidates (and one possible DAB star) but we are still confident that most of the candidates listed in Table 4.3 are indeed degenerate binaries. Further monitoring of these stars, such as radial velocity measurements, will be required to confirm their binary nature. Incidentally, all SDSS spectra are in fact taken in three or more exposures, generally in the same night, to facilitate cosmic ray rejection. Badenes et al. (2009) used these individual exposures to look for large radial

---

[8] We note that the shape of Hα is a poor diagnostic, since the dilution by a DC produces an *apparent* broadening similar to the real enhanced broadening of a dense helium-rich atmosphere.

velocity shifts (120 km s^{-1} or more) and found one such object. There are 25 of our binary candidates that were also examined as part of their SWARMS survey (C. Badenes 2010, private communication). In most cases, no obvious radial velocity shifts can be detected. For J002322.44+150011.6, however, a strong cross correlation is observed between individual exposures and there is a hint of a large velocity shift although the lines are very weak. 8-meter class telescopes will obviously be needed to achieve good radial velocity measurements for our faint candidates.

4.4.5 Helium-Rich DA White Dwarfs

Bergeron et al. (1991) were the first to show on a quantitative basis that the pressure effects produced on the hydrogen lines in a cool ($T_{\rm eff} \lesssim 12,000$ K) DA star with a high surface gravity could not be distinguished from those produced by the presence of large amounts of helium. The authors also suggested that the higher than average $\log g$ values inferred from spectroscopic analyses of cool DA stars could be the result of the presence of helium brought to the surface by convective mixing. But the non-detection of He I lines in high-resolution Keck observations of cool DA stars by Tremblay et al. (2010) ruled out the systematic presence of helium in these atmospheres. However, there are rare white dwarfs, such as GD 362 and HS 0146+1847, that were interpreted as massive DA stars, but the detection of the weak He I λ5877 line in high-resolution spectroscopic data suggested instead that these stars had normal masses with helium dominated atmospheres (Koester et al. 2005; Zuckerman et al. 2007). Both of these white dwarfs are DAZ stars with circumstellar disks, and the source of hydrogen and metals in these helium-dominated atmospheres is likely due to accretion from a water-rich asteroid (Jura et al. 2009).

Broad and shallow Hα features are also observed in cool white dwarfs, indicative of a trace of hydrogen (H/He $\sim 10^{-3}$) in a helium-dominated atmosphere (see, e.g., Fig. 12 of Bergeron et al. 2001). The hottest of these objects is the DZA white dwarf Ross 640 at $T_{\rm eff} \sim 8500$ K. While no circumstellar disk has been reported for this object, the simultaneous presence of metals in its spectrum again suggests an external source for hydrogen. Alternatively, the presence of mixed H/He compositions could be the result of the mixing of the thin superficial hydrogen atmosphere with the deeper and more massive helium convection zone (Tremblay & Bergeron 2008). White dwarfs with mixed atmospheric compositions become increasingly common at even cooler temperatures ($T_{\rm eff} \lesssim 6000$ K) where they can be easily identified from their strong infrared flux deficiency due to collision-induced absorption by molecular hydrogen (Kilic et al. 2010).

We identified in our SDSS sample two cool and massive DA white dwarfs, J090150.74+091211.3 and J170204.81+593635.5, that we believe are probably helium-rich objects. These stars were initially flagged as 2σ outliers in the $T_{\rm phot}$ vs. $T_{\rm spec}$ diagram shown in Figure 4.8, but we were unable to fit them with binary models. In both cases, the photometric temperature was significantly larger than the spectroscopic value (by 23% and 37%, respectively), and the $\log g$ value was unusually high (9.89 and 9.66, respectively). In Figure 4.15, we present our best fits assuming helium-rich compositions. Because of the degeneracy between surface gravity and helium abundance, we simply assume here a value of $\log g = 8$. For the photometric fits, both the surface gravity and the hydrogen abundance are fixed, the latter set at the spectroscopic value. We can see that the spectroscopic and photometric temperatures are now in agreement to within ∼10%, which shows that by relying on *ugriz* observations, one can partially break the degeneracy between extremely high $\log g$ stars and normal mass helium-rich objects.

The first object in Figure 4.15, J170204.81+593635.5, is also a DAZ white dwarf with the obvious Ca II λ3969 blended with Hϵ. It appears like a cooler counterpart of GD 362 and HS 0146+1847, although with significantly smaller metal abundances. It would be interesting to confirm if the simultaneous presence of hydrogen and metals in the photosphere of this star could be explained by the existence of a circumstellar disk. The second object shown in Figure 4.15, J090150.74+091211.3, is even cooler at $T_{\rm eff} \sim 8500$ K, and is similar to Ross 640 in terms of temperature and hydrogen abundance, even though no metal lines are detected in the spectrum of this object. These helium-rich white dwarf candidates are also interesting because they bridge the temperature gap between DAZ white dwarfs like GD 362 and Ross 640. Obviously, higher S/N spectroscopic observations and trigonometric parallax measurements would help to confirm our interpretation of these stars, although these measurements for such faint ($g \sim 18.5$) objects are admittedly difficult to secure.

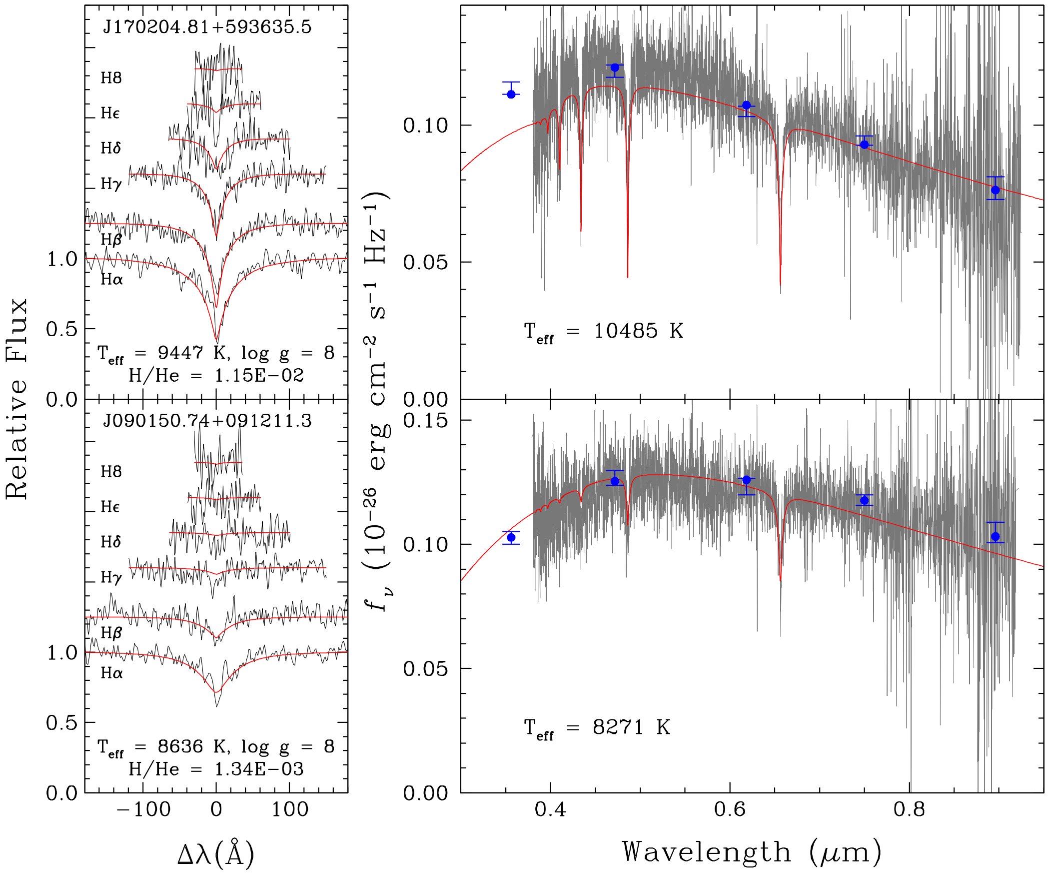

FIGURE 4.15 – Left panels: our best fits to two DA stars with mixed H/He model atmospheres; a value of $\log g = 8$ is assumed in both cases. The atmospheric parameters are given in each panel. Both the predicted and observed spectra have been binned by a factor of two for clarity. Right panels: our best photometric fits for the same objects assuming a value of $\log g = 8$ and H/He abundances determined from the spectroscopic fits. Both the fluxed spectra (in gray) and synthetic model fluxes (in red), calculated at the spectroscopic parameters given in the left panel, are then scaled to the r photometric band.

4.5 Discussion

4.5.1 Reappraisal of Previous Analyses of the SDSS Data Release 4

Prior to this work, individual atmospheric parameters for most stars in the DR4 catalog could only be found in the original Eisenstein et al. (2006a) paper. These authors were careful to define the largest white dwarf sample ever identified so far, but their spectroscopic analysis was preliminary, and as emphasized by the authors, their `autofit` program was only designed to offer a first-pass estimate of temperatures and surface gravities and to flag outliers. Also, most spectroscopic fits were not visually and individually inspected, unlike in our analysis. The model atmospheres between both analyses differ as well. In particular, our models rely on improved Stark broadening profiles and we also account for NLTE effects at high temperatures. Our atmospheric parameters should thus represent a significant improvement over previous estimates, especially given the latest improved DR7 data reduction (Kleinman et al. 2009).

In Figure 4.16, we compare our atmospheric parameters with those obtained by Eisenstein et al. (2006a). The agreement is surprisingly good considering the differences in the data reduction, model spectra, and fitting procedures. We find very few outliers, which implies that both fitting techniques are robust, the main exception being the DA−M dwarf binaries, although Eisenstein et al. stress that their atmospheric parameters are appropriate only if the spectral classification is DA or DB, without other subtle variations. We note that our surface gravities are significantly lower at cool temperatures ($T_{\rm eff} \lesssim 8500$ K, by as much as 1 dex), most likely due to the fact that the models used by Eisenstein et al. only include Stark and Doppler broadening (see also Section 2 of Kepler et al. 2007 where similar models are used), while our models also take into account neutral broadening. Finally, most subtypes identified here are identical to those reported in Eisenstein et al. In addition to the double degenerate candidates reported in Table 4.3, there are 36 objects in Table 4.1 for which our classification differs from that of Eisenstein et al. Most of them have faint or questionable features (Zeeman splitting, M−Dwarf contamination and He II or Ca lines) and our different classifications might only result from different thresholds in the detection of these features. We thus conclude that the `autofit` program and method of analysis employed by Eisenstein et al. are reasonable, except that a more careful visual inspection would identify additional subtypes and problematic observations, which is an essential step in determining individual parameters for these stars, and to compute accurate mean values for the sample.

The second important study of the DA stars in the DR4 is that of Kepler et al. (2007) who went further and mainly focused on the mass distribution of the sample, neglecting subtypes (DA−M dwarf binaries, magnetics, DAZ, and DAB stars), as we did in Section 4.3.2. They used a more extensive model grid than that of Eisenstein et al. (2006a), but the

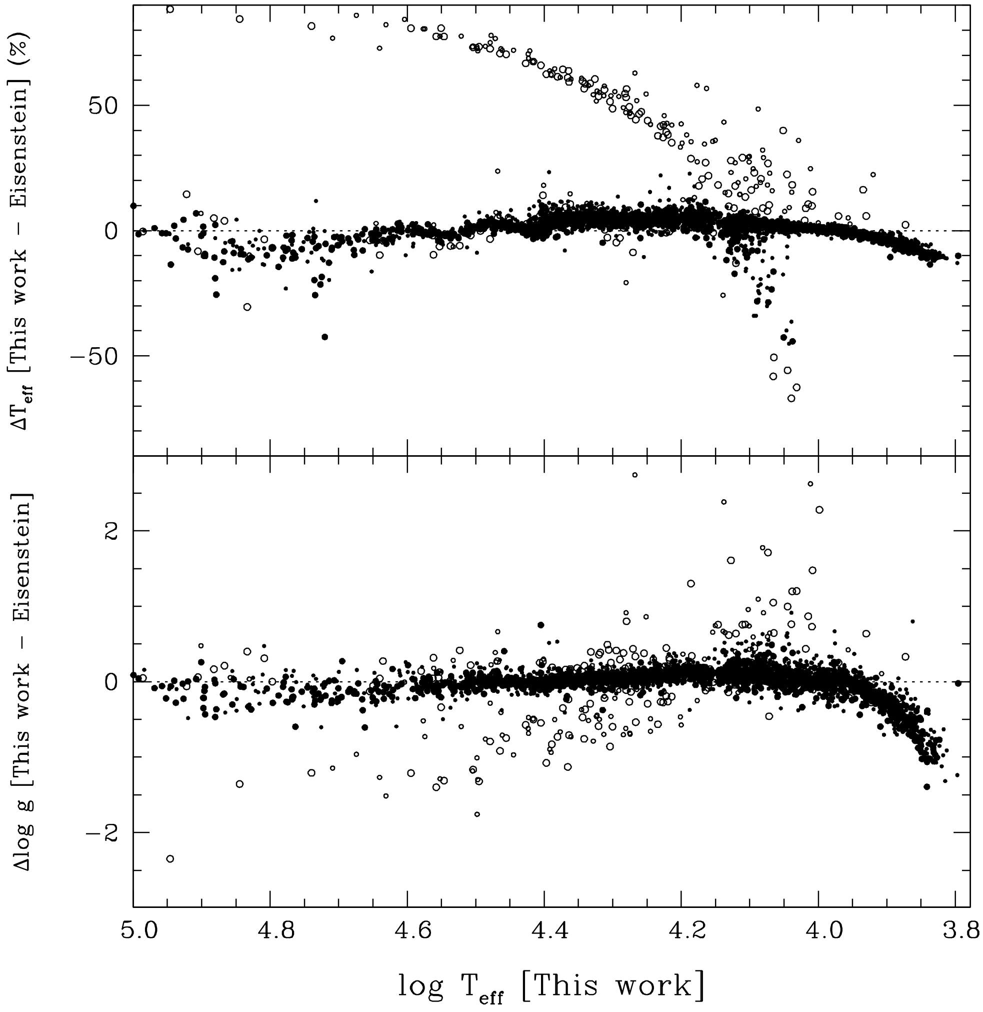

FIGURE 4.16 – Comparison of atmospheric parameters, $T_{\rm eff}$ and $\log g$, between our analysis and that of Eisenstein et al. (2006a). The open circles represent DA−M dwarf binaries, while smaller symbols indicate spectra with $20 > {\rm S/N} > 12$. We note that the model grid used by Eisenstein et al. is limited to $\log g < 9$, hence some of the discrepancies observed here result from this shortcoming.

physics included in these models is similar. Even though Kepler et al. argue that the fits at low effective temperatures cannot be trusted since this corresponds to the temperature range where the high-$\log g$ problem is encountered, we believe that a proper understanding of this problem begins with the best achievable analysis of these cool DA stars. Furthermore, it is not explicitly stated in Kepler et al. (2007) whether individual fits were visually examined in order to define a clean sample of single white dwarfs.

The optimal way of comparing our mean mass determination to that of Kepler et al. (2007) would be to start with a 1:1 study of individual objects, to evaluate the differences in the models and sample selections, as noted above, and also in the fitting procedures[9]. Unfortunately, since individual atmospheric parameters were not published in their work, a detailed comparison is not possible here, and only average values can be compared. We note that Kepler et al. still give the atmospheric parameters of some low-mass and high-mass outliers identified in their mass distribution, a discussion we postpone to Section 4.4.5.

We recomputed the mean mass of our sample in the range 100,000 K $> T_{\rm eff} > 12,000$ K, i.e. the same range of temperature used by Kepler et al. (2007), and we find the same value as before, $\langle M \rangle = 0.61\ M_\odot$, which can be compared to the value reported by Kepler et al., $\langle M \rangle = 0.59\ M_\odot$. This small difference is entirely consistent with the shift produced by the use of our improved Stark profiles, and it is comparable to the shift observed for the PG sample (Tremblay & Bergeron 2009) where we found a significantly higher mean mass (by ~5%) compared to calculations with older models. This suggests that the effects of using different model spectra, data reductions, sample selections, and fitting techniques, are small, after all.

4.5.2 Comparison with Bright DA White Dwarfs

We now compare our results for the DA stars in the SDSS with the ongoing spectroscopic survey of bright ($V \lesssim 17$) DA white dwarfs of Gianninas et al. (2011) drawn from the Villanova White Dwarf Catalog (McCook & Sion 1999). The obvious advantage of this comparison is that we are using the same model atmospheres and fitting technique in both analyses, and therefore any disparity can be attributed to differences in the sets of observations only. Unlike the SDSS spectra, however, the wavelength coverage used in the Gianninas et al. survey does not extend to Hα. We thus repeated our analysis of the SDSS spectra without including Hα

---

[9] Kepler et al.'s fitting method includes the full spectrophotometric spectra, which they argue provides the lowest internal uncertainties. One should be cautious, however, with external uncertainties stemming from data reduction, such as those presented in Figure 4.4 (bottom panel) and discussed in Section 4.3.1. While we do not claim that our fitting method is better, we suggest that it is equivalent, and more easily comparable to other DA surveys, which rely on an approach similar to ours.

in our fitting procedure, and found nearly identical results. We can therefore safely compare the results between both surveys without further ado.

We find 89 stars in common between both surveys. These correspond of course to the brightest DA stars in the SDSS, which were already known prior to that survey. The comparison between both sets of atmospheric parameters is displayed in Figure 4.17. We can see that the SDSS temperatures are systematically larger by about 2%, on average, in the range 40,000 $> T_{\rm eff} >$ 13,000 K, than those obtained using the Gianninas et al. spectra, while the $\log g$ values are lower by about 0.06 dex, on average, in the same range of temperature, with differences increasing at higher effective temperatures. As mentioned above, since we are using the same theoretical framework and fitting method, these differences can only be attributed to the use of different spectra.

We compare in Table 4.4 the values of the mean mass, the standard deviation, as well as the median mass for the SDSS sample, the Gianninas et al. sample, and the PG sample (Liebert et al. 2005); note that the PG sample is a subset of the Gianninas et al. sample. The mean mass is quite sensitive to the number of low-mass and high-mass outliers in each sample, while the median mass is more closely related to the peak value of the mass distribution. For internal consistency, we use the same range of effective temperatures to determine the average properties of each sample. We also remove all magnetic stars, double degenerates, and DA−M dwarf composite systems. We should mention that the PG sample has already been analyzed in Tremblay & Bergeron (2009) but the values reported here differ slightly from those published as a result of three minor improvements in our analysis: the addition of the nonideal electronic perturbations in the equation of state (see Section 4.2.2), our slightly different line normalization technique (see Section 4.2.3), and our exclusion of DA subtypes, which all contribute to lower the mean mass.

TABLE 4.4 – Mean Properties of DA White Dwarf Samples

Sample	$\langle M/M_\odot \rangle$	Dispersion	Median Mass	Sample Description
SDSS	0.613	0.126	0.594	Eisenstein et al. (2006a)
Palomar-Green	0.629	0.128	0.610	Liebert et al. (2005)
White Dwarf Catalog	0.638	0.143	0.610	Gianninas et al. (2009)

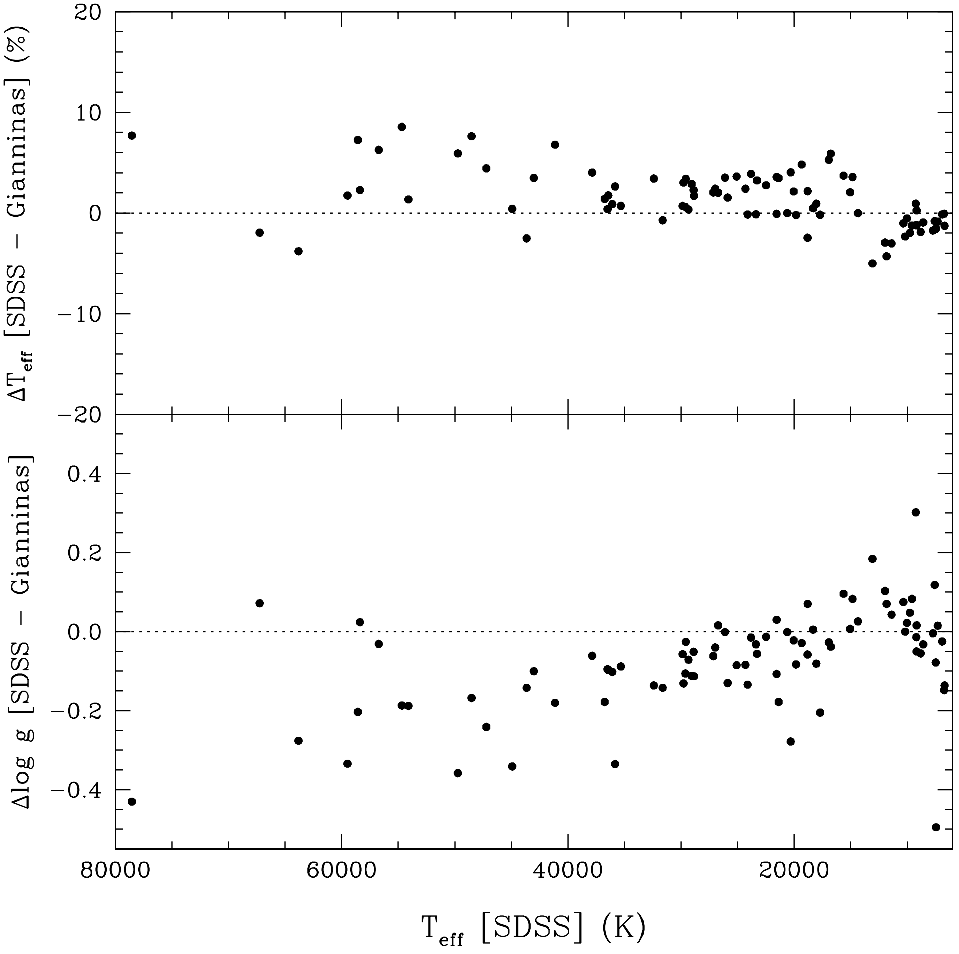

FIGURE 4.17 – Top panel: effective temperature differences (in %) for the 89 DA stars in common between the SDSS and Gianninas et al. samples. The observed spectra have been analyzed with the same models and fitting technique discussed in Section 4.4.2. The horizontal line represents a perfect match. Bottom panel: similar to the top panel but for differences in $\log g$ values.

We first notice that the values of the mean mass and standard deviation for the Gianninas et al. sample are slightly larger than the PG sample, although their median masses are nearly identical. This suggests that there are a bit more high-mass outliers in the Gianninas et al. sample, which is not surprising since the Villanova White Dwarf Catalog contains a large number of massive white dwarfs detected in X-ray surveys (see, e.g., Vennes 1999). Therefore, we feel it is more appropriate, in what follows, to restrict our comparison to median values only.

The results presented in Table 4.4 indicate that the median mass of the SDSS sample is about 0.02 $M_{\odot}$ lower than the PG and Gianninas et al. samples (corresponding to a $\log g$ value ~0.04 dex lower). This difference is of course consistent with the results shown in the bottom panel of Figure 4.17, which compares $\log g$ values for objects in common between SDSS and Gianninas et al. We must then conclude that the differences in the median values are mostly likely due to problems in the data reduction rather than to selection effects. Since the Gianninas et al. sample includes white dwarf spectra secured over many years using various telescopes and instruments, systematic data reduction effects are less likely to be present. Furthermore, problems with the calibration of the SDSS spectra have been known to exist in the first few data releases (Kleinman et al. 2004; Eisenstein et al. 2006a). Even though these are believed to have been fixed in the new Data Release 7 (Kleinman et al. 2009), we suggest here that a small (~3%) but systematic calibration problem may still remain. As discussed in Section 4.3.3, a systematic shift in the spectroscopic temperatures could also explain part of the problem observed in the comparison with photometric temperatures.

Another way to look at this problem is to compare the mass distribution as a function of effective temperature for both the SDSS and Gianninas et al. samples, as shown in Figure 4.18. We first notice that the number of high-mass outliers is larger in the Gianninas et al. sample due to the selection effects discussed above; the most massive white dwarfs in this distribution are actually ROSAT objects. We thus prefer to focus our attention on the peak of the distributions; lines of constant mass at 0.55 $M_{\odot}$ and 0.70 $M_{\odot}$ have been included in Figure 4.18 to guide the eye. It is obvious that there is a systematic offset between both distributions. The mass values in the SDSS increase from the hot end of the sequence down to about 12,500 K, while they remain more uniformly distributed around the mean in the Gianninas et al. sample. We note that the Gianninas et al. distribution was shown to be more uniform (Tremblay et al. 2010) when using the improved model spectra from Tremblay & Bergeron (2009). These results reinforce our conclusions that a problem with the calibration of the SDSS spectra still exists, even in the latest data release.

We finish this section with a short discussion of the cool end ($T_{\rm eff} \lesssim 13,000$ K) of the mass

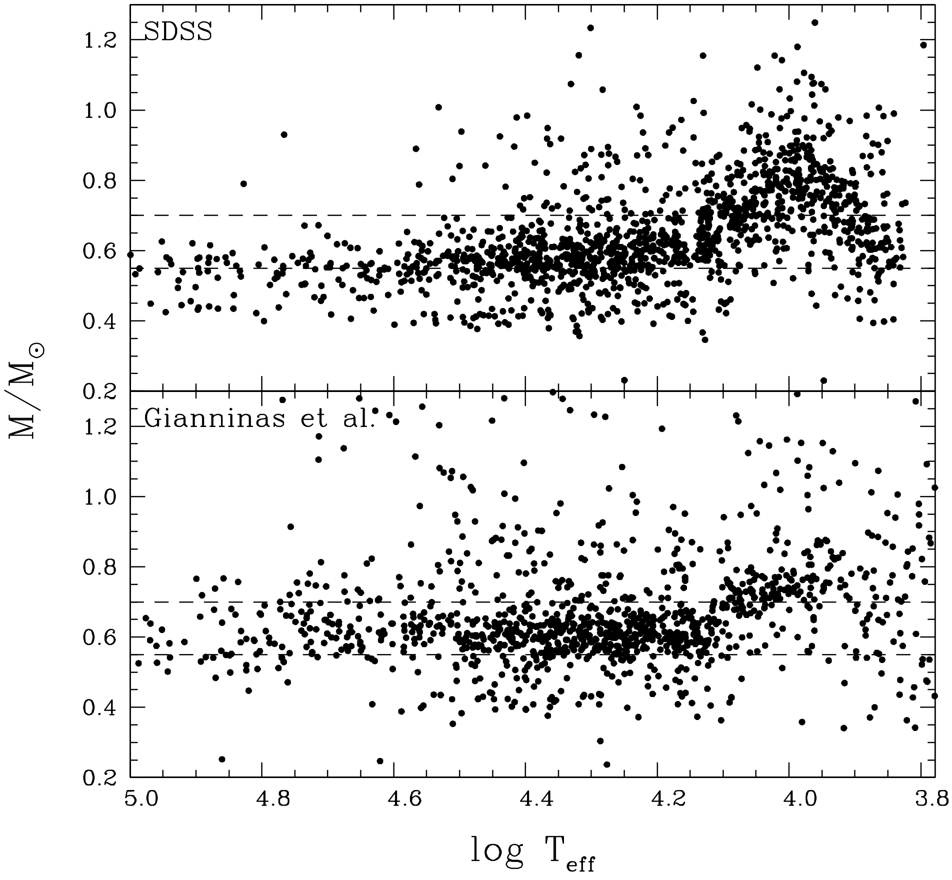

FIGURE 4.18 – Mass distributions as a function of $T_{\rm eff}$ for the SDSS sample (top panel) and the Gianninas et al. sample (bottom panel). Lines of constant mass at 0.55 $M_\odot$ and 0.70 $M_\odot$ are shown as a reference.

distribution shown in the top panel of Figure 4.18, where close to half of the SDSS stars are located. We can clearly see an important increase in the mean mass in this particular range of temperature, which corresponds to the well known high-log g problem discussed at length by Koester et al. (2009a) and Tremblay et al. (2010). These unrealistic mass values prevent us from going much further in the analysis of these cool DA stars, but the mass distribution can prove itself useful in better understanding the nature of this problem. To better illustrate the shift in the mean mass, we average in Figure 4.19 the distribution into temperature bins of 1000 K, and compute the corresponding mass standard deviation. We observe that the SDSS mass distribution exhibits an important and distinct triangular bump, with the mass dispersion remaining fairly small and constant as a function of temperature, even down to the very cool end of the distribution. The fact that the mean mass appears to *decrease* again below 10,000 K should be viewed with caution, however, since our model atmosphere calculations include a free parameter in the treatment of the nonideal effects from neutral particles, which allows some extra leverage to "calibrate" the $\log g$ values (see Section 5.1 of Tremblay et al. 2010). The SDSS sample definitely provides the clearest picture so far of the high-$\log g$ problem, and it will certainly be helpful in future investigations of this problem.

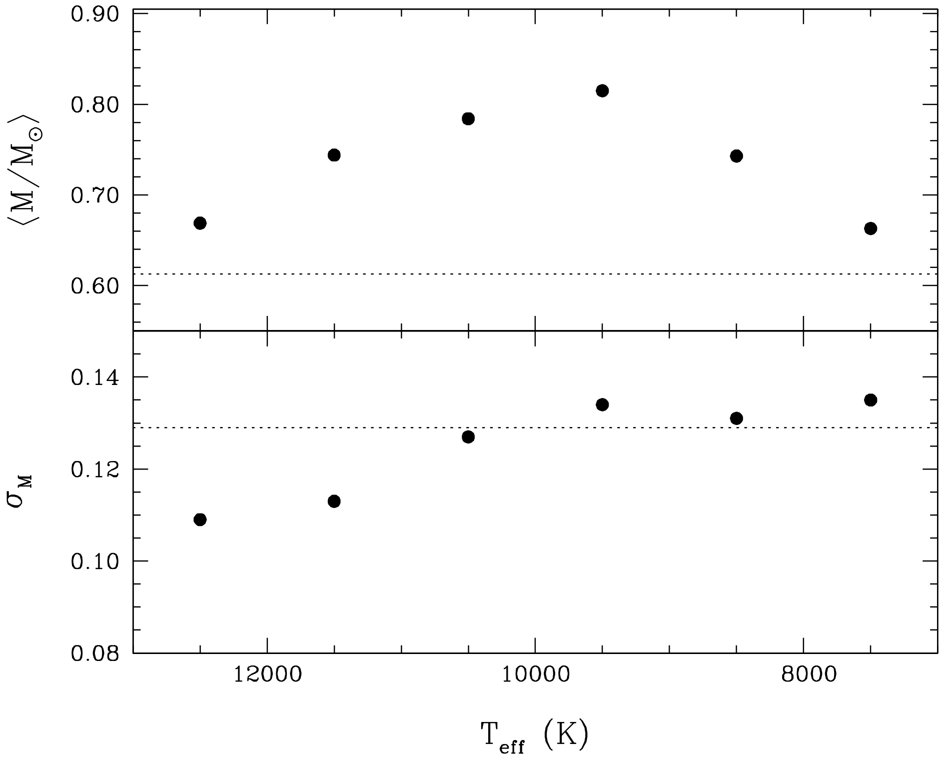

FIGURE 4.19 – Top panel: mean mass of the SDSS sample for $T_{\rm eff} < 13,000$ K computed in 1000 K temperature bins. The dotted line is the mean mass obtained from Figure 4.7 for hotter objects. Bottom panel: similar to the top panel but for the mass standard deviation.

4.5.3 Hot DA and DAO White Dwarfs

We have postponed our discussion of the 184 hot DA stars ($T_{\rm eff} > 40,000$ K) until now due to the few extra steps needed to analyze these objects. First of all, we uncovered 17 hot DAO stars in the SDSS-E06 catalog, characterized by the He II λ4686 absorption line. All but two of these objects were previously classified as DAO in the SDSS-E06 (the DAO J130815.21−015904.4 and DAO+dM J094720.94+111734.7 were identified as DA and DA+dM, respectively). We observe the so-called Balmer-line problem (see Gianninas et al. 2010, and references therein) in all of these DAO stars, but also in many of our hot DA stars, especially at Hα and Hβ. This problem manifests itself as an inability of the model spectra to reproduce simultaneously all Balmer line profiles. A solution to the Balmer-line problem was presented by Werner (1996) when they included carbon, nitrogen, and oxygen (CNO) – with proper Stark broadening – in their model atmospheres. The main effect is a cooling of the upper layers of the atmospheres, the formation region of the core of the lower Balmer lines. These improved models are shown to provide much better fits to the observed line profiles. More reliable atmospheric parameters are then obtained, even if the CNO metals are merely a proxy for all metals in the atmosphere and it is by no means a determination of the CNO abundances. The 15 DAO stars identified in the SDSS-E06 have already been analyzed with mixed H/He models by Hügelmeyer et al. (2007)[10] but without metals included in the model calculations to account for the Balmer-line problem.

We rely upon the NLTE model atmospheres with homogeneous H/He/CNO compositions introduced by Gianninas et al. (2010) to fit the DAO stars in our SDSS sample. These models, computed with TLUSTY and using improved Stark broadening from Tremblay & Bergeron (2009), are similar to the pure hydrogen models presented in Section 4.2.2 except for their chemical compositions. The CNO metal abundances are fixed at the Asplund et al. (2005) solar values. Our fitting procedure is very similar to the one previously described in this work, except that we also fit the helium abundance based on the profile of He II λ4686. The improved atmospheric parameters for 16 DAO stars are presented in Table 4.5. The DAO−dM composite system J094720.94+111734.7 is instead fitted with regular DA models since the Hα and Hβ lines are contaminated by the M dwarf, and the parameters are given in Table 4.1. We also find that 27 hot DA stars in SDSS show the Balmer-line problem (DA+BP). We fitted these objects with the H/CNO models also discussed in Gianninas et al. (2010); the atmospheric

---

[10] Their sample also includes J163200.32−001928.3, clearly a DAO star but identified as a DO in the SDSS-E06 catalog, hence it was not selected in this work.

parameters are reported in Table 4.1 (see Note 6). The Balmer-line problem is resolved for the majority of the 43 DAO and DA+BP objects fitted with CNO models. Also, the fits without CNO tend to underestimate surface gravities by ∼0.1-0.2 dex (see also Gianninas et al. 2010 for more details), hence the effects are important on the properties of the hot end of the SDSS mass distribution.

The size of our sample of hot DA white dwarfs is similar to that of Gianninas et al. (2010), who analyzed 152 DA stars above $T_{\rm eff} > 40,000$ K. The fraction of objects showing the Balmer line problem is roughly the same, suggesting that this discrepancy can be efficiently detected even at the lower average S/N of the SDSS sample. The additional diagnostic that can be performed with Hα in the SDSS helps in identifying the Balmer-line problem at lower S/N. In the course of our visual inspection, however, it was obvious that only extreme DA+BP could be detected for some objects with S/N $<$ 20. The atmospheric parameters of hot DA stars below this threshold should therefore be viewed as a pure hydrogen approximation.

In Figure 4.18, both the SDSS and Gianninas et al. mass distributions include the improved atmospheric parameters of objects fitted with H/He/CNO models. We find a mean mass of $\langle M \rangle = 0.54\ M_\odot$ for our SDSS hot DA sample, which is significantly lower than mean mass identified for cooler stars. This is expected, however, considering that the data reduction problem identified in the previous section is worse at the hot end of the distribution (see Figures 4.17 and 4.18). For the DAO stars, we obtain a mean mass of $\langle M \rangle = 0.52\ M_\odot$, a value very similar to the hot DAs, which further confirms the suggestion of Gianninas et al. (2010) that the DA and DAO share a common history. If we make abstraction of the reduction problem, it is very interesting to note that in both the SDSS and Gianninas et al. surveys, the hot end of the mass distribution is a smooth continuation of the sequence at cooler temperatures. This result is a direct consequence of the new models computed in Gianninas et al. (2010), including NLTE effects, CNO metals (for a majority of stars at $\log T_{\rm eff} > 4.8$) and improved Stark broadened profiles.

TABLE 4.5 – SDSS DR4 Sample of DAO White Dwarfs with S/N > 12

SDSS name	Plate−MJD−Fiber	$T_{\rm eff}$ (K)	$\log g$	log He/H	$M/M_\odot$	M_V	$\log \tau$
J034831.33+004616.3	1242-52901-412	90730 (2980)	7.15 (0.11)	−2.12 (0.18)	0.54 (0.02)	6.76	4.78
J081618.79+034234.1	1184-52641-171	51740 (3550)	7.53 (0.30)	−1.06 (0.39)	0.51 (0.10)	8.30	6.31
J082705.53+313008.2	0932-52620-126	78550 (2280)	7.33 (0.08)	−2.41 (0.13)	0.54 (0.02)	7.35	5.38
J101015.59+115711.3	1745-53061-218	52500 (2820)	7.38 (0.27)	−0.68 (0.22)	0.47 (0.08)	8.00	6.02
J120927.93−030206.2	0332-52367-184	79530 (4870)	7.13 (0.16)	−1.95 (0.25)	0.50 (0.04)	6.91	4.93
J121743.11+623118.2	0779-52342-152	98170 (5220)	6.98 (0.20)	−1.19 (0.19)	0.53 (0.04)	6.26	4.35
J125029.51+505317.3	1279-52736-450	71660 (13240)	7.08 (0.40)	−1.03 (0.61)	0.46 (0.11)	6.98	5.04
J130815.21−015904.4	0340-51691-358	53040 (1480)	7.73 (0.10)	−2.49 (0.25)	0.58 (0.04)	8.64	6.31
J131925.92+531715.0	1040-52722-015	96320 (16210)	6.73 (0.53)	−1.19 (0.52)	0.48 (0.11)	5.73	3.33
J135356.88−025630.4	0914-52721-214	53290 (1890)	7.76 (0.13)	−2.15 (0.28)	0.59 (0.05)	8.68	6.30
J145606.73+491116.5	1048-52736-619	93050 (6230)	6.64 (0.18)	−1.15 (0.19)	0.45 (0.05)	5.61	3.78
J153102.39+534900.6[a]	0616-52442-320	78680 (7970)	6.85 (0.25)	−1.96 (0.40)	0.44 (0.06)	6.35	4.16
J160236.07+381950.5	1055-52761-473	84630 (5290)	7.03 (0.17)	−2.14 (0.28)	0.49 (0.04)	6.62	4.57
J161441.98+370548.1	1056-52764-546	55640 (1710)	7.66 (0.10)	−3.22 (0.34)	0.56 (0.04)	8.45	6.24
J170508.81+212019.2	1425-52913-570	50300 (1000)	7.67 (0.08)	−2.70 (0.24)	0.55 (0.03)	8.59	6.36
J235137.23+010844.2	0684-52523-370	89500 (8920)	7.56 (0.33)	−1.39 (0.40)	0.63 (0.09)	7.65	5.59

[a] Observational glitch.

4.5.4 White Dwarf–M Dwarf Binaries

We analyzed in our study a large number of DA−M dwarf binaries that are part of the DR4 sample. Their atmospheric parameters are given in Table 4.1, although these were not included in the calculations of the mean properties of the SDSS sample in order to define a cleaner sample of single DA stars. Most of these objects have already been analyzed in detail by Silvestri et al. (2006) and Heller et al. (2009), although both studies were not necessarily restricted to the DR4 sample. One of the reason is that the SDSS-E06 catalog was not meant to be complete in terms of the white dwarf−M dwarf binary content. The colors of these objects can be significantly different from those of single white dwarfs, especially when the total flux is dominated by the M dwarf (i.e., the colors are very red). In those cases, the object colors can be close to the low-mass end of the main-sequence stellar locus, and rejected by the cutoffs. In contrast, Silvestri et al. (2006) resorted to an algorithm to automatically identify spectral features of white dwarfs in all DR4 spectra in addition to the color selection. They claim that their sample comprises almost all spectroscopically observed DA−M dwarf in the SDSS up to Data Release 4.

The deconvolution technique developed by Heller et al. (2009) is the most sophisticated in terms of the determination of the atmospheric parameters of both the DA white dwarf and the main sequence companion. They fit simultaneously the effective temperature and surface gravity of both stars, as well as the metallicity of the M dwarf component. However, the precision on the white dwarf parameters is rather low, with uncertainties as large as 0.5 dex in $\log g$. This approach is not really convenient in the present context since we are mostly interested in the white dwarf component of the system. Silvestri et al. (2006) developed a more approximate method to fit the main sequence star by using a series of spectral templates with average atmospheric parameters. Then, by iteration, they subtracted the contribution of the M dwarf component until a clean white dwarf spectrum is obtained. This procedure has some flaws since it is not possible to completely remove all spectral features from the M dwarf companion, but it still allows a larger number of Balmer lines to be fitted in comparison with the contaminated spectrum.

We compare in Figure 4.20 our atmospheric parameters — determined by simply excluding from the χ^2 fit the Balmer lines that are contaminated by the M dwarf companion — with those of Silvestri et al. (2006). We find a very good agreement between both sets of measurements, especially considering the differences in the model atmospheres. Our values of $T_{\rm eff}$ and $\log g$ are slightly larger, on average, than those of Silvestri et al., but this small offset is entirely consistent with our use of the improved Stark profiles of Tremblay & Bergeron (2009). These comparisons are similar to those shown in Figure 4.16 for single stars, which suggests that our method for fitting DA−M dwarf binaries is fairly reasonable and comparable to that of Silvestri et al. There are also a few outliers observed in Figure 4.20, which are explained by the particular choice between the cool or hot solutions for the DA star. It is a more complicated choice when analyzing such systems, with any fitting method, but we believe our identifications are good since our model fluxes are well matched by the observed $u-g$ color index.

We finally show in Figure 4.21 the mass distribution of the DA−M dwarf binaries in our SDSS sample, which can be compared to that for single stars displayed in Figure 4.7. The average masses and the shape of both distributions are clearly different. It is perhaps not surprising that the high-mass tail is absent from the DA−M dwarf mass distribution since massive white dwarfs have smaller radii and are less luminous, and they can thus be easily overshadowed by their M dwarf companion. But even the peak of the mass distribution appears at a slightly lower value than for single stars, a conclusion that can also be reached by looking at Figure 6 of Silvestri et al. (2006). Given these selection effects, it is difficult to conclude whether the observed differences are real, another reason why we have refrained from including these white dwarfs in our computation of the average properties of DA stars.

4.5.5 Outstanding Objects

Several extreme low-mass and high-mass white dwarfs have been identified in the SDSS and these have been the subject of numerous studies, including that of Kepler et al. (2007, see their Section 7). We find that our improved line profiles do not affect significantly the results of these earlier analyses. The shift in $\log g$ of these extreme mass white dwarfs is comparable to that of typical DA stars. For example, we find a value of $\log g = 6.40$ for J123410.36−022802.8,

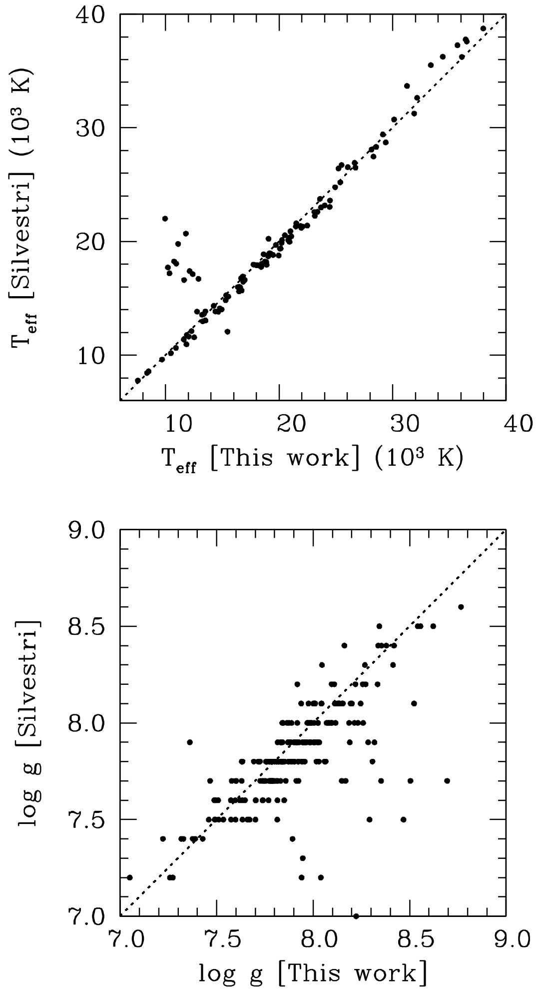

FIGURE 4.20 – Comparison of our $T_{\rm eff}$ and $\log g$ determinations with those of Silvestri et al. (2006) for the sample of DA−M dwarf binaries in the SDSS. The dashed line in each panel represents the 1:1 correspondence.

a value similar to that obtained by Liebert et al. (2004), $\log g = 6.38$, based on the same SDSS spectrum and a similar fitting method. This object was later reobserved by Kilic et al. (2007) at higher signal-to-noise ratio using the MMT, and we simply refer to their analysis for a determination of improved parameters for this star, as well as for other low-mass white dwarf candidates identified in the SDSS (see their Table 1).

For extreme high-mass white dwarfs close to the Chandrasekhar limit, the asymptotic relation between surface gravity and mass implies that a typical change in the value of $\log g$ will

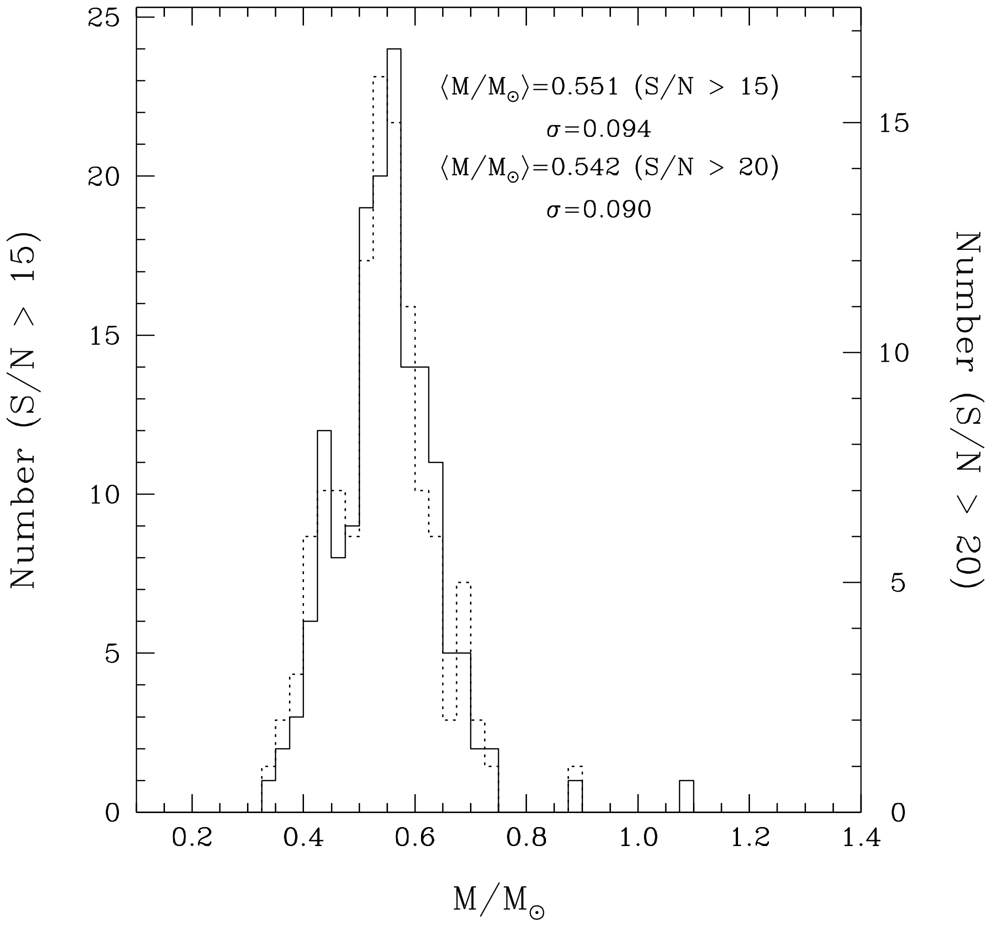

FIGURE 4.21 – Same as Figure 4.7 but for the mass distribution of our sample of DA−M dwarf binaries with a DA component in the range 40,000 K > $T_{\rm eff}$ > 13,000 K.

result only in a negligible change in mass. Therefore, we do not expect significant changes compared to published values. And as it turns out, our mass determinations for the most massive white dwarfs in our sample are in the same range as those reported in Table 6 of Kepler et al. (2007). We should note, however, that some of them have been flagged in our Table 4.1 as problematic observations (e.g., J155238.21+003910.3 and J110735.32+085924.5) and one should thus be cautious about their mass determinations. Furthermore, we suspect that some of the lower S/N candidates could be weakly magnetic stars. For instance, J154305.67+343223.6, identified in Table 6 of Kepler et al., is actually a magnetic white dwarf (Külebi et al. 2009).

We believe that in any case, higher S/N observations are required to properly constrain the mass of these stars (these objects are indeed extremely faint with $18 < g < 19$).

4.6 Conclusion

We presented an updated spectroscopic analysis of the DA white dwarfs identified in the SDSS Data Release 4 catalog of Eisenstein et al. (2006a), with the most recent data reduction from DR7, using our improved NLTE model grid including Stark profiles with non-ideal gas effects (Tremblay & Bergeron 2009; Tremblay et al. 2010). A careful visual inspection of each individual spectroscopic fit (S/N > 12), together with a comparison with *ugriz* photometric fits, allowed us to obtain a significantly cleaner sample and improved atmospheric parameters for these DA stars compared to previous studies.

We also performed a simulation of DA+DA and DA+DB/DC double degenerate binaries analyzed both photometrically and spectroscopically using single DA star models. We showed that DA+DA unresolved binaries could not be easily detected with the SDSS data, but that most DA+DB/DC systems would appear as outliers when comparing spectroscopic and photometric temperatures. Using this approach, we were able to identify 35 DA+DB/DC double degenerate candidates in the SDSS sample, most of them discussed for the first time in our analysis. We find, however, that it is rather difficult to confirm unambiguously our interpretation of the binary nature of DA+DC candidates at low S/N since these objects can easily be mistaken for magnetic white dwarfs or helium-rich DA stars.

We evaluated that a lower cutoff at S/N = 15 in the computation of the mean mass of DA white dwarfs provides the best statistical significance for these stars in the SDSS sample. Our calculations yielded a mean mass of 0.613 $M_\odot$ compared to a value 0.593 $M_\odot$ previously reported by Kepler et al. (2007). This difference is entirely consistent with the shift of $\sim$0.03 $M_\odot$ expected from our improved models. We also compared our results for bright DA stars in common between the SDSS survey and the Villanova White Dwarf Catalog sample of Gianninas et al. (2011) using the same grid of model atmospheres and fitting techniques. We unexpectedly found a mean mass for this subsample that is significantly higher (by $\sim$0.03 $M_\odot$)

in the Gianninas et al. survey. We concluded that a small problem with the data reduction still remains in the spectroscopic calibration of the SDSS Data Release 7.

Since no white dwarf survey is as large in volume as the SDSS, resolving this issue will be important to characterize the mass distribution of DA stars using SDSS data. This will also help in understanding the absolute temperature scale of DA white dwarfs, for which an offset is actually observed between spectroscopic and photometric temperatures. Inevitably, this work will also be beneficial as a guide for the analysis of new objects identified in the SDSS Data Release 7, which are likely to have properties very similar to those identified here.

We thank Carles Badenes, Vincent Cardin, and Audrey Maiuro for their contribution to this project. This work was supported by the NSERC Canada and by the Fund FQRNT (Québec).

4.7 References

Abazajian, K. N., et al. 2009, ApJS, 182, 543

Althaus, L. G., Serenelli, A. M., & Benvenuto, O. G. 2001, MNRAS, 323, 471

Asplund, M., Grevesse, N., & Sauval, A. J. 2005, in ASP Conf. Ser. 336, Cosmic Abundances as Records of Stellar Evolution and Nucleosynthesis, eds. T. G. Barnes III & F. N. Bash, (San Francisco: ASP), 25

Badenes, C., Mullally, F., Thompson, S. E., & Lupton, R. H. 2009, ApJ, 707, 971

Beauchamp, A., Wesemael, F., Bergeron, P., Liebert, J., & Saffer, R. A. 1996, in ASP Conf. Ser. Vol. 96, Hydrogen-Deficient Stars, ed. S. Jeffery & U. Heber (San Francisco: ASP), 295

Bergeron, P., Leggett, S. K., & Ruiz, M. T. 2001, ApJS, 133, 413

Bergeron, P., Saffer, R. A., & Liebert, J. 1992, ApJ, 394, 228

Bergeron, P., Wesemael, F., & Fontaine, G. 1991, ApJ, 367, 253

Bergeron, P., Wesemael, F., Lamontagne, R., Fontaine, G., Saffer, R. A., & Allard, N. F. 1995, ApJ, 449, 258

DeGennaro, S., von Hippel, T., Winget, D. E., Kepler, S. O., Nitta, A., Koester, D., & Althaus, L. 2008, AJ, 135, 1

Dufour, P., Liebert, J., Fontaine, G., & Behara, N. 2007, Nature, 450, 522

Eisenstein, D. J., et al. 2006, ApJS, 167, 40

Fontaine, G., Brassard, P., & Bergeron, P. 2001, PASP, 113, 409

Gianninas, A., Bergeron, P., Dupuis, J., & Ruiz, M. T. 2010, ApJ, 720, 581

Gianninas, A., Bergeron, P. & Fontaine, G. 2005, ApJ, 631, 1100

Gianninas, A., Bergeron, P., & Ruiz, M. T. 2009, Journal of Physics Conference Series, 172, 012021

Gianninas, A., Bergeron, P., & Ruiz, M. T. 2011, ApJ, in preparation

Hamada, T., & Salpeter, E. E. 1961, ApJ, 134, 683

Harris, H. C., et al. 2003, AJ, 126, 1023

Harris, H. C., et al. 2006, ApJ, 131, 571

Heller, R., Homeier, D., Dreizler, S., & Østensen, R. 2009, A&A, 496, 191

Holberg, J. B., & Bergeron, P. 2006, ApJ, 132, 1221

Hubeny, I., & Lanz, T. 1995, ApJ, 439, 875

Hügelmeyer, S. D., Dreizler, S., Rauch, T., & Krzesiński, J. 2007 in Proc. 15th European Workshop on White Dwarfs, eds. R. Napiwotzki & M. Burleigh (San Francisco: ASP), 372, 187

Hummer, D. G., & Mihalas, D. 1988, ApJ, 331, 794

Jura, M., Muno, M. P., Farihi, J., & Zuckerman, B. 2009, ApJ, 699, 1473

Kepler, S. O., Kleinman, S. J., Nitta, A., Koester, D., Castanheira, B. G., Giovannini, O., Costa, A. F. M., & Althaus, L. 2007, MNRAS, 375, 1315

Kilic, M., Allende Prieto, C., Brown, W. R., & Koester, D. 2007, ApJ, 660, 1451

Kilic, M., et al. 2010, ApJS, 190, 77

Kleinman, S. J., et al. 2004, ApJ, 607, 426

Kleinman, S. J., Nitta, A., & Koester, D. 2009, Journal of Physics Conference Series, 172, 012020

Koester, D., Kepler, S. O., Kleinman, S. J., & Nitta, A. 2009, Journal of Physics Conference Series, 172, 012006

Koester, D., Napiwotzki, R., Voss, B., Homeier, D., & Reimers, D. 2005, A&A, 439, 317

Külebi, B., Jordan, S., Euchner, F., Gänsicke, B. T., & Hirsch, H. 2009, A&A, 506, 1341

Lemke, M. 1997, A&AS, 122, 285

Liebert, J., Bergeron, P., Eisenstein, D., Harris, H. C., Kleinman, S. J., Nitta, A., & Krzesinski, J. 2004, ApJ, 606, L147

Liebert, J., Bergeron, P., & Holberg, J. B. 2005, ApJS, 156, 47

Liebert, J., Bergeron, P., & Saffer, R.A. 1991, in 7th European Workshop on White Dwarfs, NATO ASI Series, ed. G. Vauclair & E. M. Sion (Dordrecht: Kluwer Academic Publishers), 409

Limoges, M.-M., & Bergeron, P. 2010, ApJ, 714, 1037

McCook, G. P., & Sion, E. M. 1999, ApJS, 121, 1

Schmidt, G. D., et al. 2003, ApJ, 595, 1101

Silvestri, N. M., et al. 2006, AJ, 131, 1674

Tremblay, P.-E., & Bergeron, P. 2008, ApJ, 672, 1144

Tremblay, P.-E., & Bergeron, P. 2009, ApJ, 696, 1755

Tremblay, P.-E., Bergeron, P., Kalirai, J. S., & Gianninas, A. 2010, ApJ, 712, 1345

Vanlandingham, K. M., et al. 2005, AJ, 130, 734

Vennes, S. 1999, ApJ, 525, 995

Werner, K. 1996, ApJ, 457, L39

Wesemael, F., et al. 1994, ApJ, 429, 369

Wood, M. A. 1995, in 9th European Workshop on White Dwarfs, NATO ASI Series, ed. D. Koester & K. Werner (Berlin: Springer), 41

York, D. G., et al. 2000, AJ, 120, 1579

Zuckerman, B., Koester, D., Melis, C., Hansen, B. M., & Jura, M. 2007, ApJ, 671, 872

Chapitre 5

SOLUTION TO THE PROBLEM OF THE SURFACE GRAVITY DISTRIBUTION OF COOL DA WHITE DWARFS FROM IMPROVED 3D MODEL ATMOSPHERES

P.-E. Tremblay[1], H.-G. Ludwig[2], M. Steffen[3], P. Bergeron[1] and B. Freytag[4]

[1] *Département de Physique, Université de Montréal, C.P. 6128, Succ. Centre-Ville, Montréal, QC H3C 3J7, Canada*

[2] *Zentrum für Astronomie der Universität Heidelberg, Landessternwarte, Königstuhl 12, 69117 Heidelberg, Germany*

[3] *Astrophysikalisches Institut Potsdam, An der Sternwarte 16, D-14482 Potsdam, Germany*

[4] *CNRS, Université de Lyon, École Normale Supérieure de Lyon, 46 allée d'Italie, F-69364 Lyon Cedex 7, France*

Submitted to *Astronomy & Astrophysics*

May 2011

5.1 Abstract

The surface gravities of cool ($T_{\rm eff} < 13,000$ K) hydrogen-atmosphere DA white dwarfs, determined from spectroscopic analyses, are found to be significantly higher than the canonical value of $\log g \sim 8$ expected for these stars. It was recently concluded that a problem with the treatment of convective energy transport within the framework of the mixing-length theory was the most plausible explanation for this high-$\log g$ problem. We pursue the investigation of this discrepancy by computing model spectra of cool convective white dwarfs from a small sequence (11,300 K $< T_{\rm eff} <$ 12,800 K) of 3D hydrodynamical model atmospheres, which feature a sophisticated treatment of convection and radiative transfer. Our approach is to proceed with a differential analysis between 3D and standard 1D models. We find that the 3D spectra predict significantly lower surface gravities, with corrections of the right amplitude as a function of effective temperature to obtain values of $\log g \sim 8$ on average. We conclude that the surface gravity distribution of cool convective DA white dwarfs is much closer to that of hotter radiative objects when using, for the treatment of the convection, 3D models instead of the mixing-length framework.

5.2 Introduction

The shape of Balmer lines in hydrogen-atmosphere DA white dwarfs is particularly sensitive to variations of the atmospheric parameters ($T_{\rm eff}$ and $\log g$). Therefore, the spectroscopic technique, which consists in comparing the observed line profiles of the Balmer series with the predictions of detailed model atmospheres, is by far the most accurate method for determining the atmospheric parameters. This technique was initially applied to a sample of 37 cool ($T_{\rm eff} < 13,000$ K) DA white dwarfs by Bergeron et al. (1990) who showed that the $\log g$ values measured for these white dwarfs were significantly higher than the expected canonical value of $\log g \sim 8$, which is about the mean value determined later for hotter DA stars (e.g., Bergeron et al. 1992). This discrepancy is now observed in all large spectroscopic surveys of DA white dwarfs (e.g., Eisenstein et al. 2006; Gianninas et al. 2009) and no satisfactory explanation has been reported until now. In Fig. 5.1, we present our current view of this high-$\log g$ problem for the spectroscopically identified DA stars in the Sloan Digital Sky Survey (SDSS). This long-standing problem implies that we cannot obtain reliable atmospheric parameters determined from spectroscopy at the cool end of the white dwarf evolutionary sequence. Since the problem manifests itself for white dwarfs older than ~1 Gyr, it has important implications on our ability to use these objects as cosmochronometers and distance indicators (Winget et al. 1987; Fontaine et al. 2001).

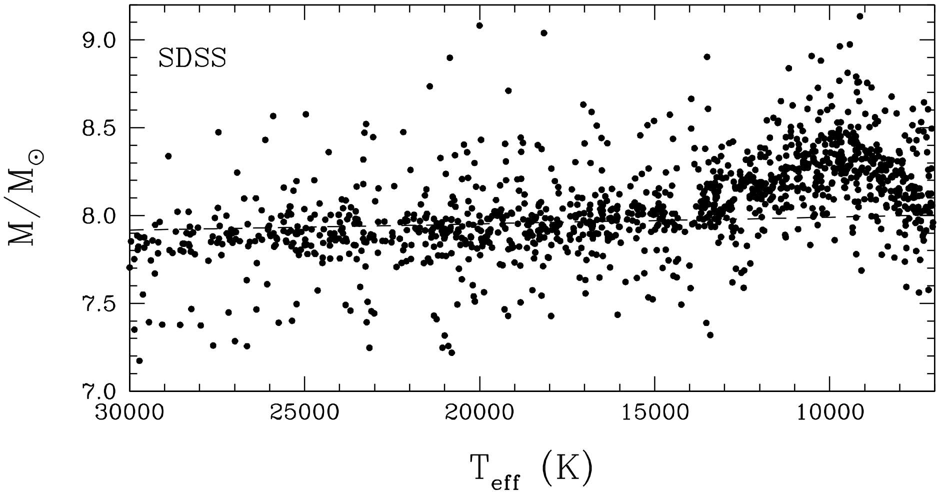

FIGURE 5.1 – Surface gravity distribution as a function of $T_{\rm eff}$ for the SDSS sample; see Tremblay et al. (2011) for details on these determinations. An evolutionary model from Fontaine et al. (2001) at the median mass of the sample (0.59 $M_\odot$) is shown as a dashed line.

Since white dwarf stars are expected to cool at constant mass and almost constant radius, the sudden and significant increase in $\log g$ cannot be explained in terms of simple astrophysical arguments. Tremblay et al. (2010, hereafter TB10; see also Koester et al. 2009a) made an extensive review of the possible solutions, which range from inadequate assumptions about the composition of these stars to inaccuracies in the model atmosphere calculations. The non-detection of He I lines in high-resolution Keck observations of cool DA stars by TB10 ruled out the systematic presence of helium in the atmospheres, which would mimic higher spectroscopic $\log g$ determinations, as initially proposed by Bergeron et al. (1990). TB10 concluded – as Koester et al. (2009a) did – that a problem with the treatment of convective energy transport, currently based on the mixing-length theory (MLT; Böhm-Vitense 1958), is the only viable explanation for the high-log g problem.

The MLT approximation is a phenomenological description of the complex convective fluid movements in a star. According to this model, *bubbles* transport energy in the convection zone over a characteristic distance – the mixing length – where they dissolve and release their extra energy in the environment. Even though the MLT framework, properly calibrated, provides a reasonable description of white dwarf model atmospheres (TB10 and references therein), even small changes in the convective efficiency, or equivalently the mixing-length parameter, can have a significant impact on the predicted line profiles (see, e.g., Fig. 3 of Bergeron et al. 1995) in the regime where the high-log g problem is most important. This comes from the fact that convective energy transport may affect dramatically the temperature and pressure structures of the atmosphere, and consequently the shape of the broad hydrogen lines, formed at different depths in the atmosphere. The observations reveal that the high-log g problem seems to be related to the line profiles only, and not to the continuum flux (as demonstrated from photometric analyses of these stars; see, e.g., TB10 and Koester et al. 2009a), and that the problem occurs when convection becomes important in the photosphere (TB10). This is consistent with the MLT framework being the source of the problem.

A more detailed multidimensional radiation-hydrodynamics (RHD) treatment of convective motions in DA white dwarfs, based on first physical principles, has already been studied by Ludwig et al. (1994), Steffen et al. (1995), and Freytag et al. (1996). These studies revealed that the differences between 2D spectra and those computed from standard 1D hydrostatic models were qualitatively small. However, a visual inspection of Fig. 13 from TB10 reveals that the model predictions do not need to change by much to rectify the high-log g problem. These 2D calculations have not been pursued further, and in the meantime, full three dimensional RHD simulations (hereafter 3D models) have become more sophisticated, and accurate enough to make realistic predictions (see, e.g., Asplund et al. 2000 and references therein).

In this work, we present an updated investigation of the differences between standard DA spectra and those calculated from 3D model atmospheres. In Sect. 2, we describe our computation of a small number of 3D model atmospheres for cool convective DA white dwarfs. We then address, in Sect. 3, the status of the high-log g problem from a purely differential analysis between the Balmer line profiles predicted by the 3D models, and those computed from 1D models with the same underlying microphysics.

5.3 Improved 3D model atmospheres

We computed a small set (11,300 K $< T_{\rm eff} <$ 12,800 K) of pure-hydrogen 3D model atmospheres at $\log g = 8$ with the CO^{5}BOLD code[1] (Freytag et al. 2002; Wedemeyer et al. 2004). This code solves the time-dependent hydrodynamical equations (conservation of mass, momentum, and energy) for a fully compressible fluid with a finite-volume approach, coupled to the radiative transfer. The DA white dwarfs investigated here have a shallow convective zone, which can be included entirely in the simulation domain (for the vertical direction). This allows for dynamically stable layers at the top and bottom of the domain, and accounts for the entire overshooting layer. The lateral boundaries are periodic, and the radiative flux entering the domain at the bottom defines the effective temperature. We rely on a standard stellar equation of state, and the opacities are the same as those used in the simulations of Ludwig et al. (1994). We computed both gray and non-gray models, the latter using 7 opacity bins for the radiative transfer (Ludwig et al. 1994). Table 5.1 presents the basic properties for our set of models. In Fig. 5.2, we illustrate the structure of the non-gray 11,975 K model. We find that our new models are qualitatively similar to those computed by Ludwig et al. (1994) and Steffen et al. (1995) in terms of the properties of the convective zone (i.e., depth and maximum velocities).

In order to make our comparison strictly differential, we also employ 1D models in which the microphysics and radiation transfer numerical schemes (e.g., the opacity binning) are identical to those included in the 3D models. We computed these hydrostatic 1D models with the LHD code (Caffau & Ludwig 2007), which treats convection within the MLT framework using our most recent ML2/$\alpha = 0.8$ parameterization (see TB10 for details). In Fig. 5.3, we present these models hereafter named 1D$_{\rm MLT}$ (the gray models are omitted for clarity). In addition, we computed mean 1D structures that correspond to the $\langle T^4 \rangle^{1/4}$ and $\langle P \rangle$ spatial average of the 3D models over surfaces of constant Rosseland optical depth. We followed

---

[1] www.astro.uu.se/~bf/co5bold_main.html

TABLE 5.1 – Parameters of our 3D model atmospheres

$T_{\rm eff}$ (K)	$\log g$	Opacity bins	Time^a (s)	$\lvert dF\rvert^b$ (%)
Non-gray models				
11,300	8.0	7	10	2.46
11,975	8.0	7	10	0.07
12,390	8.0	7	10	0.16
12,800	8.0	7	10	0.02
Gray models				
11,350	8.0	1	40	1.20
11,975	8.0	1	10	0.70
12,390	8.0	1	15	0.03
12,800	8.0	1	15	0.06

[a] Total stellar time. [b] Maximum flux error, defined as ($\max|F(z)/F^* - 1|$), taken over the whole depth of the computation box. F^* is the nominal flux $\sigma T_{\rm eff}^4$, and $F(z)$ is the total energy flux (radiative, convective, kinetic, viscous and potential fluxes) averaged over 2 seconds (or 5 seconds for the coolest gray and non-gray models) at the end of the simulation. Note that the maximum flux error generally occurs at the base of the simulation and that in the line forming layers, the flux error is much smaller.
Notes: The box size is 7.45 km (150 grid points) for both horizontal directions and 4.17 km for the vertical direction (100 grid points).

this procedure with temporal averages over 12 selected snapshots. These averages, called ⟨3D⟩ models and shown in Fig. 5.3, have had their horizontal temperature and pressure fluctuations removed, and therefore, a comparison of 3D and ⟨3D⟩ models highlights the effect of these fluctuations.

At first, we rely on the Linfor3D three-dimensional spectral synthesis code[2] to compute Hβ line profiles from our DA model atmospheres. Figure 5.4 presents the 3D, ⟨3D⟩, and 1D$_{\rm MLT}$ profiles at $T_{\rm eff} = 11,300$ K and 12,390 K. It is already obvious that the 3D spectra are indistinguishable from the spectra computed from the corresponding averaged ⟨3D⟩ models, an effect also observed by Steffen et al. (1995) in their 2D simulations. This is a non-trivial result since significant temperature and pressure inhomogeneities are present in the hydrodynamical simulations (see Fig. 5.2). In the case of main-sequence stars, for instance, differences between 3D and ⟨3D⟩ spectra can be important (Ludwig et al. 2009). However, in the case of DA white dwarfs, an optical spectrum can be safely computed using a single averaged atmospheric

---

[2] www.aip.de/∼mst/linfor3D_main.html

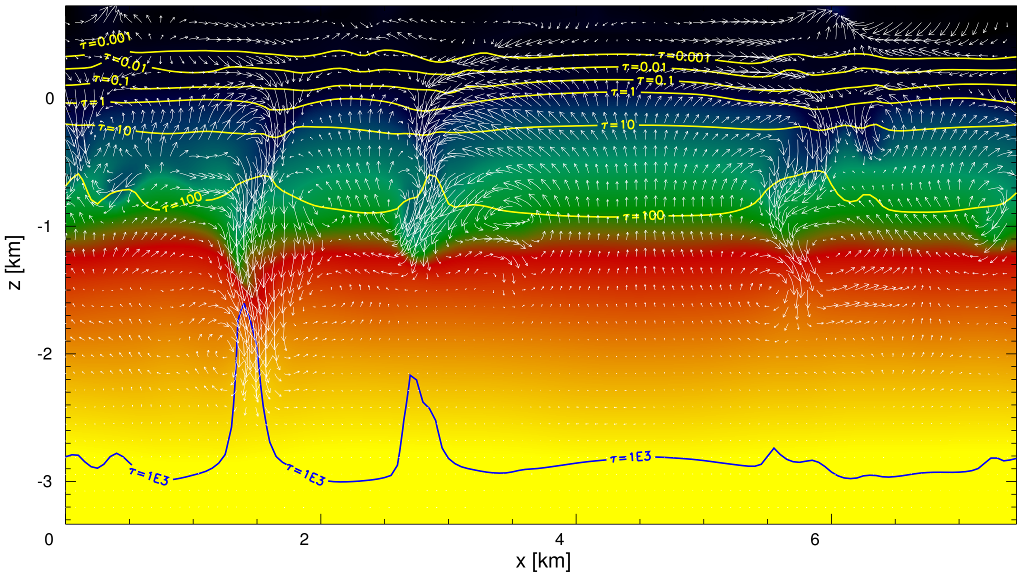

FIGURE 5.2 – Temperature structure for the 3D white dwarf model at $T_{\rm eff} = 11,975$ K and $\log g = 8$, for a slice in the horizontal-vertical xz plane through a box with coordinates x, y, z (in km). The temperature is color coded from 60,000 K (yellow) to 8000 K (blue). The arrows represent relative convective velocities (integration time of 20 ms), while thick lines correspond to contours of constant Rosseland optical depth.

structure. In this context, one can therefore neglect the time-consuming task of 3D spectral synthesis.

On the other hand, Fig. 5.4 also demonstrates that the differences between the ⟨3D⟩ and $1{\rm D}_{\rm MLT}$ models are significant. This suggests that most of the effects from the RHD treatment of convection originate from changes in the mean vertical atmospheric structure. An examination of Fig. 5.3 indeed reveals that the ⟨3D⟩ – hereafter equivalent to 3D – and $1{\rm D}_{\rm MLT}$ structures have a significantly different shape in the photosphere. For the remainder of this study, our goal is to quantify the differences between these models.

We chose to compute optical synthetic spectra (3500 Å $< \lambda <$ 5500 Å) for all our 3D and $1{\rm D}_{\rm MLT}$ structures calculated in this work using the standard spectral synthesis code for DA white dwarfs from the Montreal group (Tremblay & Bergeron 2009, TB10). The rationale behind this choice is that, as described above, one can neglect the 3D spectral synthesis, and moreover, our code relies on an equation of state and opacity sources that are more

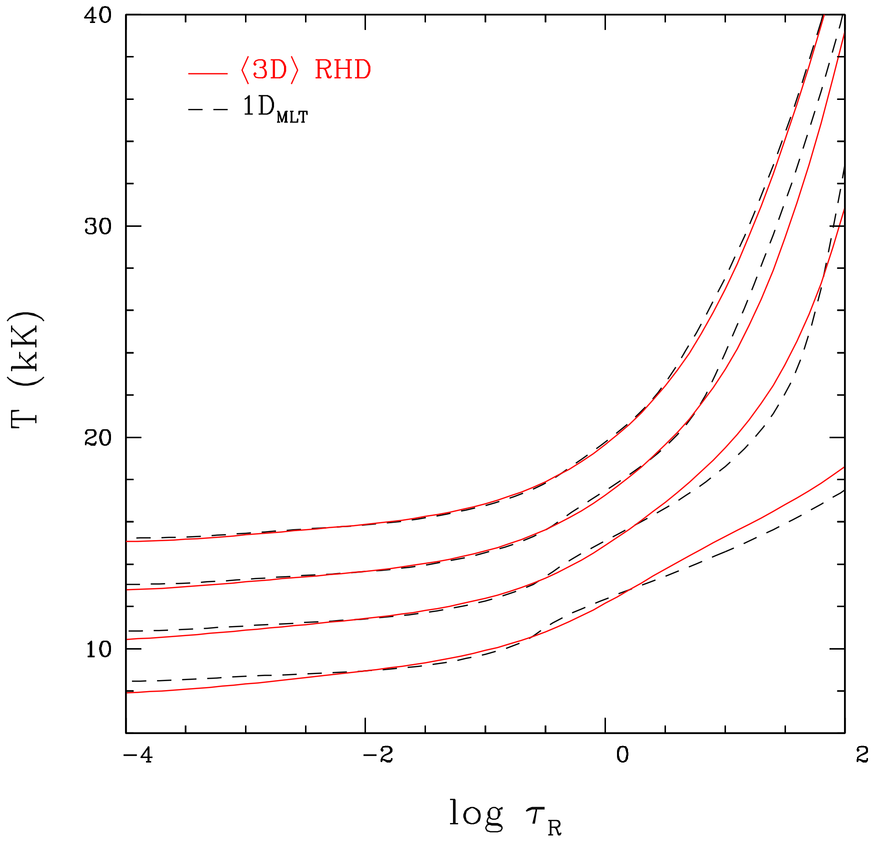

FIGURE 5.3 – Temperatures versus Rosseland optical depth for ⟨3D⟩ (solid lines) and 1D$_{\mathrm{MLT}}$ (dashed lines) non-gray simulations at T_{eff} = 11,300, 11,975, 12,390 and 12,800 K (shifted on the vertical axis by 0, 2, 4 and 6 kK, respectively, for clarity).

appropriate for DA white dwarfs (e.g., with a proper account of line blending, including non-ideal gas effects). We verified that the structures calculated in this work from the LHD and CO^{5}BOLD codes (with the microphysics dating from Ludwig et al. 1994) are comparable to those computed with the Montreal code. This implies that the differences in the microphysics are small, after all, and that our procedure is adequate for a differential analysis.

5.4 Application to the high-$\log g$ problem

To quantify the effects of the 3D white dwarf models, we compute in this section the 3D atmospheric parameter corrections with respect to the reference 1D$_{\mathrm{MLT}}$ models. These are defined as the differences in T_{eff} and $\log g$ when we fit the normalized line profiles of both the

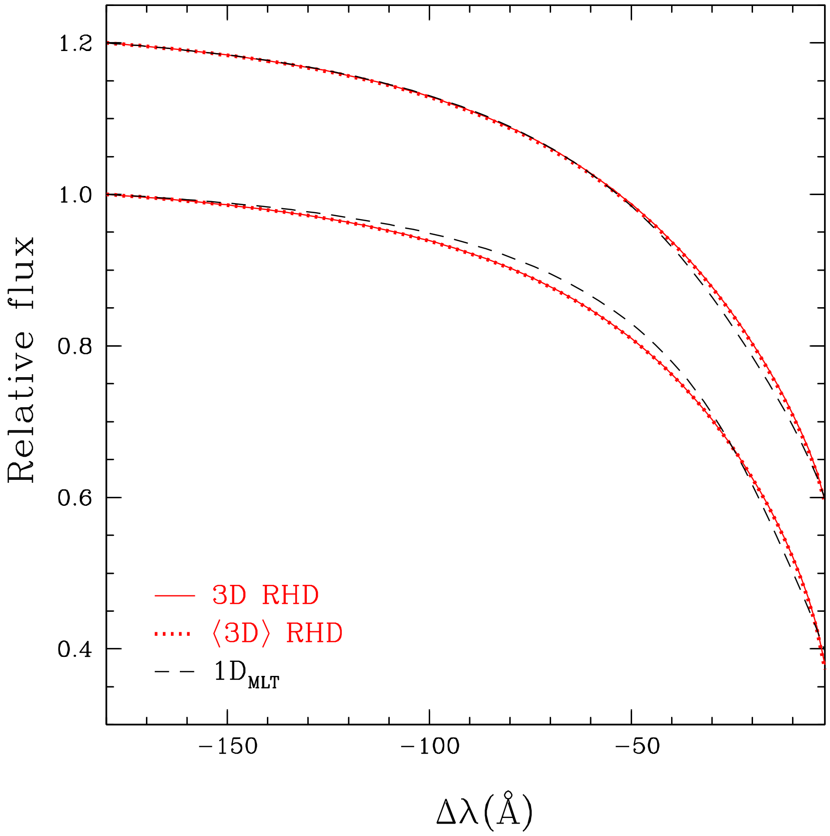

FIGURE 5.4 – Comparison of Hβ line profiles calculated with Linfor3D for the 3D (solid lines, averaged over 12 selected snapshots) and $1D_{\rm MLT}$ (dashed lines) models in the case of two non-gray simulations at $T_{\rm eff}$ of 11,300 K and 12,390 K (the latter shifted by 0.2 units of flux for clarity). The dotted lines (indistinguishable from the 3D spectra in the figure) also show the ⟨3D⟩ profiles resulting from spatial and temporal averages of the 3D structures.

$1D_{\rm MLT}$ and 3D spectra with a reference grid[3]. More specifically, the corrections are defined as $1D_{\rm MLT}-3D$, since we are interested in how much the atmospheric parameters of real stars would change when using 3D model spectra. Our approach is similar to that of Ludwig et al. (2009) who studied these corrections for late-type main sequence stars. We use as a reference grid the spectra computed in TB10[4]. Obviously, the atmospheric parameter corrections will not be *exact* since the independent reference grid does not exactly reproduce the spectra computed in this analysis. Nevertheless, the good quality of our fits achieved in all cases implies that our approach should be valid to within a few percents. The 3D $\log g$ corrections

---

[3] We neglect the center of the lines ($|\Delta\lambda| < 3$ Å), which are formed at low values of $\tau_{\rm R}$ where the number of frequencies taken into account in the structure calculations can have a strong impact on the predictions.

[4] We also calculated a similar reference grid from gray structures to fit our gray models.

are presented in Fig. 5.5. In the case of the 3D corrections in effective temperature, we find that they are all relatively small ($\sim$ 200 K at $T_{\rm eff} \sim 12,000$ K). They are certainly of the same order as the accuracy of the spectroscopic method, and therefore we do not discuss them further. We note that the 3D corrections should approach zero for $T_{\rm eff} \gtrsim 13,000$ K, since the convection zone is rapidly shrinking, and the $1{\rm D}_{\rm MLT}$ and 3D spectra are otherwise identical.

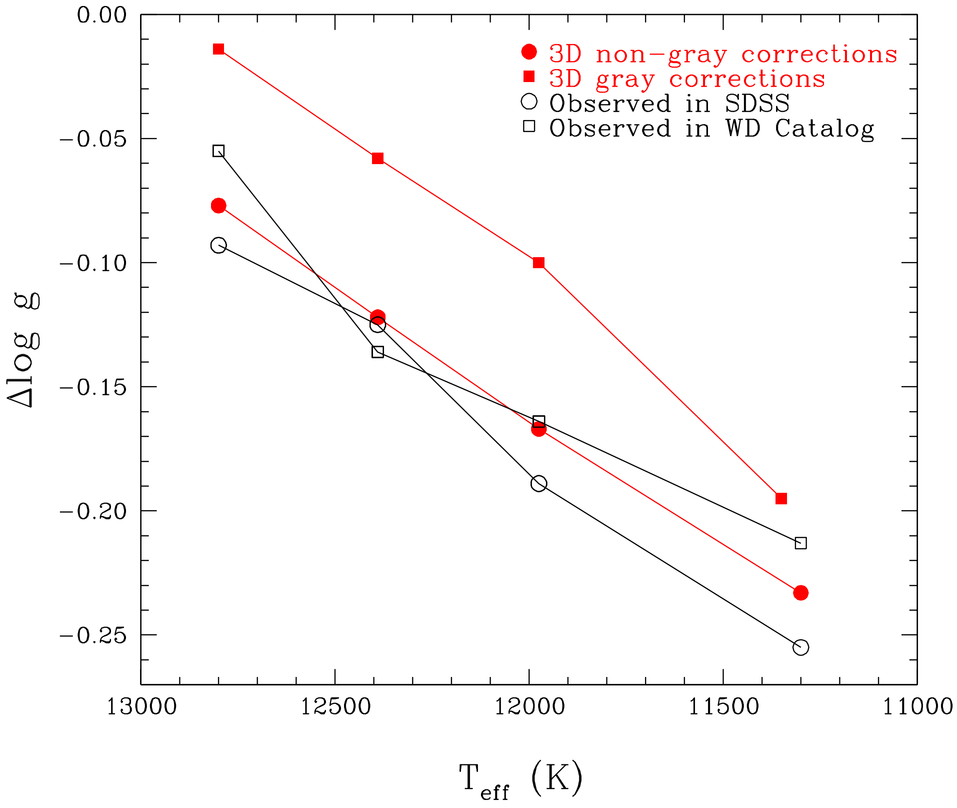

FIGURE 5.5 – Non-gray (filled circles) and gray (filled squares) 3D $\log g$ corrections. In comparison, we show the shifts in surface gravity required to obtain a stable $\log g$ distribution as a function of $T_{\rm eff}$ using the samples of the SDSS (open circles, also displayed in Fig. 5.1) and Gianninas et al. (2009; open squares). The points are connected for clarity.

The non-gray 3D $\log g$ corrections are the key values to assess the high-$\log g$ problem. A preliminary observation reveals that these corrections are negative for all spectra (i.e., the 3D models predict lower surface gravities), which is in the appropriate direction to correct the problem. The mean amplitude of the corrections is significant (~ -0.15 dex), which may not be surprising since the complicated flow patterns are not expected to be fully represented by a unique free parameter for all atmospheric depths, and for all white dwarfs. Also given in Fig. 5.5 are the *observed* shifts in $\log g$ derived from the SDSS white dwarf sample displayed in Fig. 5.1. These shifts correspond to the corrections required, in a bin of 1000 K around the model temperature, to match the median mass value obtained from hot DA stars, represented by the dashed line in Fig. 5.1. We also computed similar shifts from the sample of Gianninas et al. (2009), drawn from the Villanova White Dwarf Catalog, to account for observational uncertainties. We can see that the 3D corrections have *almost exactly the right slope and amplitude* to solve the high-$\log g$ problem. This result clearly indicates that the surface gravity distribution of cool convective DA stars ($T_{\rm eff} \gtrsim 11,000$ K) would be much more stable, as a function of $T_{\rm eff}$, if 3D model atmospheres were used instead of the 1D standard models.

We also verified that the non-gray $\log g$ corrections are fairly independent of the $T_{\rm eff}$ corrections by redoing our fits at fixed temperatures ($T_{\rm eff} = T_{\rm 3D}$). The corrections we obtain with this method are within $\sim 20\%$ of those found in Fig. 5.5. Finally, the fact that we have a set of 3D gray models allows us to evaluate the impact on our results of the opacity binning procedure in the non-gray models. The shifts in $\log g$ that we obtain with 1 opacity bin (gray models) are smaller than those with 7 bins (non-gray models), but still correct to a large degree the high-$\log g$ problem. This shows that further improvements in the binning procedure of the RHD models are not expected to change our differential analysis significantly.

5.5 Conclusion

We conducted a differential analysis of synthetic spectra for cool convective DA white dwarfs computed from model atmospheres with a detailed 3D radiation-hydrodynamical treatment of convective motions, and with the standard 1D mixing-length theory. We introduced the concept of 3D atmospheric parameter corrections, which are defined as the difference in $T_{\rm eff}$ and $\log g$ between $1{\rm D}_{\rm MLT}$ and 3D spectra when fitted with an independent grid. These corrections illustrate by how much the atmospheric parameters of DA stars would change if we were to use a grid of 3D spectra to fit the observations. We find that the 3D surface gravity corrections have the correct amplitude (~ 0.15 dex) to solve the high-$\log g$ problem for DA white dwarfs in the range 11,300 K $< T_{\rm eff} <$ 12,800 K. This indubitably suggests that a weakness with the standard MLT theory is creating the high $\log g$ values reported in recent spectroscopic analyses (e.g., TB10).

Our next goal will be to review the microphysics and the opacity binning procedure in the CO^{5}BOLD code to connect the absolute properties of these hydrodynamical models with those of standard white dwarf models. We will then be able to compute improved 3D model spectra that can actually be compared with observations to determine the atmospheric parameters. We also plan to look at convective white dwarfs cooler than those studied in this work, where the MLT theory predicts an increasingly adiabatic convection, which is less sensitive to the mixing-length parameter. It remains to be seen how the 3D $\log g$ corrections would behave in this regime.

This work was supported in part by the NSERC Canada and by the Fund FQRNT (Québec). B.F. acknowledges financial support from the *Agence Nationale de la Recherche* (ANR), and the *"Programme Nationale de Physique Stellaire"* (PNPS) of CNRS/INSU, France.

5.6 References

Asplund, M., Ludwig, H.-G., Nordlund, Å., & Stein, R F. 2000, A&A, 359, 669

Bergeron, P., Saffer, R. A., & Liebert, J. 1992, ApJ, 394, 228

Bergeron, P., Wesemael, F., Fontaine, G., & Liebert, J. 1990, ApJ, 351, L21

Bergeron, P., Wesemael, F., Lamontagne, R., et al. 1995, ApJ, 449, 258

Böhm-Vitense, E. 1958, ZAp, 46, 108

Caffau, E., & Ludwig, H.-G. 2007, A&A, 467, L11

Eisenstein, D. J., Liebert, J., Harris, H. C., et al. 2006, ApJS, 167, 40

Fontaine, G., Brassard, P., & Bergeron, P. 2001, PASP, 113, 409

Freytag, B., Ludwig, H.-G., & Steffen, M. 1996, A&A, 313, 497

Freytag, B., Steffen, M., & Dorch, B. 2002, Astron. Nachr., 323, 213

Gianninas, A., Bergeron, P., & Ruiz, M. T. 2009, Journal of Physics Conference Series, 172, 012021

Koester, D., Kepler, S. O., Kleinman, S. J., & Nitta, A. 2009, Journal of Physics Conference Series, 172, 012006

Ludwig, H.-G., Behara, N. T., Steffen, M. & Bonifacio, P. 2009, A&A, 502, 1L

Ludwig, H.-G., Jordan, S., & Steffen, M. 1994, A&A, 284, 105

Steffen, M., Ludwig, H.-G. & Freytag, B. 1995, A&A, 300, 473

Tremblay, P.-E., & Bergeron, P. 2009, ApJ, 696, 1755

Tremblay, P.-E., Bergeron, P. & Gianninas, A. 2011, ApJ, 730, 128

Tremblay, P.-E., Bergeron, P., Kalirai, J. S. & Gianninas, A. 2010, ApJ, 712, 1345 (TB10)

Wedemeyer, S., Freytag, B., Steffen, M., Ludwig, H.-G. & Holweger, H. 2004, A&A, 414, 1121

Winget, D. E., Hansen, C. J., Liebert, J., et al. 1987, ApJ, 315, L77

Chapitre 6

Conclusion

Les résultats présentés dans cette thèse ont comme point commun une meilleure compréhension ainsi que l'amélioration de la méthode spectroscopique, qui compare des spectres visibles de naines blanches à atmosphère riche en hydrogène à des spectres synthétiques afin d'en déterminer les paramètres atmosphériques ($T_{\rm eff}$, $\log g$). Notre approche passe principalement par l'augmentation de la précision et du réalisme des modèles d'atmosphère qui servent à calculer les spectres théoriques, avec, comme point de départ, la grille de modèles présentée dans Liebert et al. (2005). Les codes exploités par ces auteurs ont également été utilisés dans les Chapitres 2 à 4 pour le calcul de modèles, mais avec une microphysique améliorée.

6.1 Profils Stark incluant des effets non-idéaux du gaz

Dans le Chapitre 2, il est question d'un premier problème bien identifié dans les modèles de DA, soit le paramètre libre pour décrire les effets non-idéaux dans l'élargissement des raies d'hydrogène par l'effet Stark. Cet obstacle a été surpassé en combinant, dans un cadre cohérent, la théorie unifiée de l'élargissement Stark de Vidal, Cooper & Smith avec l'équation d'état non-idéal de Hummer & Mihalas. Ces deux théories, faisant partie des modèles de naines blanches depuis les travaux de Bergeron et al. (1991), sont responsables de beaucoup des succès obtenus avec la méthode spectroscopique. Pour la première fois, il est possible de les utiliser ensemble de façon cohérente. Notre approche est basée sur la proposition de Seaton (1990) d'inclure directement les perturbations non-idéales des protons et des électrons dans le calcul du profil des raies avec la théorie unifiée, ce qui permet d'obtenir une description réaliste du chevauchement entre les raies.

Une nouvelle grille de spectres de DA a été calculée avec nos profils améliorés. En premier lieu, nous avons étudié l'effet *total* des nouveaux profils Stark, c'est-à-dire par rapport aux profils originaux de VCS sans paramètre libre ($\beta_{\rm crit} \times 1$). La Figure 6.1, similaire à la Figure 2.8 mais avec une couverture à toutes les températures d'intérêt pour l'analyse des DA, montre l'effet de ces nouveaux profils. On peut voir l'importance majeure des effets non-idéaux dans le calcul des profils de raies. Cela démontre que l'approximation, selon laquelle toutes les transitions se font à deux niveaux (avec l'effet Stark linéaire) dans l'atmosphère dense des naines blanches, n'est pas satisfaisante.

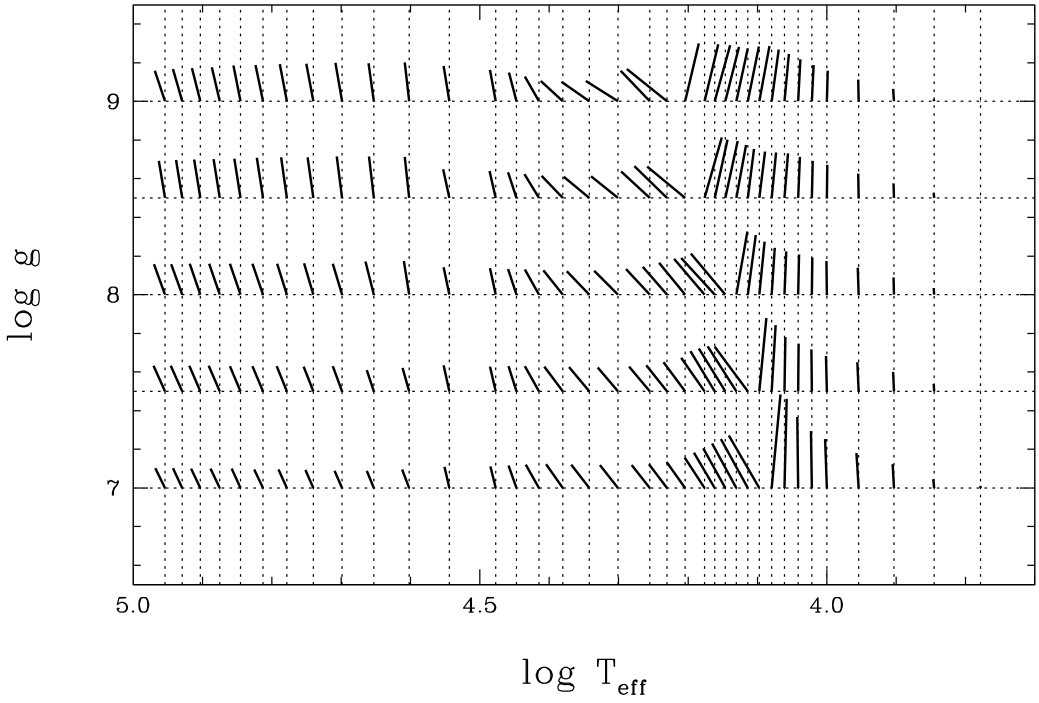

FIGURE 6.1 – Similaire à la Figure 2.8, mais avec une plus large couverture en $T_{\rm eff}$.

6.2 Application de la technique spectroscopique

Au Chapitre 2, nous avons appliqué les nouveaux spectres dans l'analyse spectroscopique de l'échantillon PG. Ce choix s'avère logique puisque ces étoiles ont déjà été étudiées en détail avec la précédente grille de modèles (Liebert et al. 2005) utilisant le paramètre libre $\beta_{crit} \times 2$ introduit par Bergeron (1993) pour imiter les effet non-idéaux dans le profil des raies. L'application de la technique spectroscopique a d'abord été limitée au régime des atmosphères radiatives et en équilibre thermodynamique local (40,000 K $> T_{\rm eff} >$ 13,000 K). Cette restriction a permis de minimiser les incertitudes théoriques externes dans la vérification de nos profils. La nouvelle masse moyenne trouvée pour l'échantillon PG est près de 0.03 $M_\odot$ supérieure aux résultats précédents. Ce changement n'est pas entièrement surprenant, puisqu'on pouvait s'attendre à ce que le paramètre libre utilisé précédemment ne reproduise pas exactement la complexité physique du phénomène qu'il cherche à imiter. En outre, il a été démontré que les nouveaux modèles permettent d'obtenir des paramètres atmosphériques raisonnables qui sont en excellent accord avec les contraintes photométriques indépendantes. Nous obtenons également une distribution de masse qui est plus stable qu'auparavant en fonction de $T_{\rm eff}$.

La Figure 6.2 montre l'effet de nos nouveaux profils par rapport à la génération précédente de modèles[1] (Liebert et al. 2005), et donc, le changement prédit des paramètres atmosphériques en comparaison avec ceux trouvés dans la littérature. Ceci permet de visualiser l'implication des modèles dans tous les régimes de température. Dans le Chapitre 3, nous avons présenté l'effet des profils sur la technique spectroscopique à basse température. Nous avons vu que, globalement, cela n'avait aucun impact sur le problème des gravités élevées dans les naines blanches froides. Il faudra donc attendre d'avoir corrigé ce problème avant de comprendre toutes les implications des nouveaux profils. On remarque toutefois, à la Figure 6.2, que le changement des paramètres atmosphériques diminue de façon très abrupte autour de 8000 K, ce qui correspond à la transition de la domination de l'élargissement par les particules chargées vers celui par les particules neutres.

Pour ce qui est du régime à haute température ($T_{\rm eff} >$ 40,000 K), la première application des nouveaux profils se retrouve dans Gianninas et al. (2010). Ces derniers auteurs observent que, bien que les profils Stark changent les paramètres atmosphériques de façon significative, l'effet des métaux et du traitement hors-ETL des populations sont plus importants. Néanmoins, leur distribution $T_{\rm eff}$ versus $\log g$ est satisfaisante d'un point de vue astrophy-

---

[1] Notons que notre grille procède également à une nouvelle calibration de la théorie de la longueur de mélange pour la convection (voir le Chapitre 3).

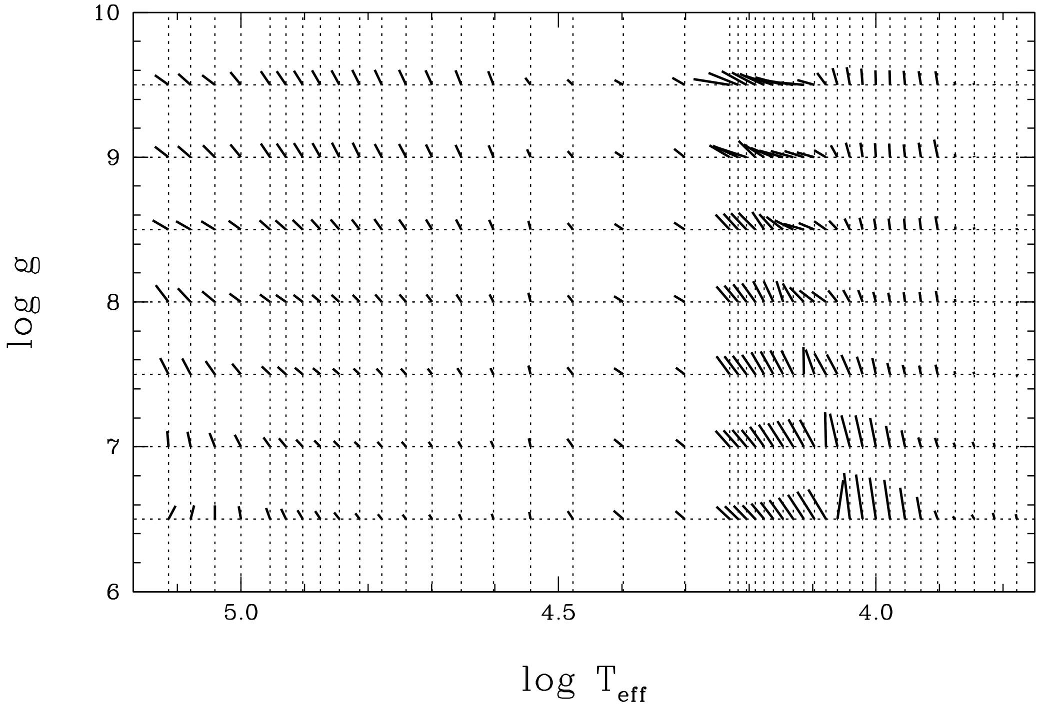

FIGURE 6.2 – Changement prédit des paramètres atmosphériques pour les modèles calculés dans cette thèse (Chapitre 2 et 3) par rapport à la grille utilisée dans Liebert et al. (2005).

sique, et donc, nos profils demeurent certainement acceptables. Finalement, nos profils furent rapidement acceptés et utilisés avec succès dans la communauté (e.g., Marsh et al. 2010; Rauch et al. 2010). Nous avons donc, à partir du Chapitre 4, fait le saut définitif vers notre nouvelle grille de spectres.

Comme démonstration de l'impact de la technique spectroscopique, l'analyse de l'échantillon de DA du SDSS DR4 (Eisenstein et al. 2006a) a été revisitée au Chapitre 4. Le point central de ce travail est la première publication de l'inspection visuelle et minutieuse de tous les résultats individuels de l'analyse spectroscopique (avec $S/N > 12$), couplée avec l'examen de la photométrie *ugriz*. Notre nouvelle analyse a permis de définir un échantillon plus propre, et d'obtenir des paramètres atmosphériques plus précis par rapport à ce qui a été trouvé jusqu'à maintenant. Nous avons déterminé qu'une limite inférieure de $S/N = 15$ convenait pour calculer la masse moyenne, pour laquelle nous trouvons une valeur de 0.613 $M_{\odot}$. Ce résultat est compatible avec les estimations précédentes pour cet échantillon, si l'on tient compte des effets de nos nouveaux modèles. Néanmoins, il apparaît que la masse moyenne est environ 3%

plus petite dans le SDSS en comparaison avec l'échantillon de Gianninas et al. (2009). Nous concluons que cette différence est due à un problème avec la calibration des spectres dans le SDSS.

Finalement, notre grille de modèles peut maintenant être appliquée à d'autres régimes de longueur d'onde, comme l'ultraviolet (Tremblay & Bergeron 2009) et l'infrarouge (Bohlin et al. 2011). Dans le premier cas, la Figure 6.3 illustre nos profils Stark du Chapitre 2 en comparaison avec ceux de VCS pour les raies de la série de Lyman. Les effets non-idéaux produisent des changements similaires à ce qui est observé pour les raies de Balmer, ce qui provoque un effet significatif dans le spectre en raison de la forte opacité des raies de Lyman. Il est possible d'utiliser la technique spectroscopique pour trouver les paramètres atmosphériques à partir des raies de Lyman, ces paramètres pouvant ensuite être comparés à ceux calculés à partir des raies de Balmer. La Figure 6.4 présente un exemple de cette détermination avec nos nouveaux profils pour deux spectres provenant de FUSE. Une prochaine étape sera donc de revisiter les analyses existantes des spectres UV à l'aide de notre grille de modèles. Bien que la qualité de l'ajustement des spectres observés à la Figure 6.4 soit satisfaisante et similaire aux résultats avec la grille précédente (e.g., Hébrard et al. 2003; Barstow et al. 2003), il n'est pas évident que nous obtiendrons simplement une translation des paramètres atmosphériques comme dans l'analyse des raies de Balmer. Il faut également tenir compte des propriétés uniques de l'analyse du spectre ultraviolet, comme la calibration différente des observations et les opacités supplémentaires en raison des collisions avec les neutres (Allard et al. 2004, voir aussi la section 3.6.3), ce qui pourrait influencer les résultats.

6.3 Le problème des gravités élevées

Les nouveaux modèles présentés dans le Chapitre 2 ont permis de réduire l'incertitude sur la microphysique. Cependant, nous avons démontré au Chapitre 3 que des gravités beaucoup plus élevées que la moyenne sont toujours observées pour les DA en dessous de $T_{\rm eff} \sim 13,000$ K. Ce problème est majeur puisqu'il nous empêche d'obtenir une précision de plus de $\sim$20% sur la masse des naines blanches plus vieilles que $\sim$1 Ga. C'est-à-dire que nous obtenons une inexactitude importante dans notre étude de l'évolution des naines blanches, dont les plus

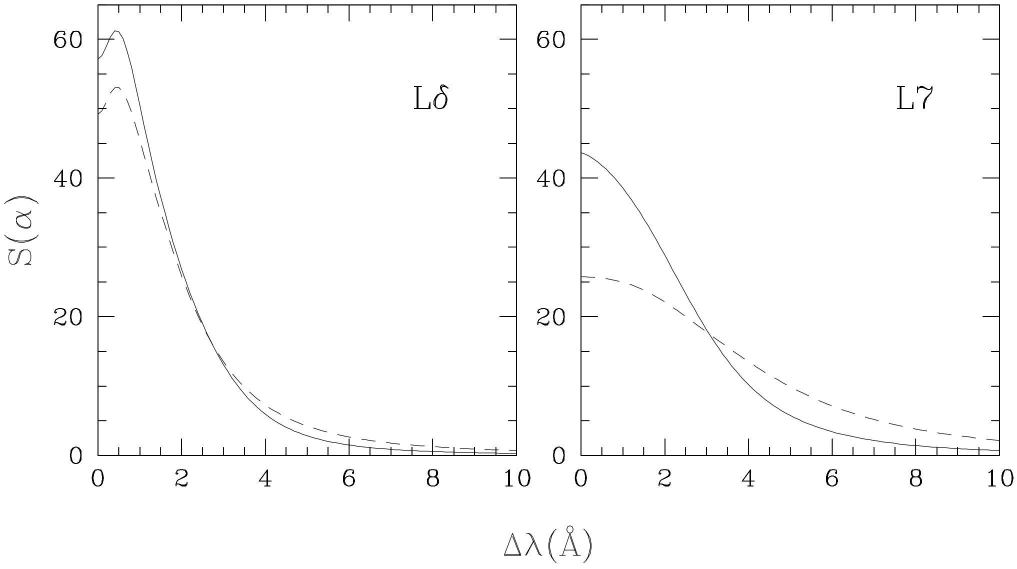

FIGURE 6.3 – Similaire à la Figure 3.5, mais pour deux raies de la série de Lyman pour un plasma à $T = 40{,}000$ K et $\log N_e = 17$.

vieilles dans notre galaxie peuvent avoir jusqu'à 10 Ga. Ce problème est observé dans tous les sondages de naines blanches, et jusqu'à maintenant, aucune explication robuste ne fut proposée.

Cet ouvrage a permis de faire converger les pistes de solutions pour résoudre ce problème, en commençant par la confrontation du modèle de Bergeron et al. (1990) aux observations. Ce scénario suggère que la contamination des atmosphères avec de l'hélium, transporté par le mélange convectif, simulerait des gravités plus élevées. Nous avons testé ce modèle en obtenant des spectres haute résolution de la raie He I $\lambda5877$ à très haut S/N pour 6 naines blanches froides brillantes. Aucune trace d'hélium n'a été détectée et nous avons obtenu des limites inférieures de près d'un ordre de grandeur en deçà de la quantité d'hélium nécessaire pour expliquer, en moyenne, le problème des gravités élevées. Par la suite, les incertitudes restantes dans les modèles ont été quantifiées, pour conclure qu'un problème avec le modèle actuel de la convection, la théorie de la longueur de mélange (MLT), était l'explication la plus plausible en l'absence d'autres choix.

Dans tous les modèles de naines blanches actuellement utilisés, la convection est traitée avec la théorie MLT, un modèle phénoménologique en une dimension et peu robuste. Ce

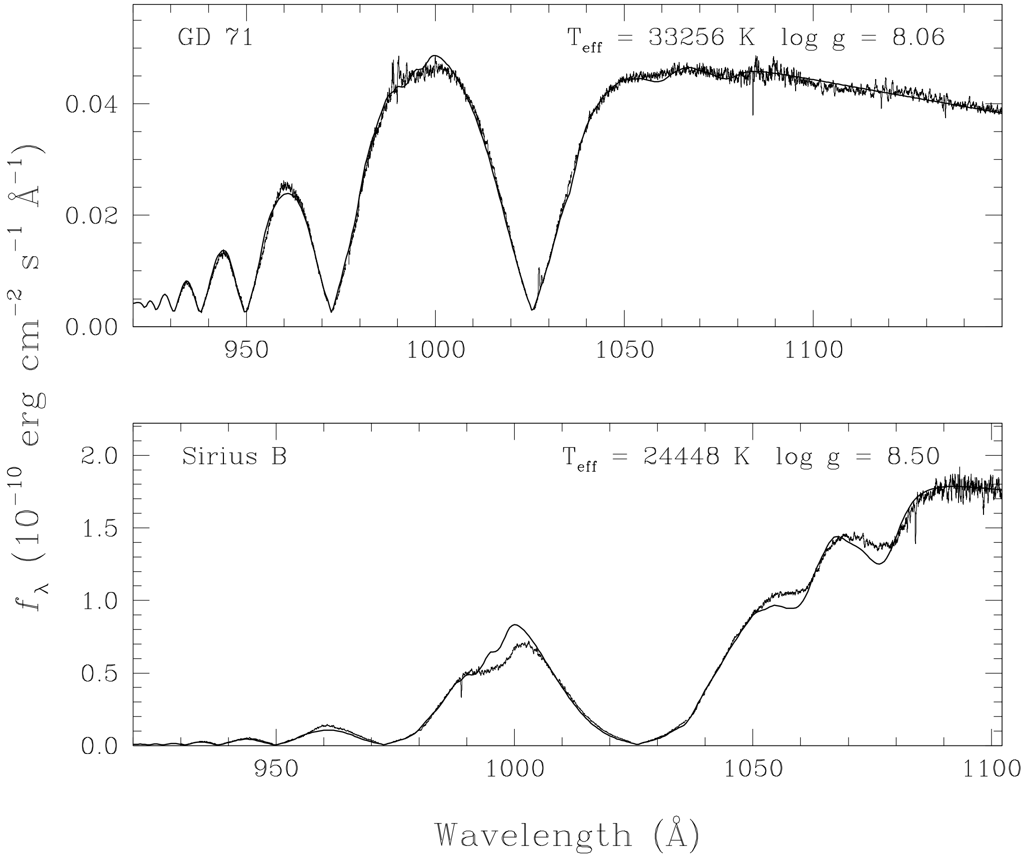

FIGURE 6.4 – Ajustement du χ^2 pour deux spectres UV provenant de FUSE en utilisant des modèles avec nos profils Stark améliorés. La $T_{\rm eff}$, le $\log g$ et l'angle solide sont considérés comme des paramètres libres. Les raies d'absorption interstellaire, ainsi que le coeur des raies ne sont pas inclus dans la procédure de minimisation. Les paramètres atmosphériques obtenus sont identifiés dans la figure.

cadre conceptuel utilise un paramètre libre qui décrit la distance verticale parcourue avant que les bulles convectives soient diluées dans l'atmosphère. La prochaine étape logique est donc d'utiliser un modèle de convection plus précis pour vérifier la validité du modèle présent ($1D_{\rm MLT}$) de façon indépendante. C'est justement ce qui a été fait par Ludwig et al. (1994) et Steffen et al. (1995) avec un modèle hydrodynamique en 2D, et ce, à partir de principes physiques premiers et sans paramètres libres. À l'époque, il avait été conclu que les structures atmosphériques calculées dans ce cadre étaient sensiblement différentes de celles découlant de la MLT, mais que les spectres 2D et $1D_{\rm MLT}$ étaient qualitativement similaires. Cependant, aucune analyse quantitative n'a été réalisée pour prédire le changement des valeurs de $\log g$.

Dans cette thèse, nous avons poursuivi cette étude en collaboration avec H. Ludwig et M. Steffen, avec comme trame de fond, le problème des gravités élevées. En utilisant le code CO^{5}BOLD, proposant un traitement d'hydrodynamique radiative en 3D de la convection, nous avons produit les premiers modèles 3D non-gris de naines blanches froides (12,800 K $> T_{\rm eff} >$ 11,300 K), sans paramètres libres pour décrire la convection. Le Chapitre 5 a exposé le résultat d'une analyse différentielle entre ces modèles 3D et des modèles 1D$_{\rm MLT}$ avec une microphysique et des routines numériques identiques, sauf pour le traitement de la convection. En Annexe A, nous présentons en détails les structures 3D, 3D moyennes et 1D$_{\rm MLT}$ qui ont servi à faire ces calculs. Nos résultats montrent que les spectres 3D prédisent une diminution significative des gravités par rapport aux spectres découlant du traitement avec la MLT. Les corrections 3D à la gravité ont presque exactement les bonnes valeurs pour corriger le problème des gravités élevées (pour $T_{\rm eff} > 11,000$ K). Il apparaît déjà fort probable que le problème soit causé par les limitations du modèle MLT et que les modèles hydrodynamiques corrigent cette faiblesse.

6.4 La prochaine génération de modèles

Cette thèse a permis d'en arriver à la conception de modèles de spectres de naines blanches DA que l'on pense fiables pour décrire les observations d'objets chauds et radiatifs ($T_{\rm eff} \gtrsim$ 13,000 K, Chapitres 2 à 4). On peut maintenant se demander ce qu'il reste à faire du point de vue théorique. Le Chapitre 5 a ensuite décrit les étapes pour produire des spectres réalistes de naines blanches froides convectives. On voudrait maintenant définir ces étapes. Cette section vise à répondre à ces deux questions et à entrevoir ce que cela pourrait nous apporter au-delà de l'étude des naines blanches.

Le flux absolu de certaines naines blanches est assez bien connu par la mesure de la parallaxe trigonométrique. De plus, le flux relatif prédit par les modèles de spectres de naines blanches DA radiatives est réputé pour être assez précis (à ~1%, voir Bohlin 2000) pour servir de standard de flux pour la calibration d'instruments astrophysiques. Dès lors, ce fut en quelque sorte une surprise pour la communauté de voir que l'effet des nouveaux profils Stark était d'environ 5% sur les masses par rapport à la génération précédente de modèles, un changement qui demeure non négligeable dans les circonstances. Par une situation fortuite, nous avons trouvé que les flux absolus (ou magnitudes absolues) prédits par nos modèles sont pratiquement inchangés, en raison d'une compensation de l'effet d'une masse élevée par celui d'une température plus élevée. De plus, le changement dans le flux relatif satisfait encore aux contraintes des données du Space Telescope Imaging Spectrograph (STIS) dans le télescope spatial HST (R. Bohlin, communication privée). En fin de compte, c'est simplement l'observation que la distribution de masse en fonction de $T_{\rm eff}$ apparaît plus stable qu'auparavant (Chapitre 3, voir aussi Gianninas 2011) qui nous permet de dire que nos nouveaux modèles deviennent plus satisfaisants face aux contraintes indépendantes (ici, celle de la conservation de la masse). Il faut ajouter à cela que l'on a augmenté la cohérence physique. Faut-il maintenant considérer ces modèles comme ceux qui vont vraiment atteindre une précision de 1% sur tous les paramètres atmosphériques? Cette thèse montre que l'on doit faire attention. On pourrait remplacer, par exemple, les théories de HM88 et de VCS, pour lesquelles il existe peu d'alternatives indépendantes, par un cadre quantique selon les principes physiques premiers (i.e. avec un calcul exact et simultané des états propres). Même si nous sommes confiants que l'effet sera petit, on peut croire que l'avenir nous réserve certaines surprises. Avec la nécessité de calibrer des instruments de plus en plus précis (comme le JWST, voir Bohlin et al. 2011), de nouveaux défis à surmonter pourraient survenir.

Dans un autre ordre d'idée, il apparaît maintenant évident que l'objectif ultime suggéré par les résultats du Chapitre 5 est de remplacer, pour les DA froides, la grille de modèles présentée dans cet ouvrage par une grille de modèles 3D. Bien que notre analyse différentielle ait montré que le traitement en 3D de la convection produisait des résultats réalistes, il est encore trop tôt pour comparer le résultat global des calculs du code CO^{5}BOLD aux observations. Nous devrons ainsi réaliser une connexion rigoureuse entre ce code et les codes standards de naines blanches. Nous pourrons faire le pont avec le code LHD, qui comprend une physique identique à CO^{5}BOLD mais qui se base sur la MLT pour traiter la convection. La procédure de triage des fréquences dans les modèles 3D et LHD sera fort probablement un facteur dominant dans les prédictions absolues. Puisqu'il est difficile d'augmenter la dimension des matrices définissant le transfert radiatif dans le code CO^{5}BOLD tout en gardant un temps de calcul réaliste, cela pourrait rapidement devenir une limite pour la continuation de ce projet. Il faut donc penser que le remplacement de la théorie MLT par les modèles 3D sera une démarche très progressive. Entre-temps, la microphysique dans les modèles 3D devra être revue pour s'assurer qu'elle correspond à notre version la plus récente.

On peut se demander de ce qu'il adviendra de la théorie de la longueur de mélange. Avec la limite des modèles 3D décrite plus haut, il devient probable que les modèles 1D MLT soient utilisés encore pendant plusieurs dizaines d'années. D'une part, les modèles 1D seront toujours adéquats pour décrire les naines blanches chaudes et radiatives et il ne semble pas évident que les modèles 3D vont faire des prédictions différentes de la MLT pour les naines blanches très froides où la convection est adiabatique. Il serait donc souhaitable, en lumière des résultats de cette thèse, de trouver une recette pour imiter les effets 3D dans les modèles 1D standards (e.g. en recalibrant la longueur de mélange en fonction de la profondeur optique), dans le but de maximiser l'utilisation de la théorie MLT.

Notons finalement que le code CO^{5}BOLD est à la fine pointe de la modélisation en 3D, non seulement des naines blanches mais de toutes les atmosphères d'étoiles convectives comme le Soleil. Un succès dans la modélisation 3D des naines blanches DA, dont certaines ont une zone convective relativement simple à modéliser (petite dimension, absence de champ magnétique et composition à un élément), pourra apporter de nouveaux outils pour un domaine de recherche en plein essor et qui arrive tout juste à maturité. De plus, nos résultats ouvrent la voie à diverses applications, dont certaines pouvant résoudre d'autres problèmes de longue date dans le domaine des naines blanches. La modélisation 3D de l'atmosphère d'autres types de naines blanches convectives (DB, hot-DQ) serait l'application la plus directe. Puisque les modèles de DB sont eux aussi sensibles à la paramétrisation de la longueur de mélange (Bergeron et al. 2010), il semble probable que les prédictions 3D soient fortement différentes de celles avec les modèles 1D standards.

La modélisation hydrodynamique de l'intérieur des naines blanches DA permettra aussi de relever de nouveaux défis. Notons toutefois que le code CO^{5}BOLD n'est pas forcément le plus adapté pour les intérieurs stellaires, où ses atouts en termes de transfert radiatif ne deviennent plus nécessaires. Il serait souhaitable de mieux comprendre la bande d'instabilité des ZZ Ceti, dont la détermination théorique des limites *bleu* et *rouge* (à haute et basse température respectivement) pourrait bénéficier d'un meilleur traitement de la convection (Fontaine & Brassard 2008). Dans le premier cas, les modèles MLT permettent de définir une limite, mais les modèles hydrodynamiques pourraient le faire de façon cohérente, sans avoir à redéfinir la longueur de mélange dans les couches profondes. Pour ce qui a trait à la limite froide de la bande d'instabilité, tout reste à faire et on peut croire que les modèles 3D permettront de comprendre ce phénomène. Un autre défis théorique est de mieux comprendre l'évolution spectrale des naines blanches. En particulier, les modèles 3D seraient idéaux pour étudier le mélange convectif (ou la dilution convective) entre l'hélium et l'hydrogène (MacDonald & Vennes 1991; Tremblay & Bergeron 2008). Il n'est pas trop optimiste de croire que d'ici quelques années, nous aurons finalement assez bien compris la distribution de la quantité totale d'éléments légers (hélium, hydrogǹe) dans les naines blanches.

Bibliographie

Allard, N. F., Kielkopf, J. F., & Loeillet, B. 2004, A&A, 424, 347

Baglin, A. & Vauclair, G. 1973, A&A, 27, 307

Barstow, M. A., Good, S. A., Burleigh, M. R., Hubeny, I., Holberg, J. B., & Levan, A. J. 2003, MNRAS, 344, 562

Bergeron, P. 1993, in NATO ASIC Series 403, White Dwarfs: Advances in Observation and Theory, ed. M. A. Barstow, 267

Bergeron, P., Saffer, R. A., & Liebert, J. 1992, ApJ, 394, 228

Bergeron, P., Wesemael, F., Dufour, P., Beauchamp, A., Hunter, C., Fontaine, G., Dufour, P., Gianninas, A., Desharnais, S., Saffer, R. A., Liebert, J., & Ruiz, M. T. 2010, in American Institute of Physics Conference Series, ed. K. Werner & T. Rauch, Vol. 1273, 7

Bergeron, P., Wesemael, F., & Fontaine, G. 1991, ApJ, 367, 253

Bergeron, P., Wesemael, F., Fontaine, G., & Liebert, J. 1990, ApJ, 351, L21

Bergeron, P., Wesemael, F., Lamontagne, R., Fontaine, G., Saffer, R. A., & Allard, N. F. 1995, ApJ, 449, 258

Bohlin, R. C. 2000, AJ, 120, 437

Bohlin, R. C., Gordon, K. D., Rieke, G. H., Ardila, D., Carey, S., Deustua, S., Engelbracht, C., Ferguson, H. C., Flanagan, K., Kalirai, J., Meixner, M., Noriega-Crespo, A., Su, K. Y. L., & Tremblay, P. 2011, AJ, 141, 173

Böhm-Vitense, E. 1958, ZAp, 46, 108

Dantona, F. & Mazzitelli, I. 1979, A&A, 74, 161

Dufour, P., Liebert, J., Fontaine, G., & Behara, N. 2007, Nature, 450, 522

Eisenstein, D. J., Liebert, J., Harris, H. C., Kleinman, S. J., Nitta, A., Silvestri, N., Anderson, S. A., Barentine, J. C., Brewington, H. J., Brinkmann, J., Harvanek, M., Krzesiński, J., Neilsen, Jr., E. H., Long, D., Schneider, D. P., & Snedden, S. A. 2006a, ApJS, 167, 40

Eisenstein, D. J., Liebert, J., Koester, D., Kleinmann, S. J., Nitta, A., Smith, P. S., Barentine, J. C., Brewington, H. J., Brinkmann, J., Harvanek, M., Krzesiński, J., Neilsen, Jr., E. H., Long, D., Schneider, D. P., & Snedden, S. A. 2006b, AJ, 132, 676

Finley, D. S., Koester, D., & Basri, G. 1997, ApJ, 488, 375

Fontaine, G., Bergeron, P., Lacombe, P., Lamontagne, R., & Talon, A. 1985, AJ, 90, 1094

Fontaine, G. & Brassard, P. 2008, PASP, 120, 1043

Fontaine, G., Brassard, P., & Bergeron, P. 2001, PASP, 113, 409

Fontaine, G. & Wesemael, F. 1987, in IAU Colloq. 95, Second Conference on Faint Blue Stars, ed. A. G. D. Philip, D. S. Hayes, & J. W. Liebert, 319

Fontaine, G. & Wesemael, F. 1991, in IAU Symposium, Vol. 145, Evolution of Stars: the Photospheric Abundance Connection, ed. G. Michaud & A. V. Tutukov, 421

Freytag, B., Ludwig, H., & Steffen, M. 1996, A&A, 313, 497

Gianninas, A. 2011, Ph.D. Dissertation, Université de Montréal

Gianninas, A., Bergeron, P., Dupuis, J., & Ruiz, M. T. 2010, ApJ, 720, 581

Gianninas, A., Bergeron, P., & Ruiz, M. T. 2009, Journal of Physics Conference Series, 172, 012021

Hamada, T. & Salpeter, E. E. 1961, ApJ, 134, 683

Hébrard, G., Allard, N. F., Kielkopf, J. F., Chayer, P., Dupuis, J., Kruk, J. W., & Hubeny, I. 2003, A&A, 405, 1153

Holberg, J. B., Basile, J., & Wesemael, F. 1986, ApJ, 306, 629

Holberg, J. B., Wesemael, F., Wegner, G., & Bruhweiler, F. C. 1985, ApJ, 293, 294

Hubeny, I., Hummer, D. G., & Lanz, T. 1994, A&A, 282, 151

Iben, Jr., I. 1984, ApJ, 277, 333

Koester, D. 1976, A&A, 52, 415

Koester, D., Allard, N. F., & Vauclair, G. 1994, A&A, 291, L9

Koester, D., Kepler, S. O., Kleinman, S. J., & Nitta, A. 2009a, Journal of Physics Conference Series, 172, 012006

Koester, D., Napiwotzki, R., Voss, B., Homeier, D., & Reimers, D. 2005, A&A, 439, 317

Koester, D., Schulz, H., & Weidemann, V. 1979, A&A, 76, 262

Koester, D., Voss, B., Napiwotzki, R., Christlieb, N., Homeier, D., Lisker, T., Reimers, D., & Heber, U. 2009b, A&A, 505, 441

Liebert, J., Bergeron, P., & Holberg, J. B. 2005, ApJS, 156, 47

Liebert, J. & Wehrse, R. 1983, A&A, 122, 297

Liebert, J., Wesemael, F., Hansen, C. J., Fontaine, G., Shipman, H. L., Sion, E. M., Winget, D. E., & Green, R. F. 1986, ApJ, 309, 241

Ludwig, H., Jordan, S., & Steffen, M. 1994, A&A, 284, 105

MacDonald, J. & Vennes, S. 1991, ApJ, 371, 719

Marsh, T. R., Gaensicke, B. T., Steeghs, D., Southworth, J., Koester, D., Harris, V., & Merry, L. 2010, ArXiv e-prints

Mihalas, D. 1978, Stellar Atmospheres (2nd ed., San Francisco: Freeman)

Paquette, C., Pelletier, C., Fontaine, G., & Michaud, G. 1986, ApJS, 61, 197

Rauch, T., Werner, K., & Kruk, J. W. 2010, Ap&SS, 329, 133

Schatzman, E. L. 1958, White dwarfs (New York: Interscience)

Schulz, H. & Wegner, G. 1981, A&A, 94, 272

Seaton, M. J. 1990, Journal of Physics B Atomic Molecular Physics, 23, 3255

Shipman, H. L. 1977, ApJ, 213, 138

—. 1979, ApJ, 228, 240

Sion, E. M. 1984, ApJ, 282, 612

Sion, E. M., Greenstein, J. L., Landstreet, J. D., Liebert, J., Shipman, H. L., & Wegner, G. A. 1983, ApJ, 269, 253

Steffen, M., Ludwig, H., & Freytag, B. 1995, A&A, 300, 473

Strittmatter, P. A. & Wickramasinghe, D. T. 1971, MNRAS, 152, 47

Tremblay, P. & Bergeron, P. 2008, ApJ, 672, 1144

Tremblay, P. & Bergeron, P. 2009, in American Institute of Physics Conference Series, ed. I. Hubeny, J. M. Stone, K. MacGregor, & K. Werner, Vol. 1171, 101

Vauclair, G. & Reisse, C. 1977, A&A, 61, 415

Wegner, G. & Schulz, H. 1981, A&AS, 43, 473

Weidemann, V. & Koester, D. 1980, A&A, 85, 208

Werner, K. & Herwig, F. 2006, PASP, 118, 183

Wesemael, F., van Horn, H. M., Savedoff, M. P., & Auer, L. H. 1980, ApJS, 43, 159

Wickramasinghe, D. T. 1972, MmRAS, 76, 129

Wood, M. A. 1995, in NATO ASI Series 443, 9th European Workshop on White Dwarfs, ed. D. Koester & K. Werner, 41

Zuckerman, B., Koester, D., Melis, C., Hansen, B. M., & Jura, M. 2007, ApJ, 671, 872

Annexe A

Complément sur le calcul de modèles hydrodynamiques

Nous présentons un complément d'information sur les modèles 3D présentés dans le Chapitre 5. Puisque ce chapitre prend le format d'une lettre à l'éditeur, nous avons omis certaines figures par contrainte d'espace. Nous restreignons notre étude aux quatre modèles non-gris du Tableau 5.1, puisque les modèles gris sont utilisés, dans le cadre de notre analyse, à fin de vérification seulement. Nous rappelons que la physique fondamentale (datant de Ludwig et al. 1994) n'a pas été réévaluée dans le cadre de ces travaux. Les valeurs absolues données par les structures 3D doivent être considérées comme une première approximation.

A.1 Structures 3D

De façon similaire à la Figure 5.2, les Figures A.1, A.2 et A.3 montrent, pour les autres modèles 3D, une coupe horizontale$-$verticale de la structure au temps final de la simulation. Ceci permet de mieux comprendre la progression des propriétés de la zone convective d'une naine blanche DA (11,300 K $< T_{\rm eff} <$ 12,800 K). On remarque que la dimension physique de la zone est similaire à toutes les températures. Cependant, cette zone convective, qui ne s'étend que légèrement sous la photosphère ($\tau_R \gtrsim 10$) à 12,800 K, atteint une couche plus opaque ($\tau_R \sim 10^4$) à 11,300 K, et à donc une fraction de masse beaucoup plus grande.

Ce résultat est cohérent avec celui de la Figure 3.5, où on a plutôt utilisé la théorie de la longueur de mélange. Notons qu'il est cependant difficile, avec les simulations 3D, de bien définir l'épaisseur d'une zone convective. Les bulles convectives descendent, sous leur poids, dans une zone stable à la convection ($\partial S/\partial z < 0$, où S est l'entropie). Ce phénomène (en anglais dit "overshooting") n'est pas tenu en compte avec la théorie de la longueur de mélange. Notons finalement, qu'à basse température, la structure convective est plus complexe et la cohérence des bulles convectives est diminuée par la turbulence accrue (Freytag et al. 1996).

A.2 Structures moyennes

Il a été démontré au Chapitre 5 que la moyenne horizontale des structures en 3 dimensions, dénommée $\langle 3D \rangle$, suffisait pour calculer le spectre optique de naines blanches de type DA. Dans cette section, nous discutons plus amplement de ces structures, aussi présentées à la Figure 5.4 en comparaison avec les structures $1D_{\rm MLT}$ calculées avec le cadre de la longueur de mélange. L'écart entre les structures $1D_{\rm MLT}$ et $\langle 3D \rangle$ augmente de façon importante lorsque la température diminue. Ce résultat n'est pas entièrement une surprise en considérant que la zone convective s'élargit également de façon significative dans le même intervalle de températures. De plus, les deux types de structure doivent converger vers une même structure pour $T_{\rm eff} \gtrsim 13,000$ K, lorsque l'atmosphère devient purement radiative. Ce qui surprend davantage est que, bien que l'écart entre les spectres prédits est relativement petit (Figure 5.3), l'écart entre les structures à la photosphère ($0.5 < \tau_R < 5$) peut être très important. Cela découle du caractère non-linéaire de la synthèse spectrale.

Finalement, la comparaison des structures permet aussi de caractériser le haut et le bas de la zone convective ainsi que les conditions frontières des modèles hydrodynamiques. Nous remarquons que l'écart est très important entre les modèles pour $\tau_R < 0.01$, ce qui correspond à une région optiquement mince où le traitement du transfert radiatif dans les modèles 3D influence fortement la structure. C'est dans cette région que se forme le coeur des raies ($\Delta\lambda \lesssim 3$ Å). Sans même tenir compte de la convection, la structure en température et pression de cette région dépend fortement des fréquences qui sont retenues dans le calcul de transfert radiatif, puisque les fortes raies d'hydrogène s'opposent de façon très efficace au rayonnement. Le fait que les modèles non-gris utilisent seulement 7 fréquences moyennées suggère de ne pas mettre trop de poids sur les valeurs absolues trouvées pour cette partie de la structure. Par contre, il est néanmoins surprenant que les différences 1D versus 3D soient grandes puisque dans les deux cas, les mêmes routines pour le transfert radiatif furent utilisées. Une étude plus poussée, dans les modèles 3D, de l'interaction entre le rayonnement et la convection résiduelle en surface, des conditions frontières ainsi que de la turbulence, permettront de répondre à ces questions.

A.3 Figures

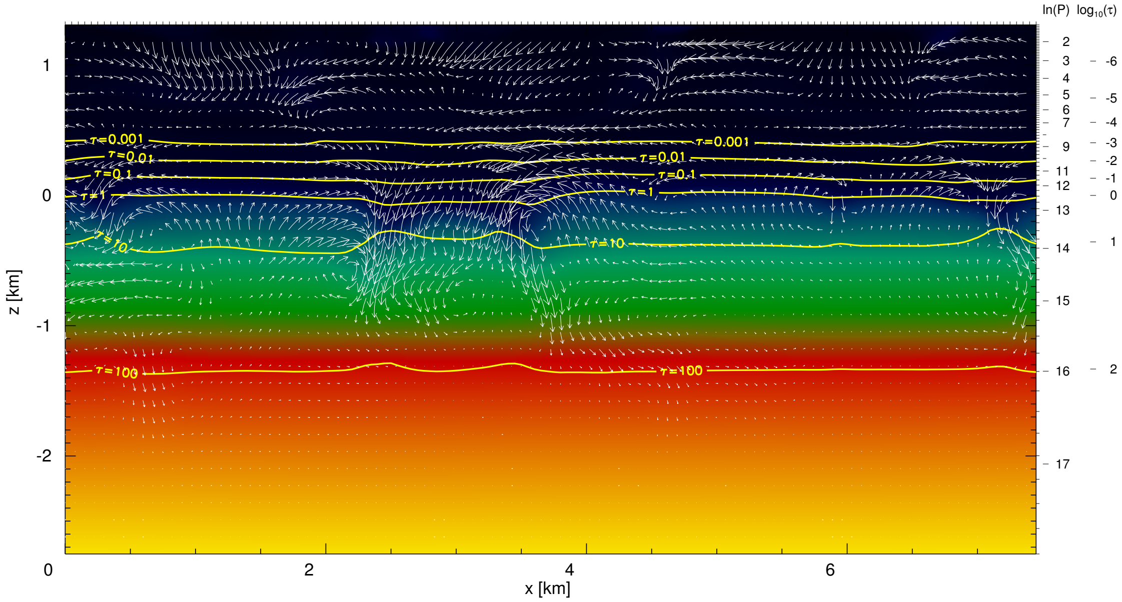

FIGURE A.1 – Similaire à la Figure 5.3 mais pour le modèle à $T_{\rm eff}$ = 12,800 K.

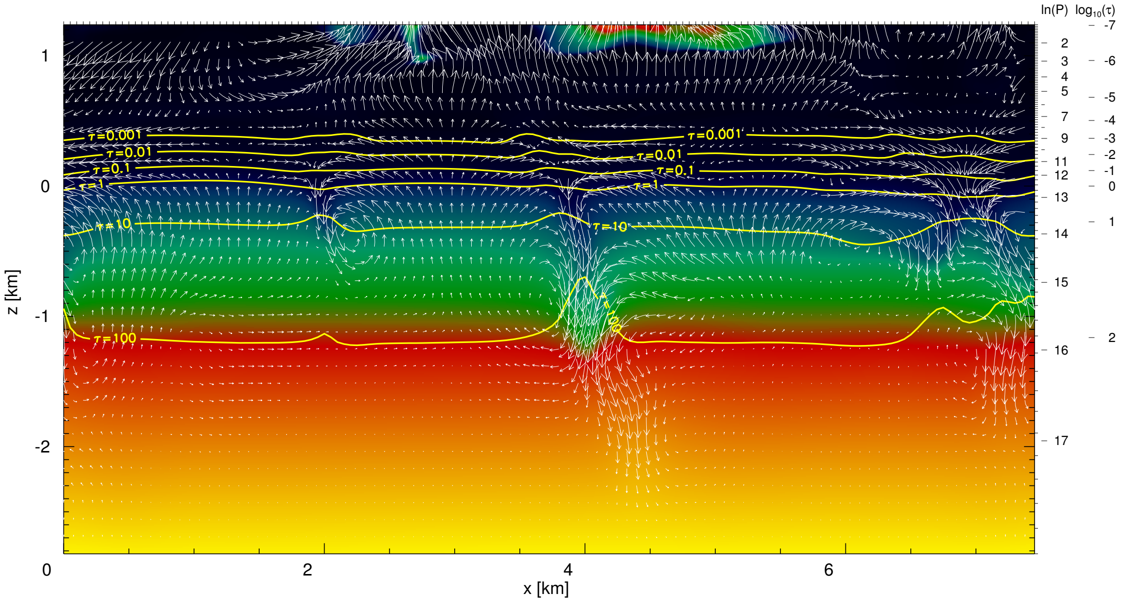

FIGURE A.2 – Similaire à la Figure 5.3 mais pour le modèle à $T_{\rm eff}$ = 12,390 K.

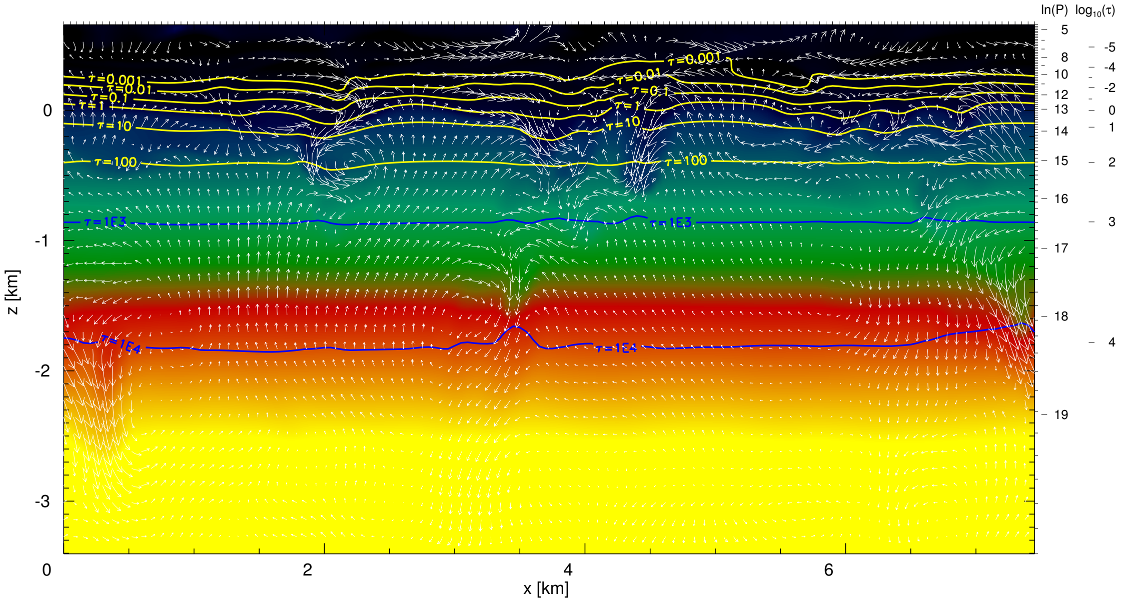

FIGURE A.3 – Similaire à la Figure 5.3 mais pour le modèle à $T_{\rm eff}$ = 11,300 K.